Dynamic Mesh Framework for Morphing Wings CFD

Chawki Abdessemed

Department of Engineering Design and Mathematics

University of the West of England

A thesis submitted in partial fulfilment of the requirements for the degree of Doctor of Philosophy at the University of the West of England

Bristol

May 2019

Abstract

In this work, a framework to perform high fidelity Computational Fluid Dynamics (CFD) analysis of dynamically morphing airfoils and wings is presented. An unsteady parametric method to model the deforming motion is proposed and then implemented in a User-Defined Function (UDF). The UDF is used for driving dynamic mesh in ANSYS Fluent.

First, the framework is applied to a 2D airfoil equipped with a morphing Trailing-Edge Flap (TEF) at a chord-based Reynolds number of 0.675×10^6 for a range of angles of attack (AoA) between 0^o to 14^o and for a morphed airfoil with a maximum trailing edge (TE) deflection equal to 5% of the chord. A numerical validation of the steady and unsteady predictions is then performed against published data. Furthermore, the aerodynamic efficiency of the morphing concept is compared to an airfoil with a hinged TEF. It is found that an average of 6.5% increase in lift-to-drag ratio can be achieved with the morphed flap.

The framework is then used to study the flow response to a 2D downward flap deflection at various morphing frequencies. The slope of time histories of lift and drag coefficients were found to be proportional to the morphing frequency during the morphing phase. Contrary to the lift, however, the drag experiences an overshoot in its instantaneous values, resulting in efficiency loss for all frequencies before settling to a steady state. This finding indicates the presence of unsteady effects that need to be taken into account during the design phase. Qualitative analysis reveals some similarities between rapid morphing and ramp-type pitching motion.

The framework is developed further to study continuous active flow control using a harmonically morphing TEF and its effect on the aerodynamic performance and acoustic spectra. The parametric method is modified to model the low amplitude (0.1 and 0.01% of the chord) harmonic morphing (combined upward and downward motion) in the TEF and the Ffowcs-Williams and Hawkings acoustic analogy was used for noise prediction. For this part of the work, a hybrid Reynolds-averaged Navier–Stokes–Large Eddy Simulation (RANS-LES) model, Stress-Blended Eddy Simulation (SBES), is used. It is shown that the 0.1% morphing

amplitude induces higher sound pressure levels around the morphing frequency, and that all the morphing cases induce a shift in the main tone to a higher frequency, with a 1.5 *dB* reduction in the sound pressure levels. Apart from noise abatement, it is found that for a morphing frequency of 800 *Hz* and 0.01% amplitude it is possible to achieve up to 3% increase in aerodynamic efficiency.

Finally, a framework extension from 2D to 3D is proposed, by extending the parametrization method to model both the morphed TEF and the seamless flap side-edge transition between the morphing and static parts. A comparative study between a wing with a statically morphed flap and one with a hinged flap, at a chord-based Reynolds number of 0.62×10^6, reveals that the morphed flap produces higher lift and lower drag resulting in an enhanced aerodynamic efficiency (C_L/C_D) of up to 40%, for a range of AoA up to 8º with a 5% of the chord flap deflection for both configurations. This enhanced efficiency is mainly due to the absence of gaps and the contribution of the seamless transition to lift generation. The unsteady analysis of the 3D dynamically morphed wing shows the presence of the drag overshoot, which is consistent with the 2D results. Finally, when comparing 2D and 3D CFD results, it is observed that 2D results tend to over-predict both the lift and drag. This is because 2D analysis assumes that the entire span is deflecting whereas the 3D wing would only have a portion of the flap deflecting.

The framework established in this thesis can be easily applied to other types of airfoils, leading-edge morphing, as well as wind and tidal turbine blades.

Acknowledgment

First and foremost, I am profoundly grateful to my director of studies Professor Yufeng Yao for his continuous help, patience, support and technical skills. I am very thankful for my supervisor Dr Abdessalem Bouferrouk for his constant academic and personal support and having his door always open for discussions. I would also like to thank my supervisor Dr Pritesh Narayan for his sound advice and everlasting enthusiasm. This thesis would not have been possible without your guidance and constant support. I consider myself immensely fortunate to have had you as my supervisors.

Above all, I am forever indebted to my parents and siblings, for their understanding, encouragement and indefectible support for all my academic and personal endeavours throughout the years. This effort would not have come to fruition without your support.

My friends and fellow doctoral students also deserve my sincere gratitude. They have helped to provide a great environment to learn, grow and have stimulating discussions. I would like as well to express my gratitude to the staff of the Graduate School at UWE Bristol. Thank you to all who have helped.

Finally, I wish to acknowledge the financial support during my doctoral studies provided by the Engineering Modelling and Simulation Research Group, University of the West of England, Bristol, UK.

Declaration of Originality

I hereby confirm that I am the sole author of the present work and that all the work presented in this thesis was undertaken over the course of my PhD course at The University of the West of England. No portion of this work has been submitted in support of an application for another degree or qualification at any university or other institute of education.

Information derived from the published and unpublished work of others has been acknowledged in the text and a list of references is provided. Proper permissions to reproduce all figures were obtained.

Chawki Abdessemed

Word cloud of the complete thesis where the size of each word indicates the frequency it has been used in the text.

Table of Contents

List of Figures

List of Tables

Nomenclature and Symbols

AoA	Angle of attack, °
c	Airfoil chord length, *m*
C_D	Drag coefficient
C_f	Skin friction coefficient
C_L	Lift coefficient
$C_{L,max}$	Maximum lift coefficient
C_p	Pressure coefficient
f	Morphing frequency, *Hz*
f_s	Shedding frequency, *Hz*
h	Half-amplitude of the control surface deflection
Re	Reynolds number
S	Wing span, *m*
St	Strouhal number
T	Morphing period, *s*
t	Time, *s*
U	Freestream velocity, *m/s*
w_{te}	Non-dimensional maximum TE deflection value
x, y, z	Cartesian coordinates
x_s	Non-dimensional morphing start location
$\overline{x}$	Non-dimensional distance along the chord
y_c	Non-dimensional camber line
y_c	Non-dimensional camber line
y_t	Non-dimensional thickness distribution
y_t	Non-dimensional thickness distribution
$\overline{z}$	Non-dimensional spanwise transition distribution

z_t	Non-dimensional vertical TE displacement for the transition part

Acronyms

AFC	Active Flow Control
AR	Aspect Ratio
BL	Boundary Layer
CAA	Computational Aeroacoustics
CFD	Computational Fluid Dynamics
CST	Class Shape Transform
DES	Detached Eddy Simulation
DNS	Direct Numerical Simulation
DLM	Doublet Lattice Method
FFT	Fast Fourier Transform
FishBAC	Fish Bone Active Camber
FW-H	Ffowcs-Williams & Hawkings
HPC	High-Performance Computing
ITA	Iterative Time Advancement
LBL	Laminar Boundary Layer
LE	Leading Edge
LEV	Leading Edge Vortex
LES	Large Eddy Simulation
LSB	Laminar Separation Bubble
NACA	National Advisory Committee for Aeronautics
NASA	National Aeronautics and Space Administration
NITA	Non-Iterative Time Advancement
NS	Navier–Stokes
PIV	Particle Image Velocimetry
PSD	Power Spectral Density
RANS	Reynolds-Averaged Navier–Stokes

SA	Spalart-Allmaras
SIMPLE	Semi-Implicit Method for Pressure Linked Equations
SBES	Stress Blended Eddy Simulation
SDES	Shielded Detached Eddy Simulation
SPL	Sound Pressure Level
SST	Shear Stress Transport
TE	Trailing Edge
TEF	Trailing Edge Flap
UDF	User-Defined Function
URANS	Unsteady Reynolds-Averaged Navier–Stokes
VLM	Vortex Lattice Method

“Morph /mɔːf/:

From Ancient Greek μορφή (morphḗ, “form, shape”). Undergo or cause to undergo a gradual process of transformation.”

Oxford English Dictionary

1. Introduction

Chapter 1

Contents

1.1. Problem Background

With the steady growth of air traffic around the world, it is anticipated that the passenger demand will double every 20 years (European Commission , 2011; Oxley, 2016). The global demand for air passenger services has also grown significantly, with passenger numbers increasing by 65% in the decade since 2007 (ICAO, 2017). This booming in air traffic would result in an irreversible environmental impact, causing extra CO_2 (152 million tonnes) and NO_x emissions into the atmosphere. This has prompted various regulating organisms, such as the European Commission, to set target goals for the horizon 2020 and 2050 for aircraft efficiency (ACARE, 2010). To keep up with these goals, the ancient quest for efficient flight needs to accelerate.

The traditional design of an aircraft is optimised only for a single design condition for a fixed set of parameters such as altitude, Mach number, or weight. However, during the course of the entire flight profile, these parameters are constantly changing leading to a sub-optimal aircraft operation in off-design conditions.

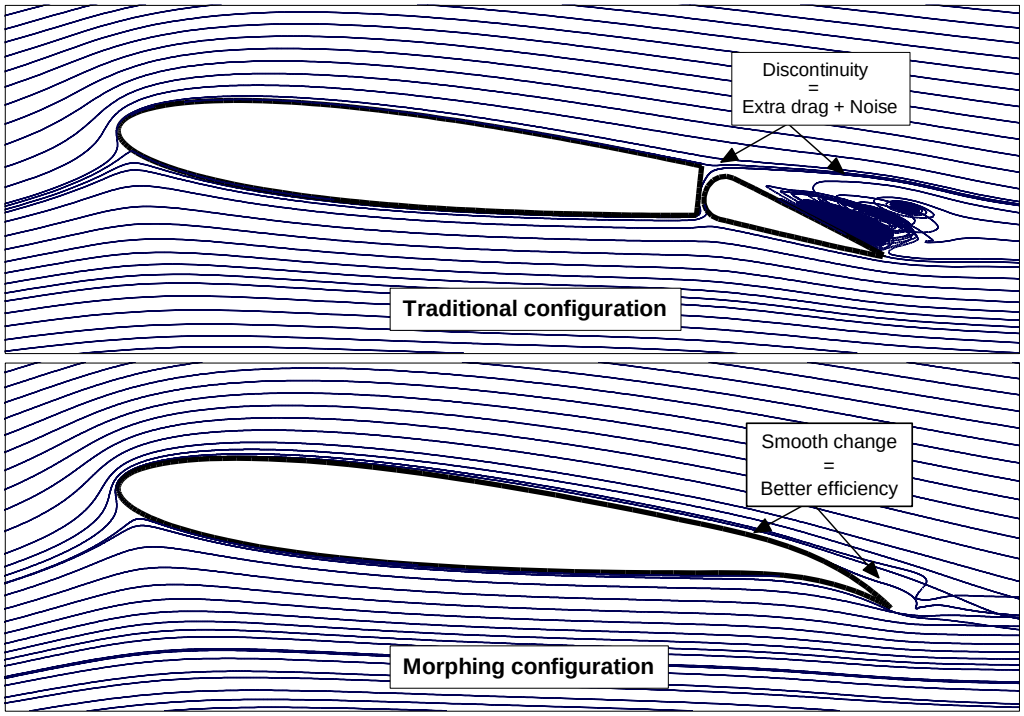

Figure 1.1: Main benefits of morphing wings.

Besides, the presence of discrete surfaces (flaps, slats and ailerons) creates instabilities and recirculation regions in the flow, which contribute to the drag and airframe noise (Macaraeg, 1998). All these factors increase drag, leading to extra fuel burn and more polluting fumes, in addition to the extra noise pollution. This major disadvantage could be alleviated by integrating smart adaptive wing structures, more commonly known as morphing wings. These wings could be optimised seamlessly in-flight depending on the flight condition, which would produce superior performances at off-design points or achieve design conditions with less drag and noise. Such technology would also enable smooth seamless and gapless lifting surfaces that would contribute to the reduction of pressure drag and aerodynamic noise by filling the gaps formed by discrete surfaces (Khorrami *et al.*, 2014a; Woods *et al.*, 2016; Kudva, 2004). **Error! Not a valid bookmark self-reference.** illustrates how morphing could eliminate the discontinuities and gaps present in traditional configurations

Coupling the benefits obtained by the use of "passive" morphing structures (i.e. streamlining the geometry by filling various gaps) with Active Flow Control (ACT) devices would provide extra aerodynamic enhancements and noise reduction, which will significantly increase aircraft efficiency contributing to the future green aircraft goal. Overall, the following advantages are expected from morphing wings:

- Higher aerodynamic efficiency due to the optimised lift to drag ratio, which would lead to an extended cruise range (Szodruch and Hilbig, 1988; Urnes and Nguyen, 2013; Monner *et al.*, 2000)
- Reduction in aerodynamic noise (Khorrami *et al.*, 2014a)
- Use of smart materials would significantly reduce the weight by eliminating the need for complex hydraulic actuators (Barbarino *et al.*, 2011)
- More operational flexibility would be gained with mission adaptability (Peter and Stumpf, 2018)

Despite recent efforts, there remain some key challenges that hinder the implementation of morphing technology. For a start, more research to develop

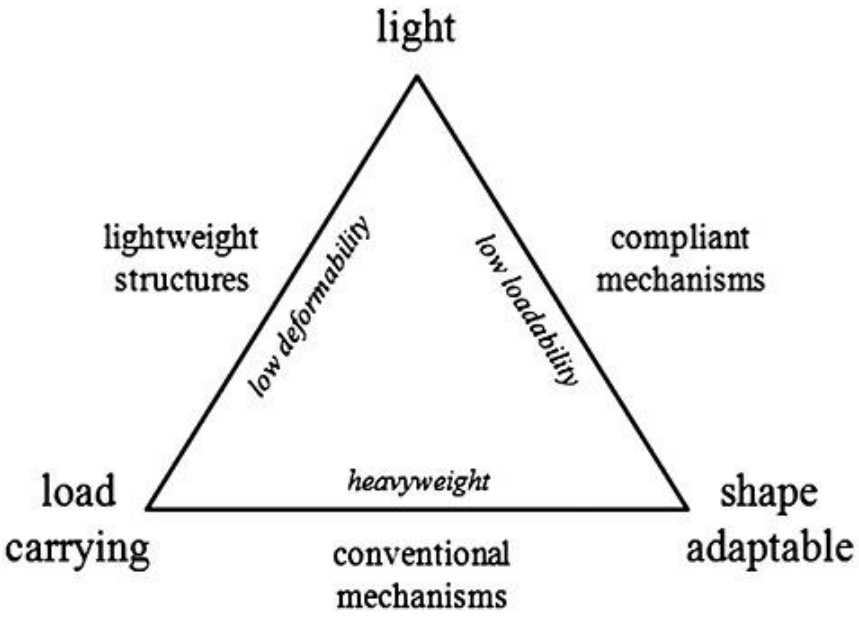

Figure 1.2:Diagram illustrating criteria that need to be fulfilled by any morphing structure (Lachenal et al., 2013). (Used with permission of the publisher)

smart morphing materials is still needed, which will provide information about materials suitability and behaviour under real-life operating conditions (e.g. fatigue, maintenance, reliability). Also, appropriate structural balance should be maintained to obtain morphing mechanisms which are load carrying, adaptable and relatively lightweight as illustrated in Figure 1.2 (Lachenal *et al.*, 2013). In addition, the material used depends on the mission targeted, since morphing structures could be utilized in a passive or active manner, so there is a need for careful matching between the adaptable structures and various loads, as illustrated

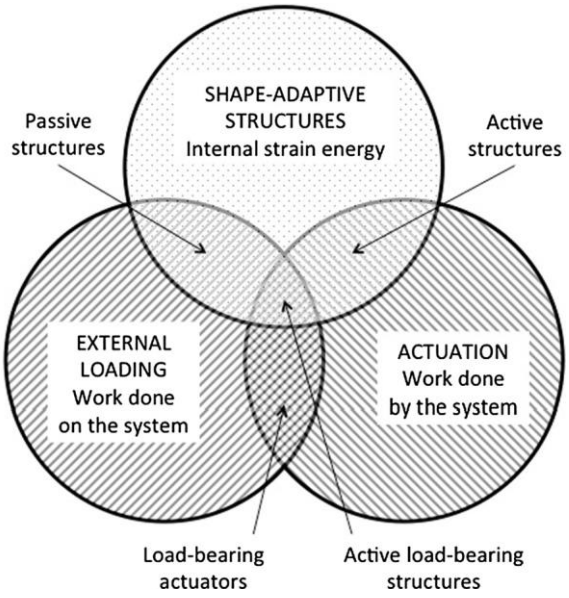

Figure 1.3: The interaction between an adaptive structure, its external loading and actuation for a generic morphing system (Nicassio et al., 2018) . (Used with permission of the publisher)

in Figure 1.3.

Innovative control strategies and algorithms need to be tailored for the innumerable applications of morphing i.e., to optimise geometry shapes, and to drive the appropriate actuators necessary for morphing realisation. Morphing control needs to take into account this distinct class of problems as it may involve large deflections mid-flight, open loop geometry optimization, in addition to flight control. Various approaches have been considered in an effort to tackle the problem of morphing flight control such as the independent flight control or the integrated shape flight control, which are illustrated in Figure 1.4 (Seigler *et al.*, 2007). These

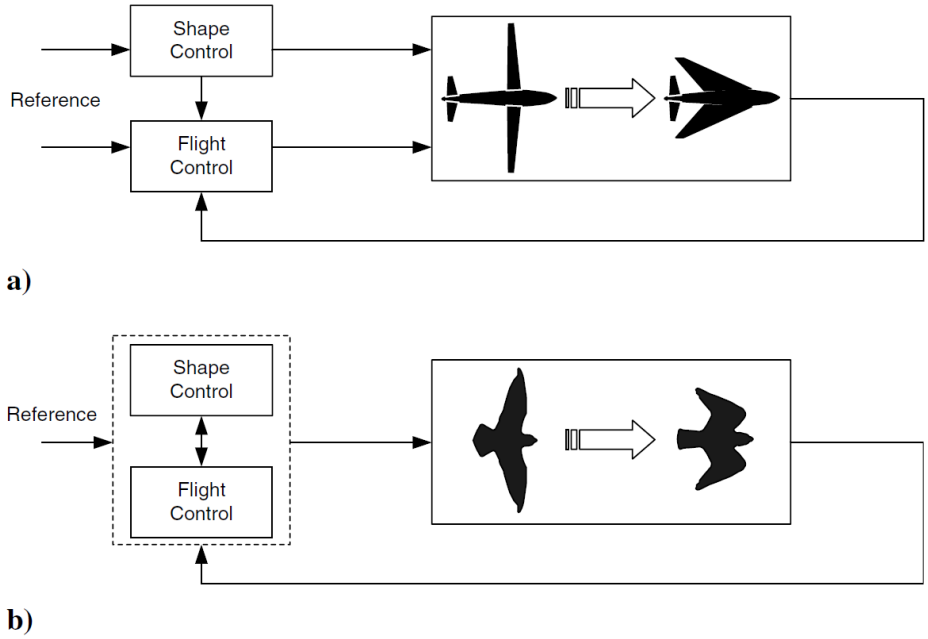

Figure 1.4: Methods of morphing flight control: a) independent shape and flight control, b) integrated shape and flight control (birdlike flight) (Seigler *et al.*, 2007). *(Used with permission of the publisher)*

approaches are still being explored and augmented with the use of artificial intelligence and reinforced learning (Lampton *et al.*, 2010; Valasek *et al.*, 2008).

Most importantly, however, a deeper understanding of the aerodynamic behaviour of morphing configurations, a realistic aerodynamic load representation, and accurate predictions of time dependent lift and drag would primarily provide engineers with greater insight into the physical effects of morphing, leading to an optimal use of this technology. Figure 1.5 summarises the effect of an enhanced aerodynamic understanding on the rest of the involved fields.

That is why the work presented in this thesis will exclusively focus on the aerodynamics of morphing wings, specifically for enhancing aerodynamic efficiency and noise reduction.

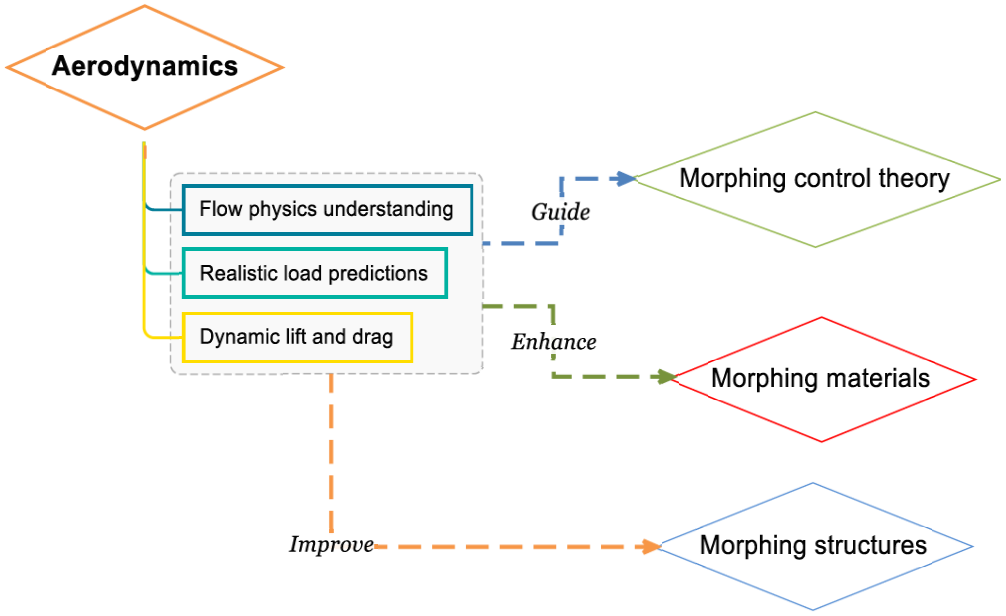

Figure 1.5: Effect of an enhanced aerodynamic understanding on the rest of the involved fields.

1.2. Motivations of the research project

The aerodynamic modelling of morphing wing vehicles brings its fair share of challenges. Large and rapid deformations of a wing moving at high speed strongly influence the aerodynamics; this has contributed to the added complexity of morphing wings aerodynamic analysis. However, focusing on the aerodynamic aspects of morphing has several advantages:

- A deeper understating of the underlying flow physics created by morphing mechanisms would enable the utilization of their full potential which would enhance the expected benefits (e.g. higher efficiency, efficient use of active flow control)
- The ability to predict correctly the time history of the forces (lift, drag) and moments acting on a wing while deforming would provide multidisciplinary benefits i.e., in control algorithms, material science and structural design (Figure 1.5)

- Most importantly, an accurate analysis of morphing wings would provide a better estimate of the aerodynamic performance expected from the use of such configurations making a stronger case for its adoption in future aircraft

Being confident about the flow understanding and the accuracy of predictions would inform as to whether the benefits of using morphing wings would surpass the penalties of added weight and complexities of the systems. Therefore, it would ensure that the investments in fields such as structures, materials and control systems are worthwhile.

Development of numerical analysis tools such as CFD can be an enabler for accurate aerodynamic loads predictions and a deeper understanding of the flow behaviour during the morphing motion, which will be crucial for the design optimization of the wing. Therefore, the scope of this project will focus on the following points:

- Development of a CFD framework that incorporates mathematical modelling of the geometry deformation, dynamic mesh and a high-fidelity solver with the inclusion of aeroacoustics modelling when required
- Physical understanding of the flow response to the morphing motion

1.3. Research Objectives

The main aim of this research is the development of a CFD tool that includes a model for geometry deformation, dynamic meshing and integration with a high-fidelity solver for performance prediction of the aerodynamic behaviour of a morphing wing configuration during the deformation process. This would be achieved by targeting the following objectives:

- A comprehensive literature review of the published research in the field of numerical modelling of morphing wings to gain an understanding of the issues surrounding morphing wing CFD and the challenges facing various numerical approaches in order to identify suitable choices and suggest areas of improvements.

- An appropriate parametrization method will be chosen, and modified, in order to account for unsteady deformation of the morphing wing geometry during the morphing process.
- To perform unsteady analysis of adaptive wings, dynamic meshing will be considered, to account for shape changing geometry in 2D and 3D. To do this accurately, it will be important to create a high quality deforming mesh that captures the fine details of unsteady flow.
- Geometry deformation and meshing tools will be integrated with a suitable high fidelity CFD solver that will have the capabilities to solve this class of problems.
- Deliver a comparative study between higher accuracy CFD methods, which take into account unsteady effects, and the ones already explored in the literature (i.e. static morphing) to observe the fundamental differences between the two methodologies.
- Consider the use of morphing wing/flap as an active flow control device for influencing both the aerodynamic and aeroacoustic characteristics, in addition to passive morphing using the developed framework.
- Conduct parametric studies in order to determine key parameters and their effects on the aerodynamic and aeroacoustic performance of airfoils/wings which would provide general guidelines for practical implementation

1.4. Research Novelty and List of Publications

The main novelty of this work is the development of a framework comprising of a modified unsteady parametrization method for airfoils equipped with a morphing Trailing-Edge Flap (TEF) concept. The parametrization, which relies on defining geometry based on thickness and camber distributions, was adapted from an existing method in order to account for real time, unsteady deformation. In order to implement the parametrization method in the commercial software ANSYS Fluent (ANSYS, 2018), an in-house User-Defined Function (UDF) was developed. The UDF then drives the dynamic mesh schemes implemented in the software to provide the mesh deformations needed.

The framework was applied to various problems including: 1) 2D analysis of a dynamically morphing TEF with a low morphing frequency and high amplitude downward deflection. 2) The study of an Active Flow Control (AFC) concept based on harmonic morphing (high frequency, low amplitude oscillations) to explore both aerodynamic and aeroacoustic effects of such a concept. 3) The parametrization method was further modified and implemented to model a 3D morphing wing with seamless side-edge transitions.

The following list of papers validates the originality of the work:

Journal papers

- Abdessemed, C., Yao, Y., Bouferrouk, A., and Narayan, P.,(2017) "Morphing Airfoils Analysis Using Dynamic Meshing" *International Journal of Numerical Methods for Heat and Fluid Flow*. , Vol. 28 Issue: 5, pp.1117-1133. doi.org/10.1108/HFF-06-2017-0261

- Abdessemed, C., Bouferrouk, A., Yao, Y., and Narayan, P., "Dynamic Meshing Based Framework for the Aeroacoustic Analysis of Harmonically Morphing Trailing-Edge Flaps." *Aerospace Science and Technology*. (Under review).

- Abdessemed, C., Bouferrouk, A., Yao, Y., and Narayan, P., "Dynamic Morphing Effect on Flow Characteristics near Stall." *International Journal of Numerical Methods for Heat and Fluid Flow*. (Under review)

- Abdessemed, C., Yao, Y., Bouferrouk, A., and Narayan, P., "Effects of an Unsteady Morphing Wing with Seamless Side-edge Transition on the Aerodynamic Performance" *Chinese Journal of Aeronautics*. (prepared for submission)

- Abdessemed, C., Yao, Y., Bouferrouk, A., and Narayan, P., Influence of Non-Iterative Time-Advancement Schemes on the Aerodynamic Prediction of Pitching Airfoils Using Dynamic Mesh" *Computers & Fluids*. (prepared for submission)

Conference Papers

- Abdessemed, C., Yao, Y., Narayan, P. and Bouferrouk, A. (2017) "Unsteady parametrization of a morphing wing design for improved aerodynamic performance" In: *52nd 3AF International Conference on Applied Aerodynamics, Lyon, France, 27-29 March 2017*.

- Abdessemed, C., Yao, Y., Bouferrouk, A. and Narayan, P. (2018) "Aeroacoustics Investigation of A Harmonically Morphing Trailing-Edge Flap". In: 53rd 3AF International Conference on Applied Aerodynamics, Salon de Provence, France, 26 – 28 March 2018.

- Abdessemed, C., Yao, Y., Bouferrouk, A. and Narayan, P. (2018) "Analysis of a 3D Unsteady Morphing Wing with Seamless Side-edge Transition". In: *2018 Applied Aerodynamics Conference Atlanta, Georgia, 25 - 29 June 2018. doi: 10.2514/6.2018-3178*

- Abdessemed, C., Yao, Y., Bouferrouk, A. and Narayan, P. (2018) "Aerodynamic Analysis of a Harmonically Morphing Flap Using a Hybrid Turbulence Model and Dynamic Meshing", In: *2018 Applied Aerodynamics Conference Atlanta, Georgia, 25 - 29 June 2018. doi: 10.2514/6.2018-3813*

- Abdessemed, C., Yao, Y., Bouferrouk, A., and Narayan, P., (2019) "Flow Response to Rapid Morphing Flap Deflection", in: *54th 3AF International Conference on Applied Aerodynamics, Paris, France, 26 – 28 March 2019.*

- Abdessemed, C., Yao, Y., Bouferrouk, A., and Narayan, P., "Influence of Non-Iterative Time-Advancement Schemes on the Aerodynamic Prediction of Pitching Airfoils Using Dynamic Mesh" *8th International Symposium on Physics of Fluids (ISPF8). 10-13 June, 2019, Xian, China.*

1.5. Structure of the Thesis

The structure of the subsequent chapters is given in this section to guide the reader on how the research is structured.

Chapter 2 –*Literature Review*

A brief history of the evolution of morphing concepts is first presented, along with key definitions, classifications and several concepts of adaptive wings and morphing high-lift devices are described. Afterwards, a systematic review of the numerical methods applied to morphing wings is detailed ranging from low to high fidelity methods. For the sake of completeness, a brief overview of experimental work and prototypes tested in wind tunnels is given, additionally, Active Flow Control (AFC) is defined, and then a state of the art of harmonic AFC is briefly presented. Moreover, the studies focusing on side-edge transitions are reviewed. Finally, knowledge gaps are identified and the focus of this research is outlined.

Chapter 3 – *Theoretical Background*

This chapter covers a few of the theoretical concepts on which various numerical analyses rely. Starting with the governing equations of fluid flow along with the turbulence models addressed in this work. Additionally, a brief overview of parametrization methods, dynamic meshing theory and the commercial solver used in this work is presented.

Chapter 4 – *Framework Development and Validation for Dynamic Morphing CFD Analysis*

In this chapter, a framework for the study of dynamic morphing airfoils is developed, a modified unsteady parametrization method is introduced and detailed, along with its implementation in a UDF. Afterwards, validation and verification of the framework is carried out. First, a steady state CFD study verifying the validity of the deformed mesh is performed, then a study comparing the aerodynamic performance of an airfoil equipped with a morphing Trailing-Edge Flap (TEF) to an airfoil with a hinged flap is conducted, and results are cross-validated with

published numerical data. In addition, dynamic mesh-based unsteady predictions are validated against experiments data. Finally, the framework is applied on a test case as a proof of concept.

Chapter 5 – *2D Downward Dynamic Morphing Flap*

The framework developed in Chapter 4 is applied in this chapter to perform a parametric study showing the forces (lift and drag) and flow response to various morphing frequencies of a 2D downward deflection. First, the problem is defined and the computational setup detailed, mesh quality before and after deformation is assessed. Finally, the results are presented and discussed.

Chapter 6 – *2D Harmonic Morphing Trailing-Edge Flap*

In this chapter, a numerical framework for the aerodynamic and aeroacoustic study of harmonically morphing TEFs is introduced. The unsteady parametric method introduced in Chapter 4 is further modified to model the harmonic morphing.

Afterwards, a brief theoretical background for the Ffowcs-Williams and Hawkings (FW-H) acoustic analogy used for the far-field noise prediction is presented. Finally, the framework was used to perform a parametric study of the effects of the morphing frequency and amplitude on the aerodynamic and aeroacoustic performance of a harmonically morphing TEF.

Chapter 7 – *Morphing Wing with Seamless Side-edge Transition*

An extension from 2D to 3D is proposed for the investigation of morphing wings with a seamless side-edge transition. First, an unsteady parametrization method for the side-edge transition based on previous concepts is introduced. Furthermore, a steady state comparative CFD study to compare the aerodynamic performance of the morphing wing against a hinged flap configuration is presented. Finally, dynamic morphing is applied and the effects of various frequencies are investigated.

Chapter 8 – *Conclusion & Future Work*

The main findings of this research work on morphing wings are summarised and discussed in this last chapter, and recommendations to guide future investigations are suggested beyond symmetrical airfoils, morphing TEF or aerospace.

“Not everything that can be counted counts and not everything that counts can be counted.”

Albert Einstein

2. Literature review

Chapter 2

Contents

2.1. Overview

This chapter will mainly focus on the state of the art of the aerodynamic techniques previously applied in morphing research. It will start with a brief history of the evolution of morphing concepts (section 2.2), then a systematic review of the numerical methods used for morphing wings studies is presented (section 2.3) from low-order methods to higher-fidelity methods, afterwards, a brief overview of experimental work and prototypes tested in wind tunnels along with side-edge transition prototypes (section 2.4). Finally, Active Flow Control (AFC) is defined in Section 2.5.1, and then a state of the art of harmonic AFC is provided in Section 2.5.2.

2.2. A Brief History of Morphing Wings

2.2.1. What are morphing wings?

The configuration where the wing can be deformed, actively or passively, is commonly referred to as morphing, which is a diminutive for metamorphose. In Aerospace, various definitions are used to define a morphing wing; Weisshaar (2006) defined morphing as "*a set of technologies that increase a vehicle's performance by manipulating certain characteristics to better match the vehicle state to the environment and task at hand"*. However, there is consent in the aeronautical community to use the morphing term not for variable wing aircraft for instance but for more drastic geometry deformation.

DARPA's Morphing Aircraft Structures (MAS) defines the morphing wing aircraft as a multi-role platform which changes its state substantially to adapt to changing mission environments and provides capabilities that could not be provided by a classical configuration (Seigler, 2005). Typically, morphing technology integrates a combination of advanced smart materials, actuators, and flow controllers to achieve the required adaptability.

Why do we need morphing wings?

Using adaptive wings would allow for improvement of the aerodynamic performance in off-design operating conditions by adjusting the wing surfaces in real time to the changes occurring in freestream (flight) conditions (Stanewsky, 2001). The ability to do this will not only result in aerodynamic performance gains during cruise and various manoeuvres (Smith and Nelson, 1990), but would improve the structural design and reduce airframe weight.

Many researchers have focused on adaptive structures and morphing wings to prove their possible benefits. Wittmann *et al.* (2009) showed that a 23% improvement in lift-to-drag ratio was achievable when morphing parameters were optimized. Moreover, maximizing wing area and camber could yield a 74% increase in lift coefficient. Smith *et al.* (2007) demonstrated that the improved aerodynamics resulting from the use of morphing wings could outweigh the penalties related to additional weight and energy consumption; for instance, an air-to-air fighter could cut around 22% of fuel consumption using morphing technology even with a weight factor of two and an actuation penalty of 10%.

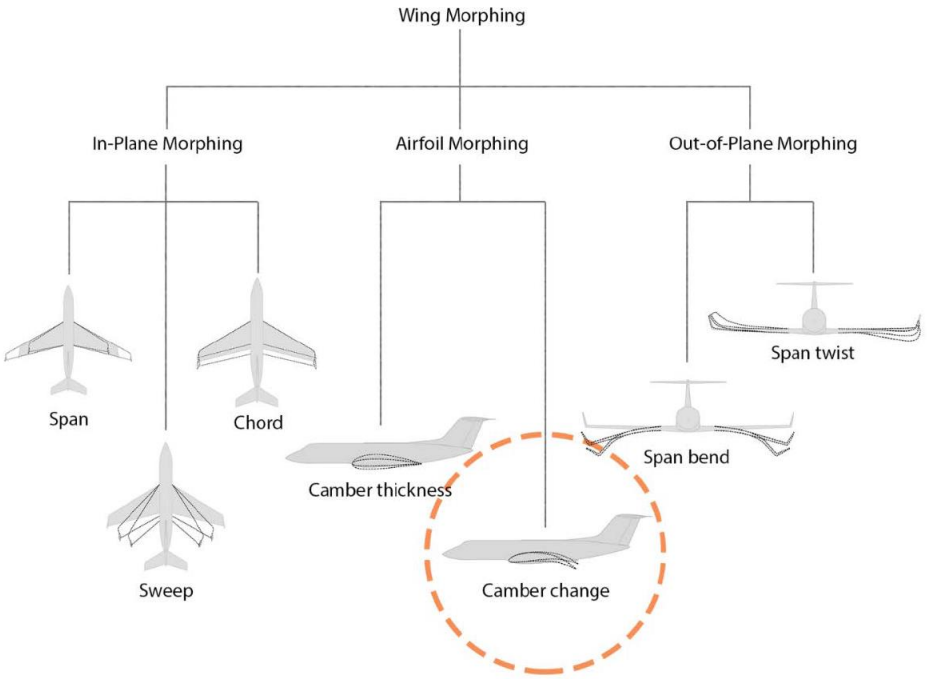

Figure 2.1: Classification of wing morphing classes with an emphasis on camber change configuration investigated in this work (La et al.*, 2018). (Used with permission of the publisher)*

Finally, the use of morphing wings could save about 5% of the fuel burned for a medium range transport aircraft, where even a 1% reduction in fuel consumption could save $140 million/year for the US fleet (Barbarino *et al.*, 2011).

Several comprehensive reviews of morphing aircraft have been conducted, where the classification of morphing technologies is based on the geometrical aspect being morphed. Three major classes of morphing are usually identified:

- *Planform morphing*: which involves a variable span, chord elongation or sweep changes
- *Out of plane transformation*: which includes twist, dihedral/gull, and spanwise bending
- *Airfoil morphing*: includes mainly the variable camber concepts or variable thickness

A few combinations of the above concepts have also been proposed in order to fully harness morphing capabilities as illustrated in Figure 2.1. However, in the current work, the focus is on variable camber concept as shown in Figure 2.1 with a dashed circle. This choice is justified by the fact that camber morphing offers the possibility to adapt a given wing to a wide range of flight conditions by optimizing its aerodynamic efficiency which would result in significant fuel savings. This made variable camber an optimal morphing method to investigate.

2.2.2. History of morphing wings

Origin in Bio-inspiration

Morphing wings have been around long before the first human attempted to fly, as the concept is inspired primarily from nature. Most natural flyers (insects, birds, bats or even extinct Pterosaurs) used this mechanism in order to harness the full capabilities of their wings, and exploit all the unsteady aerodynamic effects (e.g. lift enhancement by using leading-edge vortices (Muijres, Johansson and

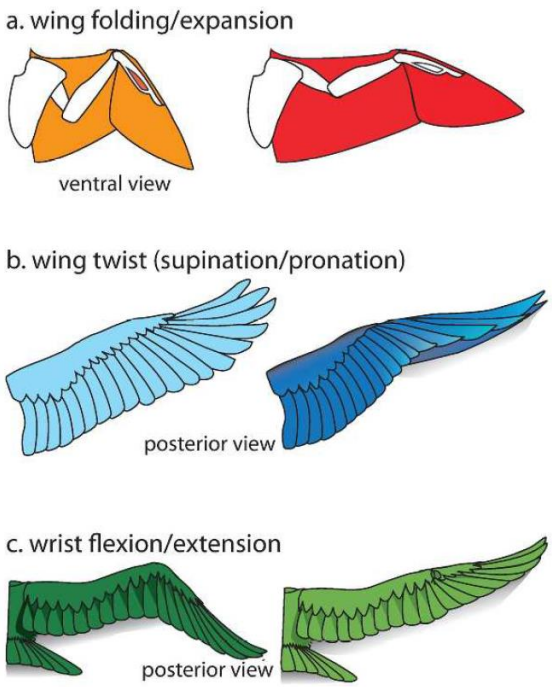

Figure 2.2: Various aspects of active morphing in nature's flyers (Altshuler *et al.*, 2015). *(Used with permission of the publisher)*

Hedenstrom, 2012)) to their advantage, while spending the least energy possible (Taylor *et al.*, 2012).

Morphing in its broadest sense is omnipresent in nature's flyers and across a large scale of sizes. Insects such as locusts have a variable camber, which changes depending on the stroke. In downstroke for instance, the wing has an increased positive camber to resist inertia and drag (Keil, 1997; Wootton, 2006; Wootton *et al.*, 2000). It is worth noting that a positive camber of a wing means that the upper surface is the more convex whereas a negative camber is the opposite.

The same insect is equipped with variable planform where wings are pulled in, which helps to minimize drag during the upstroke (Walker, Thomas and Taylor, 2009). Additionally, some insects, like the hoverfly, have wings capable of spanwise twist which enables them to produce 10% more lift requiring 5% less power compared to a rigid wing (Ennos, 1995; Walker, Thomas and Taylor, 2010; Du and Sun, 2010).

Birds, with the help of their feathers, can accomplish one of the most bewildering display of morphing wings (and tail) in nature, as they have the ability to rapidly switch between various planform and camber (Tucker and Heine, 1990; Tucker, 1992). They also can adapt their wing span by bending their wings which enable them to perform manoeuvres such as perching where they intentionally stall to produce a high drag needed for aero-braking (Carruthers *et al.*, 2010). Variable camber is widely prominent in birds as well, e.g. high photometry methods were used in order to capture the camber change in steppe eagles during perching, allowing them to adapt to a wide range of missions (Carruthers *et al.*, 2010). Figure 2.2 shows various aspects of morphing present in birds (Altshuler *et al.*, 2015).

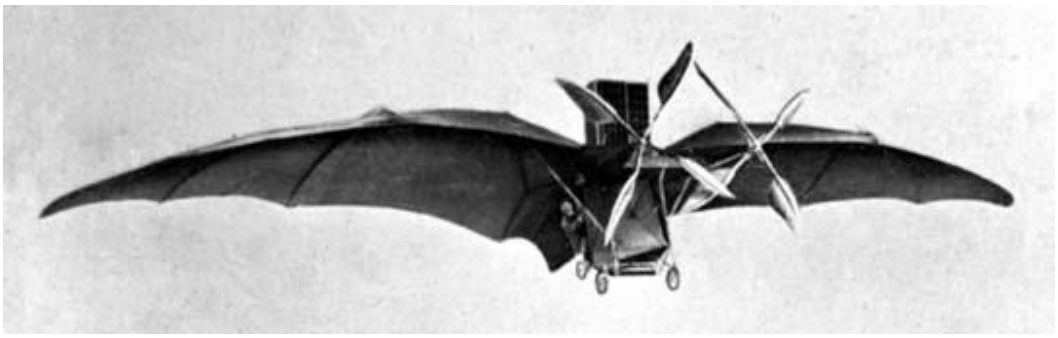

Figure 2.4: Clement Ader Avion III (Ader, 1897).

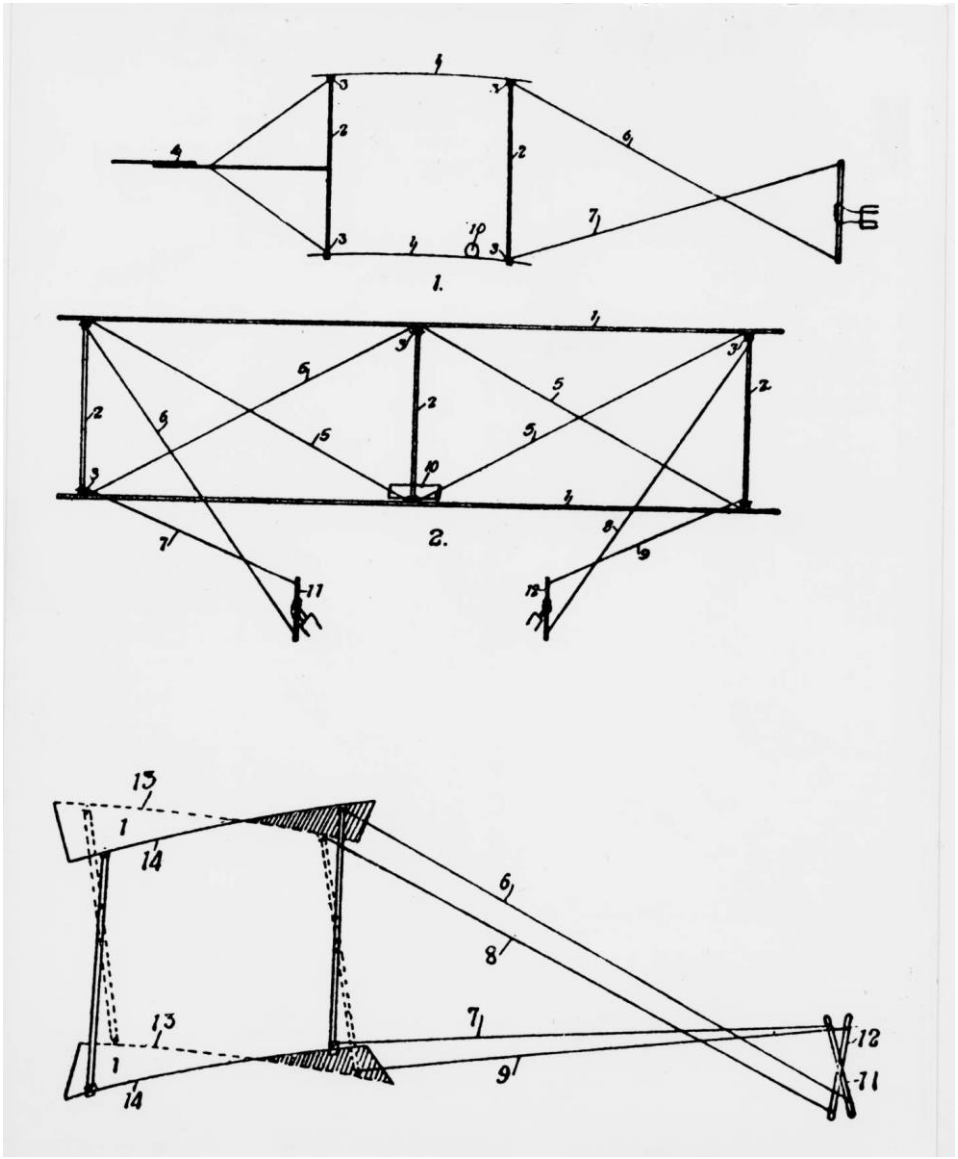

Figure 2.3: Sketch of the wing-warping concept developed by the Wright brothers (Smithsonian, 1899).

Finally, a bat wing planform changes significantly during various phases and manoeuvres. For instance, they reduce the wing span during the upstroke for the purpose of drag reduction, likewise they use their wings deformations in order to modulate lift, drag or pitching moment (Hubel *et al.*, 2010; Bowman, Sanders and Weisshaar, 2002).

Aviation pioneers took inspiration from the aforementioned mechanisms to pursue their endeavour to build a heavier than air flying machine. This inspiration started from the early years of aviation, which were mainly bio-inspired with several attempts of biomimetic.

Before the first controlled human flight, an experiment was conducted by Clément Ader in France where he proposed a morphing wing design as early as 1890 based on Bat wings (Figure 2.4) that could reduce its size to half or one-third of its full deployment (Weisshaar, 2006). Moreover, unlike current conventional aircraft, the Wright brothers did not have any hinges or moving ailerons in their first Flyer, but instead they controlled the aircraft using wires and pulleys that bent and twisted

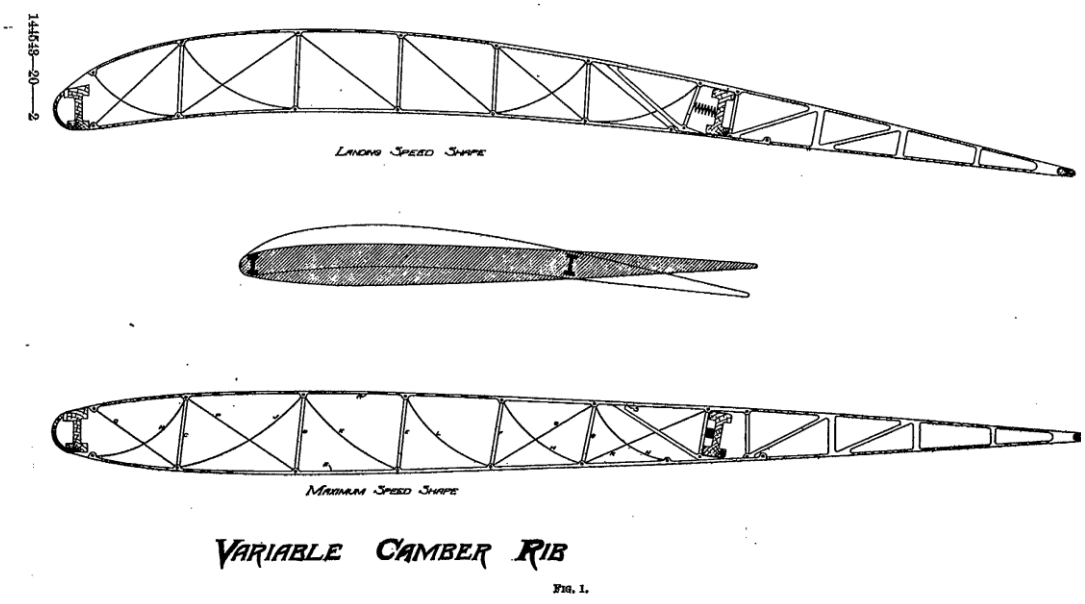

Figure 2.5: Sketch of the variable camber wing designed by H.F. Parker (1920).

the wood and canvas wings, efficiently using wrapping for aircraft control (Figure 2.3).

Soon after the Wright flyer, Parker (1920) presented his design of a variable camber wing, which allowed the wing to cope with the various speeds required during a typical flight. The design consists of combining a flexible wing portion placed between a spar at the leading edge and another rear spar at 2/3 of the chord and a rigid portion behind the rear spar (Figure 2.5). This model would passively deform depending on the load acting on it. At larger AoA (e.g. landing), the camber increases coping with lower velocity needs, while at maximum velocity (e.g. cruise) the wing stands at its optimised shape for minimum drag (Parker, 1920; Concilio and Lecce, 2018).

Parker's vision for the variable morphing wing did not spread into the aircraft design of that time, due to the lack of compliant structures capable of withstanding higher aerodynamic loads at high speeds. This requirement made the full morphing mechanisms (such as Parker's wing) unfeasible, which led to the use of rigid, metallic, variable surface and discreet hinged parts such as ailerons and rudders or flaps, which permitted fight control and provided the geometry change needed to adapt it to certain flight conditions (take-off, landing). Thus, with the advent of these rigid metallic structures, the future of morphing was limited with respect to geometry changes by means of various combinations and arrangements of conventional hinges, pivots and rails rather than wrapping, twisting or camber change.

The Pterodactyl IV tailless monoplane was probably one of the first airplanes to have variable sweep (Weisshaar, 2006). It was first flown in 1931. Another span-varying configuration, which was pioneered in France around 1933, was the Makhonine MAK-101; its main aim was to improve cruise performance by reducing the induced drag which is achieved by a variable span (i.e. increased span in cruise).

Variable geometry configuration was used later on as a means to achieve supersonic flight and to achieve laminar flow over the wing body such as the Wild

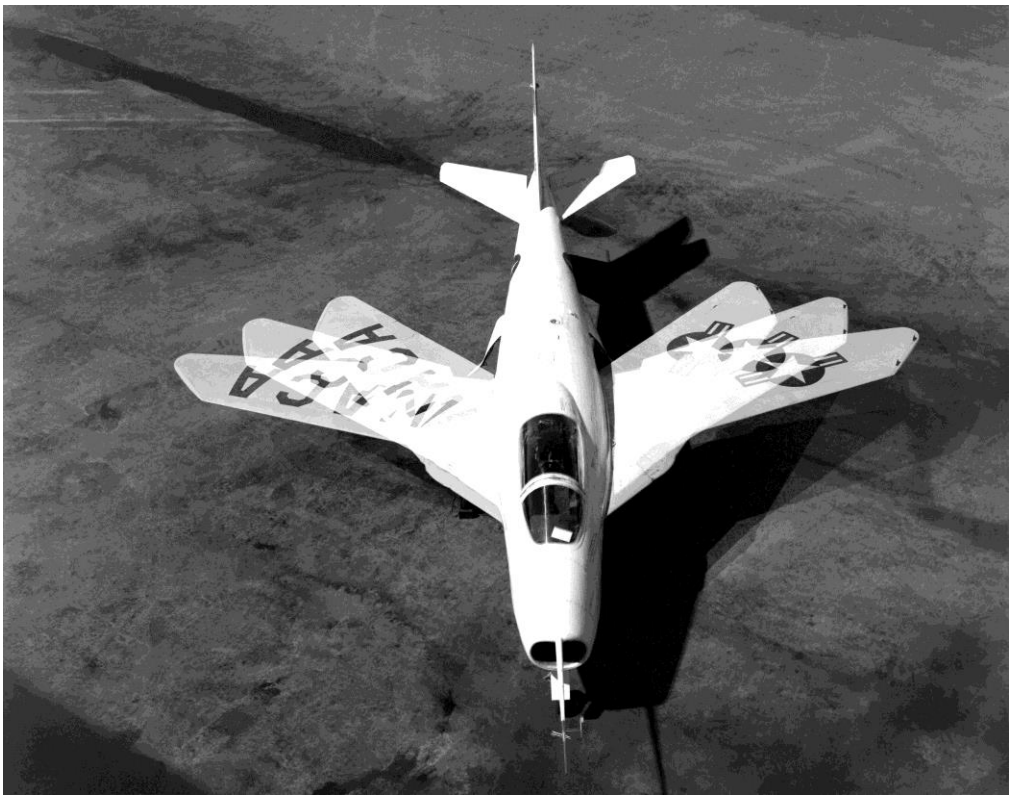

Figure 2.6: Bell X-5 showing variable sweep wing positions (NASA, 2006) (Public domain).

Goose which was a supersonic concept with a slender laminar flow body and swing-wings (Valasek, 2012). It inspired several designs afterwards such as the Bell X-5 (Figure 2.6) which was the first full scale aircraft to be flown with the capabilities of sweeping wings, the performances were improved in both low and high speeds, fully extended wings improved the take-off and landing performances and with the wing swept back drag was reduced in high speeds.

Meanwhile, the continuous technological progress made in aerospace structures and actuations powered by the everlasting need for better performance motivated many players in the industry to re-explore morphing concepts. NASA contracted Boeing in the 80s in order to assess the aerodynamic gains obtainable from such concept. The design in question is illustrated in Figure 2.7, it aims to seamlessly deform the leading and trailing edge in various flight stages (take-off, cruise, landing) in order to optimize fuel saving and aerodynamic performance. These

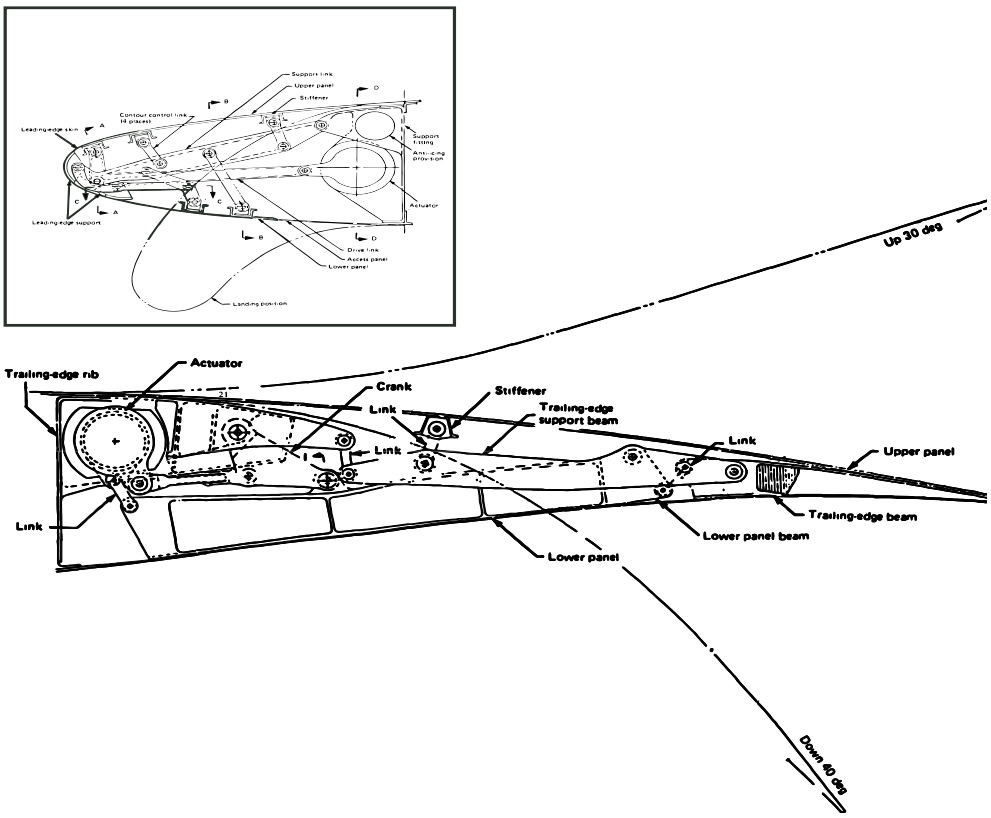

Figure 2.7: Leading-Edge (LE) and the Trailing-Edge (TE) mechanisms for the NASA variable camber concept (Brissenden et al., 1980). ©NASA

development efforts around continuous morphing culminated in the ambitious Mission Adaptive Wing (MAW) project (Brissenden *et al.*, 1980).

The AFTI F-111 Mission Adaptive Wing (MAW) experimental aircraft paved the way to incorporate more morphing strategies (Figure 2.9). It incorporated a variable camber concept in addition to traditional variable geometry (Bonnema and Smith, 1993). MAWs have an arrangement of internal rods and linkages, powered by hydraulic actuators, which allows the mechanism to bend the wing into different chord wise shapes (Figure 2.8). The ability to achieve the seamless in-flight wing optimization would effectively put under disposition a family of wings that could be optimized for minimum drag depending on the mission profile or objective as illustrated in the minimum drag envelope in (Figure 2.8) (Concilio and Lecce, 2018).

Figure 2.9: MAW airfoil cross-section in its deformed, cambered position (Weisshaar, 2006).©NASA

This concept optimized its camber in-flight for various targets; peak aerodynamic efficiency, manoeuvre enhancement, and gust alleviation over a range of speeds by deflecting both the Leading-Edge (LE) and the Trailing-Edge (TE) while conserving a smooth seamless continuity of wing surface (Weisshaar, 2006; NASA, 2015). Several test flights of the AFTI F-111/MAW (Figure 2.10) have

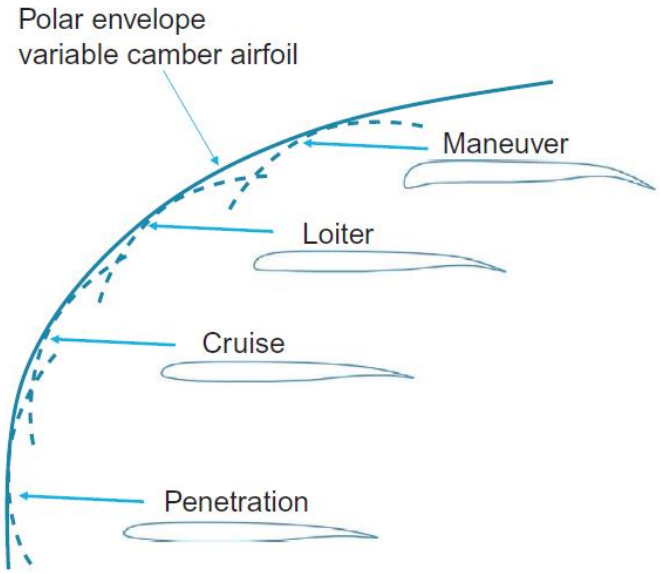

Figure 2.8: Minimum drag envelope for variable camber wings (Bonnema and Smith, 1993). *(Used with permission of the publisher)*

been performed to validate wind tunnel experiments and to assess realistic benefits such systems could offer. Nevertheless, the complexity and the extra weight added by the actuators and extra morphing mechanisms counterbalanced the aerodynamic gains obtained, putting the future of morphing on hold until the gradual advances in various other fields (smart materials mainly) would enable utilizing morphing mechanisms without inflecting further penalties.

Figure 2.10: NASA AFTI F-111 Mission Adaptive Wing (NASA, 2015). ©NASA

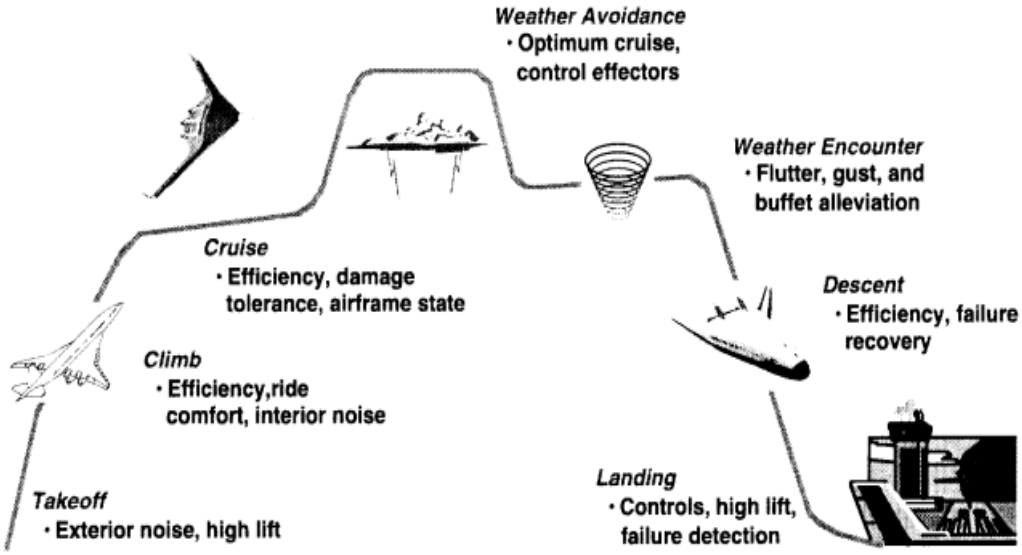

Figure 2.11:Range of application of active morphing technologies (Wlezien et al., 1998). ©NASA

NASA persevered to materialise morphing concepts with its Morphing Aircraft Project to enable full scale wing morphing (Wlezien *et al.*, 1998; McGowan *et al.*, 2002). The project's main goal was to integrate newly available smart technology (embedded actuation, sensing, and control logic in a closely coupled feedback loop) into a high payoff application that would facilitate the design and production of multipoint adaptable and efficient aircraft, where the range of the morphing applications could extend from take-off, to cruise to decent.

Figure 2.11 summarizes the goals set by the project, whilst NASA morphing unmanned air vehicle is shown in Figure 2.12, which was the focus of all the cross-disciplinary research works and had several morphing technologies embedded such as bio-inspiration, warping, shape-changing (including variable camber and sweep), variable geometry, smart materials (Valasek, 2012).

In recent years, the breakthrough in various Shape Memory Alloys (SMA) has made it possible to produce truly morphing concepts. The SMAs provide a suitable solution for lightweight actuators that are at the same time load bearing and easily deformable to obtain the required shape. FlexSys *Inc.* developed a mission adaptive

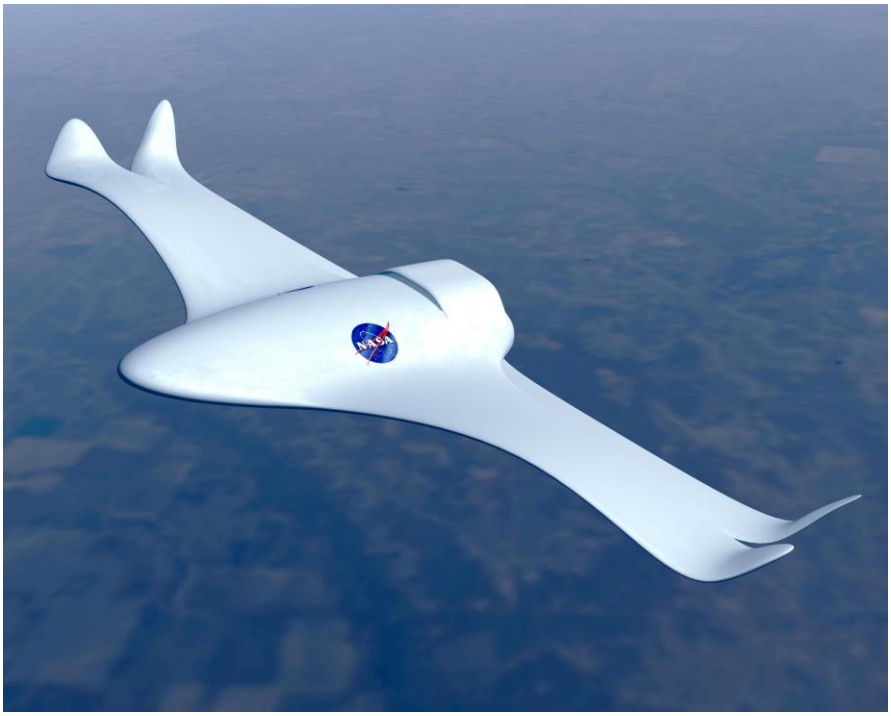

Figure 2.12: NASA morphing unmanned air vehicle concept (NASA, 2009). ©NASA

Figure 2.13: FlexSys Morphing flap (FlexSys, 2016).

compliant flap (shown in Figure 2.13) which can effectively control surface pressure distribution while minimizing flow separation and drag. It is the only concept that has reached the flight test stage. The flight tests conducted in cooperation with NASA showed that even at high operating lift conditions laminar flow runs up to 60% of the chord (Kota, Hetrick and Osborn, 2003; Kota *et al.*, 2006). Moreover, load alleviation control could be attained by imposing a deflection along the span, which would effectively change the twist.

Likewise, NASA and MIT jointly worked on a new bendable morphing wing (Jenett *et al.*, 2016) composed of cellular composite structures and whose design includes wing structure, skin, fuselage, and actuation system, motors, controls, and mechanisms. The wing prototype was tested and results compared with a rigid version of the prototype with flaps as shown in Figure 2.14. Active twist of the wing was used to replicate the rigid wing performances, and it was found that through active wing twist various benefits could be achieved including the ability to increase roll efficiency and possible stall mitigation *(*Jenett *et al., 2016)*.

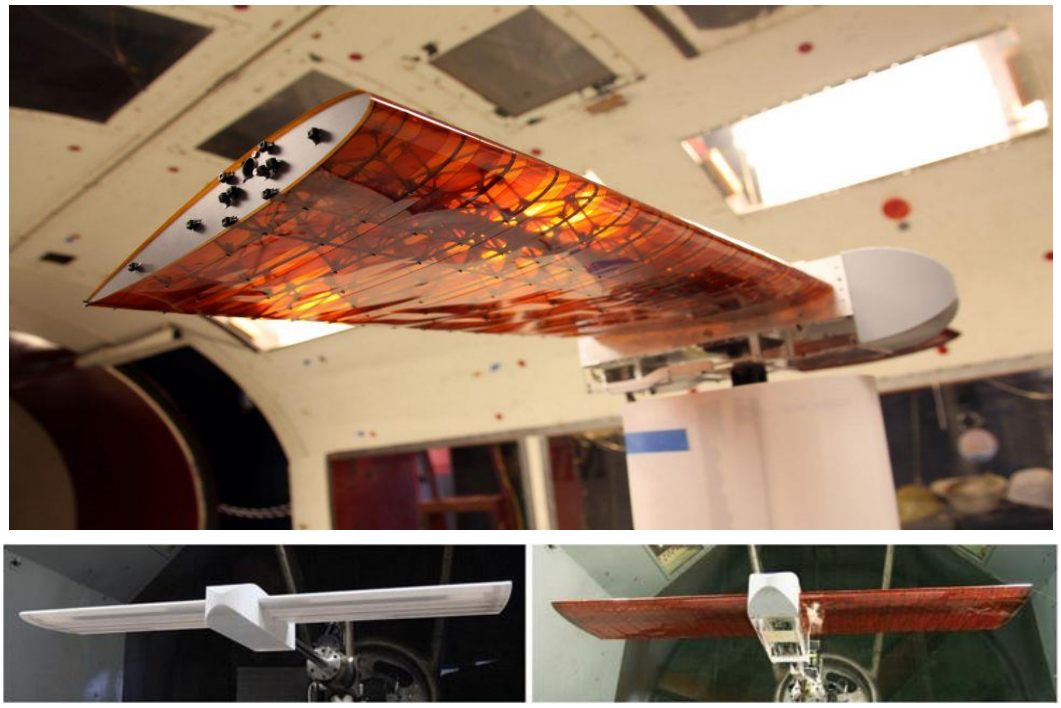

Figure 2.14: Testing setup in NASA Langley wind tunnel. (Lower Left) Rigid wing model. (Lower Right) Flexible wing model (Jenett et al., 2016). (Used with permission of the publisher)

2.2.3. Other Morphing Applications

Morphing was traditionally investigated for fixed wings configurations, as wings are the main lift contributor in an aircraft, however, recent years have seen a trend where morphing has been extended to other parts of the aircraft, to helicopter

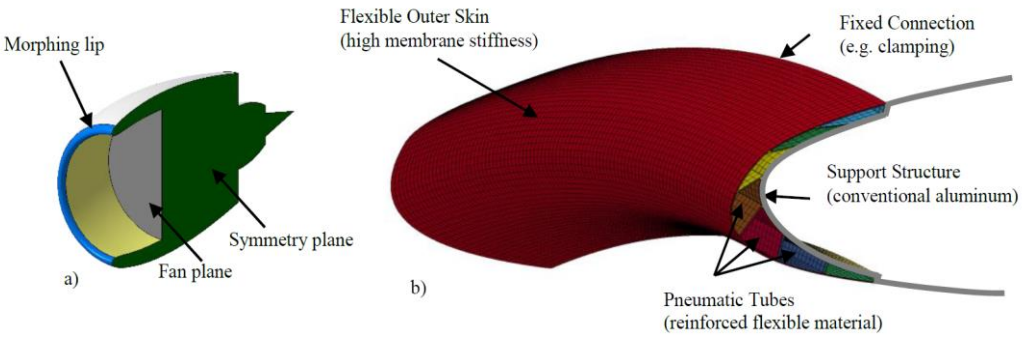

Figure 2.15: Pneumatically actuated morphing inlet of nacelle. Overview (a) and detail (b)(Baier, 2015).

blades or even wind turbines in order to extend the capability the mechanism designed.

The European funded project, *MorphELLE* (Morphing Enabling Technologies for Propulsion System Nacelles) (Baier, 2015) undertook the task of designing a Morphing Inlet Lip Concept (Figure 2.15) to optimize the air intake based on freestream conditions. In order to achieve the desirable inlet lip shape, an arrangement of pneumatically actuated tubes is clustered around the internal structure, and on top of the tubes, a sturdy flexible elastomeric outer skin is placed. Preliminary results showed a promising fuel reduction of 5% compared with a classic reference aircraft, a 1.8% reduction in the maximum take-off weight (MTOW) was also obtained, however the authors of the final project report stressed that additional investigations are required to obtain more accurate estimates (Baier, 2015).

Rotary wings have had their share of interest from various research efforts to apply and mature morphing technology for helicopter use as illustrated in Figure 2.16. For instance, a consortium of six leading European universities initiated the Shape Adaptive Blades for Rotorcraft Efficiency (SABRE) research action (SABRE, 2018). SABRE has a main objective of developing a helicopter blade morphing technology, which would reduce fuel burn in addition to CO_2 and NO_x emissions. The focus of the project was both on the numerical analysis of various blade related aspects such as the morphing concept or acoustic emissions, in addition to the maturation of structural concepts and prototypes wind tunnel testing.

The FishBAC concept, first introduced by Woods *et al.* (2012), is being further developed for the active camber part of the blade (Rivero *et al.*, 2018) (Figure 2.17). Recent results confirmed the superior aerodynamic performance of the morphing blade compared with traditional configuration. Active camber morphing showed power reductions of up to 5.5% in hover. Whereas the active tendon concept showed the capability to change the dynamic response of the rotor blade (Rauleder *et al.*, 2018).

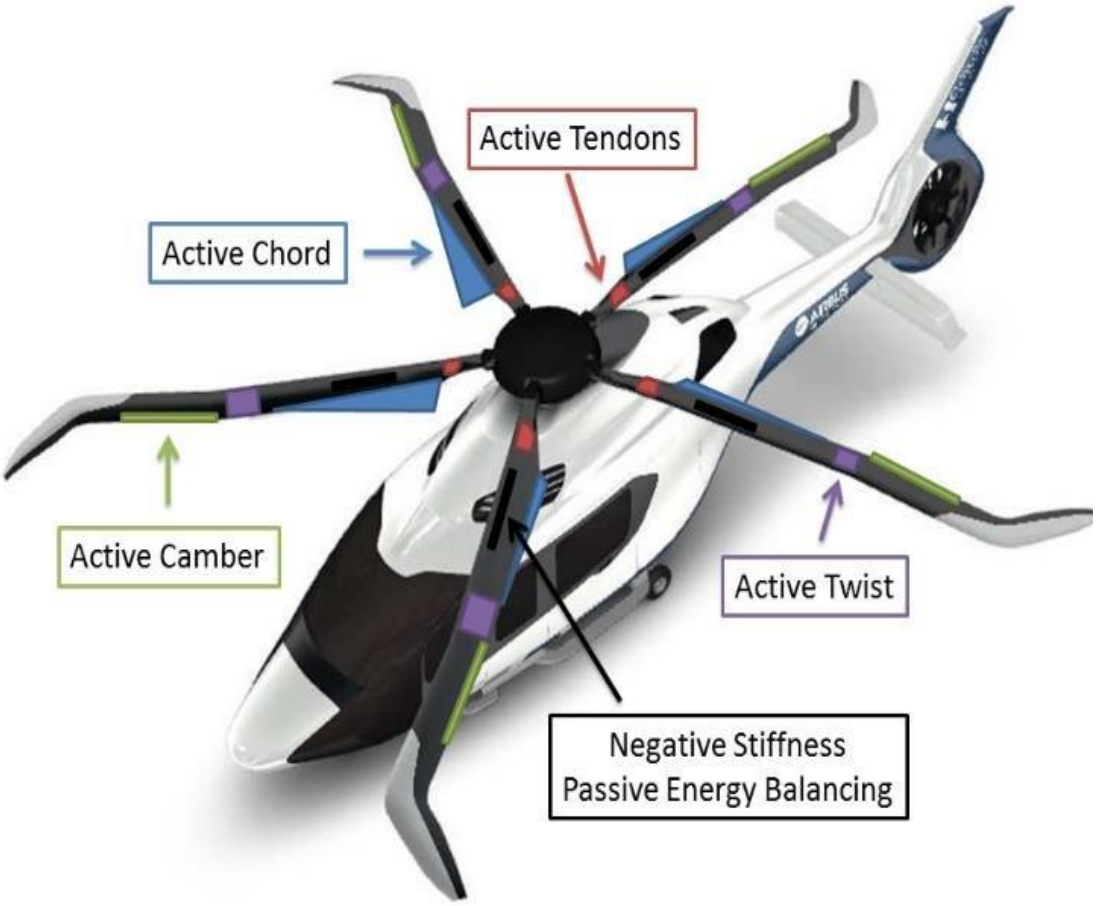

Figure 2.16: Multi-morphing rotor concept (Rauleder et al., 2018). (Used with permission of the publisher)

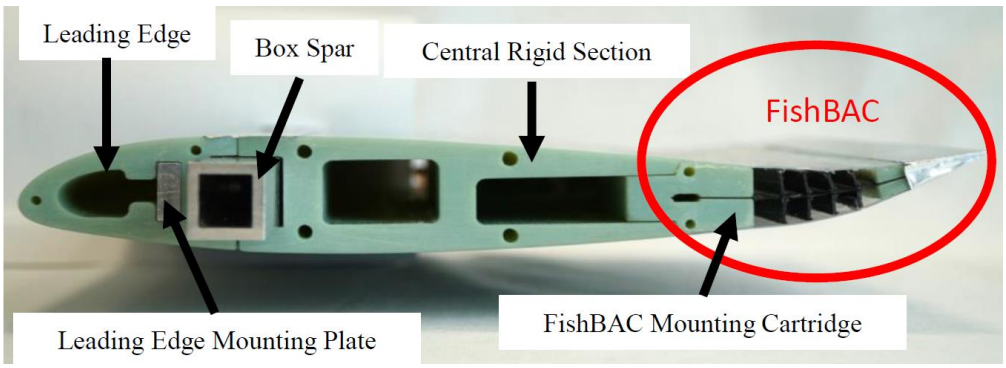

Figure 2.17: FishBAC wind tunnel model (Rivero et al., 2018). (Used with permission of the publisher)

Morphing also extended beyond aerospace applications to the renewable energy field; specifically in the optimization of wind turbines for higher efficiency, energy capture, lower noise emission and for load alleviation purposes, which is important given the unpredictable wind conditions. Figure 2.18 illustrates how morphing blades would enhance the power output of wind turbines at off-design conditions (Macphee and Beyene, 2019).

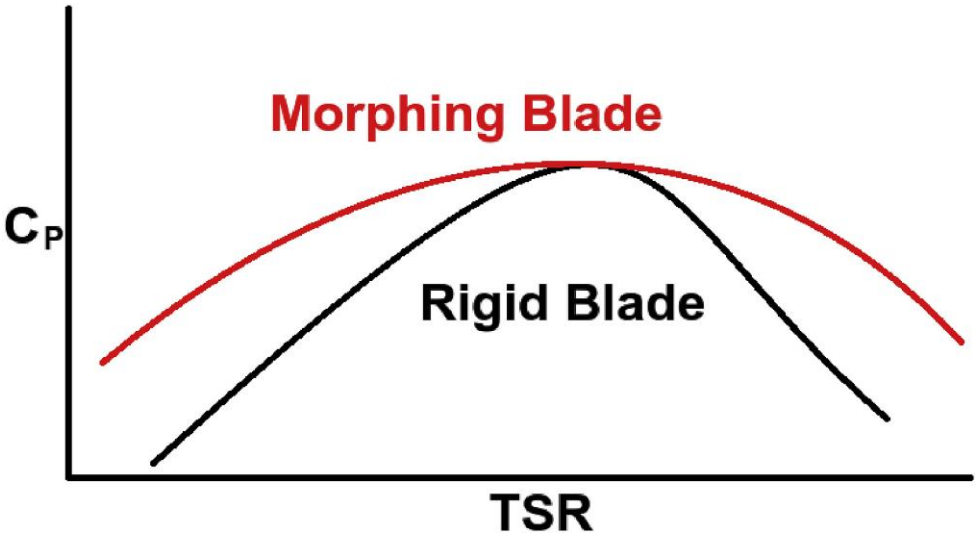

Figure 2.18: Power curve expected for morphing blades compared with rigid blade. C_P is power coefficient while TSR is the tip-speed ratio (Macphee and Beyene, 2019). (Used with permission of the publisher)

Lachenal *et al.* (2013) compiled an extensive review of morphing devices applied to wind turbine up to year 2012 with some interesting findings. In the study by Daynes and Weaver (2012), a morphing trailing edge device was specifically designed for a wind turbine using an anisotropic cellular structure to allow morphing, which enabled the turbine to withstand large deflections and high strains. An improved version of this design was also produced and recently a demonstrator was tested (Ai *et al.*, 2019). The proposed morphing flap comprises a lightweight carbon fibre laminate, 3D printed honeycomb core and a flexible silicone surface (Figure 2.19).

Another approach was the use of flexible passively morphing wind turbine blades to increase the operational range of small horizontal wind turbines (Macphee and Beyene, 2019). Both experiments and numerical predictions showed up to 32.6% increase in maximal efficiency and a 34.5% increase in operational range when compared to rigid blades.

(a) The integrated actuation mechanism in the blade section.

(b) Flaps and blade section mounting design.

Figure 2.19: Morphing flap concept for wind turbine applications (Ai et al., 2019). (Used with permission of the publisher)

This brief historic overview of the development of morphing concepts gives a general view of the evolution of such concepts, their benefits and applications. Yet as the focus of this work is purely numerical, the next section will delve into the numerical tools used for the aerodynamic investigation of morphing configurations.

2.3. Review of Numerical studies Focusing on Morphing Configuration

In order to develop an efficient morphing technology a focus on various disciplines is needed such as the structural mechanics, aeroelasticity or dynamic control. All of these disciplines require an input of the load predictions from the aerodynamic solver. This makes the aerodynamic prediction central in all design phases of successful morphing concept. Yet, the aerodynamic modelling of morphing configurations brings additional challenges:

i. Non rigid morphing structures interact differently with the flow compared with traditional rigid configurations (extensively studied) therefore, morphing concepts still need higher-fidelity methods for an in-depth understanding of the flow behaviour
ii. Large and rapid morphing deformations need proper geometrical modelling in addition to adequate treatment of the mesh deformation to ensure high accuracy. This adds extra difficulties to the design process which may require further simplifications, as discussed later in the this section
iii. Morphing in general includes a large design space where additional parameters specific to morphing (e.g. morphing speed, structural and material requirements) interact, this results in larger parameter sweep studies which constraint the use of high-fidelity methods in order to balance computational cost with accuracy
iv. Introduction of new materials such as piezoelectric actuators permits the use of novel active flow control techniques for morphing skins and flaps, but these have not been investigated in depth numerically

To comprehend the benefits of morphing and its effects on flow behaviour, it is imperative to model the lift, drag and moments as accurately and as practically as possible, not only to understand the flow behaviour, but to contribute in other aspects of the morphing analysis. Some of these aspects for instance are the deformation modelling a dynamic wing or load calculations throughout the flight trajectory of a morphing aircraft.

Three aerodynamic approaches are available for morphing wing analysis: analytical methods (or strip theory), low-order methods (Panel potential flow method, steady or unsteady Vortex-Lattice Methods (VLM)) and high-order methods consisting of Computational Fluid Dynamics (CFD).

Analytical methods suffer from an inherent lack of accuracy due to the over-simplifications embedded in such methods in addition to their dependence on appropriate empirical calibration (Obradovic and Subbarao, 2012). This makes the use of low-order methods more attractive given their low computational cost (despite the accuracy drawbacks), and high fidelity CFD methods more desirable for their higher accuracy despite the increased computational load. Li *et al.* (2018) provided a review of previous studies investigating morphing airfoils and wings using either lower-order methods such as panel codes and VLM or higher fidelity CFD.

Studies that applied lower-order methods and CFD to morphing configurations are discussed in the following sections.

2.3.1. Application of low-order methods

Panel method (XFOIL)

Panel codes are widely used for the steady aerodynamic analysis of morphing configurations, mostly at early design and optimization phases. The panel method models the 2D flow past an airfoil as a summation between a uniform flow and a series of singularity panels (source, doublets, vortices) approximating the geometry.

A number of codes have been developed based on this method. XFOIL (Drela, 1989b) is one of the most used panel codes; it combines an inviscid panel method, and a Karman-Tsien compressibility correction for better subsonic flow predictions. For viscous flow calculations, a viscous boundary layer component for skin friction drag and separation modelling is added based on a two-equation lagged dissipation integral boundary layer formulation (Drela, 1989a) and the transition prediction is implemented using the e^n transition criterion (Drela, 2003).

The strength of XFOIL and similar codes is that they could provide comparable aerodynamic predictions to CFD at a fraction of the computational cost especially at lower Angles of Attack (AoA) (Woods, Bilgen and Friswell, 2014).

Gabor *et al.* (2012) used aerodynamic predictions obtained by XFOIL for the optimization of a morphing wing demonstrator by delaying the transition from laminar to turbulent flow over the airfoil suction surface which resulted in 26% reduction in the drag coefficient. The same wing demonstrator design was optimized for delayed transition using various optimization approaches using XFOIL for the aerodynamic predictions (Koreanschi *et al.*, 2017).

Likewise, XFOIL was used for an optimization study of a variable camber flap concept (Marques, Gamboa and Andrade, 2009) for drag reduction of a low speed UAV which enabled a 2.7% wing drag reduction. For the design of a novel bidirectional variable-camber airfoil, Bilgen *et al.* (2010, 2011) integrated XFOIL in a MATLAB-based framework for lift, drag and pressure predictions, this framework was used as the main aerodynamic analysis tool, however given the limitation of the code, only AoA in the linear region were investigated. Woods *et al.* (2014) compared two aerodynamic analysis methods for load predictions of the Fish Bone Active Camber (FishBAC) concept. XFOIL's predictions were compared to the open source CFD solver OpenFOAM (Jasak, Jemcov and Tukovic, 2007), and they confirmed the superiority of CFD prediction over XFOIL

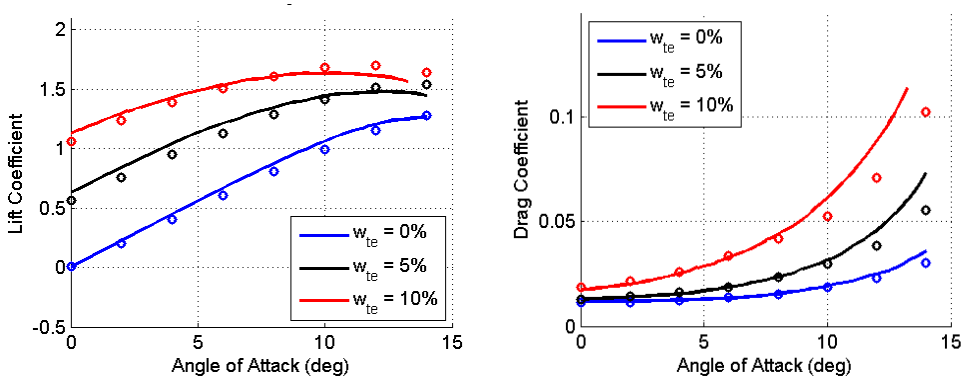

Figure 2.20: Lift and Drag prediction comparison between XFOIL (Solid lines) and OpenFOAM (circles), Woods *et al. (2014). (Used with permission of the publisher)*

especially closer to stall (Figure 2.20) . Nevertheless, XFOIL was significantly computationally inexpensive making a case for its use, especially for iterative design problems or optimization.

Beaverstock *et al.* (2015) utilised XFOIL for viscous drag predictions on airfoil and strip theory for the integration of the viscous drag component across the wing. The tool was employed for the optimization of the aerodynamic efficiency of an integrated FishBAC plus span morphing (AdAR) concept where various parameters and mission profiles were investigated and recommendations were proposed for different scenarios (Figure 2.21).

Similarly, using XFOIL for aerodynamic predictions, Fincham *et al.* (2015) performed a multi-objective optimisation using genetic algorithms for FishBAC airfoil configuration, and showed that significant performance improvement were obtained using the morphing concept with a drag reduction in off-design conditions varying from 30% to 60% for matched performance in on-design conditions.

Finally, XFOIL is still being actively used especially in the design process of wind tunnel prototypes and novel morphing concepts (Rocha dos Santos *et al.*, 2018; Popov *et al.*, 2010; Koreanschi, Oliviu and Botez, 2014; Nicassio *et al.*, 2018).

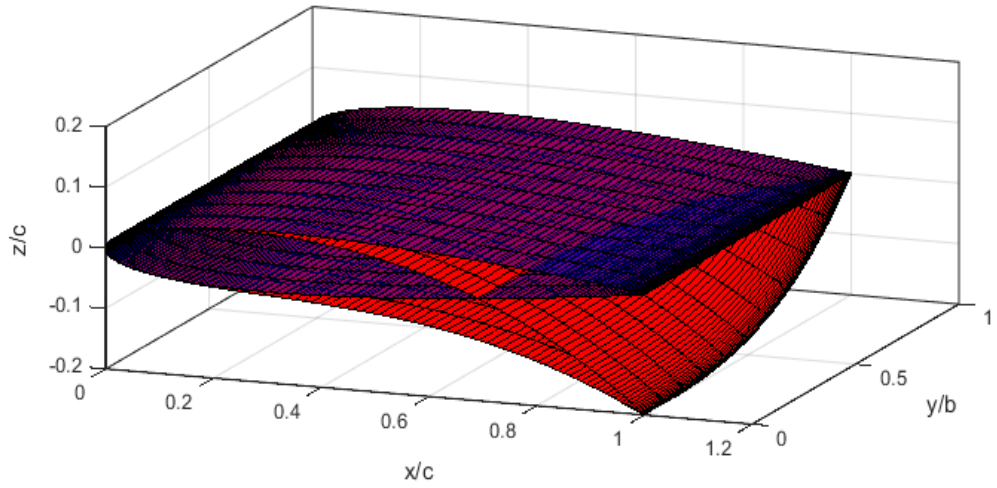

Figure 2.21: Representation of FishBAC spanwise and chordwise morphing concept (Beaverstock et al., 2015). (Used with permission of the publisher)

Vortex Lattice Method (VLM)

Vortex Lattice Method (VLM) is another approach frequently used for morphing wing studies. This method uses singularities placed on the surface of the wing to calculate its aerodynamic properties. However, as opposed to the panel method, VLM boundary conditions are applied on a mean surface not the actual surface of the airfoil, i.e. ignoring any thickness distribution, making it suitable for thin lifting surfaces. VLM assumes an inviscid and incompressible flow field that can be corrected using the Prandtl-Glauert compressibility correction. Various VLM codes have been developed and widely used like the NASA-Langley VLM code (Lamar and Herbert, 1982) or the most recent 3D conceptual VLM code Tornado (Melin, 2000).

Martins *et al.* (1997) optimized a morphing wing concept using VLM and a multivariable function optimizer algorithm where the wing box was constrained and the rest morphed. Up to 2.3% reduction in the induced drag was obtained.

Sanders *et al.* (2003) used VLM for the investigation of morphing control surfaces suitable for an active aeroelastic wing technology. They were able to confirm the experimental results showing the superiority of conformal morphing control surfaces compared with the traditional configurations. Similarly, Johnston *et al.* (2003) integrated VLM in a framework to predict the energy requirements of morphing wing actuators, and provided some initial insights into actuators design. A similar approach was also used by Gern *et al.* (2005).

Tornado (a VLM implemented in Matlab) was used for the assessment of span morphing technology where a total drag reduction of 13% was achieved (Ajaj *et al.*, 2013). Gabor *et al.* (2016) introduced a new non-linear formulation of the classical VLM method to better account for viscous effects, the viscous forces were obtained using a 2D flow solver then interpolated on to the wing surface.

Figure 2.22: Morphing wingtip design investigated using DLM (Cooper et al., 2015). (Used with permission of the publisher)

Obradovic *et al.* (2011) introduced a model for a morphing aircraft flight dynamics where wing geometry experiences rapid and large changes using an Unsteady VLM (UVLM) approach. This study stressed on the fact that the traditional approach of rigid body modelling is insufficient when the aircraft experiences rapid or large deformations. UVLM is a method extensively used to model the morphing process like the study of the unfolding wing effect at subsonic regimes (Jung and Kim, 2011). Similarly, UVLM was used for the optimization and aerodynamic study of bio-inspired concepts (e.g. actively morphing flapping wing) (Ghommem *et al.*, 2012; Verstraete *et al.*, 2015).

Doublet Lattice method (DLM)

Another "flavour" of the VLM method is the use of a Doublet singularity instead of a Vortex yielding the Doublet Lattice Method (DLM) which was also used in the study of morphing concepts. Airoldi *et al.* (2012) employed DLM for the calculation of unsteady aerodynamic forces in the design process of a morphing airfoil with composite chiral structures. DLM has also been heavily used in aeroelastic and flutter analysis of various morphing concepts (e.g. Jung and Kim, 2013; Ni *et al.*, 2015). Lastly, the DLM method was used by Cooper *et al.* (2015) to design a morphing wingtip concept (Figure 2.22). Their DLM prediction was corrected by high-fidelity CFD data (needed by the transonic Mach number investigated) which yielded better representations of the aerodynamic loads. The

morphing wingtip concept showed superior lift-to-drag ratio throughout the entire flight envelope, with up to a 2% reduction in fuel over the reference mission.

2.3.2. Application of Computational Fluid Dynamics (CFD)

Despite the practicality of the methods mentioned above, they still suffer from some inherent deficiencies particularly when it comes to separated flow prediction and laminar to turbulent transition location, and so they fail to give a deeper insight into the flow behaviour, this is where CFD is most useful.

Spadoni *et al.* (2007) investigated the aerodynamic behaviour of a morphing airfoil based on a chiral-core structural topology. The loads were obtained from a finite-volume solver but only solving the inviscid Euler equations. Given the prohibitive computational requirements needed to solve for the full Navier-Stokes equations at practical Reynolds numbers, a more realistic approach is the use of the Reynolds-Averaged Navier–Stokes equations (RANS) augmented with a turbulence model such as the one equation Spalart-Allmaras model (Spalart and Allmaras, 1992) or a two-equations model like the Shear-Stress Transport SST k-ω model (Menter, 1994). Another alternative to DNS is to resolve only the large scale eddies and approximate the other scales, which is the approach followed in the Large Eddy Simulation (LES) (Moeng, 1984). But the ability of LES to resolve smaller scales meant it was still too computationally expensive for real life industrial problems, which prompted the development of hybrid RANS-LES models such us the Detached Eddy Simulation (DES) and its variants (Spalart, 2009). All these models have been applied to the design, optimization, or control of morphing configurations. A survey of the studies using each turbulence model is presented in the following.

Spalart-Allmaras (SA) model

Secanell *et al.* (2006) developed an in-house viscous parallel solver with the SA turbulence model in order to optimize a morphing airfoil at different flight conditions; the deformation of the mesh was achieved using a transfinite interpolation augmented with a spring analogy approach. It was found that starting

with a morphing thin airfoil yielded best performance throughout the flight envelope. Similarly, Thill *et al.* (2010) studied a morphing airfoil with different corrugated skin shapes that enabled chordwise camber and length changes. The steady, implicit, incompressible, viscous Navier-Stokes solver SimpleFOAM available in OpenFOAM was used. The authors noted that the SA model performed well with an attached flow, but its predictions deteriorated when separation occurred.

A study of the Variable Camber Continuous Trailing Edge Flap (VCCTEF) was performed using both SA and SST model implemented in NASA's OVERFLOW solver (Kaul and Nguyen, 2015, 2016). Results from both turbulence models were compared to experimental data; it was indicated that SA model results were in better agreement than the SST. The SST overpredicted lift and drag after AoA 6º. SA was used for the drag optimization study, the results showed that the aerodynamic efficiency *L/D* increased with the continuous morphing TEF, and it stalled later.

Lyu *et al.* (2015) integrated a RANS-based CFD solver in a gradient-based optimization framework and applied it for the study of a NASA Common Research Model (CRM) equipped with a morphing TE. Up to 5% drag reduction was achieved at off-design conditions using this concept, with about 1% fuel saving. Similar findings were found when an aerostructural optimization was performed on the same configuration (Burdette *et al.*, 2015). De Gaspari *et al.* (2015) also used a similar approach for morphing aircraft optimization. It was found that the optimization algorithm improved the aerodynamic efficiency by 3%. Additionally, it was able to move backward the shock wave occurring on the wing as shown in (Figure 2.23).

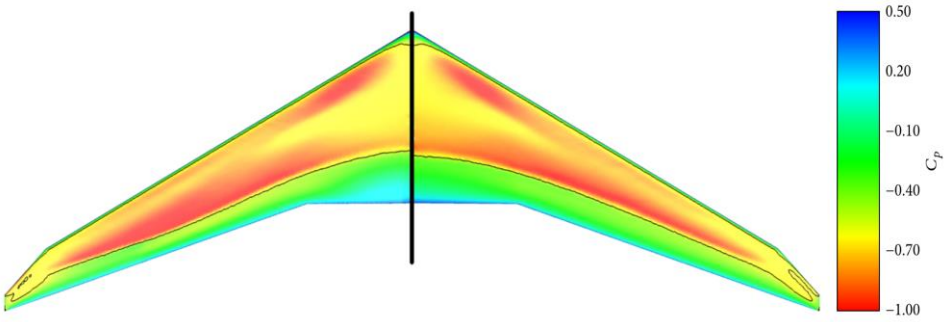

Figure 2.23: Comparison between the C_p distributions at cruise Mach number over the reference wing (right) and over the wing equipped with morphing trailing edge (left) from De Gaspari et al. (2015). (Used with permission of the publisher)

Ai *et al.* (2016) studied, both experimentally and numerically, the aerodynamic performance of the NACA 0012 airfoil when fitted with morphing trailing edges. It was established that the improvement in aerodynamic performance was dependent on the amount of camber introduced at the trailing edge. The amount of camber also controlled the level of flow separation delay near the trailing edge at high angles of attack. However, the numerical simulations were limited to AoA in the linear region and only steady state RANS were used to validate their experimental work on static deflections.

Wolff *et al.* (2014) used steady and unsteady RANS with SA to analyse the performance of a thin wind turbine airfoil fitted with actively morphing trailing edge flaps. The dynamic trailing edge deflections were simulated with the help of structured multi-block deformable meshes within the code FLOWer (Kroll and Fassbender, 2002). The authors discovered that such morphing trailing edge sections could have a significant impact on the lift coefficient and stall behaviour of the wind turbine. Similar type of mesh deformation was used by Zhang *et al.* (2012) to simulate the unsteady flow-field created by wing rigid movement. The mesh was deformed using the spring-based analogy in ANSYS Fluent.

SST k-ω model

The SST model is widely used in both academia and industry due to its good stability and accuracy especially with separated flows (Menter, 1994). Fincham *et*

al. (2014) used both SA and SST for the 2D and 3D study of a corrugated skin for spanwise morphing. It was found that the SST model overpredicts the drag by up to 15% compared with SA at an AoA of 4º but higher AoA were not investigated. Matteo *et al.* (2010) used a RANS-based CFD analysis with *k-ω SST* turbulence closure to design a morphing TEF; the loads obtained from the CFD solver were used to conduct a stress and strain analysis of the morphing wing.

Likewise, a transient CFD analysis was used for the design of a morphing wing mechanism using an SMA wire actuator, the aerodynamic efficiency was improved for the morphed case. However, it was found that higher deflections caused more separation which resulted in a decrease in *L/D*. A Fluid-structure interaction (FSI) study was performed on a compliant MAV wing (Ismail *et al.*, 2013) where SST was used to examine the behaviour of the Leading Edge Vortices (LEV) around the deforming wing.

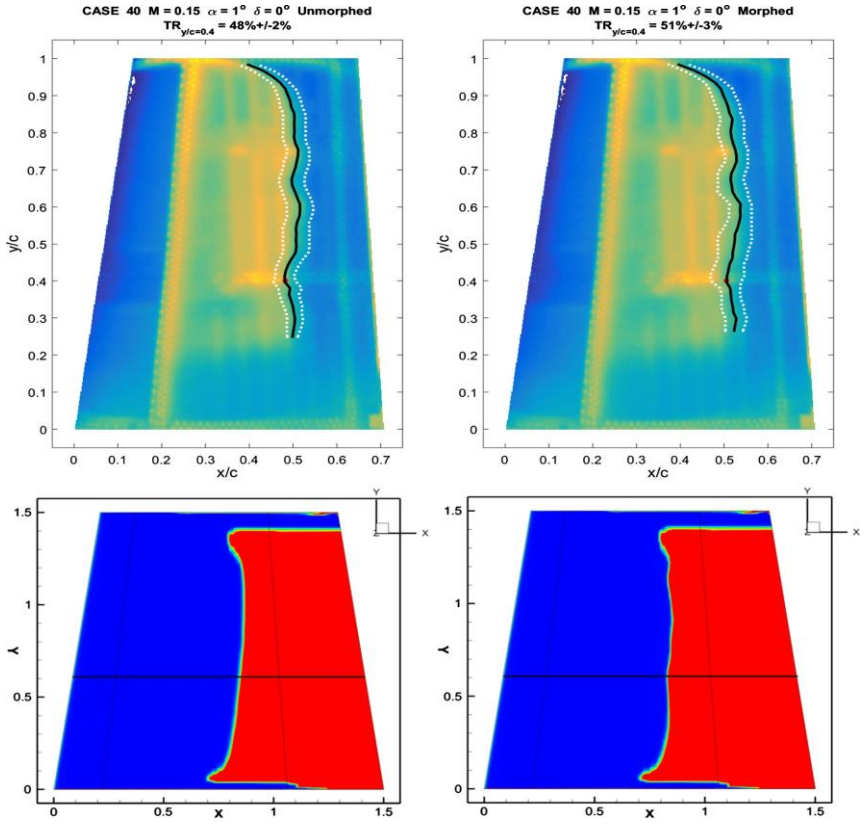

Figure 2.24: Comparison between experimental and numerical transition location on the wing upper surface for a morphing case, for both un-morphed (left) and morphed (right) geometries Gabor et al. (2016). (Used with permission of the publisher)

Gabor *et al.* (2016) compared numerical simulation and experimental wind tunnel data for a morphing wing-tip demonstrator targeting transition delay. The SST-based CFD results were compared with infrared thermography measurements (Figure 2.24) and good agreement was found for the pressure distributions and transition location. However, the experiment showed a larger transition delay compared with CFD. Additionally, the authors found that the turbulence model was unable to predict the drag reduction observed in the experiments.

Finally, Moosavian *et al.* (2017) conducted a parametric study on a bio-inspired continuously morphing trailing edge using RANS and SST, and was found that a higher lift was achievable compared with the baseline configuration.

Other higher fidelity methods

There have not been, to the author's best knowledge, any use of hybrid turbulence models or LES on morphing configuration, except some ongoing work by Kamliya Jawahar *et al.* (2017) in which airfoils fitted with TEF were investigated both numerically and experimentally to gain some insight into the flow behaviour. DES was first used (Kamiliya Jawahar *et al.*, 2017) then a recent study (Kamliya Jawahar *et al.*, 2018) used LES. Both studies were interested in the acoustic impact of morphing configuration which explains the use of these models. Both studies showed that the morphing airfoil has better aerodynamic efficiency compared with hinged flap configurations. Up to 6% increased efficiency was observed due to the larger region of attached flow near the morphing TEF. However, this trend is only viable at lower AoA (less than 7º). At higher AoA, it appears that the morphing and the hinged configurations behave in a similar fashion, because the separation is fixed at the hinge for the hinged flap whereas on the morphing flap, separation point moves upstream, beyond the hinge location.

Although the present work is purely numerical, for the sake of completeness a brief review of a few prototypes investigating the aerodynamic benefits of morphing are presented in the next section.

2.4. Review of Experimental studies focusing on Morphing Configuration

Over the past decades, a fair amount of prototypes have been constructed as proof of concept for adaptive structures and which mainly focused on the structural design, novel smart material implementation, control systems, and for aerodynamic validations of the numerical methods, the later will be the topic of this section.

Figure 2.25:MDO505 wing model setup in a wind tunnel test section (Gabor et al., 2016). (Used with permission of the publisher)

Popov *et al.* (2009) tested a rectangular wing equipped with a morphing skin on the suction side, the flexible skin is controlled by smart material actuators so that it can be optimized depending on the flow condition (Figure 2.25). Various tests and experiments were conducted on this demonstrator, one of which was the optimization for delayed transition (Gabor *et al.*, 2016) and viscous drag reduction.

Woods *et al.* (2013) designed, manufactured and experimentally investigated the FishBAC concept. The model was made from four parts: a skeleton, a matrix composite (EMC) skin, a tendon drive and a rigid non-morphing main spar (Figure 2.27). This concept, which is capable of large camber deflections, was tested in a subsonic wind tunnel for various deflection angles and AoA.

Figure 2.27: FishBAC wind tunnel model: (top) baseline state (lower) deformed state (Woods et al., 2013). (Used with permission of the publisher)

The results were compared with a wing with a hinged flap and results showed up to 25% increase in the aerodynamic efficiency for the morphing flap resulting from higher lift generation for drag levels similar to the unmorphed wing.

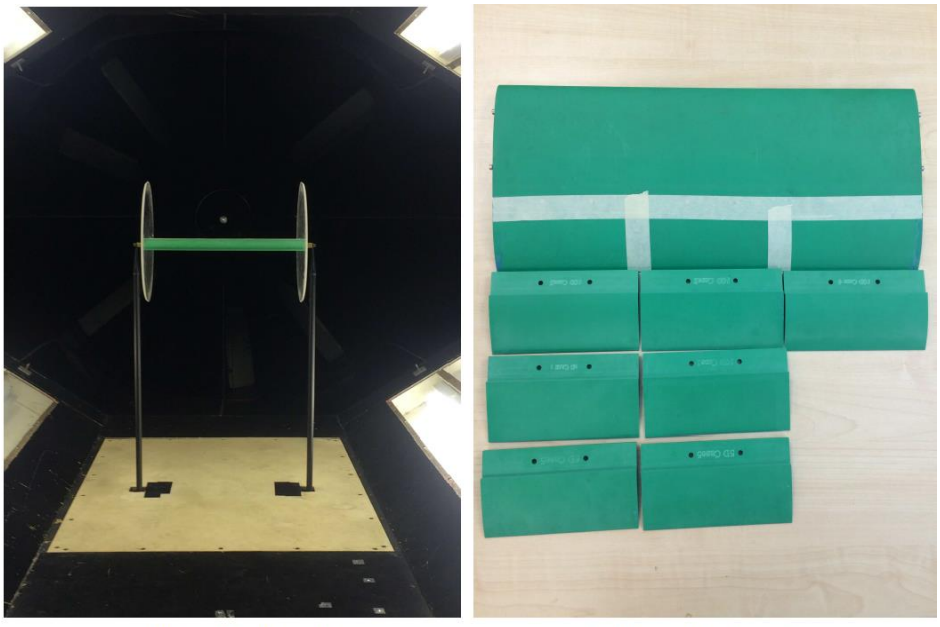

a) Wing set-up in tunnel b) Wing and trailing edges

Figure 2.26: Prototypes for various morphing TEF tested by Ai et al.(2016). (Used with permission of the publisher)

Ai *et al.* (2016) designed and tested an airfoil fitted with a novel trailing-edge design (Figure 2.26). Using a honeycomb core of axial variable stiffness, various camber profiles were tested in a low speed closed-circuit wind tunnel from a plain flap to highly cambered conformal morphing trailing edges. Aerodynamic force measurements and steady and unsteady flow field measurements using hot-wire were performed over a wide range of AoA (−5º to 20º). Results demonstrated that the $C_{L,max}$ experienced up to 13% increase for the morphed profile with a favourable delayed separation on the suction side.

A variable camber wing with a morphing leading and trailing edge using corrugated structures was proposed by Takahashi *et al.* (2016). Figure 2.28 shows the prototype with various deflections. Preliminary wind tunnel test showed that the observed deformation shape is well correlated with simulated shape proving the feasibility of the concept.

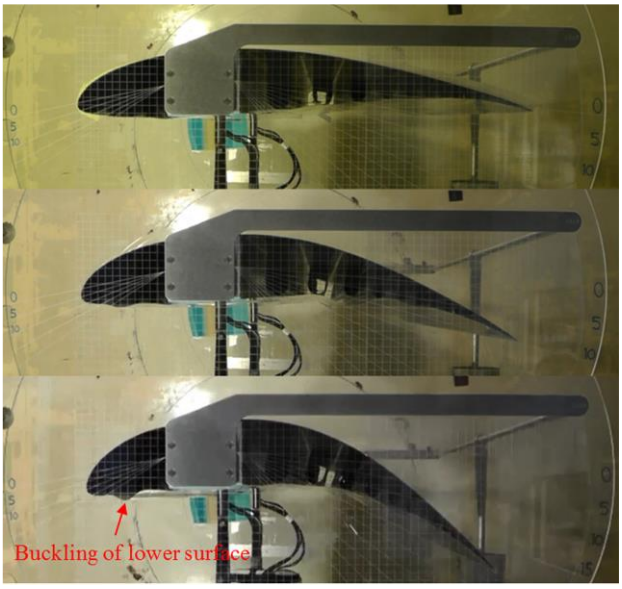

Figure 2.28: Details of morphing wing structure with wire actuating Takahashi et al. (2016).
(Used with permission of the publisher)

A set of experiments has also been conducted on a conventional aircraft wing with a morphing wing tip variable in twist and dihedral angle (Figure 2.29) in order to cross validate a range of lower fidelity methods such as VLM (Gabor *et al.*, 2016).

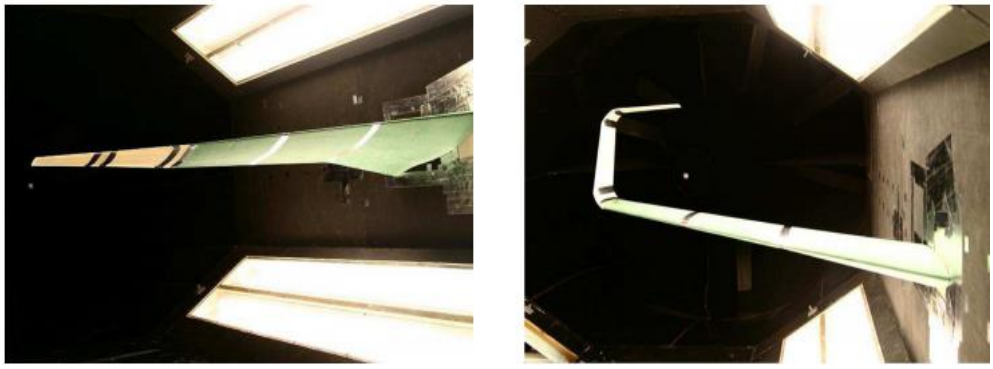

Figure 2.29: Aircraft wing with a morphing wing tip (Gabor et al. 2016). (Used with permission of the publisher)

2.4.1. Efforts for Sealing the Gaps on Wing Control Surfaces

As discussed in the previous sections, one of morphing's major advantages is the ability to remove discontinuities present around various lifting surfaces such as the flap side-edge. Figure 2.30 illustrates a wing with a deployed flap where the flap side-edge is shown along with the disturbances and vortices caused by its presence, making the side-edge gaps extra noise generators and drag sources due to the presence of recirculation regions within the gaps. Studies conducted by NASA in its Elastically Shape Future Air Vehicle project (e.g. Nguyen, 2010; Urnes and Nguyen, 2013) showed that a morphing TEF would seal the gaps present at the end

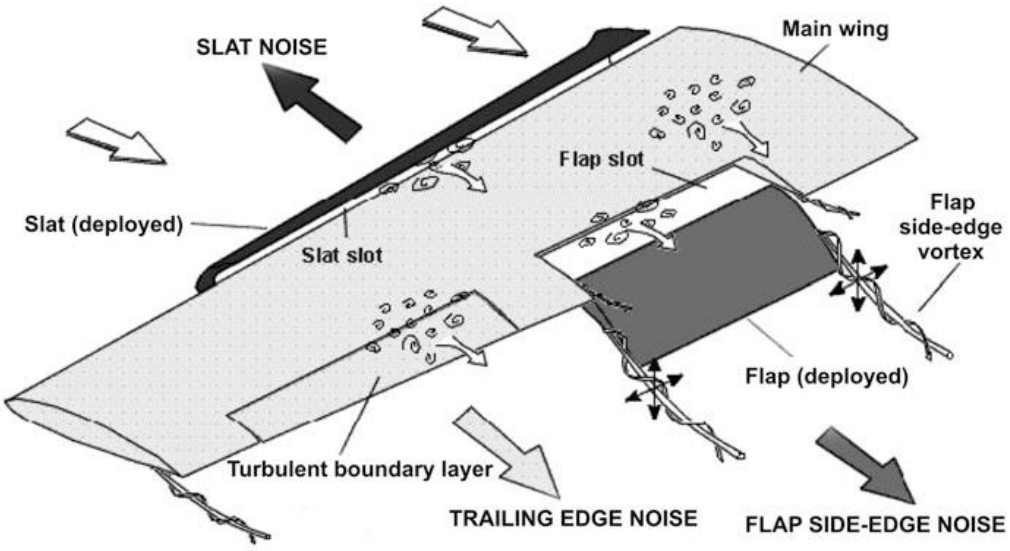

Figure 2.30: Sources of sound generation on the wing of the aircraft with a focus on deployed flaps (Rašuo and Jazarević, 2017). *(Used with permission of the publisher)*

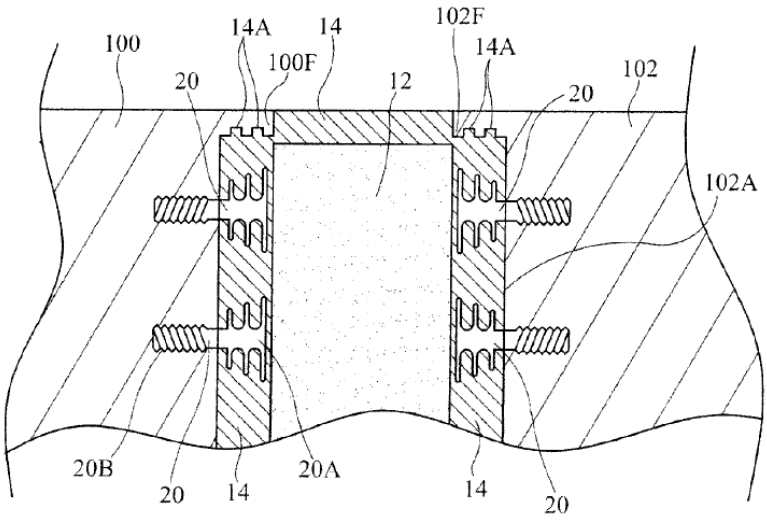

Figure 2.31: Flexible flap side-edge concept introduced by (Khorrami et al.*, 2014b).*

of the control surfaces in both chord-wise and spanwise directions. This would eliminate the slits which are known for their high vorticity and for being a significant source of airframe noise (Macaraeg, 1998).

Several different approaches have been proposed to seal the flap side-edge such as the concept presented by Khorrami *et al.* (2014b) where elastically deformable structures are introduced at each side-edge to passively deform with the flap and seal the gap (Figure 2.31). In the concept introduced by FlexSys Inc. (Figure 2.13), the flap side-edge of a Gulfstream III business jet were replaced by a morphing transition structure with a compliant fairing at the end of each flap to seal the gap. Subsequent flight tests of this concept demonstrated that it is possible to reduce aircraft noise by as much as 30 percent (NASA, 2017). However, this concept did not offer a completely smooth transition, which still leaves room for further improvements.

Recently, Woods *et al.* (2016) proposed a Morphing Elastically LofteD (MELD) design for a compliant morphing flap transition that offers a smooth continuous deformation. The concept has the additional advantage that can be integrated. The concept has the advantage of the Fish Bone Active Camber (FishBAC) morphing airfoil concept (Woods and Friswell, 2012).

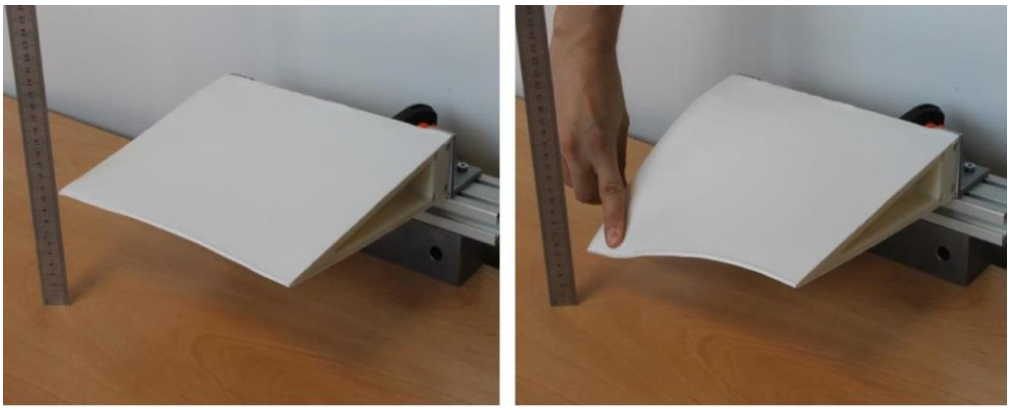

Figure 2.32: Morphing, Elastically LofteD (MELD) seamless transition demonstrator introduced by Woods et al. (2016). (Used with permission of the publisher)

To the author's best knowledge, there are no experimental studies focusing on the morphing process or the dynamic effects of the motion of morphing flaps, with the exception of experiments dealing with high frequency active flow control that will be detailed in the next section

2.5. Review of Active Flow Control Morphing

2.5.1. Active Flow Control (AFC)

Active Flow Control (AFC) is defined as any technological process which actively interacts with the flow (usually in boundary layer) in order to reach a more desired flow state. Gad-el-Hak (1998) preferred the following definition to describe AFC "*Boundary layer control includes any mechanism or process through which the boundary layer of a fluid flow is caused to behave differently than it normally would were the flow developing naturally along a smooth straight surface*". AFC could be used for separation mitigation, transition suppression (or induction) or for inducing the decay of Large Coherent Structures (LCS).

Research has explored the use of morphing mechanisms as active flow control devices for drag reduction, separation mitigation, and noise abasement. The concepts are based on the harmonic forcing of the flow e.g. as investigated by Greenblatt *et al.* (2000) who suggested that the formation of LCS are affected and accelerated by periodic excitation. Periodic motion in a flow is known to enhance the transfer of high momentum fluid across the flow domain (Winant and Browand,

1974). This transfer of high momentum fluid leads to a reduction in the size of the recirculation zones on the suction side of the airfoil which is associated with aerodynamic performance losses. Cattafesta *et al.* (2011) reviewed and categorized

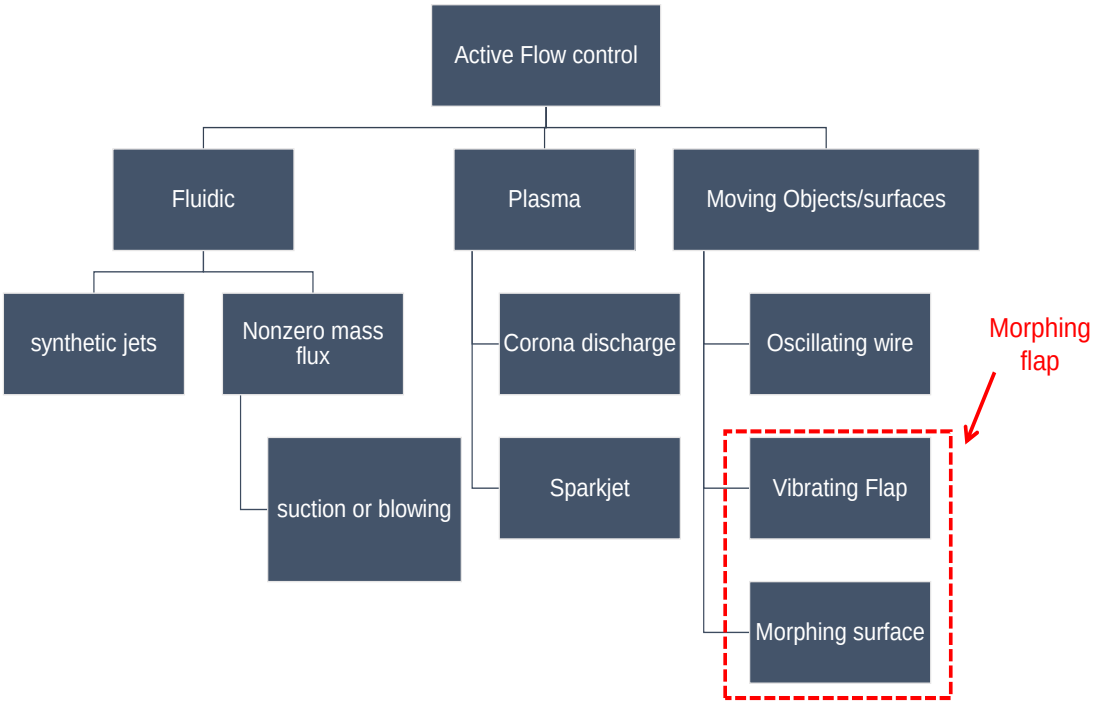

Figure 2.33: Various AFC mechanisms with the morphing flaps highlighted.

various methods used for harmonic forcing as follows:

i. Fluidic methods, which use steady / unsteady fluid injection (blowing) or suction to delay separation (e.g. Huang *et al.*, 2004; Hue *et al.*, 2017; Kim and Liou, 2019)
ii. Plasma-based actuators (e.g. Jukes and Choi, 2009; Ebrahimi and Hajipour, 2018)
iii. Moving surfaces method such as rigidly vibrating flaps (Krzysiak and Narkiewicz, 2006), vibrating diaphragm (Di, Wu and Huang, 2017) and morphing surfaces (Jones, Santer and Papadakis, 2018)

The combination of vibrating flaps and moprhing surfaces (as highlighted in Figure 2.33) is the focus of this chapter.

2.5.2. State of the Art of Harmonic AFC

The aerodynamic modelling of aircraft equipped with morphing wings has been addressed extensively in the literature; the focus has been mainly on the study of the possible benefits from using this technology as a passive way to control the flow. The studied morphing concepts were not being used actively to influence the flow focusing on overall performance enhancement by shape optimization (Fincham and Friswell, 2015; Afonso *et al.*, 2017) as the review performed in Section 2.3 indicates. However, the use of morphing flaps as an active flow control mechanism has not thoroughly been explored as opposed to the use of other mechanisms such as oscillating, discreet hinged flaps for instance.

Krzysiak (2006) investigated a pitching NACA 0012 airfoil with a harmonically deflecting TEF in a subsonic wind tunnel and compared the results with theoretical calculations. It was found that an increase in the maximum lift coefficient is possible when both the angle of attack of the airfoil and flap deflection increase simultaneously. Lee *et al*. (2009) carried out a similar study where a pitching NACA 0015 airfoil with a harmonically deflected flap was experimentally tested; the study showed evidence of a great impact on the C_L and C_M hysteresis while the leading-edge vortex formation and detachment was found to be unaffected by the flap motion.

Seifert *et al.* (1998) successfully used a piezoelectric rigid flap actuator for separation control, where a stall delay of 2º to 4º was obtained, with up to 20% enhancement in the maximum lift coefficient $C_{l,max}$. Several other studies then used the same concept e.g. Kegerise *et al.* (2007) who applied a piezoelectric bimorph cantilever beam with its tip situated at a leading edge cavity and moved it periodically in the direction normal to the flow, for control purposes. It was found that only the tonal component of the cavity wall-pressure fluctuations could be suppressed, with no effect on the broadband noise.

Liggett *et al.* (2013) investigated the impact of an oscillating flap with and without flap gap (Figure 2.34) using a hybrid RANS/LES turbulence model. It was found that the presence of the gaps caused a decrease in performance due to flow

recirculation, and confirmed that the oscillating movement drives the unsteadiness in the flow.

Most recently, Jones *et al.* (2018) used wind tunnel tests and Direct Numerical Simulation (DNS) to investigate the use of periodic surface morphing for separation control at a low Reynolds number (50,000). The amplitude distribution and the angular frequency of the morphing surface was parametrized using a Bézier curve (Figure 2.35) yielding the physical motion obtained in their experimental setup (Jones *et al.*, 2018).

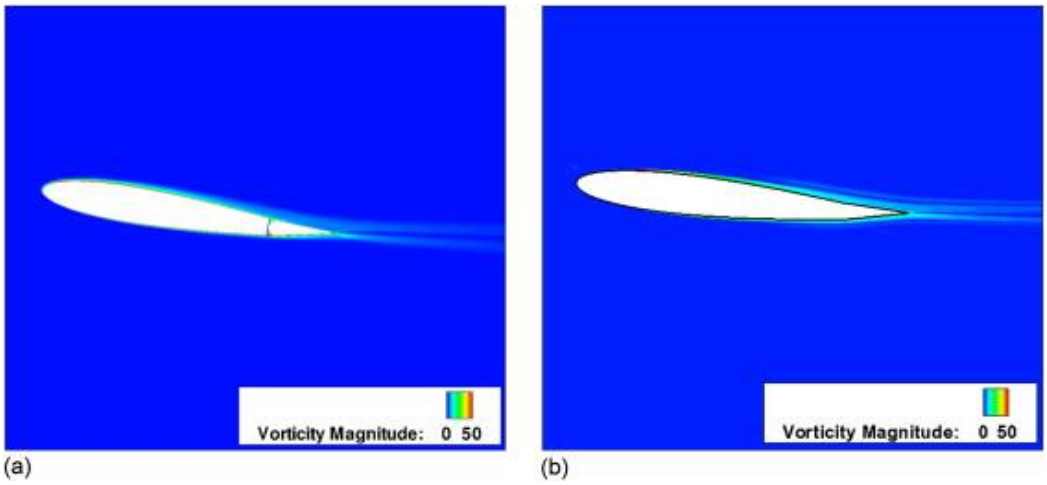

Figure 2.34: NACA 0012 airfoil flow field vorticity for dynamic oscillations (a) discrete flap and (b) integrated flap (Liggett et al.*, 2013). (Used with permission of the publisher)*

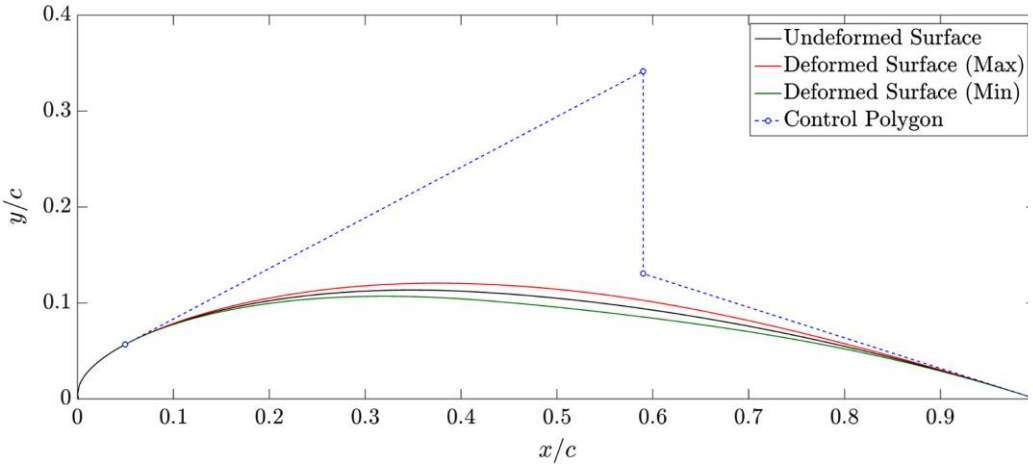

Figure 2.35: Surface morphing Bezier curve used by Jones et al., (2018) to model the dynamic motion. (Used with permission of the publisher)

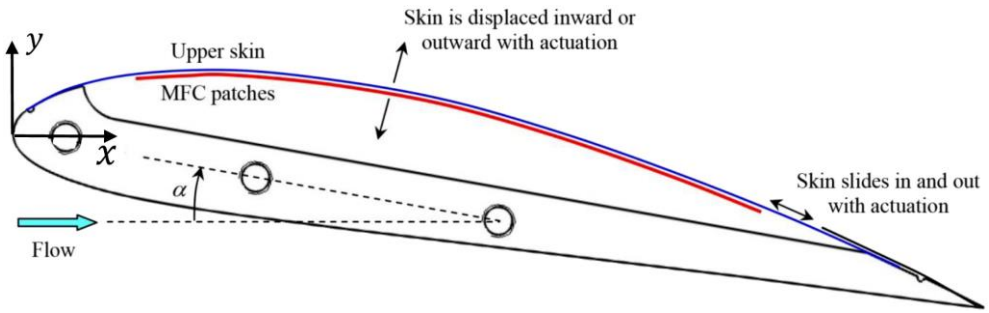

Figure 2.36: A schematic of the surface morphing prototype tested in (Jones *et al.*, 2018). *(Used with permission of the publisher)*

In their experimental work (Jones *et al.*, 2018), a small wing was designed with a dynamically morphing upper skin and actuated by very thin Macro-Fiber Composite (MFC) actuators (Figure 2.36). Results showed that periodic morphing had limited effects on the flow when actuating at a low frequency (10 *Hz*). However, when the forcing frequency was increased to 70 *Hz*, it became the dominant frequency in the spectra, causing LCSs to add momentum to the flow,

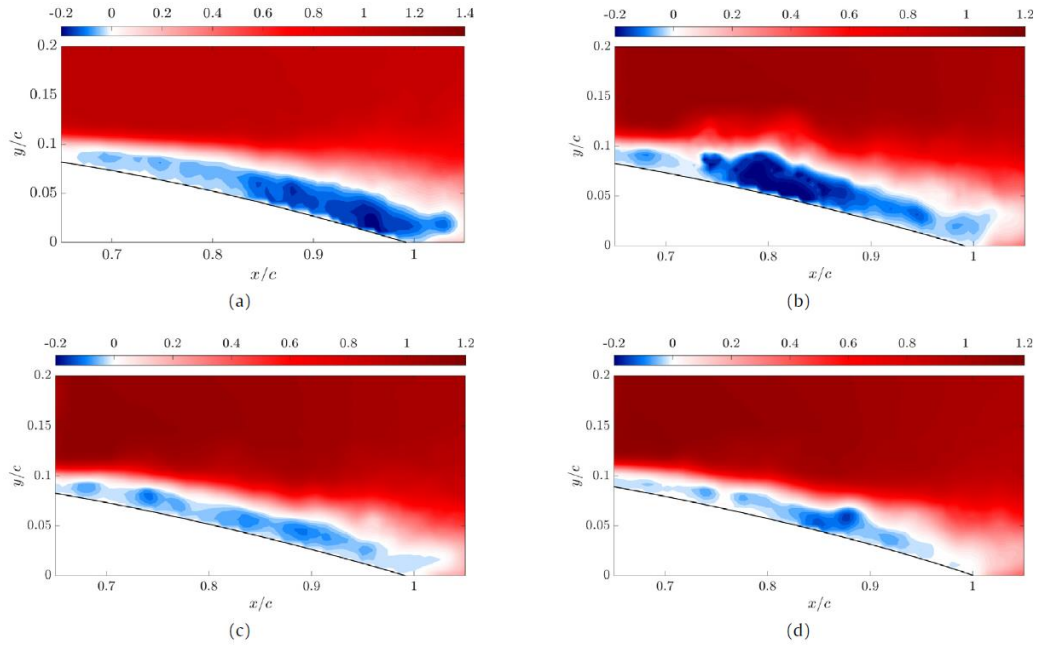

Figure 2.37: Iso-contours of the non-dimensional radial velocity around the airfoil when AoA = 0º for showing the separation mitigation at various forcing frequencies (Jones *et al.*, 2018). *(Used with permission of the publisher)*

effectively reducing the separation (Figure 2.37), and as a result, reducing the drag coefficient C_d.

Scheller *et al.* (2015) performed Particle Image Velocimetry (PIV) measurements on a piezoelectric actuation mechanism integrated into the TE of an aileron at high Reynolds numbers. The effects of high-frequency, low-amplitude oscillations were investigated and it was found that an attenuation of the high-frequency Kelvin–Helmholtz vortices was achievable using optimal morphing frequencies (60 *Hz* for this setup).

Likewise, Jodin *et al.* (2017) used the same concept in an experiment on the TEF of an Airbus A320 hybrid morphing wing concept (Figure 2.38). It was shown that a significant reduction in large-scale instabilities could be obtained, translating into a reduction of up to 20 *dB* in the dominant frequency. Additionally, with optimal

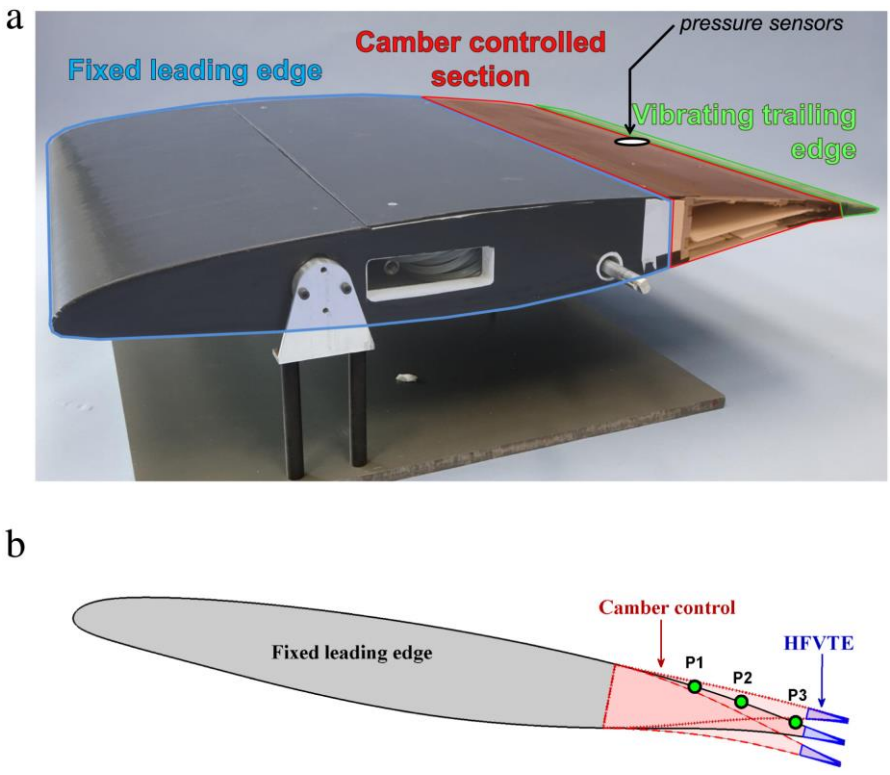

Figure 2.38: (a) Picture of the hybrid wing model on its stand out of wind tunnel stand. (b) Illustration of the maximum deformed shapes of the airfoil (Jodin et al., 2017). (Used with permission of the publisher)

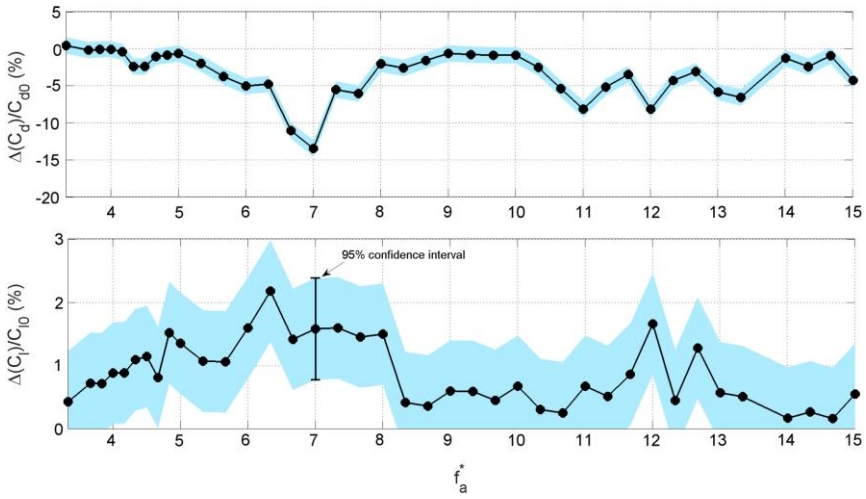

Figure 2.39: Percent gain of mean drag (top) and lift (bottom) coefficients obtained with (Jodin et al., 2017). (Used with permission of the publisher)

conditions, a 5% pressure drag reduction and a 2% increase in lift was achieved (Figure 2.39).

Further research work is still required to gather more data and to establish a more consistent understanding of the effects of morphing TEFs on the performance of wings. In particular, there is a need to investigate such effects using high fidelity CFD methods that offers greater capability for resolving unsteady flows characteristics of morphing applications.

Most studies to date, mainly experimental, have demonstrated that optimal morphing frequency/amplitude pairing is critical for achieving best performance. However, given the large design space, it is extremely costly and time consuming to explore these parameters in full using only experiments, especially when it comes to acoustic effects. The same is true if an expensive numerical approach like DNS is used at high Reynolds numbers. Therefore, to fully investigate such effects for a harmonically morphing TEF, there is a need to develop a practical numerical framework to perform aerodynamic and aeroacoustic studies using reasonably accurate, high fidelity CFD methods at practical, high Reynolds numbers.

.

2.6. Research Gaps in the literature

The literature review has shown that most studies have emphasized that accurate prediction of the aerodynamic forces (lift, drag and moments) is a necessity for a deformable morphing wing. However, due to the lack of computational resources and time, the majority of the work accomplished so far have had to balance accuracy and computational efficiency in their methods when dealing with morphing.

The limitations of the literature reviews regarding the aerodynamic investigations of morphing wings are listed below

i. The majority of studies surveyed for this work used aerodynamic analysis to perform shape optimization, structural design or control. There is a lack of studies that focus on deeper understanding of the flow physics around morphing wings, on the key differences between traditional and morphing configurations and on the transient forces evolution in the deformation process. Figure 2.40 illustrates clearly the lack of in-depth aerodynamic studies.

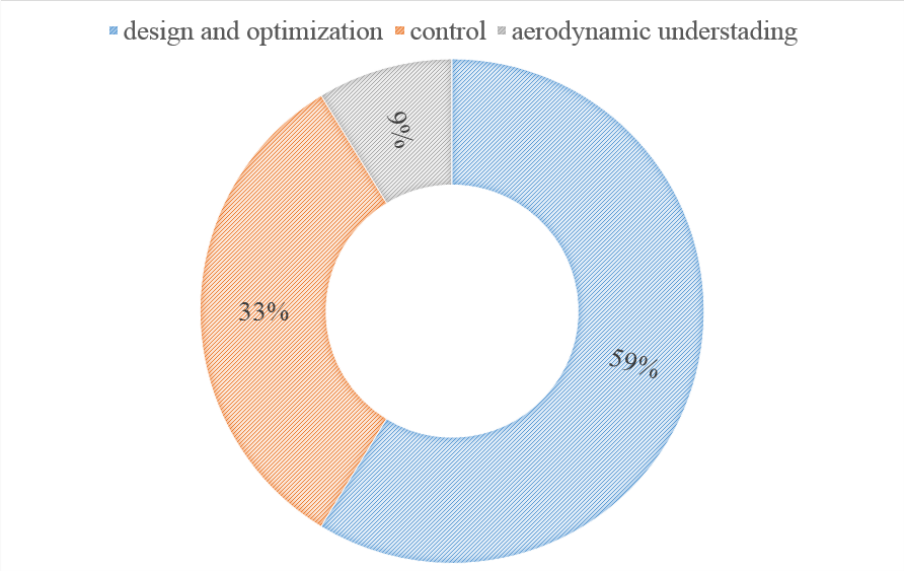

Figure 2.40: Focus of previous morphing wing studies.

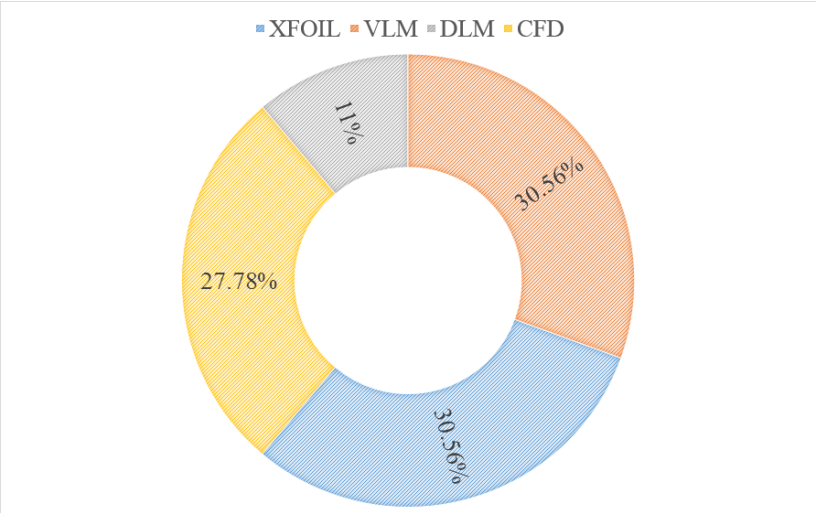

Figure 2.41: Turbulence models used in literature when addressing morphing configurations.

ii. Given the very low computational requirements and the objective targeting practicality rather than in-depth understanding, the use of lower-order methods was dominant compared with higher-fidelity CFD methods. Figure 2.41 shows clearly that the lower fidelity methods (DLM, VLM, and XFOIL) have been used in over 70% of the studies reviewed in this work. Furthermore, when focusing on the studies conducted using CFD most of the studies to date prefer to use a RANS approach with one or two equation models such as the SA or SST as opposed to higher fidelity turbulence models (Hybrid RANS-LES or wall resolved LES) as seen in Figure 2.42. Only one recent study on morphing (Kamliya Jawahar *et al.*, 2018) used LES the rest used mainly SA and SST.

iii. The review has shown that the study of a dynamically morphing trailing edge flap is yet to be performed. From the studies reviewed only one dealt with the dynamic response of a morphing turbine blade (Wolff *et al.*, 2014), however the study used simple interpolation between regenerated meshes at various time steps and did not use mesh deformation techniques. This evidently shows that there is a lack for a framework in the current literature,

which models a wing's geometric deformation while using robust mesh deformation techniques and high fidelity CFD methods to study

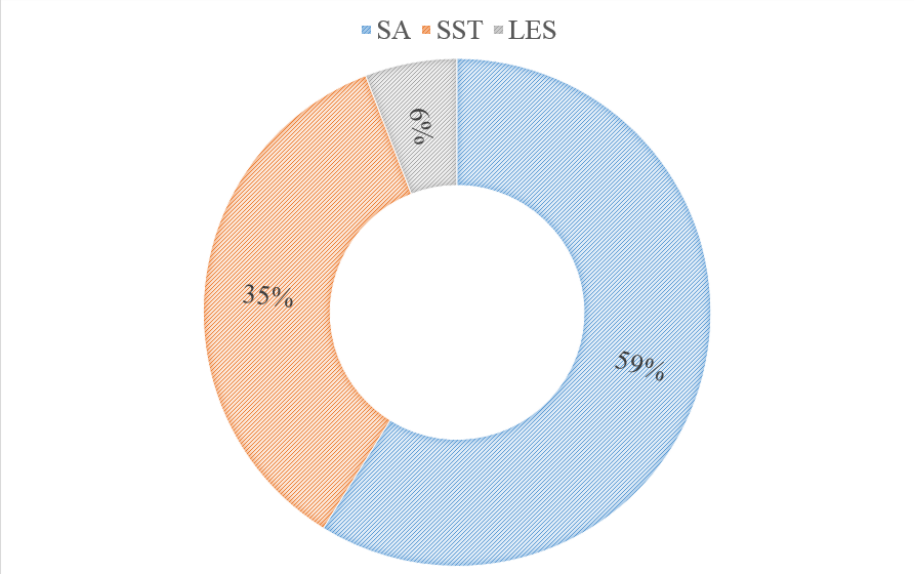

Figure 2.42: Aerodynamic approaches used for morphing analysis.

dynamically morphing wings.

iv. The majority of studies only investigated morphing as a passive flow control concept but using morphing as an active flow control mechanism has not been much explored.

v. Finally, even though the focus of our current work is numerical, our survey of experimental studies shows a lack in wind tunnel experiments of dynamic morphing wings, which would complement numerical studies and provide vital clues on unsteady phenomena and the unsteady evolution of lift and drag.

2.7. Summary

This chapter summarizes and discusses various aspects related to the state of the art of morphing wings. First a brief history of the development of morphing was presented along with definitions and reasoning behind their use. A classification of morphing wings was presented emphasizing that camber change is the focus of this work.

The second part of the chapter focused on a review of the numerical studies performed on morphing configurations along with the goals and level of fidelity used. It was recognised that numerical studies, in order to balance accuracy and computational requirements, compromised by using low accuracy turbulence models or neglecting unsteady dynamic effects. Many prototypes of morphing mechanisms were built and experiments conducted. Validations of numerical methods were conducted for different levels of accuracies but dynamic morphing wings have not been investigated experimentally. Finally, a review of AFC using morphing was provided with a focus on the use of high frequency, low amplitude harmonic morphing.

Table 2.1 summarises the main gaps found in the literature. The present research work will attempt to bridge the gaps found in the analysis of morphing wings; this would be accomplished by investigating dynamic morphing wings. To achieve it, a framework will be developed, which includes an unsteady parametrization method to model the deformation. An integration of the modified parametrization method with a high fidelity CFD solver and mesh deformation will be addressed using appropriate dynamic mesh schemes. Furthermore, the study will mainly focus on the aerodynamic understanding of the flow behaviour around morphing configurations and will present a case study of active morphing for possible aerodynamic and aeroacoustic control purposes.

Table 2.1: Issues addressed in literature and the ones lacking.

Aspect	What has been done	What needs to be addressed
Focus of the studies	Optimization, structures ,control	In-depth studies of the flow features
Numerical accuracy	Lower-order methods, and lower-fidelity CFD (SA,SST)	Higher-fidelity CFD methods with enhanced turbulence methods (hybrid or LES)
Dynamic morphing	Mostly static morphing	dynamic morphing and unsteady evolution of the lift and drag
Dynamic mesh	Not explored	Efficient dynamic mesh methods
Deformation modelling	none	Unsteady parametrization
Experimental work	Static morphing	Dynamic morphing experiments

"A bird is an instrument working according to mathematical law, an instrument which is within the capacity of man to reproduce with all its movements."

Leonardo da Vinci

Treatise on the Flight of Birds, 1505

3. Theoretical Background

Chapter 3

Contents

3.1. Overview

In this chapter, the theoretical foundations of Computational Fluid Dynamics (CFD) are presented in section 3.2 followed by a brief introduction to turbulence models used in this work in section 3.3. An overview of available parametrization methods and the method of choice used in this work is presented in section 3.4. Finally, theory of dynamic mesh schemes and their implementation in ANSYS Fluent is presented in section 3.5.

3.2. Governing flow equations

The cornerstone of CFD is the fundamental governing equations of fluid dynamics; the Navier-Stokes (NS) equations. The NS equations are a system of non-linear, coupled Partial Differential Equations (PDEs). The NS equations originally refer only to the momentum conservation laws; however, in recent years, the NS equations have been used to designate the complete set of equations describing the following laws (Anderson and Wendt, 2009):

- The conservation of mass (continuity equation),
- The conservation of momentum (Newton's 2nd Law),
- The conservation of energy (1st Law of Thermodynamics).

The fundamental concept of mass conservation states that mass can be neither created nor destroyed but can only be moved in space. Mass conversation is expressed as the following continuity equation:

$$\frac{\partial \rho}{\partial t} + \frac{\partial (\rho u_i)}{\partial x_i} = 0 \tag{3.1}$$

where t is time, ρ is the fluid density, u_i, i = 1, 2, 3 denotes the i^{th} component of the flow velocity vector $\boldsymbol{u}$ and x_i, i = 1,2, 3 denotes the i^{th} component of the position vector **x**. For an incompressible fluid (where the density ρ remains constant within a parcel of fluid that moves with the flow velocity), the above equation can be simplified to:

$$\frac{\partial u_i}{\partial x_i} = 0 \tag{3.2}$$

The conservation of momentum is derived from a fundamental principle of classical physics, which is Newton's second law. The law states that the time rate change of momentum of a fluid particle equals the sum of the forces acting on that particle. It can be written as:

$$\frac{\partial (\rho u_i)}{\partial t} + \frac{\partial (\rho u_j u_i)}{\partial x_j} = \rho f_i - \frac{\partial (p)}{\partial x_i} + \frac{\partial (\tau_{ij})}{\partial x_j} \tag{3.3}$$

where f_i represents the body forces, p the pressure and τ_{ij} the viscous stress tensor, which is defined as :

$$\tau_{ij} = \mu\left[\left(\frac{\partial u_i}{\partial x_j} + \frac{\partial u_j}{\partial x_i}\right) - \frac{2}{3}\delta_{ij}\frac{\partial u_k}{\partial x_k}\right] \tag{3.4}$$

where μ is the molecular viscosity and δ_{ij} represents the Kronecker delta function, which is defined as:

$$\delta_{ij} = \begin{cases} 1, & i = j \\ 0, & otherwise \end{cases} \tag{3.5}$$

Equation (3.4) can be substituted into the governing equation (3.3) to obtain the Navier-Stokes equations, the velocity components for each dimension are $u_i(u, v, w)$ where u_i, for *i*=1, 2, 3 are u, v, w, respectively.

For an incompressible three-dimensional flow the term $-\frac{2}{3}\mu\frac{\partial u_i}{\partial x_i} = 0$ which gives the following:

$$\rho\left(\frac{\partial u}{\partial t} + u\frac{\partial u}{\partial x} + v\frac{\partial u}{\partial y} + w\frac{\partial u}{\partial z}\right) = \rho g_x - \frac{\partial p}{\partial x} + \mu\left(\frac{\partial^2 u}{\partial x^2} + \frac{\partial^2 u}{\partial y^2} + \frac{\partial^2 u}{\partial z^2}\right) \tag{3.6}$$

$$\rho\left(\frac{\partial v}{\partial t} + u\frac{\partial v}{\partial x} + v\frac{\partial v}{\partial y} + w\frac{\partial v}{\partial z}\right) = \rho g_y - \frac{\partial p}{\partial y} + \mu\left(\frac{\partial^2 v}{\partial x^2} + \frac{\partial^2 v}{\partial y^2} + \frac{\partial^2 v}{\partial z^2}\right) \tag{3.7}$$

$$\rho\left(\frac{\partial w}{\partial t} + u\frac{\partial w}{\partial x} + v\frac{\partial w}{\partial y} + w\frac{\partial w}{\partial z}\right) = \rho g_z - \frac{\partial p}{\partial z} + \mu\left(\frac{\partial^2 w}{\partial x^2} + \frac{\partial^2 w}{\partial y^2} + \frac{\partial^2 w}{\partial z^2}\right) \tag{3.8}$$

where f_i for *i*=1, 2, 3 are g_x, g_y, g_z respectively.

The third conservation law states "*energy can be neither created nor destroyed, it can only be transformed from one form to another*". The energy equation is necessary to solve when dealing with compressible flows for which density and temperature changes are important. It can be written in Cartesian coordinates as:

$$\frac{\partial \rho E}{\partial t} + \frac{\partial}{\partial x_i}[u_i(\rho E + p)] - \frac{\partial}{\partial x_i}(u_i \tau_{ij} - q_j) = 0 \quad (3.9)$$

where E is the total energy of the fluid, defined as :

$$E = \rho \left[e + \frac{1}{2} u_i u_i \right] \quad (3.10)$$

e is the specific internal energy , $u_i u_i$ represents the kinetic energy and q_j is the transferred heat energy and can be obtained using Fourier's law:

$$q_j = -k \frac{\partial T}{\partial x_i} \quad (3.11)$$

where k is the heat transfer coefficient and T is the temperature of the fluid.

3.3. Turbulence Modelling

The Navier-Stokes equations are capable of describing all flows in nature, but to describe fully the nature of real-life flows we need to account for turbulence. Turbulence describes the chaotic nature of the fluctuations of various flow properties around the mean flow. These fluctuations interact across a wide range of length and time scales in all three dimensions, making it excessively costly to provide exact solutions of the NS equations. However, reducing the complexity of the NS equations is possible with appropriate approximations and turbulence modelling.

3.3.1. Direct Numerical Simulation

Using the unsteady NS equations to directly calculate the flow is an approach called Direct Numerical Simulation (DNS), where a large range of length and time scales are computed using an extremely fine mesh and a small enough time step. However, this method is extremely costly when it comes to computational resources, and even with the recent advances in supercomputing, only low

Reynolds number ranges could be tackled, which would not make it a viable candidate for industrial use.

3.3.2. Large Eddy Simulation

Large Eddy Simulation (LES) is able to resolve the larger flow structures using a filtered version of the NS equations. The remaining isotropic small eddies are modelled using a Sub-Grid Scale (SGS) turbulence model. This would enable a much better resolution of the flows with coarser spatial and time resolution compared with DNS. This makes LES relatively computationally affordable and more applicable to industrial problems than DNS, but it is still restricted for industrial use. The spatially-filtered LES governing equations (Sagaut, 2006), for an incompressible flow read:

$$\frac{\partial \overline{u_i}}{\partial x_i} = 0 \tag{3.12}$$

$$\frac{\partial \rho \bar{u}_i}{\partial t} + \frac{\partial \rho \bar{u}_i \bar{u}_j}{\partial x_j} = \rho f_i - \frac{\partial \bar{p}}{\partial x_i} + \mu \frac{\partial^2 \bar{u}_i}{\partial x_j \partial x_j} - \frac{\partial \tau_{ij}}{\partial x_j} \tag{3.13}$$

where $\overline{u_i}$ are the filtered velocity components and $\bar{p}$ is the filtered pressure. The subgrid-scale stress is defined as:

$$\tau_{ij} = \rho \overline{u_i u_j} - \rho \bar{u}_i \bar{u}_j \tag{3.14}$$

One of the most widely used subgrid-scale models is the Smagorinsky model (Smagorinsky, 1963) :

$$\tau_{ij} - \frac{1}{3}\tau_{kk}\delta_{ij} = \mu_t \left(\frac{\partial \bar{u}_i}{\partial x_j} - \frac{\partial \bar{u}_j}{\partial x_i} \right) \tag{3.15}$$

where μ_t is the sub-grid turbulent viscosity.

3.3.3. RANS and URANS

A third approach which can be taken when it comes to solving the NS equations is the Reynolds-Averaged Navier-Stokes (RANS). As its name indicates, RANS consists of decomposing an instantaneous flow value ϕ into a mean value $\overline{\phi}$ and a fluctuating value ϕ':

$$\phi = \overline{\phi} + \phi' \tag{3.16}$$

This formulation is then inserted into the NS equations where Reynolds averaging (Reynolds, 1895) is performed. Another key feature of the RANS model is that it can be applied to both steady and unsteady flows; the difference is only in the averaging process. The Unsteady RANS (URANS) equations are obtained by time averaging over a specific time interval (time step). Due to its linear aspect, the continuity equation is unchanged by the averaging process, however the RANS form of the momentum equation reads:

$$\frac{\partial(\rho u_i)}{\partial t} + \frac{\partial(\rho u_j u_i)}{\partial x_j} = \rho f_i - \frac{\partial(p)}{\partial x_i} + \frac{\partial}{\partial x_j}\left(\mu \frac{\partial u_i}{\partial x_j} - \rho\overline{u_i u_j}\right) \tag{3.17}$$

where μ is the molecular viscosity and $\rho\overline{u_i u_j}$ is called the Reynolds stress tensor which arises from the averaging of the non-linear convective term which is unknown. The computation of the Reynolds stress provides a closure to the RANS equations, and the way the computation of this tensor is performed gives rise to various turbulence models as shown in Figure 3.1.

Various classes of turbulence models exist. The Reynolds Stress Model (RSM) is one of the most elaborate turbulence models as it solves transport equations for the Reynolds stresses, together with an equation for the dissipation rate. However, this

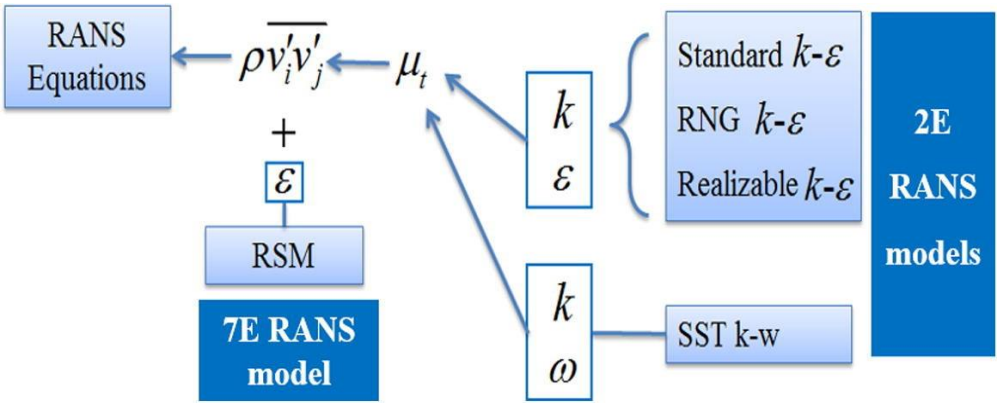

Figure 3.1: Various RANS turbulence models (Chen et al., 2017). (Used with permission of the publisher)

means that up to seven more equations must be solved which adds an additional computational cost. The eddy viscosity model on the other hand, uses the Boussinesq approximation to relate the Reynolds stress components to the mean strains in the following manner:

$$\rho\overline{u_i u_j} = \frac{2}{3}\rho k\delta_{ij} - \mu_t\left(\frac{\partial\overline{u_i}}{\partial x_j} - \frac{\partial\overline{u_j}}{\partial x_i}\right) \tag{3.18}$$

Equation (3.18) describes the eddy viscosity model for Reynolds stresses. There are various models to approximate the turbulent viscosity μ_t. For example, one-equation models like the Spalart-Allmaras model (SA) (Spalart and Allmaras, 1992) require one equation to be solved for the turbulent viscosity except in the near-wall region where a proper wall function is needed constituting the limitation of this class of turbulence models.

The most popular turbulence models are the so-called two-equation models, in which transport equations are solved for two turbulent properties, classically the turbulent kinetic energy, k, and its dissipation rate ϵ; or the alternative inverse time scale, ω. The k-ω SST model (Menter, 1994) was used in the current work therefore

it will be presented in more detail. Menter's *k-ω* SST model requires the solution of two additional equations, one for the specific turbulent kinetic energy *k* and another for the specific turbulent dissipation rate *ω* (ANSYS, 2018):

$$\frac{\partial \rho \alpha_l k}{\partial t} + \frac{\partial \rho \alpha_l u_j k}{\partial x_j} = \alpha_l P^{SST} - \alpha_l D_k^{SST} + \frac{\partial}{\partial x_j}\left[\alpha_l(\mu + \sigma_k \mu_t)\frac{\partial k}{\partial x_j}\right] \quad (3.19)$$

$$\begin{aligned}\frac{\partial \rho \alpha_l \omega}{\partial t} + \frac{\partial \rho \alpha_l u_j \omega}{\partial x_j} \quad = \quad & \alpha_l \frac{\gamma}{\nu_t} P^{SST} - \alpha_l D_\omega^{SST} + \frac{\partial}{\partial x_j}\left[\alpha_l(\mu + \sigma_\omega \mu_t)\frac{\partial \omega}{\partial x_j}\right] \\ & +2(1-F_1)\frac{\rho \alpha_l \sigma_\omega}{\omega}\frac{\partial k}{\partial x_j}\frac{\partial \omega}{\partial x_j}\end{aligned} \quad (3.20)$$

The production and destruction terms can be calculated with:

$$P^{SST} = \tau_{ij}\frac{\partial u_i}{\partial x_j}, \qquad D_k^{SST} = \beta^* \rho \omega k, D_\omega^{SST} = \beta \rho \omega^2 \quad (3.21)$$

Reynolds stresses and the rate-of-strain tensor are:

$$\tau_{ij} = \mu_t\left(2S_{ij} - \frac{2}{3}S_{kk}\delta_{ij}\right) - \frac{2}{3}\rho k \delta_{ij} \quad (3.22)$$

$$S_{ij} = \frac{1}{2}\left(\frac{\partial u_i}{\partial x_j} + \frac{\partial u_j}{\partial x_i}\right) \quad (3.23)$$

Eddy viscosity is calculated from:

$$\mu_t = \frac{\rho a_1 k}{\max(a_1 \omega, SF_2)}, \qquad S = \sqrt{2S_{ij}S_{ij}} \quad (3.24)$$

where *S* is a modulus of the rate-of-strain tensor. The function F_2 is calculated using Eq 3.25.

$$F_2 = \tanh\left[max\left(2\frac{\sqrt{k}}{\beta^*\omega d}, \frac{500\nu}{d^2\omega}\right)\right]^2 \quad (3.25)$$

A blending function is used for the constants σ_k and σ_ω which are empirically defined:

$$\phi = F_1\phi_1 + (1 - F_1)\phi_2 \quad (3.26)$$

Where F_1 is defined by:

$$F_1 = \tanh\left(\left(\min\left[\zeta, \frac{4\rho\sigma_{\omega 2}k}{CD_{k\omega}d^2}\right]\right)^4\right) \quad (3.27)$$

$$\zeta = \max\left(\frac{\sqrt{k}}{\beta^*\omega d}, \frac{500\nu}{d^2\omega}\right) \quad (3.28)$$

and

$$CD_{k\omega} = \max\left(2\rho\sigma_{\omega 2}\frac{1}{\omega}\frac{\partial k}{\partial x_j}\frac{\partial \omega}{\partial x_j}, 10^{-10}\right) \quad (3.29)$$

Both the *k-ω* and the SST variant have similar formulation, however the SST model uses modified formulation for the turbulent viscosity to account for the turbulent shear stress transport effects. Furthermore, SST uses the original formulation of the *k-ω* model in the inner regions of the boundary layer but switches to *k-* ϵ in the outer regions and free shear flows (Menter, 1994).

3.3.4. Hybrid RANS-LES models

The turbulence models introduced in the previous section have been extensively used for common engineering problems. Nevertheless, they had an essential disadvantage caused by the averaging procedure, which only models the mean characteristics of a flow without providing any spectral information of the smaller flow structures. In contrast, the LES approach provides much more detail and finer

spectral content when it comes to turbulence broadband spectrum, but the computational cost remains extremely prohibitive for industrial scale applications. To offset the limitations of RANS and reduce the cost of LES, a hybrid formulation that switches between RANS and LES was proposed by Spalart *et al.* (1997) which was named the Detached Eddy Simulation (DES).

Detached Eddy Simulation (DES)

In DES the wall boundary layer region is completely covered by a RANS model (SA or SST) whilst the free shear layers are modelled using LES, the switching between the two models is automatically performed based on the grid resolution used for calculations. The RANS length scale is replaced in DES by:

$$L_{DES} = \min(L_{RANS}, C_{DES}\Delta) \tag{3.30}$$

where Δ is the maximum edge length of the local computational cell, L_{RANS} is the RANS model turbulence-length scale and C_{DES} is a constant.

The DES was successfully used in many applications, nevertheless, one of its downfalls is that the switching could be induced by the mesh inside the RANS region which depreciates RANS prediction and triggers a "numerical separation" or what is commonly known as the Grid-Induced Separation (GIS) (Menter, 2012). An alternative was the development of the Delayed DES (DDES), which better shields the RANS region from unwanted LES interference. This model saw a few other improvements specifically the Shielded DES (SDES) and Stress Blended Eddy Simulation (SBES).

SDES and SBES

Shielded Detached Eddy Simulation (SDES) is similar to DES in all aspects except that it offers a shielding function and a different length scale which proved a much stronger shielding than previous DDES models. The hybrid model Stress-Blended Eddy Simulation, or SBES (Menter, 2012) was also used in this work to provide closure to the Navier-Stokes equations. The SBES combines the Reynolds

Averaged Navier-Stokes (RANS) using its Shear Stress Transition (SST) *k-ω* turbulence model, and Large Eddy Simulation (LES) based on the Wall-Adapting Local Eddy-Viscosity (WALE) sub-grid model (Nicoud and Ducros, 1999).

The blending function is the same used in the Shielded Delayed Eddy Simulation (SDES) (ANSYS, 2018). Moreover, a switching function is used to explicitly switch between the models:

$$\tau_{ij}^{SBES} = f_S \tau_{ij}^{RANS} + (1 - f_S)\tau_{ij}^{LES} \tag{3.31}$$

where τ_{ij}^{RANS} is the RANS portion and τ_{ij}^{LES} is the LES portion of the modeled stress tensor, f_S is the shielding function.

The main advantages of SBES is that it gives explicit control over which part of the flow the LES is applied to, it provides a rapid transition from RANS to LES region (Menter, 2016), and it has less dependency on the mesh compared with the DES model as the DES shielding based on the mesh length scale is reduced. The RANS wall boundary layer regions are protected against influences from the LES model when the shielding functions are in use, which protects against early switch to the LES model, which if it occurs, can cause a strong decline in the RANS capabilities (Spalart *et al.*, 2006).

3.4. Overview of Parametrization Techniques

In order to model an unsteady morphing wing, the first step is to define its geometry and deformation. For this purpose, a parametrization method that has the flexibility to represent a large set of aerofoils with sufficient robustness to yield a high fidelity and a smooth boundary/geometry/surface representation is needed. Moreover, the method needs a minimum set of design variables to morph from one configuration to another. Finally, the method needs to be easily extended to model the deforming motion in time if required. A brief overview of the available shape parametrization methods widely used in aerospace engineering is presented in this section, along with the method used as a basis for the test cases investigated in the next chapters.

Given the importance of parametrization in the aerospace design process, several methods have been introduced with varying degrees of robustness, flexibility, conciseness, and suitability for multidisciplinary complex application using high fidelity analysis tools such as CFD. A few review articles have been published, including the work by Samareh *et al.* (2001) who provided a comprehensive survey of parametric models up to 2001. Parameterization techniques were divided into eight categories: basis vector, domain element, partial differential equation (PDE), CAD-based, discrete approach, polynomial and spline, analytical and geometric, and Free-Form Deformation (FFD). Zhang *et al.* (2018) classified the parametrization approaches depending on their applicability to 2D or 3D problems. The following will concisely expand on four of the most commonly used methods.

Discrete approach

The most straightforward method for representing a two dimensional geometry is by using the coordinates of a set of points on its boundary and connecting these points with straight lines (Figure 3.2). This method was easily implemented (Campbell, 1992; Jameson *et al*., 1997) but it has the disadvantage that it needs a large set of points in order to maintain a smooth shape making it computationally inefficient and it is hard to maintain a smooth continuity while deforming the geometry. However, the ability to use an existing grid for optimization is one of the attractive features of this approach.

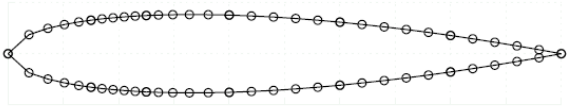

Figure 3.2: The discrete approach.

Hicks-Henne Bump Functions

In this method, a set of fluctuations or shape functions are superimposed over a baseline airfoil curve, which can be defined either numerically or analytically. An example of these functions are the Hicks-Henne bump functions (Hicks and Henne, 1978), in which different airfoil shapes are obtained by the control of weight coefficients. There are several additional perturbation methods, which vary in accuracy and complexity. However, the disadvantage of such methods is that changing one or more of the function variables is often non-intuitive and mainly suitable for fully automated processes but less for a controlled deformation.

Parametric Section (PARSEC) approach

A more intuitive method is to use geometric parameters such as leading edge radius, thickness-to-chord ratio or trailing edge angle to describe a shape. The most widely used method in this category is the PARSEC method introduced by Sobieczky (1999), which uses 11 basic design parameters , all of which have actual physical meaning. Table 3.1 lists the PARSEC variables.

With the PARSEC method, the upper and lower airfoil curves are modelled separately, and assuming a sharp trailing edge, the upper and lower curves could be expressed as the following:

$$z(x) = \sum_{n=1}^{6} a_n x^{n-\frac{1}{2}} \tag{3.32}$$

Table 3.1: Physical meanings of parameters in PARSEC method.

Parameters	Physical meaning
r_{le}	Radius of leading edge
Z_{XXup}	Curvature at upper crest location
Z_{up}	Upper crest value
X_{up}	Upper crest location
X_{lo}	Lower crest location
Z_{lo}	Lower crest value
Z_{XXlo}	Curvature at lower crest location
α_{TE}	Trailing edge direction
β_{TE}	Trailing edge wedge angle
Z_{TE}	Vertical coordinate of trailing edge
ΔZ_{TE}	Thickness of trailing edge

A similar process can be applied to the lower surface to acquire the other five design parameters.

The PARSEC method is very intuitive for airfoil design as it makes it easy to control individual physical properties. However; its disadvantage is that each shape change has to be translated into a physical property of the airfoil, which might compromise the design freedom, and this method can hardly be applied to other shape parametrizations which makes its use very limited (Zhang *et al.*, 2018).

Polynomial and spline

Using a spline or a polynomial to represent a smooth shape can greatly reduce the number of variables. A polynomial can be represented in the standards power basis form

$$y(x) = \sum_{i=0}^{p} \bar{c_i}\, x^i \tag{3.33}$$

A better way to represent a curve is using the Bezier representation, which is defined as follows:

$$y(x) = \sum_{i=0}^{p} \overline{P_i}\, B_{i,p}(x) \tag{3.34}$$

where $\overline{P_i}$ is a vector of coefficients or control points and $B_{i,p}(x)$ are the Bernstein Polynomials of degree p. The resulting curve will closely follow the control polygon defined by the control points of $\overline{P_i}$. This definition is more intuitive than the power basis. A Bezier representation is shown in Figure 3.3.

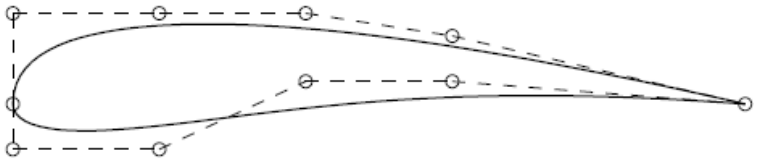

Figure 3.3: Airfoil described by a Bezier representation.

A disadvantage of using the Bezier curves is that the degree of the Bernstein polynomials increases significantly for more complex shapes, thus making it an inefficient process. A solution to this drawback is the use of a string of lower order curves called B-splines, A B-spline curve can be described as follows:

$$C(\xi) = \sum_{i=0}^{n} N_i^p(\xi)\, \overline{\mathrm{P}_1}\ a \le \xi \le b) \tag{3.35}$$

where the Bernstein polynomials have been replaced by a set of B-splines basis functions N_i^p and the Bernstein coefficient vector $\overline{P_1}$ by a B-spline control polygon $\overline{\mathrm{P}_1}$. The parametric variable ξ is used instead of the Cartesian coordinate *x*. In addition, the number of control points *n + 1* is independent of the order *p−1* of the individual Bezier curves. However, despite recent progress, the parameterization and construction of complex, three-dimensional models based only on polynomial and spline representations is still difficult to achieve. A special form of B-spline, called non-uniform rational B-spline (NURBS) can represent most parametric and implicit curves and surfaces without loss of accuracy, and not only can it be used

to represent shapes like cylinders or cubes but free form shapes as well (Piegl and Tiller, 1996; Farin, 1993; Sóbester and Forrester, 2014).

Polynomial and spline techniques are widely used for 2D and simple 3D models. However, for complex three dimensional models many curves and surfaces are required which makes them difficult to model outside CAD (Samareh, 1999) in addition it needs a large number of control points which contribute in the creation of irregularities in the geometry (Reuther and Jameson, 1995). Additionally, this class of methods suffers from the same lack of intuitiveness when it comes to controlled deformation as it does not relate physical parameters.

Free form deformation

The Free-Form Deformation (FFD) allows the deformation of an object in 2D or 3D, but instead of directly manipulating the surface of the object, the FFD techniques define a deformation field over the space embedded in a lattice, which is built around the geometry. By transforming the space coordinates inside the lattice, the FFD technique deforms the object, regardless of its geometrical description. The technique originated from computer-generated objects which comes from Computer Graphics (Sederberg and Parry, 1986).

The FFD manipulates the geometry by adopting Bernstein polynomials to map the coordinates. A lattice region in Cartesian coordinates embeds the original geometry, and each control point of the lattice could be used to deform the original geometry, then the Bernstein polynomials are used to propagate the deformation. An added advantage of the FFD is that the computational mesh used for CFD can also be deformed simultaneously to conform to the new shape of the object. This contributed to its success for optimization tasks (Samareh, 2000). However, a disadvantage of the method is that deforming the geometry surface is not intuitive as the control points are not directly on the surface, therefore the design variables have no physical meaning, which is essential for a good representation of a controlled morphing strategy. To resolve this issue in optimization the original algorithm was altered, and the modified algorithm is referred to as multidisciplinary aerodynamic-structural shape optimization using deformation

(MASSOUD) (Samareh, 2000) which parameterize the shape perturbations rather than the geometry.

CST method

The Class Shape Transformation (CST) method is another widely used parametrization method which was introduced by Kulfan *et al.* (2006). As its name suggests, the CST method is composed of an analytical function called the "Class" function and a parametric "shape" function. The class function describes a basic class of shapes and the shape function describes the permutation around this basic shape. The general formulation of the CST method reads:

$$\varsigma(\varphi) = C_{N_2}^{N_1}(\varphi) \times S(\varphi) + \psi.\Delta\zeta_u \tag{3.36}$$

where $\varphi = \frac{x}{c}$ presents the non-dimensionalized coordinates with respect to the airfoil chord (c). $C_{N2}^{N1}(\varphi)$ is the Class function and $S(\varphi)$ is the upper or lower shape function respectively. The general class function is defined as follow:

$$C_{N_2}^{N_1}(\varphi) = \varphi^{N_1}(1-\varphi)^{N_2} \tag{3.37}$$

$C_{1.0}^{0.5}(\psi)$ would represent a NACA type airfoil with a round nose and a pointed aft end which forms the basis of the CST airfoil representation. Therefore, all the other airfoils are derived from the class function as presented in Figure 3.4. In order to represent other shapes (i.e. a nacelle) the N_1 and N_2 parameters can be varied to achieve the desired class of geometries.

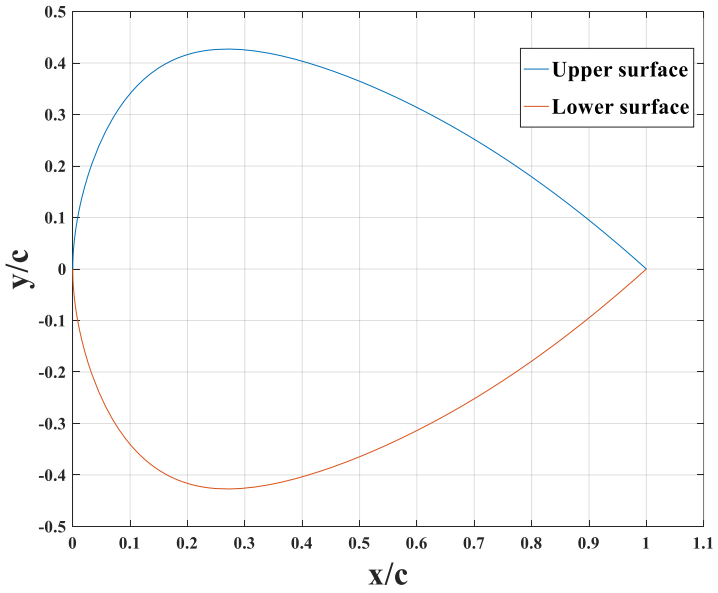

Figure 3.4: Unit Airfoil for $C_{1.0}^{0.5}(\psi)$.

The traditional CST method use Bernstein polynomials as shape functions:

$$S(\varphi) = \sum_{i=0}^{n} B_i \cdot \binom{n}{i} \varphi^i (1-\varphi)^{n-i} \tag{3.38}$$

where n is the order of the polynomial and B_i is the Bernstein coefficient. The weighting coefficients could be obtained by fitting methods such as the least square method if a specific airfoil is targeted. It is possible to use the weighting coefficients as variables in a numerical design problems or optimization, or they can be used for parametric shape variation, which is relevant for morphing wings design.

A feature of the Bernstein polynomials is that the lower the order of the term, the more influence it has closer to the leading edge, whereas the higher order terms have more effects closer to the trailing edge (Sóbester and Forrester, 2014). This makes it intuitive to tweak the terms depending on where the deformation is wanted. Figure 3.5 shows the terms of the a 10th degree Bernstein polynomial with all coefficients set to one.

However, the use of Bernstein polynomials might reduce the accuracy of the modelling. Each of these polynomials has a global effect on the airfoil shape, but the influence of each term decays relatively quickly. For instance, the effect of the 0^{th} order shape function term declines quickly and its effect on the TE of the airfoil is relatively small.

All the features described earlier made the CST method a suitable choice for several tasks requiring parametrizations, specifically optimisation. The method was thus applied for wing optimisation studies, for instance, Lane *et al.* (2009, 2010) showed the use of CST in an inverse design process of airfoils, with the emphasis on the applicability of this method to various classes of geometry. In addition, it was applied for morphing wings optimisation in the work of De Gaspari *et al.* (2015) who successfully incorporated a 3D version of CST in their optimisation framework for morphing wings. The authors used a least square fit in order to match pre-existing CAD models and extract the CST coefficients used afterwards as optimisation variables.

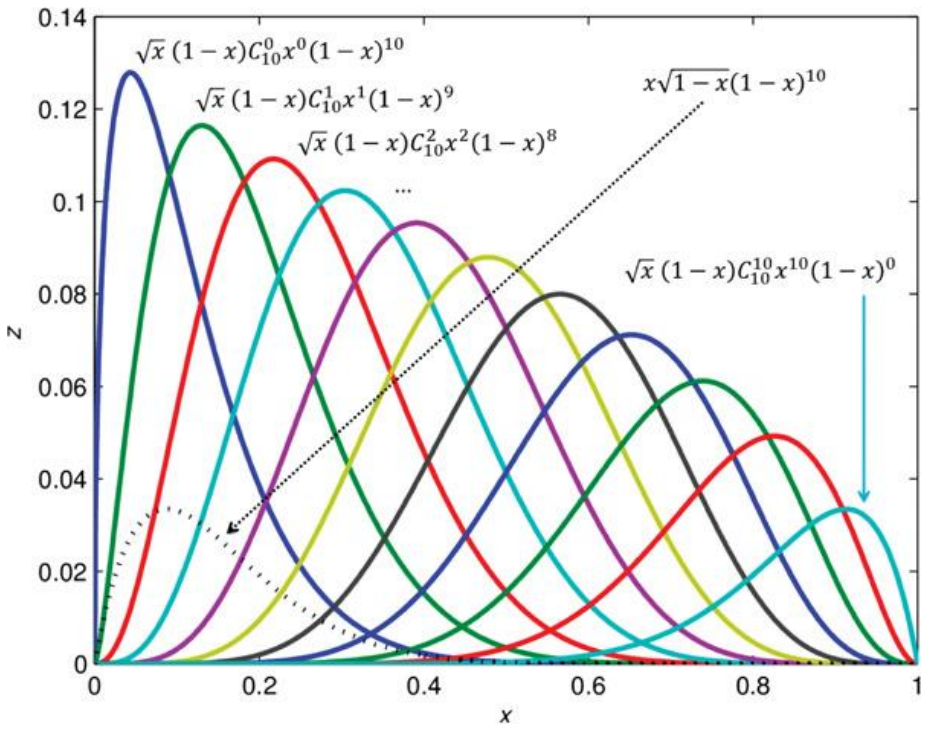

Figure 3.5:Bernstein Polynomials terms for 10th order in addition to the leading edge shaping term (Sóbester and Forrester, 2014). (Used with permission of the publisher)

There are several reasons why this method was initially chosen for use in this work:

- The easy and intuitive mathematical formulation.
- CST produces smooth curves with small errors and no discontinuities.
- Easily extendable to 3D.
- Local control on different portions of the airfoil.
- Suitable for implementation in a User-Defined Function (UDF) in ANSYS Fluent.

Specialized techniques could also be derived from experimental works done such as the one presented next.

3.4.1. FishBAC parametrization

The parametrization techniques explored in the previous section are primarily used for optimization problems. However, a few studies needed a simple parametrization method to produce various classes of the same geometry by changing two or three parameters. A method of interest was the one used by Woods *et al.* (2014) for the aerodynamic study of the FishBAC concept. The method used was a relatively simple beam-like deformation to model a NACA 0012 which undergoes trailing edge deflections starting from different chord stations and for various maximum deflection values. In that study, the baseline is morphed by the addition of a parametric camber definition to a specified region of the chord.

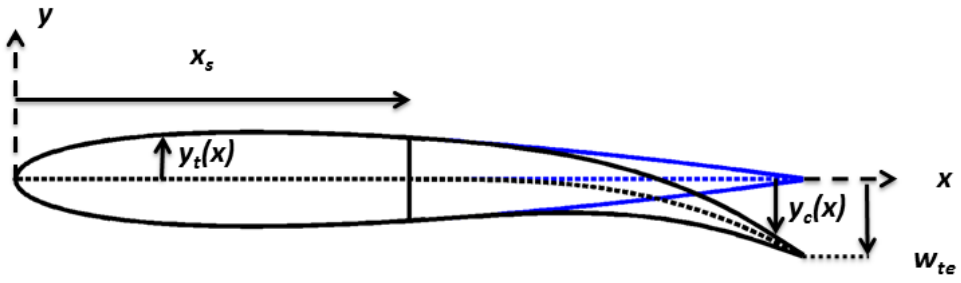

Figure 3.6:Morphing camber geometry definition (Woods *et al.*, 2014).

It is worth noting that the camber line is defined as the line that is half way between the upper and the lower surfaces of the airfoil. However, the chord is the line joining the leading and trailing edges of an airfoil.

Figure 3.6 shows different parameters that constitute the FishBAC model, the start of the morphing region is given by the parameter x_s, and the maximum TE deflection by w_{te}. The airfoil shape is obtained by the addition of a NACA thickness distribution (here NACA 0012) and a parametric camberline. The NACA four series thickness distribution is defined as (Jacobs *et al.*, 1933) :

$$y_t = \left(\frac{th}{c}\right)\left(0.2969\sqrt{\bar{x}} - 0.1260\bar{x} - 0.3516\,\bar{x}^2 + 0.2843\bar{x}^3 - 0.1015\bar{x}^4 \right) \tag{3.39}$$

where $y_t = \frac{y}{c}$ is the non-dimensional thickness distribution, $\bar{x} = \frac{x}{c}$ is the non-dimensional distance along the chord (c), th is the maximum thickness as a fraction of the chord (e.g. th=0.12 for a NACA 0012).

A third order polynomial was used to define the camberline of the morphing part of the airfoil where the chord's length is preserved for simplicity, which could be practical as well if the material used for morphing provide a certain degree of elasticity, it was parametrized to have direct control over the amount of trailing edge deflection:

$$y_c = \begin{cases} 0, & 0 \le \bar{x} < x_s \\ -w_{te}\dfrac{(\bar{x} - x_s)^3}{(1 - x_s)^3}, & \bar{x} \ge x_s \end{cases} \tag{3.40}$$

where the w_{te} is the value of maximum deflection at the trailing edge and x_s is the start location for the morphing. The thickness distribution (Eq 3.39) is then added to the camber distribution (Eq 3.40) at right angles and the upper and lower coordinates of the surface could be represented as follows:

$$x_u = \bar{x} - y_t \sin\ \theta$$
$$x_l = \bar{x} + y_t \sin\ \theta \tag{3.41}$$

$$y_u = y_c + y_t \cos\ \theta$$
$$y_l = y_c - y_t \cos\ \theta \tag{3.42}$$

where θ is the local slope of the camber line and could be obtained from:

$$\theta(x) = \tan^{-1}\left(\frac{dy_c}{dx}\right) \tag{3.43}$$

This method is simple, has three relevant parameters for morphing trailing edge flaps application (*th*, w_{te} and x_s) and is readily expandable to include unsteady deformation.

3.4.2. Method of choice for unsteady morphing

This work undertakes the task of studying the effects of the deforming motion of an airfoil (or wing). The deformation is specified for each geometrical parameter like the flap deflection angle for instance. However, from the literature survey conducted it appears that most parametric methods were used for optimization purposes or the generation of various geometry for static testing. Therefore, it is imperative to conduct limited modification on available methods in order to obtain the desired unsteady method.

The CST method was successfully modified to include a time variable yielding the unsteady CST method (u-CST), details of the u-CST and a MATLAB implementation are available in Appendix A. Nevertheless, the proposed modification still suffers from the lack of intuitiveness, even though camber and thickness deformation could be achieved with the u-CST, this method still needs further development to produce a more intuitive version of the u-CST. This could be achieved for instance by merging it with recently developed methods such as

the intuitive CST (i-CST) which combines the CST with the intuitiveness of the PARSEC method (Zhu and Qin, 2013). However, Despite u-CST being a promising method, it still needs more effort to make it as generalised and useful as it could be, and it is included in this thesis as the author hopes that it could guide future endeavours even if it will not be used in the reminder of the thesis.

Alternatively, the FishBAC parametrization method offers a suitable alternative. It is a concise method, specifically targeted at a morphing airfoil application, easily extended to include unsteadiness and could be applied to quasi-3D problems. Additionally, replicating the same geometry studied by Woods *et al.* (2014) would allow the possibility of cross validation of numerical results produced from this work with results already published. This is the reason the FishBAC parametrization method was used in the remaining test cases, details of the modifications introduced will be presented in Chapters 4, 6 and 7.

Once the parametrization method is available, the next stage of the dynamic morphing analysis is the dynamic mesh; there are various methods available to handle a deforming mesh, which is the topic of the next section.

3.5. Dynamic Mesh

Many physical problems in fluid dynamics involve moving boundaries e.g. aero-elasticity simulation (Silva and Bartels, 2004), blood flow through veins (Ding, Zhu and Friedman, 2002), flapping wings (Takizawa *et al.*, 2012) or Fluid-Structure Interaction problems (FSI) (Le Tallec and Mouro, 2001). To achieve efficient and accurate flow solutions to such problems when using mesh-based CFD, the computational domain needs to adapt seamlessly to any geometry changes. One way to achieve this is by regenerating new grids for the deforming geometry or by deforming the computational grids. Creating new meshes is a tedious, time-consuming task and computationally expensive. Additionally, mapping solution data between the old and new mesh would add extra CPU requirements and numerical errors. This would make the mesh deformation alternative a more attractive method for moving boundary problems. Various mesh deformation techniques exist which can be classified in two categories; interpolation-based methods and physical analogy methods (Selim and Koomullil, 2016). A brief overview of these methods is presented in the following sub-sections.

3.5.1. Mesh Deformation Using Interpolation-Based Methods

These methods consider mesh deformation problems as pure interpolation problems, as the deformations are interpolated from boundary points to other points in space (Luke *et al.*, 2012). These methods can be easily applied to various mesh types and although they are usually computationally inexpensive, they come with a penalty of numerical errors. The most popular approaches using interpolation are listed next.

TransFinite Interpolation (TFI)

TransFinite Interpolation (TFI) is a method which was extensively used in the last decades (Wang and Przekwas, 1994). TFI is a higher efficiency algebraic method where mesh boundary points are interpolated along grid lines to points in the interior of the mesh. This method is only suitable for structured grids as it does not

include any mechanisms to handle mesh overlapping or element crossing (Selim and Koomullil, 2016).

Delaunay graph method

Another scheme used for mesh deformation is the Delaunay graph mapping method which is suitable for any topology for computing unsteady flow problems with geometrical deformation (Liu *et al.*, 2006). In this method, a Delaunay graph of the solution domain is generated over the entire computational domain, the mesh points are afterwards located in the graph. Subsequently, a one to one mapping between the Delaunay graph and the computational grid is maintained during the mesh deformation and a new computational grid is efficiently generated after the deformation. However, for complex geometries the Delaunay graph is hard to construct.

Radial basis function interpolation

A relatively new mesh deformation method was introduced by (Boer *et al.*, 2007) based on the Radial Basis Functions (RBF) which interpolates the displacements of the boundary nodes. The method can handle large mesh deformations caused by translations, rotations and deformations, both for 2D and 3D meshes. A sum of basis function approximates the displacements through the entire domain, and then could be written as:

$$\boldsymbol{s}(\mathbf{x}) = \sum_{\boldsymbol{j=1}}^{\boldsymbol{n_b}} \boldsymbol{\alpha_j \phi}\left(\left\|\mathbf{x} - \mathbf{x}_{\mathbf{b}_j}\right\|\right) + \boldsymbol{p}(\mathbf{x}) \tag{3.44}$$

where $\mathbf{x}_{\mathrm{b}_j} = [x_{\mathrm{b}_j}, y_{\mathrm{b}_j}, z_{\mathrm{b}_j}]$ are the boundary nodes, p a polynomial, n_{b} the number of boundary nodes and ϕ a given basis function with respect to the Euclidean distance$\|\mathbf{x}\|$. The coefficient α_j and the polynomial p are subject to the following conditions:

$$\left(\mathbf{x}_{\mathrm{b}_j}\right) = \mathbf{d}_{\mathrm{b}_j} \tag{3.45}$$

$$\sum_{j=1}^{n_\mathrm{b}} \alpha_j q\left(\mathbf{x}_{\mathrm{b}_j}\right) = 0 \tag{3.46}$$

And the value of α_j and the linear polynomials could be obtained from the following linear system:

$$\begin{bmatrix}\mathbf{d}_\mathrm{b} \\ 0\end{bmatrix} = \begin{bmatrix}M_{\mathrm{b,b}} & P_\mathrm{b} \\ P_\mathrm{b}^T & 0\end{bmatrix}\begin{bmatrix}\boldsymbol{\alpha} \\ \boldsymbol{\beta}\end{bmatrix} \tag{3.47}$$

where $\boldsymbol{\alpha}$ is a vector containing the coefficients α_j, $\boldsymbol{\beta}$ is a vector containing the coefficients of the linear polynomial p, $M_{\mathrm{b,b}}$ is a $n_\mathrm{b} \times n_\mathrm{b}$ matrix which contains an evaluation function and P_b is a $n_\mathrm{b} \times 4$ matrix with row j given by $\begin{bmatrix}1 & x_{\mathrm{b}_j} & y_{\mathrm{b}_j} & z_{\mathrm{b}_j}\end{bmatrix}$. The displacements in the computational mesh can be derived by evaluating the function $s(\mathbf{x})$ to obtain the internal grid points $\mathbf{d}_\mathrm{in}$:

$$\mathbf{d}_{\mathrm{in}_j} = s(\mathbf{x}_{\mathrm{in}_j}). \tag{3.48}$$

This method produces high-quality meshes in terms of skewness and orthogonality, it avoids the need of mesh connectivity information and the system of equations solved is linear. However, the straightforward implementation is extremely costly especially when it comes to large 3D problems where the memory usage is prohibitive. Various improvements and extension have been proposed to improve this method.

3.5.2. Mesh Deformation Using Physical Analogy

This class of methods is based on physical analogies, where the grid deformation is propagated using spring-like analogies or partial differential equations. The downside of these methods is that they involve solving large systems of equations implying higher computational cost and the need for grid connectivity information

resulting in extra memory requirements (Boer *et al.*, 2007; Selim and Koomullil, 2016). Nevertheless, these methods are widely used for their easy implementation and their adequate capabilities in preserving mesh quality. The main methods in this class are discussed in the following subsections.

Spring-Based Smoothing

For unstructured mesh deformation, Batina *et al.* (1990) proposed a spring analogy where the edges of the mesh cell are modelled as a linear spring. Farhat *et al.* (1998) extended its capabilities by the addition of a torsional spring. In this method, the edges between any two nodes are idealized as a network of springs and any displacement at a boundary node will generate a virtual spring force, which can be obtained on each node using Hooke's law:

$$\overrightarrow{F_i} = \sum_{j=1}^{n_i} k_{ij}\left(\Delta\overrightarrow{x_j} - \Delta\overrightarrow{x_i}\right) \tag{3.49}$$

where Δx_i, Δx_j are the displacements of node i and its neighbour j, n_i is the number of nodes connected to i. k_{ij} is the stiffness of the spring between node i and j:

$$k_{ij} = \frac{k_{fac}}{\sqrt{\left|\overrightarrow{x_i} - \overrightarrow{x_j}\right|}} \tag{3.50}$$

where k_{fac} is a spring constant factor (between 0 and 1).

The net force from all the springs connected to the node must be zero at equilibrium, an iterative equation results from this condition that can be controlled in the solver by the number of iterations and convergence tolerance:

$$\Delta\vec{x}_i^{m+1} = \frac{\sum_j^{n_i} k_{ij}\Delta\vec{x}_j^m}{\sum_j^{n_i} k_{ij}} \tag{3.51}$$

At convergence, the node positions are updated such that:

$$\vec{x}_i^{n+1} = \vec{x}_i^n + \Delta\vec{x}_i^{converged} \tag{3.52}$$

Spring-analogy is a quick and effective method for deforming meshes. Nonetheless, it performs better when the motion is largely normal to the boundary zone; otherwise, this method is prone to have cells collision issues. A few improvements were proposed, like the use of torsional springs placed between adjacent cells (Farhat *et al.*, 1998), or the ball-vertex method where an additional set of linear springs is added opposite the original one by confining each vertex to its ball through the said linear springs (Bottasso *et al.*, 2005).

Diffusion-Based Smoothing (Laplacian)

For diffusion-based smoothing, the mesh motion is governed by the following Laplace diffusion equation:

$$\nabla \cdot (\gamma \nabla \vec{u}) = 0 \tag{3.53}$$

where u is the mesh displacement velocity and γ is the diffusion coefficient. To ensure that the interior nodes will not cross the wall boundaries the interior displacement is bounded by the values of the displacement on the surface.

In ANSYS Fluent, two different formulations of the diffusion coefficient are implemented: boundary distance formulation for which $\gamma = \frac{1}{d^\alpha}$ or the cell volume formulation for which $\gamma = \frac{1}{V^\alpha}$, where d is the normalized boundary, V is the normalized cell volume, and α is a user input parameter.

The diffusion equation is discretized using a standard finite volume method and the resulting matrix is solved iteratively, and a node's position is updated according to:

$$\overrightarrow{x_{new}} = \overrightarrow{x_{old}} + \vec{u}\Delta t \tag{3.54}$$

This method is generally more computationally expensive but tends to generate better quality meshes especially for structured grids. It preserves the mesh closer to the deforming body walls and makes the far field absorb the deformation allowing larger deformations (Helenbrook, 2003).

Solid body elasticity

Another approach is to represent the mesh as a solid body elasticity (Lynch and O'Neill, 1980). The linear elasticity equations are solved in order to get the displacements with the modulus of elasticity (E) and Poisson's ratio (ν) set depending on the grid and deformation motion.

$$\nabla \cdot \boldsymbol{\sigma}(\vec{y}) = 0$$

$$\boldsymbol{\sigma}(\vec{y}) = \lambda\big(tr\boldsymbol{\varepsilon}(\vec{y})\big)\boldsymbol{I} + 2\mu\boldsymbol{\varepsilon}(\vec{y}) \tag{3.55}$$

$$\boldsymbol{\varepsilon}(\vec{y}) = \frac{1}{2}(\nabla\vec{y} + (\nabla\vec{y})^T)$$

where $\boldsymbol{\sigma}$ is the stress tensor, $\boldsymbol{\varepsilon}$ is the strain tensor, and $\vec{y}$ is the mesh displacement. The linear system is solved using a finite element discretization. This approach is computationally more expensive than the previous methods discussed. The same limitation applies to this model compared with diffusion smoothing.

Finally, another strategy used in the literature is the point-by-point strategy where each grid node is moved individually based on its position. The hanging nodes problem is inexistent in this method, and this method is only applied to boundary nodes of multi-grid blocks and the previous elastic or spring analogy methods were adopted for the interior mesh of the blocks (Potsdam and Guruswamy, 2001).

3.5.3. Meshless methods

Another noteworthy approach is the use of the meshless (or meshfree) methods. These methods represent a relatively new research area which have the potential to bypass the use of traditional discretisation grids (and dynamic mesh), effectively

eliminating the tedious task of high quality mesh generation and deformation. This makes meshless methods attractive for moving or deforming boundaries problems.

They are also less sensitive to mesh quality if a background mesh is used (Liu, 2012). Meshless methods require clouds of points within the fluid domain and on the boundary surfaces in order to discretize the governing partial differential equations (PDE). There are various types of meshless methods which have been explored for CFD:

i. Smoothed particle hydrodynamics (SPH) (Liu and Liu, 2003) which is a Lagrangian formulation deemed the best choice for nonlinear, fast dynamics or multiphase flow problems. It is based on particles use for interpolations and no mesh is required (Liu, 2012). This method can easily trace free surfaces and moving boundaries.
ii. Gradient smoothing method (GSM) uses an Eulerian formulation with a background triangular mesh meaning that it is not completely meshfree and it is suitable for both compressible and incompressible flows.
iii. Meshless Local Petrov-Galerkin (MLPG) is a method based on the weak form of a given PDE restraining the solution to performing numerical integration which makes it computationally inefficient compared with the regular approaches in finite volume methods for instance (Katz, 2009).
iv. Meshless methods based on RBF, such as the Unsymmetric RBF collocation (Kansa, 1990). RBF based schemes have the advantage of being truly meshfree compared to some other methods.

Despite the expected advantages of meshless methods, such methods are still under active development. They still suffer from the need of sufficiently dense point distribution which makes the computations a tedious task (Chew, Yeo and Shu, 2006). Research is still being conducted to address the prohibitive computational cost of meshfree methods, some of the promising techniques are the use of hybrid meshfree-mesh-based methods to improve both the performance and the accuracy of mesh free methods (Ding *et al.*, 2004; Javed, Djijdeli and Xing, 2016). However, as some meshless methods are still mesh dependent to some level, it introduces

interpolation errors at the interfaces (Liu, 2012). Finally, as meshless methods' algorithms are still under continuous development, there is limited availability of robust accessible software, as opposed to mesh-based software. This is restraining the applicability of meshless methods at industrial levels, confining it so far to specialised research.

3.5.4. Dynamic Mesh methods using ANSYS Fluent

ANSYS Fluent is a commercially available software for CFD. It is a finite volume based solver which includes both pressure and density based solvers. Additionally, it provides various Multiphysics modelling capabilities for a wide range of applications. Most importantly, it provides a framework to analyse problems where the shape of the domain is changing with time due to motion on the domain boundaries, consequently dynamic mesh is possible by means of secondary development of user defined functions (UDF) (ANSYS, 2018).

This section will discuss the theory behind the dynamic meshing schemes in Fluent and give a brief overview of UDFs.

ANSYS Fluent dynamic model can be applied to various problems (single or multiphase flows) and for all model equations such as turbulence, energy, species, phases, etc. The following Finite Volume equation is applicable for a general scalar ϕ:

$$\frac{d}{dt}\int_V \rho\phi \, dV + \int_{\partial V} \rho\phi(\vec{u} - \overrightarrow{u_g}) \cdot d\vec{A} = \int_{\partial V} \Gamma \nabla_\emptyset \cdot d\vec{A} + \int_V S_\phi \, dV \qquad (3.56)$$

where:

ρ : fluid density
$\vec{u}$: flow velocity vector
$\overrightarrow{u_g}$: mesh velocity of the moving mesh
Γ : diffusion coefficient
S_ϕ : source term of ϕ
∂V : represents the boundary of the control volume V

By using a first-order backward difference formula for instance, the time derivative term in Equation 3.57 can be written as:

$$\frac{d}{dt}\int_U \rho\phi \, dV = \frac{(\rho\phi V)^{n+1} - (\rho\phi V)^n}{\Delta t} \tag{3.57}$$

where n and $n+1$ stand for the current and next time step, and where V^{n+1} is computed from:

$$V^{n+1} = V^n + \frac{dV}{dt}\Delta t \tag{3.58}$$

where $\frac{dV}{dt}$ is the volume time derivative of the control volume. In order to satisfy the mesh conservation law, the volume time derivative of the control volume is obtained from:

$$\frac{dV}{dt} = \int_{\partial V} \overrightarrow{u_g} \cdot d\vec{A} = \sum_j^{n_f} \overrightarrow{u_{g,j}} \vec{A}_j \tag{3.59}$$

where n_f is the number of faces on the control volume and $\vec{A}_j$ is the area of the j^{th} face. The dot product $\overrightarrow{u_g} \cdot d\vec{A}$ on each control volume face is calculated from:

$$\overrightarrow{u_g} \cdot d\vec{A} = \frac{\delta V_j}{\Delta t} \tag{3.60}$$

δV_j is the volume swept out by the control volume face j over the time step Δt.

The solver update automatically updates the volume mesh at each time step based on the new positions of the boundaries. A starting mesh needs to be provided, alongside the prescribed motion which is expressed by means of a UDF in our case.

Dynamic meshing User-defined functions (UDF)

A user-defined function is a function written in *C* programming language that can be connected to the solver to embed new features in it (ANSYS, 2018). Dynamic meshing in Fluent makes use of two types of macros depending on the type of boundary movement:

a) Rigid body motion:

The macro DEFINE_CG_MOTION is used, which allows translational and/or rotational object motion with respect to the centre of gravity of the body. All nodes associated with a moving boundary move without any relative motion to each other's and consequently no deformation is possible.

b) Non-rigid Body deformation:

As we are interested in morphing (deforming) wings, the macro most suitable for this application is the DEFINE_GRID_MOTION. This macro allows the control of each boundary node independently from the others, offering the possibility to model non-rigid body transformations.

Fluent has three of the geometrical mesh deformation approaches integrated; spring-analogy, diffusion based, and linear body elasticity. In addition, there is the possibility of remeshing certain elements that do not meet quality criteria. For large deformation problems such as morphing wings, both smoothing and remeshing methods are used in order to preserve the best mesh quality.

3.5.5. Mesh Quality Metrics in ANSYS Fluent

In CFD, mesh quality could have a large influence on the accuracy of the prediction obtained, the efficiency of the simulation and convergence. Many factors could be accounted for to quantify mesh quality such as the influence of the mesh on the accuracy of the solution or the geometric mesh property having to do with the element size and shape (Knupp, 2007). Various mesh quality metrics could be used to assess the quality of all the elements in a mesh. These metrics are convenient as

they can be computed by looping over all the elements in a mesh. This would give an overall overview of the mesh quality that could be used to follow good practice guidelines.

There is a plethora of mesh quality metrics which depend on the definition followed, thus producing different guidelines for different solvers (Knupp, 2003) The following will provide a brief definition of the key mesh quality metrics and their requirements for the particular solver (ANSYS Fluent) used throughout this work.

Orthogonal Quality

The orthogonal quality in Fluent is based on the orthogonality mesh metric, which quantifies how the deviation of a cell from the 90 degrees angle. The orthogonality of a given cell is defined in ANSYS Fluent theory guide (ANSYS, 2018) by calculating the following quantities on each face *i:*

- the normalized dot product of the area vector of a face ($\overrightarrow{A_i}$) and a vector from the centroid of the cell to the centroid of that face ($\overrightarrow{f_i}$):

$$\frac{\overrightarrow{A_i}.\overrightarrow{f_i}}{\left|\overrightarrow{A_i}\right|\left|\overrightarrow{f_i}\right|} \tag{3.61}$$

- the normalized dot product of the area vector of a face ($\overrightarrow{A_i}$) and a vector from the centroid of the cell to the centroid of the adjacent cell that shares that face ($\overrightarrow{c_i}$):

$$\frac{\overrightarrow{A_i}.\overrightarrow{c_i}}{\left|\overrightarrow{A_i}\right|\left|\overrightarrow{c_i}\right|} \tag{3.62}$$

The relevant vectors are illustrated in Figure 3.7.

The minimum value resulting from Eq 3.61 and Eq 3.62 for all the faces is defined as the orthogonality. The orthogonal quality calculation depends on cell types:

i. For triangular and tetrahedral cells the orthogonal quality is :

$$Orthogonal\ quality = min\ [Orthogonality,\ (1 - Skewness)] \quad (3.63)$$

ii. For quad and hexahedral cells, the orthogonal quality is the same as the orthogonality.

$$Orthogonal\ quality = Orthogonality \quad (3.64)$$

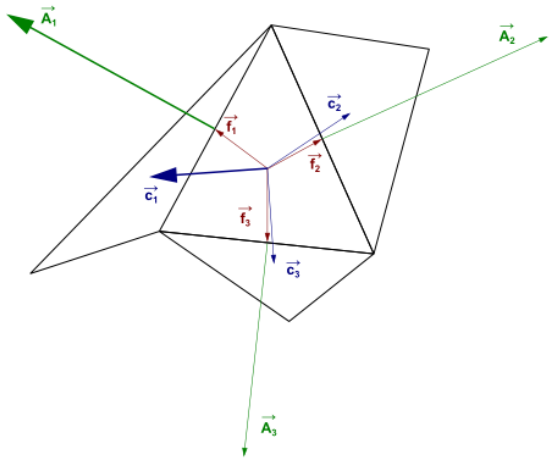

Figure 3.7: The Vectors Used to Compute Orthogonality (ANSYS, 2018). (Images used courtesy of ANSYS, Inc.)

The range for orthogonal quality is 0-1, where a value of 0 is worst and a value of 1 is best.

Skewness

The second important quality measure for a mesh is the skewness; it determines how close an element is to the ideal (equilateral or equiangular). There are a few methods to check cell skewness; the one used in the remainder of this work is the normalized equiangular skewness, which is defined in Eq 3.65.

$$Skewness = max\left[\frac{\theta_{max} - \theta_e}{180 - \theta_e}, \frac{\theta_e - \theta_{min}}{\theta_e}\right] \quad (3.65)$$

where:

θ_{max}: largest angle in the face or cell

θ_{min}: smallest angle in the face or cell

θ_e : ideal angle (60 for triangle/tetrahedral and 90 for square/hexahedral)

According to this definition, a value of 0 indicates an equilateral cell which is the best possible cell and a value of 1 indicates a degenerate cell.

3.6. Summary

This chapter focuses mainly on setting the theoretical background needed for the CFD modelling of morphing wings. First, the fundamental flow equations were detailed and then various turbulence models were presented. Afterwards, a brief overview of existing parametrization methods was given along with the rationale behind the parametric method chosen for this study. In addition, dynamic mesh methods were explored and their implementation in Fluent discussed. Finally, mesh quality metrics essential to follow adequate mesh generation practices were defined.

The next chapter will present the modification introduced in the parametrization method and its implementation in a UDF. Afterwards, both steady and unsteady validation studies are performed to verify the validity of dynamic mesh methods used. Subsequently, a 2D study comparing airfoils with morphing TEF to airfoils with a hinged flap is presented. Finally, the framework developed is applied to a test case of an airfoil fitted with a dynamically morphing TEF.

"To this purpose the philosophers say that Nature does nothing in vain, and more is in vain when less will serve; for Nature is pleased with simplicity, and affects not the pomp of superfluous causes."

Isaac Newton,
Philosophiæ Naturalis Principia Mathematica, 1687

4. Framework Development and Validation for Dynamic Morphing CFD Analysis

Chapter 4

Contents

4.1. Overview

From the literature review, it was concluded that the main gaps in morphing wings research are the lack of studies focusing on flow physics around morphing wings and the ones that incorporate the morphing motion into their analysis i.e. dynamic morphing. In this chapter, a framework to study dynamically morphing airfoils is presented. First, the modification of the selected parametrization method to model the airfoil morphing process is presented in Section 4.2, along with details of the implementation of this method in a UDF, dynamic mesh schemes used, and the results of quality metrics comparison between a deformed and regenerated mesh. Section 4.3 will present a steady morphing study comparing the aerodynamic performance of an airfoil equipped with a morphing Trailing-Edge Flap (TEF) to an airfoil with a hinged flap, and results are cross-validated with published numerical data. Finally, in Section 4.4, dynamic mesh-based unsteady predictions are validated against pitching airfoils experiments given their similarities with dynamic morphing airfoils then the framework is initially tested.

4.2. Unsteady Geometry Parameterization

Section 3.4 provided an overview of various parametric methods used in aerospace, their benefits and shortcomings. It was also noted that most of the available methods were primarily used for optimization problems or often to parametrize the deformation only in a steady, static manner. However, in order to model the dynamic morphing effect, it is essential to introduce time into the parametrization process to allow a realistic unsteady CFD analysis.

In this work, the FishBAC parametrization method used by Woods *et al.* (2014) was chosen for this work, and will be modified for unsteady morphing use. The original implementation was described in section 3.4.1; the method adopted a relatively simple approach to model a NACA 0012 wing undergoing trailing-edge (TE) deflections, starting at different chord stations and for various maximum deflections. The baseline airfoil was morphed by modifying the camber definition of the targeted morphing region of the chord, followed by reconstruction of a new airfoil shape using some control parameters. The morphing starts with the definition of a parameter x_s and the airfoil shape is built-up by the addition of the baseline NACA 0012 thickness distribution and a parametrically defined camber line. A third-order polynomial function (Eq 3.41) was used to define the camber line (y_c) of the morphing part of the airfoil, and was parametrized to have a direct control over the trailing edge maximum deflection, Eq 3.41 is repeated below:

$$y_c = \begin{cases} 0, & 0 \le \bar{x} < x_s \\ -w_{te}\dfrac{(\bar{x}-x_s)^3}{(1-x_s)^3}, & \bar{x} \ge x_s \end{cases} \tag{3.41}$$

where w_{te} is the value of maximum deflection at the TE, and x_s is the start location for the morphing. The thickness distribution is then added to the camber distribution (Eq 3.41) to get the upper and lower surface coordinates of the morphed airfoil.

In the present work, this static parametrization has been extended to include a time dependency, which makes it possible to introduce unsteady dynamic morphing motion as seen in Eq 4.1:

$$y_c = \begin{cases} 0 & , \ 0 \le \bar{x} < x_s \ and \ t_{start} \le t \le \frac{T}{4} \\ \frac{-w_{te}\sin\left(\frac{2\pi(t-t_{start})}{T}\right)(\bar{x}-x_s)^3}{(1-x_s)^3} & , \ \bar{x} \ge x_s \quad and \ t_{start} \le t \le \frac{T}{4} \\ \frac{-w_{te}(\bar{x}-x_s)^3}{(1-x_s)^3} & , \ \bar{x} \ge x_s \quad and \quad t > \frac{T}{4} \end{cases} \tag{4.1}$$

where t is time and T is the complete period of the TEF motion which would include an upward and downward flap motion from a non-morphed position, and t_{start} is the morphing start time.

Eq 4.1 is specifically modified so that the trailing edge can be deflected from the baseline geometry (starting $t = t_{start}$) to the final geometry with the maximum deflection w_{te} in a morphing time interval $t_{morph} = \frac{T}{4}$ which gives direct control over the speed of the TEF deflection. At $t_{morph} = \frac{T}{4}$ the morphing stops and the geometry is fixed for the remainder of the simulation at the maximum deflection w_{te}. For the current chapter, only the motion achieved in a quarter of a period T is simulated, equivalent to a single downward/upward deflection. This is specific to the chosen application, as it would replicate the behaviour of deploying flaps or deflecting ailerons for instance. Figure 4.1 illustrates the implementations of the method at three time steps for a NACA 0012 equipped with a morphing TEF.

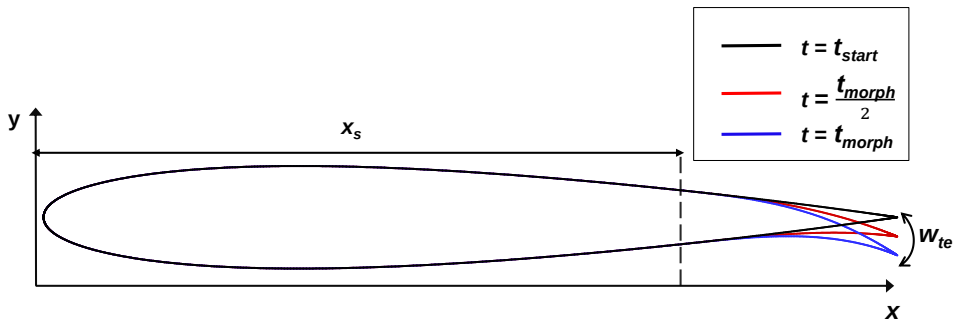

Figure 4.1: Resulting deformation of the unsteady FishBAC parametrization method.

The morphing starts at $t = t_{start}$ from the baseline airfoil and ends at t_{morph} when the TEF reaches the maximum deflection set. This formulation will be implemented in a UDF to drive the dynamic meshing scheme available in ANSYS Fluent.

4.2.1. UDF implementation

As introduced in section 3.5.4, ANSYS Fluent offers the possibility to use various mesh smoothing techniques in order to deform the computational grids. This is done using a UDF function which makes use of a built-in macro in order to enhance or customize the solver. For our application, the airfoil experiences non-rigid deformation, which means that the mesh boundary nodes would experience different relative movements, and in order to control their movement the DEFINE_GRID_MOTION macro is most suitable. Figure 4.2 illustrates the algorithm the UDF uses in order to deform the airfoil and the mesh with it. During each time step, a loop over the surface nodes is performed. The surface nodes inside the morphed portion are checked if they were updated or not, and if they are not updated the nodes will be moved according to the unsteady parametrization method.

Given the parametrization method chosen, the upper and lower surfaces of the airfoil are defined separately, which is why we need to implement two functions based on the DEFINE_GRID_MOTION macro which are named Up and Down in the code as illustrated in Figure 4.3. Variables used for calculations are also defined along with the constant non-dimensionalized by the chord length. In the implementation the frequency was used to model the speed by which the flap is deflected. Once the deforming surface is chosen through Fluent GUI, three loops are performed, one loop over the deforming boundary zone, then a loop over each boundary node making sure to flag the nodes already moved in order not to deform them again. After that, the time loop is performed (Figure 4.4).

Finally, Eq 4.1 is implemented inside two “if” loops, the first loop makes sure that only the chosen portion of the airfoil is deformed (flap size smaller than x_s) the second if condition defines the camber during the deformation (before T_{max}) and

after it (when the flap reaches the final position w_{te}). The code is illustrated in Figure 4.5.

The lower surface function is defined in a similar fashion. The complete UDF source code is attached in Appendix B.

Smoothing methods are needed in order to deform the mesh along with the geometry whilst maintaining a high quality mesh in the process. The following section will detail mesh quality results obtained when the developed UDF was tested.

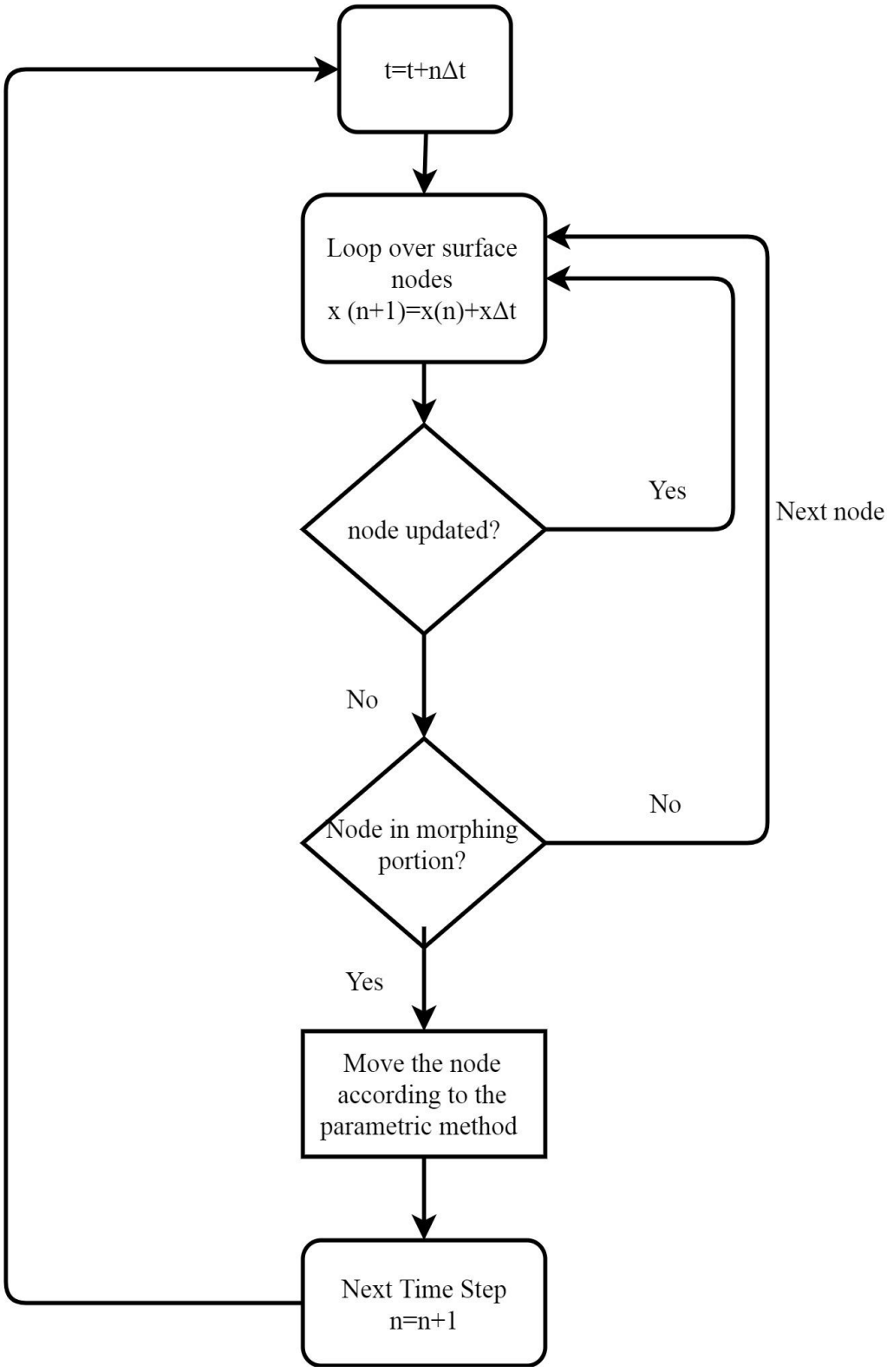

Figure 4.2: Algorithm used in the UDF to drive dynamic meshing in Fluent.

```
DEFINE_GRID_MOTION(Up, domain, dt, time, dtime)
{
  Thread *tf = DT_THREAD (dt);
  face_t f;
  Node *node_p;
  real  x, y,z,thickness,camber,theta,yupper,dy_c,x_s,xupper,W_te,T_max,Tmorph,freq;
  int n;
    freq    =   6;                    /*Morphing frequency*/
    Tmorph= 1/(4*freq);               /*Time in s needed for the morphing*/
    T_max = FTT+Tmorph;               /*Flow time in s when the morphing stops*/
    W_te= 0.05*chord;                 /*Maximum flap deflection */
    x_s = 0.75*chord;                 /*location where the morphing starts */
```

Figure 4.3: Upper surface name shown in Fluent GUI and constant definitions.

```
SET_DEFORMING_THREAD_FLAG (THREAD_T0 (tf));

  begin_f_loop (f, tf)
    {
      f_node_loop (f, tf, n)
        {
          node_p = F_NODE (f, tf, n);

          if (NODE_POS_NEED_UPDATE (node_p))
            {
              NODE_POS_UPDATED (node_p);
```

Figure 4.4: Loops used to visit each surface node and flag them if deformed.

```
            /*Loop over the morphing portion*/
        if ( x > x_s) {

            /*define motion before T_MAX*/

            if ( CURRENT_TIME >= FTT && CURRENT_TIME <= T_max) {


            /*morphing flap*/


             camber =-(W_te*sin(2*M_PI*(CURRENT_TIME-FTT)*freq)*pow((x-
x_s),3))/(pow((chord-x_s),3));

               dy_c= (-3*W_te*sin(2*M_PI*(CURRENT_TIME-FTT)*freq))*pow((x-
x_s),2)/(pow((chord-x_s),3));
```

Figure 4.5: Modelling of the airfoil deformation subject to starting location and time conditions.

4.2.2. Mesh quality after deformation

For deformation problems such as morphing wings, smoothing and remeshing methods are of interest. However, the remeshing technique is only available for tetrahedral mesh cells. Therefore, the mesh used in simulations requiring large deflections were generated to take advantage of this remeshing technique in a local region around the trailing-edge, while retaining high quality (low skewness, high orthogonality) structured mesh for most of the domain. Fluent smoothing function enables mesh adjustment in those zones where deformation occurs. It permits the interior nodes to "absorb" the deformation without any change in the number of nodes or their connectivity (i.e. topology is preserved). While diffusion-based smoothing is computationally more expensive, it tends to produce a better quality mesh particularly near the boundaries of a deforming body (ANSYS, 2018) by causing the far field nodes to absorb the deformation. Therefore, this smoothing method was chosen for this morphing airfoil application along with local cell remeshing techniques.

A precursor study was conducted to check the quality of the mesh that will be used for the unsteady dynamic morphing. The FishBAC morphing concept with a maximum deflection value of w_{te} = 0.05 or 5% of the chord was analysed in two different ways. First, the deformed mesh case, i.e. the airfoil was deformed from the baseline NACA 0012 to the maximum deflection w_{te} then a steady simulation

Table 4.1: Parameters used for the CFD analysis.

Parameters	**Value**
Reynolds number	6.75×10^5
Chord	0.3 *m*
Maximum deflection :w_{te}	5% of the chord
Morphing start :x_s	75% of the chord
Angles of Attack	0 to 10°

was run with the resulting mesh. Second, the re-generated mesh case, i.e. a good quality mesh was re-generated around the already deflected geometry after which the steady CFD analysis was performed. Table 4.1 summarises the parameters used for the simulations in the current chapter.

The discrepancy between the two cases was found to be less than 1% for all angles of attack, which clearly demonstrates that the mesh quality is preserved during the deformation. This is further supported by Table 4.2 which shows the minimum orthogonal quality for the deformed mesh to be 0.5 which is largely superior to the minimum requirement of 0.01 specified by the Fluent solver (ANSYS, 2018). Such preservation of the deformed mesh quality is mainly because the highly skewed cells within the triangular patch around the airfoil TE are systematically replaced if they do not meet the skewness or size criteria. Therefore, the deformed mesh was used as the default for the remainder of the study.

4.3. Steady Morphing Analysis

4.3.1. Dynamic Mesh Steady Validation against OpenFOAM

Before performing unsteady analysis of the dynamic airfoil, two steps are required, the first is validation of the results obtained for the unmorphed airfoil, and the second is comparison between the morphing concept and a hinged flap concept for steady (static) deflection case.

Asteady flow analysis of the baseline NACA0012 and the morphing FishBAC airfoil was presented by Woods *et al.* (2014). In Woods study both RANS CFD and XFOIL predictions were used to simulate the flow around the baseline NACA 0012 and various deflected configurations. In the present work, one case with a maximum deflection value w_{te} = 0.05 or 5% of the chord (Figure 4.6a) was replicated along with the baseline NACA0012. In addition, steady CFD analysis was performed around a hinged flap (Figure 4.6b) and the NACA 0012 fitted with the morphing TEF configuration (Figure 4.6a) to quantify the aerodynamic differences between the two. The results of the morphed case were also compared with those of Woods *et al.* (2014).

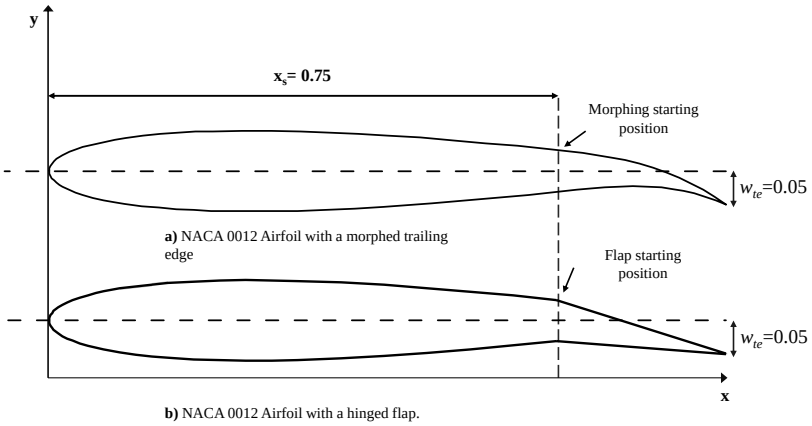

Figure 4.6: NACA 0012 airfoil with a) morphed and b) hinged flap definitions.

Table 4.2: Mesh characteristics.

Mesh	Cells	Orthogonal quality	Minimum Orthogonal Quality
Baseline mesh	58424	0.987	0.377
Deformed mesh	59120	0.973	0.500
Regenerated mesh	58108	0.993	0.183

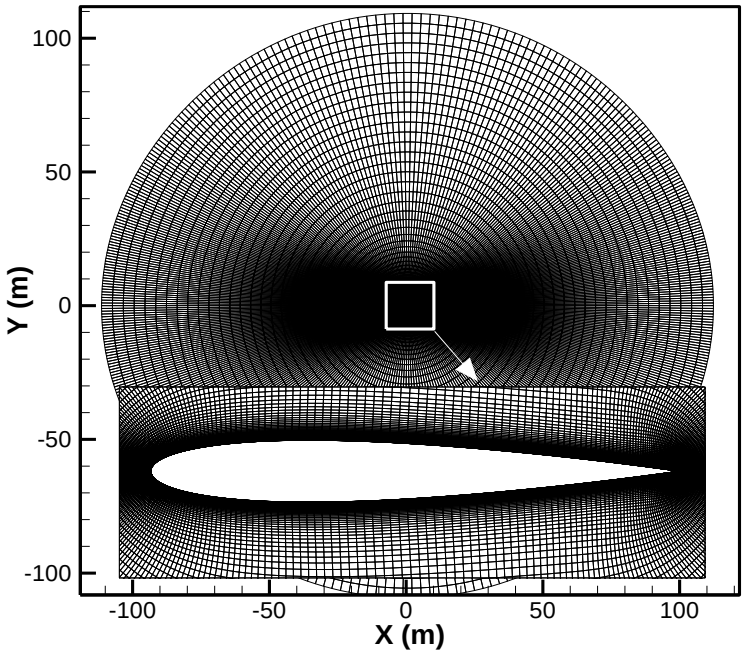

Figure 4.7: NACA 0012 O-grid mesh with a close-up on the airfoil.

The meshes that were generated around the airfoil were targeting a maximum near-

wall first-layer grid resolution of $y^+ = 1$, an expansion ratio of 1.1, a total of 400

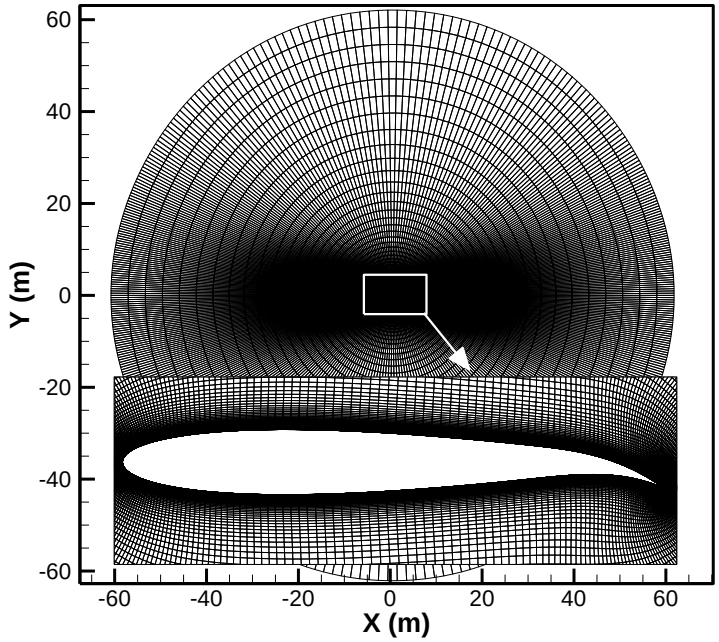

Figure 4.8: Deformed O-grid mesh for the NACA 0012 with a morphing trailing edge flap.

grid points around the airfoil surface, and a spacing of $10^{-4}\,m$ at both the leading and trailing edges. In addition, a set of refined meshes up to 900,000 elements were investigated and the discrepancies obtained in the lift and drag coefficients were generally around 1%; therefore a mesh with about 58,000 elements was used as seen in Table 4.1 which summarises the mesh characteristics. The baseline, morphed, and flapped meshes are shown in Figure 4.7, Figure 4.8 and Figure 4.9 respectively.

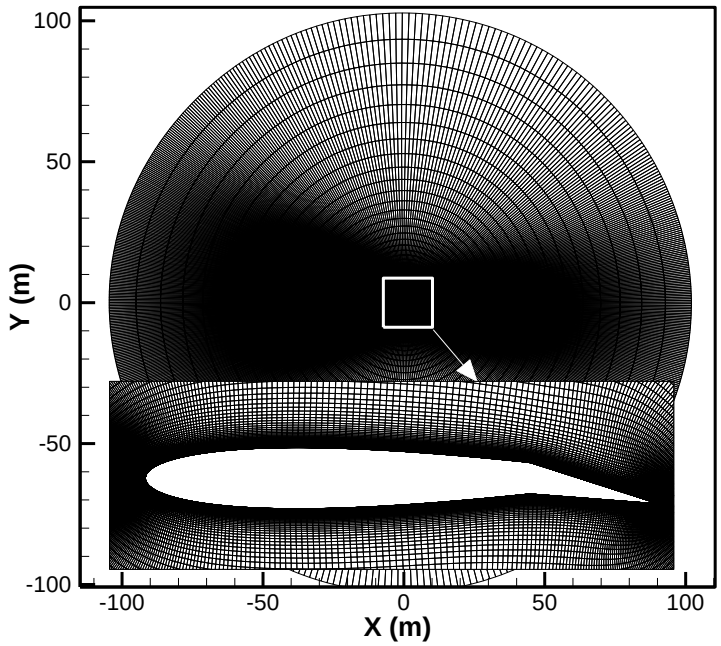

Figure 4.9: O-grid type mesh used for the airfoil with hinged flap study.

The O-grid type mesh (Figure 4.7) around the NACA 0012 was created with the deformation in mind. It was found that when the flap is morphed, the structured mesh near the trailing edge becomes highly skewed. To overcome this constraint, an unstructured patch around the trailing-edge (a small region of about 0.05% of the chord) was generated using an unstructured, triangular mesh (Figure 4.10). This

Table 4.3: Dynamic meshing parameters.

Diffusion function	**Diffusion parameter**	**Remeshing method**	**Minimum length scale (m)**	**Maximum cell skewness**	**Size remeshing interval**
Boundary distance	1.5	Local cell	7.08×10^{-6}	0.5	1

way, the mesh retains its structured nature over the majority of the computational domain. Table 4.3 sums up the parameters used for dynamic meshing.

The *k-ω* SST turbulence model was used given its suitability for modelling flows with separated regions, the pressure based SIMPLE algorithm was used for pressure-velocity coupling in addition to a least-square cell based discretization scheme, and a 2nd upwind scheme was used for the momentum and turbulence equations discretization. A pressure far-field boundary condition was imposed on the domain outer boundaries, located about 100 chord lengths around the airfoil to ensure there are no reflecting influences from boundaries. The Reynolds number based on the chord length (chord = 1 *m*) and freestream flow conditions was 6.75×10^5, and the Mach number was 0.1 (i.e. incompressible).

In the study by Woods *et al.* (2014), the airfoil chord was 0.3 *m*, so in order to ensure that the exact Reynolds number and Mach number are replicated in this study the constant dynamic viscosity was modified to 6.174×10^{-5} *kg/m.s*. This

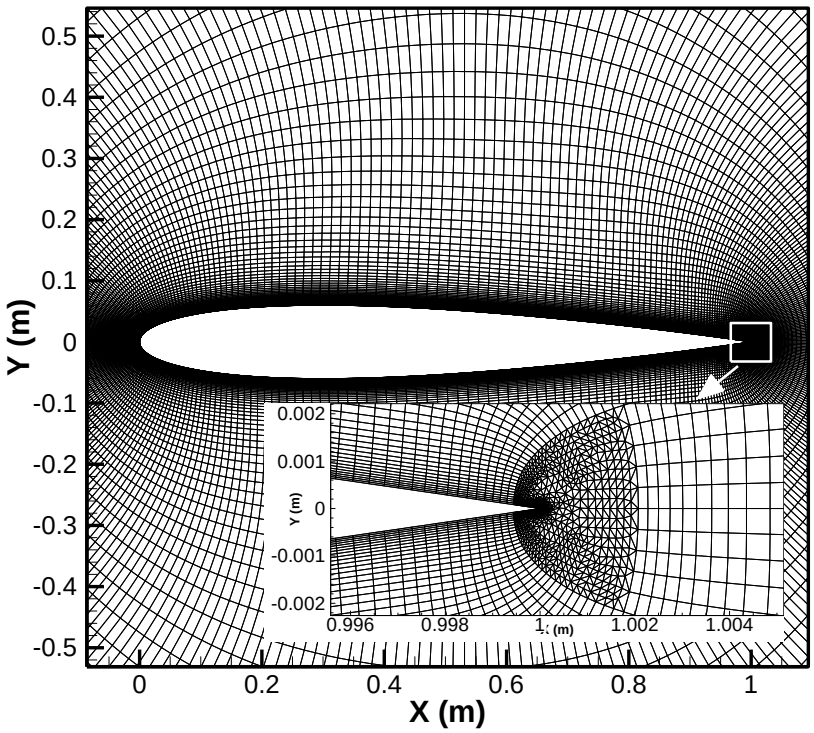

Figure 4.10: NACA 0012 mesh with a close up of the triangular patch around the morphing part for an un-deflected case.

allowed the use of a 1 *m* chord without further modifications to the parametrization method. Furthermore, to ensure that this change of dynamic viscosity has no effect on the results, the mesh created was scaled down by a factor of 0.3 (obtaining an airfoil with a chord = 0.3 *m*). Using sea level standard conditions, both configurations gave similar results.

The turbulence intensity was set to 1% with a turbulence length scale being the same as the airfoil chord. All simulations were run until both the lift and drag coefficients converged, and all residuals dropped below 10^{-6}.

4.3.1.1. Steady state results and discussion

Figure 4.11 presents the results obtained by Fluent in comparison with those from OpenFOAM and XFOIL for the baseline NACA 0012 and the 5% chord deflected morphed airfoil. For the baseline NACA 0012, Fluent and OpenFOAM exhibit very good agreement for lift coefficient throughout the entire AoA range, whereas XFOIL tends to over-predict the lift. The drag coefficient values are also in good agreement between Fluent and OpenFOAM for angles of attack smaller than 10°. However, the discrepancies grow steadily at higher angles. These discrepancies between the high fidelity solvers (Fluent and OpenFOAM) and XFOIL could be attributed to the lack of turbulence modelling in XFOIL where viscous effects are simply modelled by adding a boundary layer solver to the inviscid formulation.

An interesting trend appears in the 5% chord morphed airfoil. For AoA lower than 8°, Fluent predicts an average of a 6% higher lift compared with OpenFOAM, and a slightly lower value compared with XFOIL. At the same time, both Fluent and OpenFOAM gave a drag estimate higher than XFOIL for all angles of attack studied; again, the differences could be due to the approximation used by XFOIL to account for separation and skin friction. It is worth noting that both Fluent and OpenFOAM simulations used the k-ω SST turbulence model, yet the implementation, constants and various options available in the solvers are likely to be different which may explain the differences observed (5% on average). In addition, the differences in the meshes used can be added to the factors that may influence the results. Finally, Fluent lift coefficient results predicted that the

maximum lift coefficient is reached at AoA = 13°, which was not clearly shown in the previous study (Woods *et al.*, 2014) possibly due to the 2° increments used in their simulations.

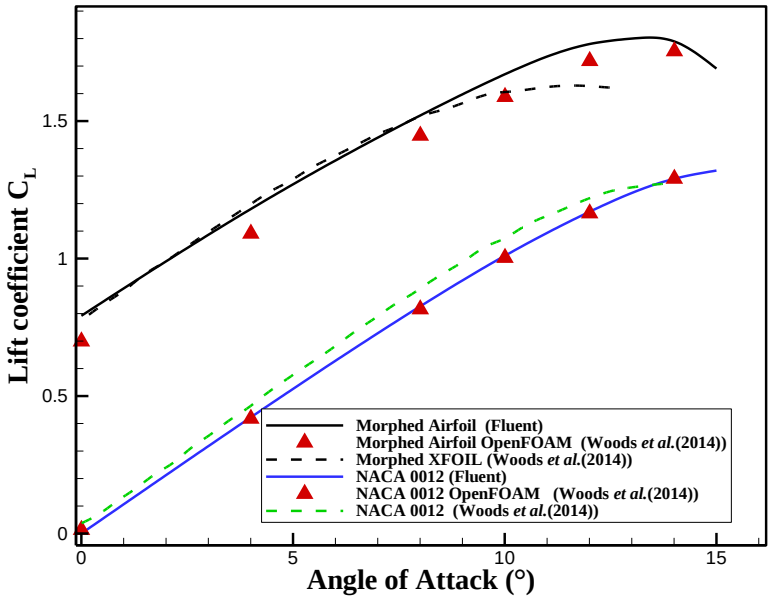

a) Lift coefficient.

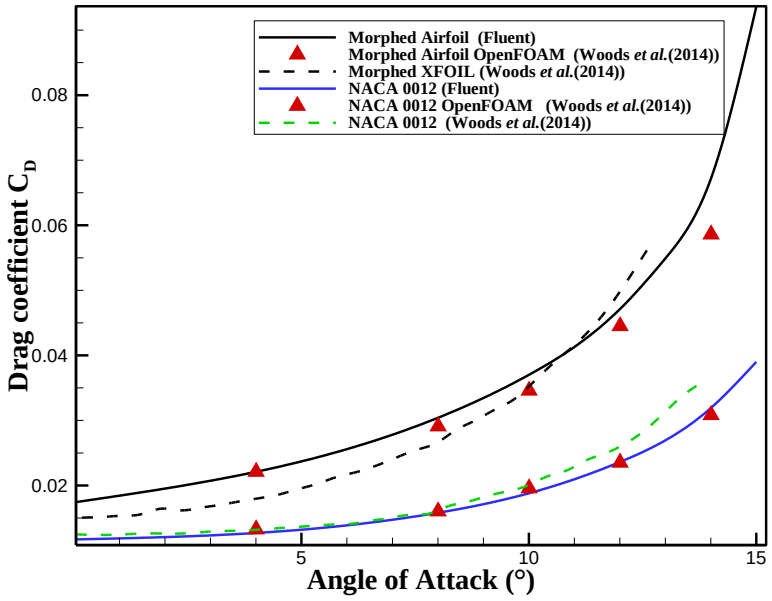

b) Drag coefficient.

Figure 4.11: Validation results for baseline NACA 0012 and morphed airfoil compared with OpenFOAM and XFOIL results of Woods et al. (2014).

4.3.2. Morphed vs Hinged Flap

The performance of the NACA 0012 airfoil with a morphing flap was compared with the case when the airfoil was fitted with a hinged flap of similar size. Figure 4.12 clearly shows a general increase in lift obtained by the morphed airfoil compared with the flapped one. However, this increase is also accompanied by a drag penalty (Figure 4.12). A better indicator is the aerodynamic efficiency (i.e. lift-to-drag ratio, C_L/C_D) plotted in Figure 4.13.

It is clear that the morphed airfoil provides a significant increase in efficiency up to an angle of attack of 12° after which the morphed airfoil efficiency decreases steadily until AoA= 13°. The maximum efficiency increase of 13% was observed at 8° AoA. This trend continues up to an angle of attack of 13°, beyond which the flapped airfoil somehow exhibits an increasingly similar performance in the aft-

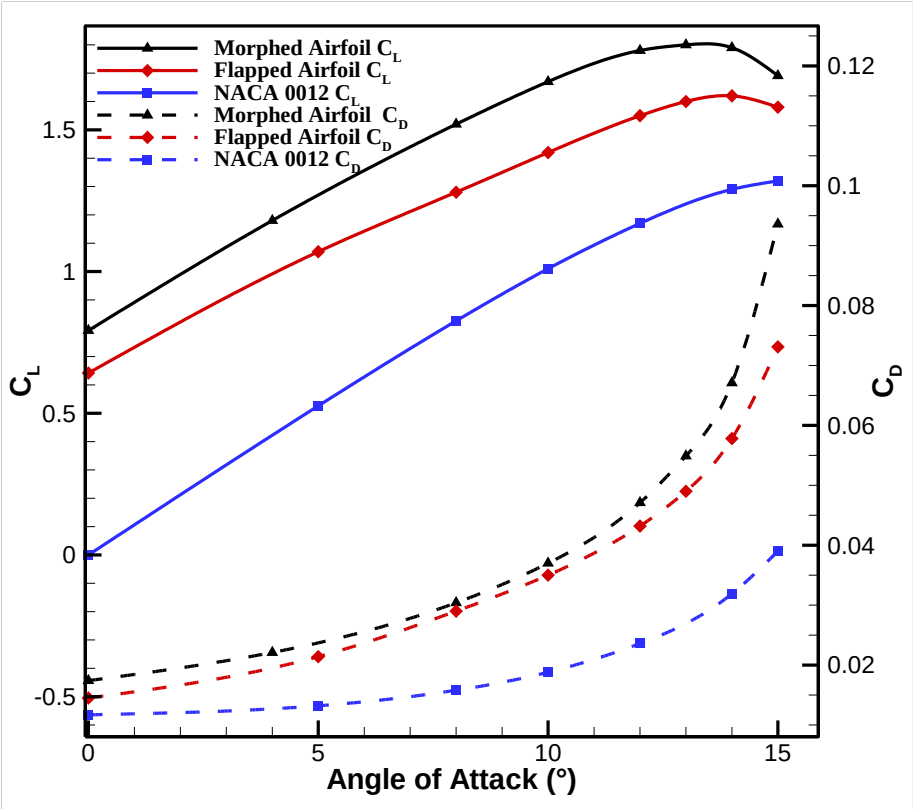

Figure 4.12: Lift and drag coefficients results for baseline NACA 0012, morphed and flapped airfoil obtained with Fluent.

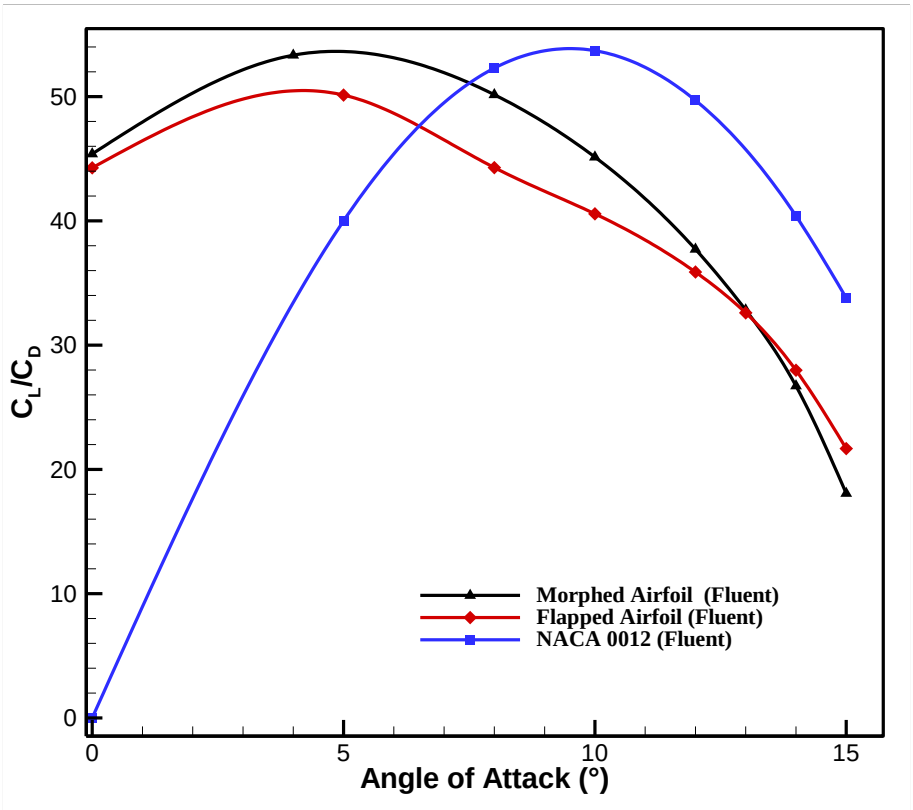

Figure 4.13: Aerodynamic efficiency (C_L/C_D) results for baseline NACA 0012, morphed and flapped airfoil obtained with Fluent.

stall regime. On average, the morphed airfoil provides a 6.5% increase in the C_L/C_D efficiency.

Figure 4.14 shows a comparison between the pressure coefficients of both configurations at three angles of attack: 0°, 8° and 14°. It is shown that most of the differences are located around the modified area (morphed or hinged) even though there are more significant differences around the leading edge at 0°, where the suction peak is always lower for the morphed airfoil. This is presumably due to the flow being accelerated more by the morphed airfoil (Ai *et al.*, 2016).

The morphed airfoil exhibits a larger C_p area around the TE with a distribution similar to supercritical airfoils (Harris, 1990) given the comparable C_p distribution between the two configurations. In Figure 4.14, results show a sudden decrease in pressure coefficient at the location where the hinged flap starts. It is likely that this sudden decrease is related to the existence of the protruding hinge and subsequent

impingement of the flow on it as this is the only difference between the two flaps. The hinge would cause the flow to take a sharp turn following the flap deflection as suggested by (Ai *et al.*, 2016).

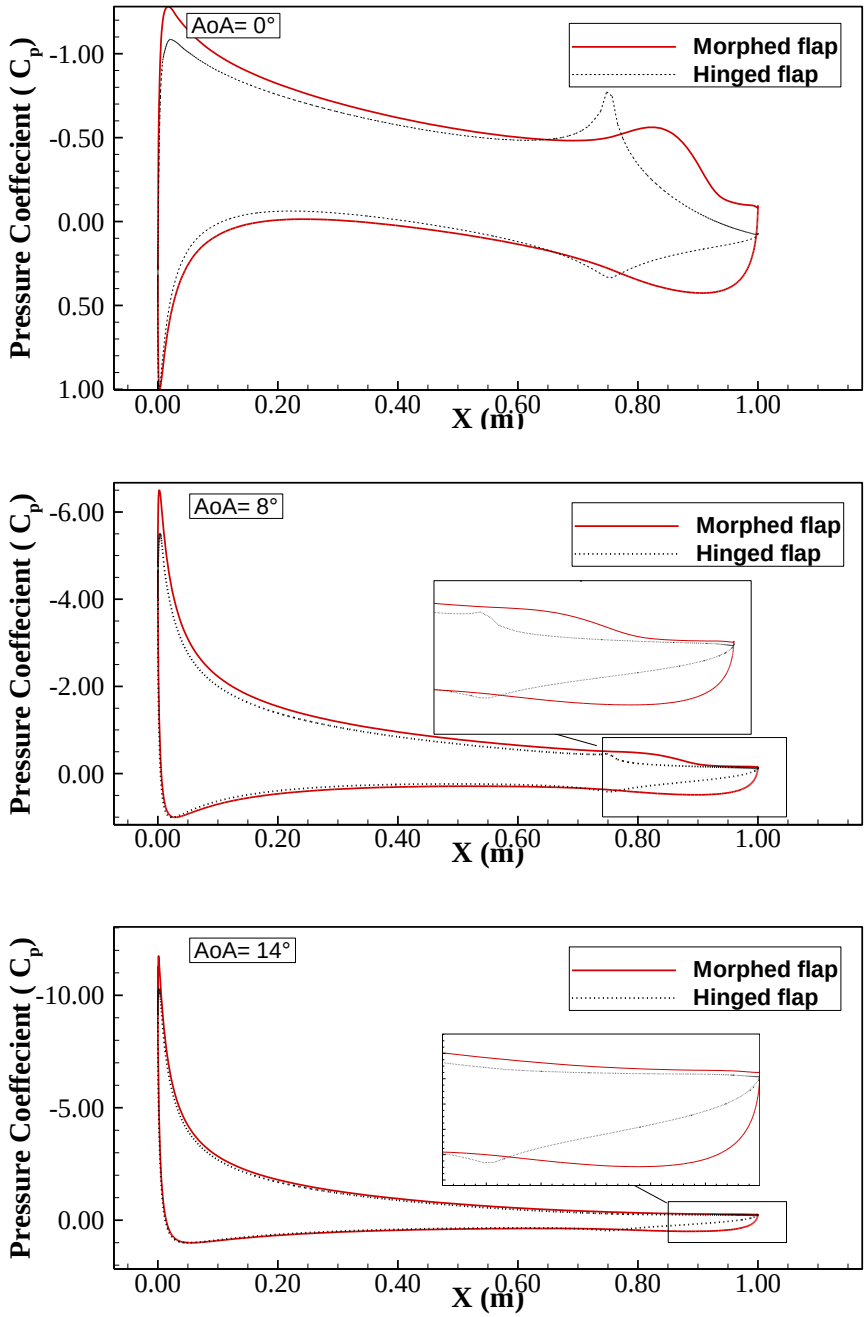

Figure 4.14: Pressure coefficient (C_P) comparisons between the morphed and flapped airfoils at AoA= 0°, 8°, 14°.

In comparison, however, the morphed flap seems to create an increase in pressure coefficient. Similar observations were reported by Ai *et al.* (2016). Figure 4.14 illustrates the maximum differences between the two airfoils at AoA = 8º.

At an AoA of 14°, there is a significant decrease in the C_p area of the morphed flap airfoil even though it is still larger than the airfoil with the hinged flap and this may explain why the morphed airfoil produces more lift. However, the drag penalty makes the morphed airfoil efficiency drop below that of the hinged flap. Further, it was also shown by Troldborg *et al.* (2014) that the performance of a hinged flap was inferior to that of a morphing flap. This behaviour is confirmed by the data produced from a wind tunnel experiment where the 3D FishBAC concept is compared with a 3D NACA 0012 hinged flap airfoil (Woods *et al*., 2014b). The Reynolds number of the experiment was around 400,000 (lower than the one used in the numerical simulations), despite the difference in Reynolds number, the behaviour of both configurations is similar. The morphed airfoil showed better performance in the majority of angles of attack, with a steadily decreasing performance until both configurations gave similar efficiency at AoA of 13°.

Figure 4.15 shows the Skin Friction Coefficient (C_f) comparisons between the morphed and flapped airfoils at AoA= 0°, 8°and 14°. From the figure, we can conclude that the airfoil with the morphed flap is able to delay the separation compared with the hinged flap. For the hinged flap, the separation occurs just at the region where the flap meets with the main airfoil (~0.75*c*) but the separation develops at 0.9*c* for the morphed flap at 0° and 0.87*c* at AoA= 8°. However, at AoA = 14°, both configurations are in stall, and their separation point is around 0.3*c*, which explains the similar behaviour at higher AoA.

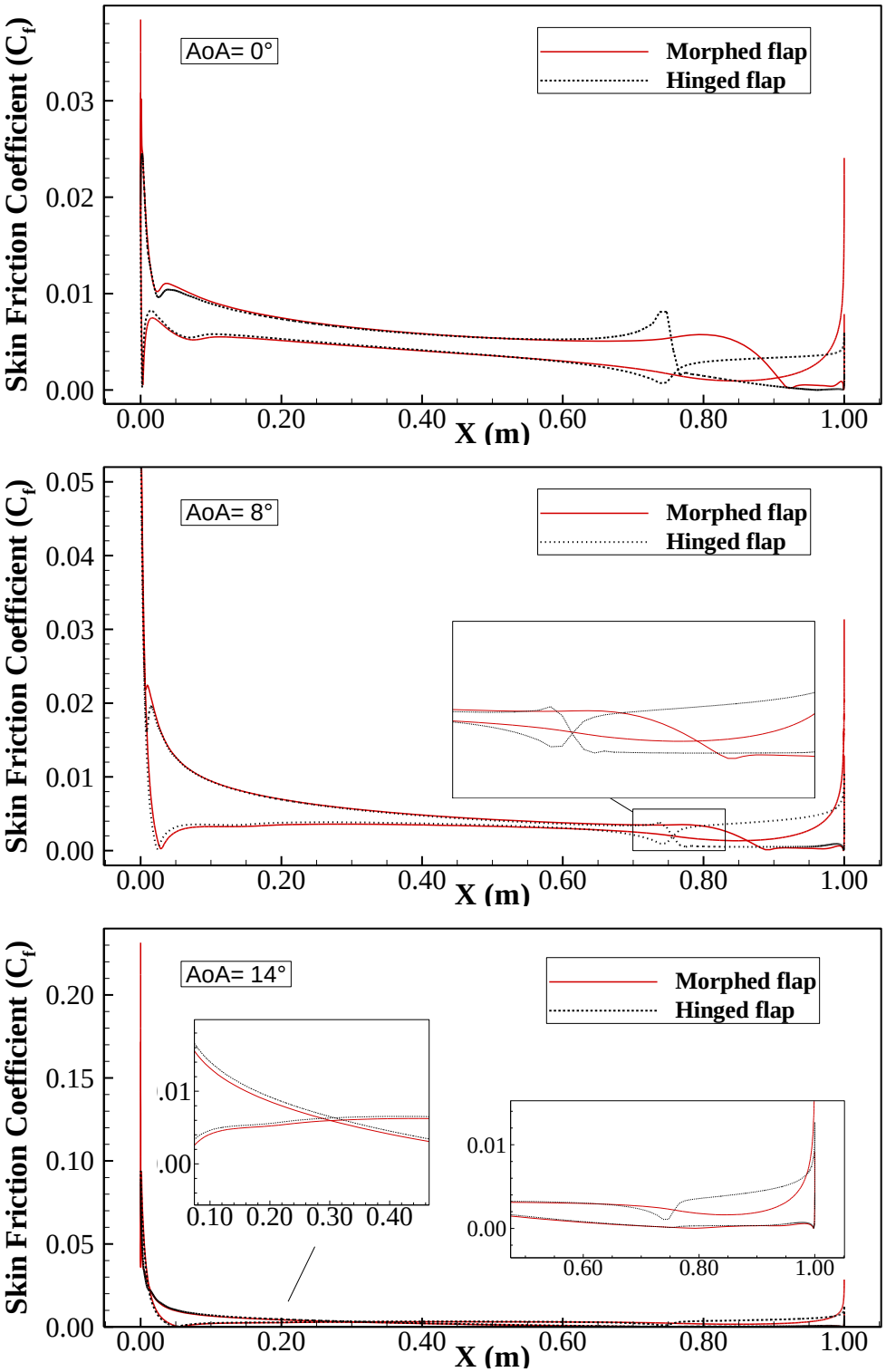

Figure 4.15: Skin Friction Coefficient (C_f) comparisons between the morphed and flapped airfoils at AoA= 0°, 8°, 14°.

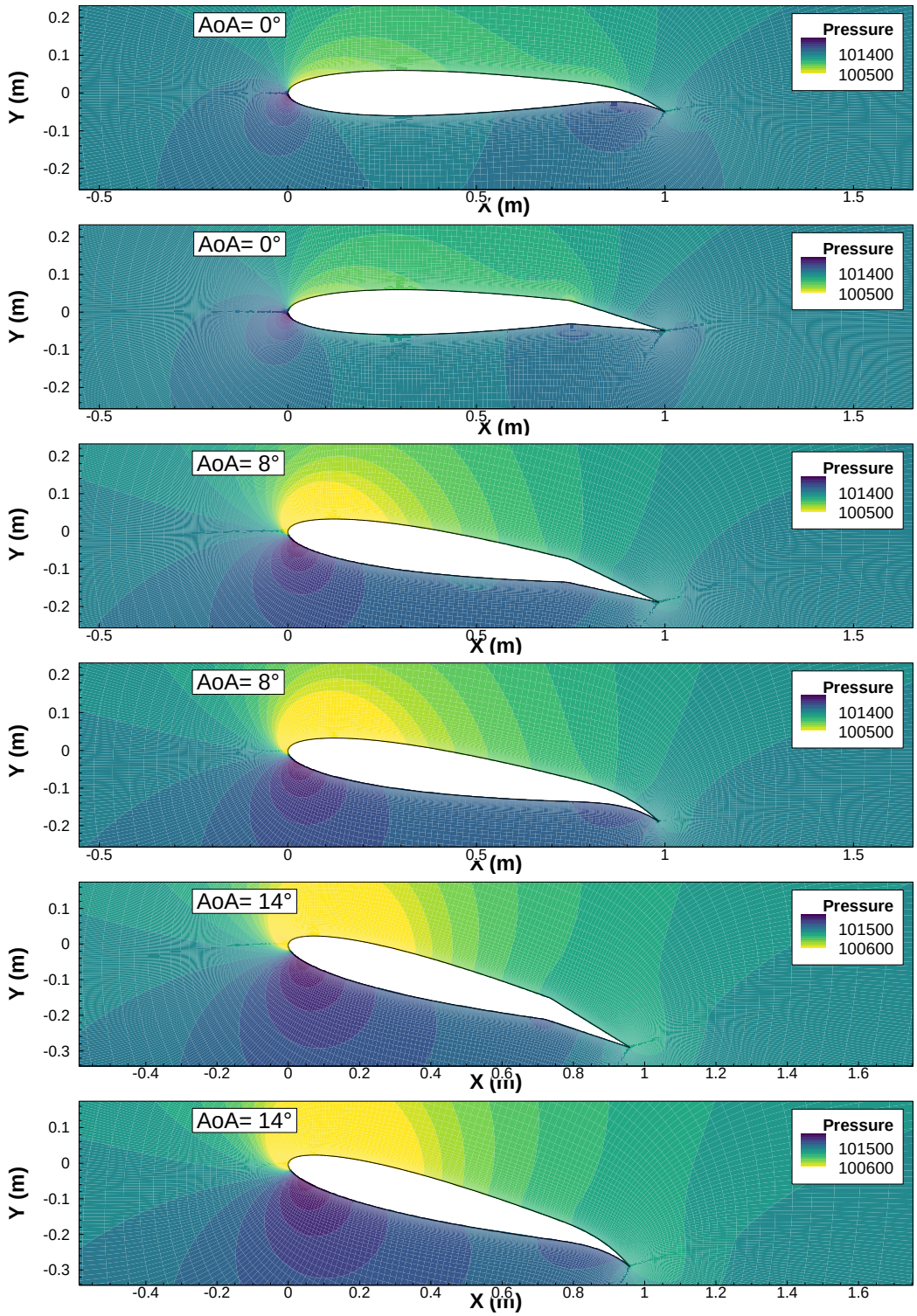

Figure 4.16: Pressure contours comparisons between the morphed and flapped airfoils at AoA= 0°, 8° and 14º.

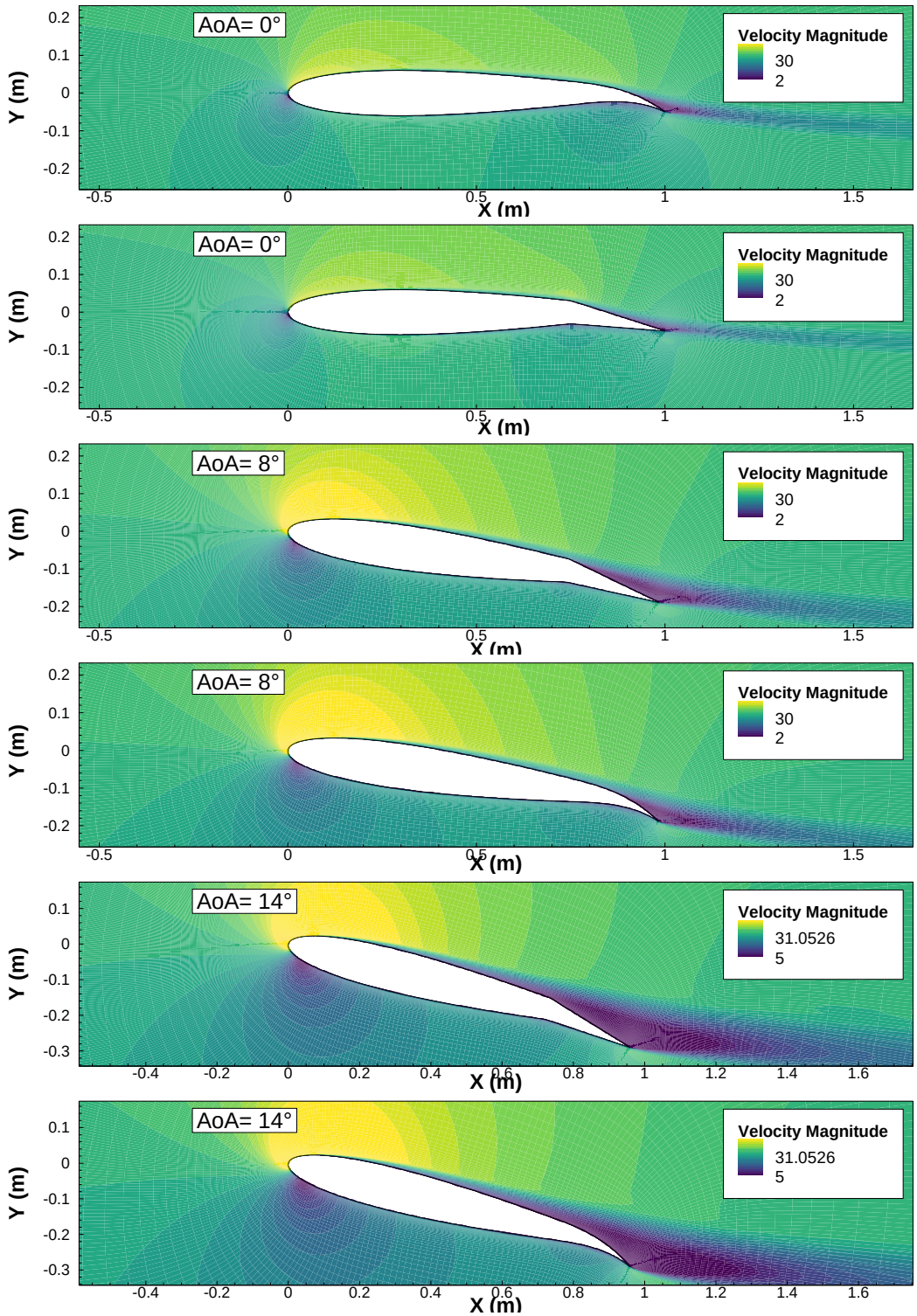

Figure 4.17: Velocity contours comparisons between the morphed and flapped airfoils at AoA= 0°, 8° and 14°.

Qualitative results detailing the differences between the airfoil with a morphed flap and the one with the hinged flap are presented in Figure 4.16 and Figure 4.17 for the three angles of attack: 0°, 8° and 14°.

From Figure 4.16 we can see clearly the pressure peak observed at the hinge of the flap in the C_p distribution at 0° whereas the morphed airfoil shows a smoother flow with no sudden change in pressure, a stagnation region is also observed on the pressure side of the hinged flap. At AoA = 8° the velocity contours show that the hinged flap has a larger separation region compared with the morphing one (Figure 4.17) which confirms the results drawn from the pressure distribution and explains the peak efficiency of the morphed airfoil, as it produces higher lift and lower drag compared with the hinged flap.

At 14°, both airfoils are in the stall region as illustrated in Figure 4.16, since the morphed airfoil produces more lift, the local AoA of attack is higher showing a slightly larger recirculation region that translated in the deteriorating performance of the morphing airfoil.

4.4. Unsteady Morphing Analysis

4.4.1. Dynamic Mesh Unsteady Validation against Experiments

In order to validate the approach used in this framework, which is based on the use of dynamic mesh, comparison with experimental work is needed. However, as concluded in the literature review, there is still a lack of experimental work investigating the dynamically morphing wings. To circumvent this issue a different class of problems which presents similarities to the morphing cases investigated in this case and requires similar (or larger) levels of mesh deformation is investigated instead, namely pitching airfoils.

Pitching airfoils are traditionally investigated in CFD using a few methods such as sliding mesh method (Gharali and Johnson, 2013) or overset mesh methods (Koomullil and Soni, 2012). Given the fact that the airfoils are rigid bodies, two computational domains are created around the airfoil, then one domain is rotated

relatively to the static domain effectively simulating the pitching motion. However, in the present validation study, the pitching motion is imposed on the airfoil itself requiring the mesh surrounding it to deform as well, this would permit prediction assessment of dynamic mesh methods used in the remainder of the work.

4.4.1.1. Details of the pitching airfoil wind tunnel experiment

Lee and Gerontakos (2004) conducted wind tunnel experiments investigating a pitching NACA 0012 airfoil at a chord-based Reynolds number $Re = 1.35\times10^5$. The airfoil had a chord $c = 0.15\ m$ and a span of 2.5c. To eliminate the 3D effect of flow leaks at the airfoil edges, two splitter plates with a diameter of 2c were mounted at the ends. The sinusoidal pitching motion was described using the following formula for the instantaneous angle of attack $\alpha(t) = \alpha_m + \Delta\alpha\sin(\omega t)$, α_m is the mean angle of attack, $\Delta\alpha$ is the oscillation amplitude and $\omega = 2\pi f_0$ is the circular frequency and t is the time, f_0 is the oscillation frequency. In the Lee and Gerontakos (2004) experiment five sets of parameters were explored to investigate the effect of variation of the reduced pitching frequency ($\kappa = \frac{\omega c}{2U_\infty}$) and oscillation amplitude, and the pitching centre is located at 0.25c from the LE.

In the present validation study, we focus on the following combination of $\alpha(t) = 10° + 15°\sin(\omega t)$ with $\kappa = 0.1$ corresponding to a frequency $f_0 = 2.97\ Hz$ for a freestream velocity $U_\infty = 14\ m/s$. This case was chosen for two reasons; 1) there are other numerical studies exploring it (Geng *et al.*, 2018) which could be used to assess the present predictions, and 2) this case is challenging from the point of view of requiring large mesh deformations (given the 15º oscillation amplitude) and from the solver point of view as the airfoil moves through dynamic stall (reaching maximum at AoA = 25º) with large flow unsteadiness.

4.4.1.2. Computational setup

All simulations were started from converged steady-state simulations where the mean AoA was set to be 10º using the inlet boundary condition. For the transient simulations, both the URANS k-ω SST intermittency turbulence model and the hybrid SBES were evaluated. Two time advancing schemes were used, iterative

and non-iterative time advancement. For the iterative time advancement (ITA) the SIMPLE algorithm was applied for the pressure-velocity coupling whereas for the non-iterative time advancement (NITA) the fractional step method (FSM) was applied. Detailed description of these methods can be found in (ANSYS, 2018).

Second-order spatial discretization schemes are used for all the remaining quantities (pressure, density, TKE, intermittency). Second order discretization is also used for momentum quantities when performing URANS whereas bounded central differencing was used with SBES.

To gain an insight into the influence of the temporal resolution on the predictions capabilities of the turbulence models and time advancement schemes used, two time steps were used : $\Delta t = 10^{-4}$ *s* and $\Delta t = 3\times10^{-5}$ *s* which are similar to the ones used in the literature (Geng *et al.*, 2018). The results of this validation study are presented next.

4.4.1.3. Validation results

Figure 4.18 shows the effect of the time resolution on the ensemble-averaged dynamic force coefficients, the SIMPLE algorithm was used with both time steps. It is clear that a smaller time step yielded a better agreement with wind tunnel tests. This could be due to the fact that for $\Delta t = 10^{-4}s$ the residuals did not go below the

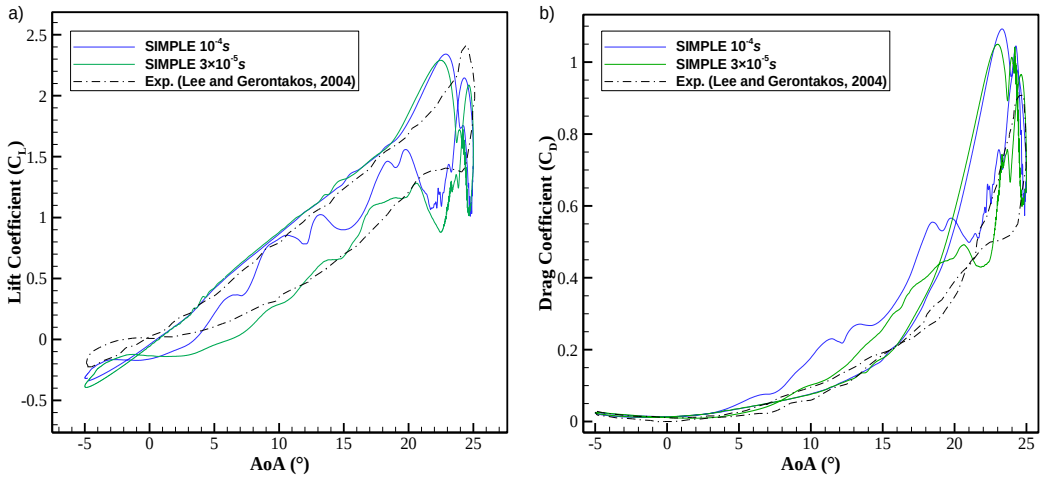

Figure 4.18: Effect of the time resolution on the ensemble-averaged dynamic force coefficients: (a) lift coefficient; (b) drag coefficient. Wind tunnel test for reference Lee and Gerontakos (2004).

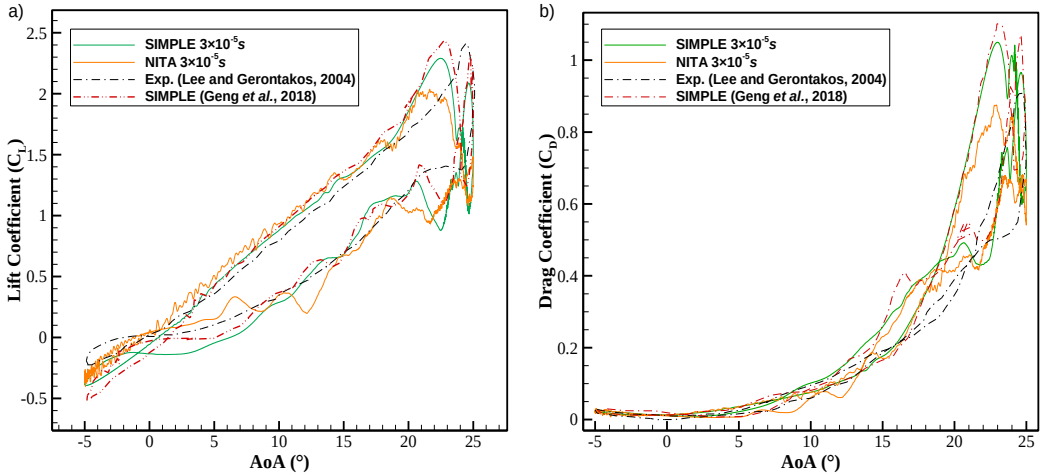

Figure 4.19: Effect of time advancement scheme on the ensemble-averaged dynamic force coefficients: (a) lift coefficient; (b) drag coefficient. Comparison with wind tunnel test for reference Lee and Gerontakos (2004) and numerical results from (Geng et al. 2018).

set value of 10^{-5}, for $\Delta t = 3\times10^{-5}s$ this was achieved with the 20 inner iterations, the same observation was made by Geng *et al.* (2018). This leads to the conclusion that the use of a dynamic mesh does not require a smaller time step to reach convergence compared with the sliding mesh method for instance.

Figure 4.19 shows the results obtained using the ITA (SIMPLE) and NITA (FSM) and their effect on the dynamic force coefficient. In terms of lift coefficient, the prediction using both methods gives an overall good agreement with published work. Like in the numerical work by Geng *et al.* (2018), during the upstroke, the values obtained by both the NITA and SIMPLE scheme oscillate closely around the test data values. However, the present simulation slightly underpredicts the value of lift near the stall AoA, the NITA scheme shows better agreement around this region and all numerical simulations underpredict the stall AoA. A secondary peak is also captured at the maximum AoA (25º), interestingly NITA captures a lower peak value during the dynamic stall. During the downstroke, both NITA and SIMPLE show similar oscillatory behaviour around the test data values, giving a better agreement with the test data at the minimum AoA (-5º).

A noticeable feature of NITA predictions is the presence of high frequency oscillations in hysteresis loops of the dynamic forces; this could be attributed to the

fact that NITA schemes are more sensitive to both the time step size and the mesh quality.

For the drag coefficient, a good agreement is present between the method used and wind tunnel test at lower AoA up to AoA = 10º. Nevertheless, at higher AoA, the agreement is less satisfactory with the test results, but follow the same trend as the numerical prediction by Geng *et al.* (2018). This is due to the fact that at high angles of attack, massive flow separation is persisting rendering the modelling of viscous effects harder especially with 2D RANS methods. Geng *et al.* (2018) attributed the presence of peaks in the drag values between the angles 20 º and 25º to the prediction of a secondary Leading Edge Vortex (LEV) at higher AoA helping with recovery of the lift and drag coefficient, whereas in experiment the secondary LEV is predicted at a lower AoA (~22º) which has less effect on the recovery. NITA schemes seem to overpredict the drag less compared with SIMPLE, which is probably due to the capture of a weaker dynamic stall.

Figure 4.20 shows additional results comparing prediction using the SBES turbulence model with SST using both time advancement schemes. SBES yields similar predictions to the SST models when using NITA schemes. However, the combination of SBES-SIMPLE shows a larger discrepancy. This could be due to either a higher sensitivity of the coupling to time step size or the need for longer

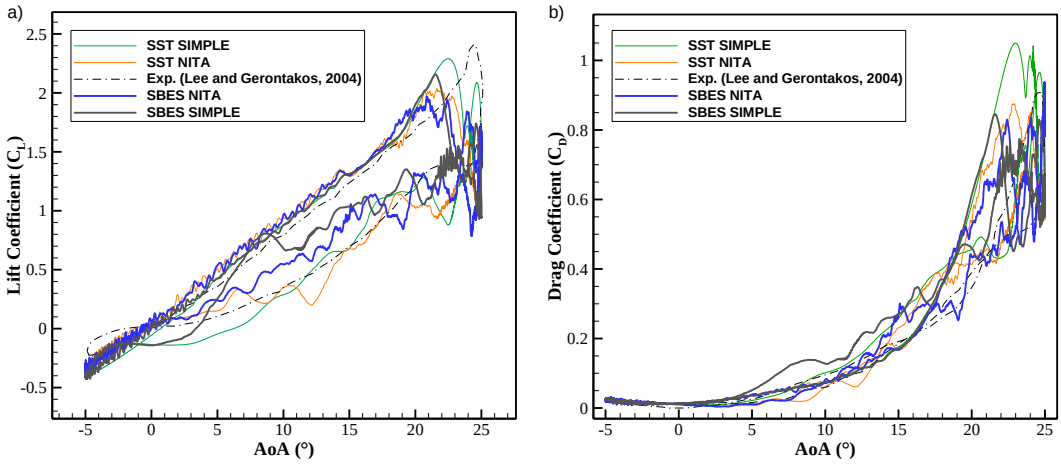

Figure 4.20: Effect of turbulence model and time advancement scheme on the ensemble-averaged dynamic force coefficients: (a) lift coefficient; (b) drag coefficient. Comparison with wind tunnel test for reference (Lee and Gerontakos, 2004).

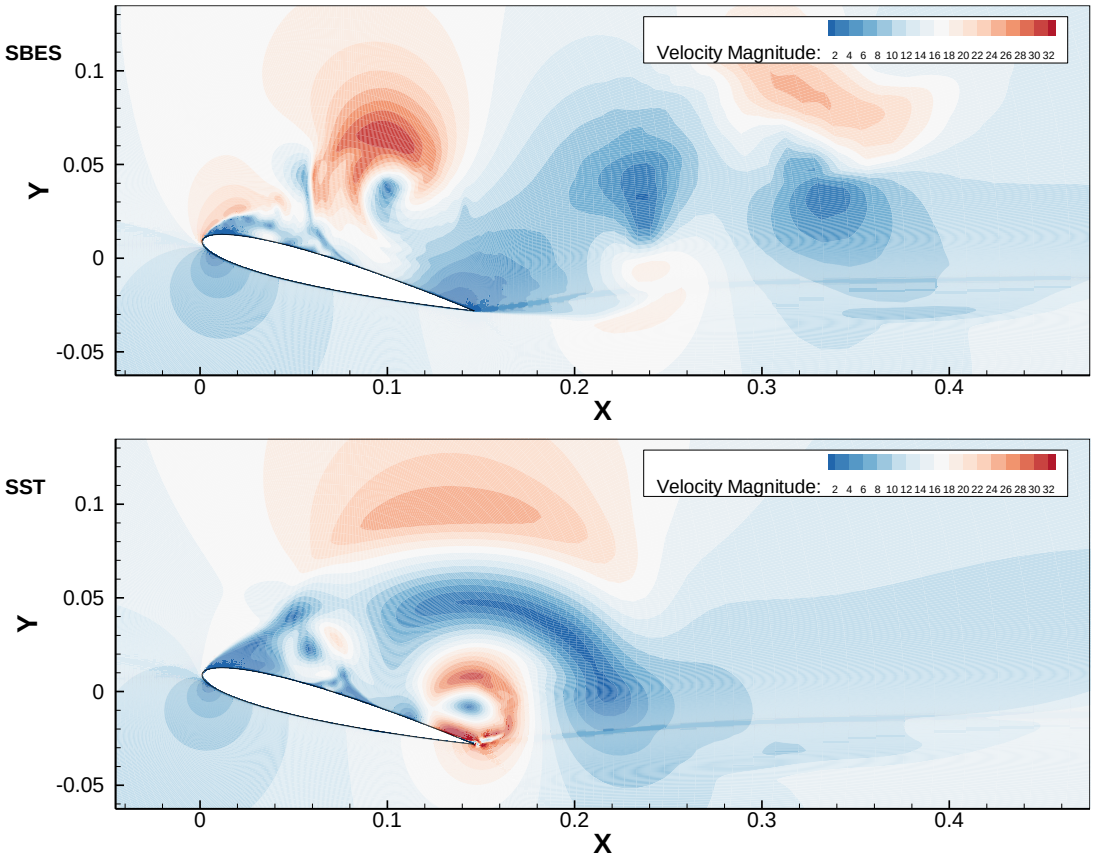

Figure 4.21: Velocity contours showing the difference between SBES and SST predictions.

runs to reach a more steady state oscillation as all the results presented in this study were obtained by ensemble averaging over four periods which was shown to be was sufficient for the SST model (Geng *et al.*, 2018).

SBES also show an enhanced ability to capture smaller scale flow structures when compared to the pure RANS simulations. This is illustrated in the dynamic force coefficients plots by the high frequency oscillation captured (Figure 4.20), especially at the dynamic stall AoA. The differences between both models could also be seen in the instantaneous velocity contours (Figure 4.21).

4.4.1.4. Mesh Quality of the Deformed Mesh

Figure 4.22 shows the mesh at three pitching instances; the baseline, at the maximum upstroke angle and at the minimum downstroke angle, the figure also shows the unstructured patch around the TE and how it deforms. From the figure,

it is clear that the mesh experiences a deformation and distortions especially at the TE region, however the triangular patch helps with absorbing the high deformation experienced at the region and prevents the formation of obsolete cells at the sharp TE. This is confirmed further by Figure 4.23 and Figure 4.24 showing the orthogonal quality and cell skewness contours.

When it comes to the orthogonal quality, the mesh retains its overall good quality close to 1 even during the deformation, the only differences observed occur inside the triangular patch. A similar observation could be made for the skewness (Figure 4.24). However, an increase in skewness is also observed around the entire airfoil which is due to the pitching motion, though the overall quality is well within the limits of the solver and no cell exceeds the prescribed limits, this is further confirmed by the quantitative comparison shown in Table 4.4. The average orthogonal quality is unchanged while the skewness experienced a 6% increase but remains within the good mesh quality range. The maximum cell skewness also increased by 7.5% but there are only four cells with skewness larger than 0.65.

Table 4.4: Mesh characteristics at three pitching instances.

Mesh Metrics	**Baseline**	**Max Upstroke**	**Min Downstroke**	**Range**	**Solver requirements**
Average Orthogonal Quality	0.9849	0.9849	0.9849	0 (worst) to 1 (best)	the closer to 1 the better
Minimum Orthogonal Quality	0.060982	0.0455845	0.0470744		Larger than 0.01
Average Skewness	0.00545	0.0058	0.0058	0 (best) to 1 (worst)	the closer to 0 the better
Maximum Skewness	0.682501	0.735916	0.736034		Lower than 0.98

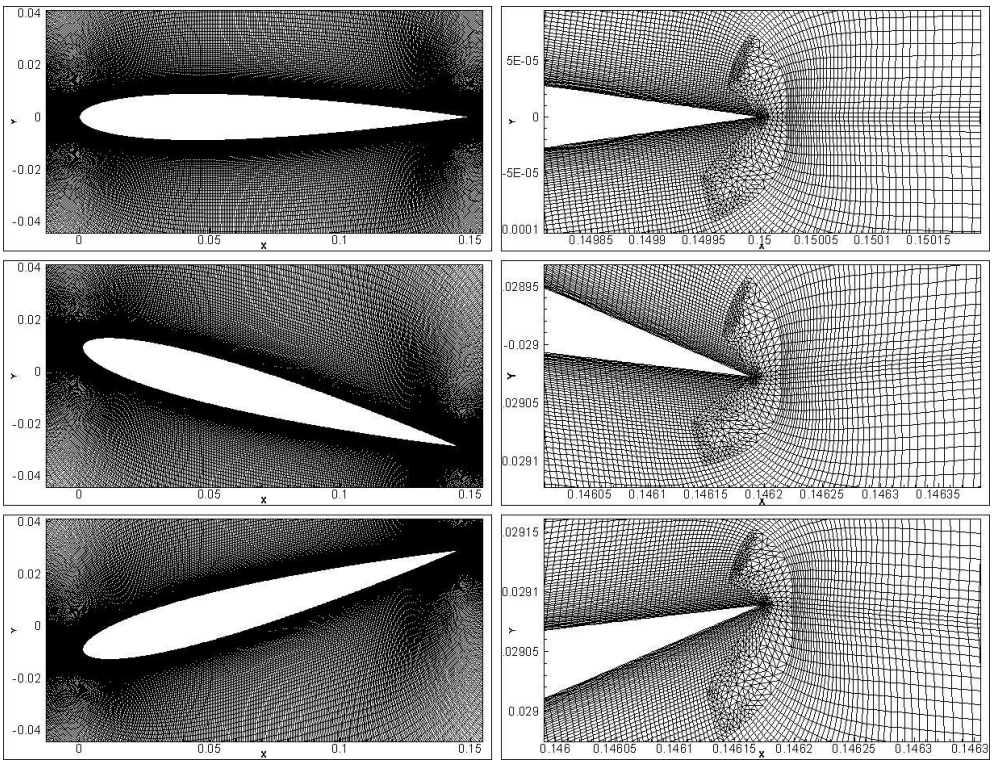

Figure 4.22: Deformed mesh at three pitching instances.

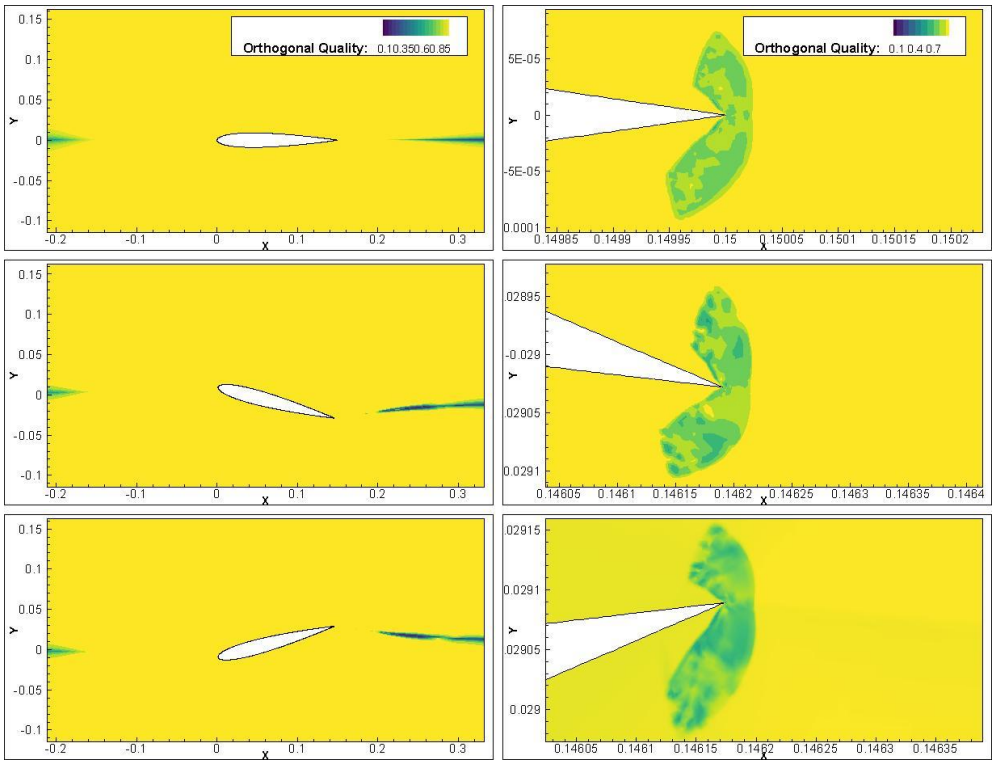

Figure 4.23: Orthogonal quality of the deformed mesh at three pitching instances.

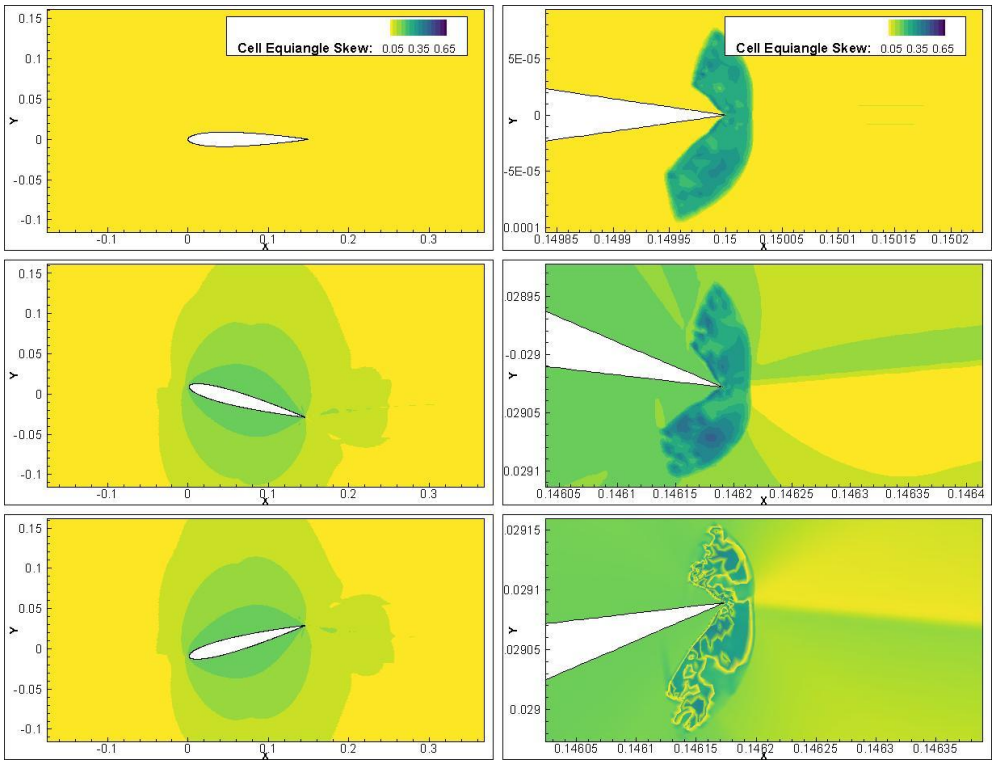

Figure 4.24: Cell skewness of the deformed mesh at three pitching instances.

4.4.1.5. Performance Comparison between SIMPLE and NITA

One of the main reasons that the NITA approach was tested in this this study is the possible computational savings that could be obtained using these schemes compared with the traditional iterative schemes. Figure 4.25 shows the performance metrics of simulations performed with both ITA based on the SIMPLE algorithm and NITA using FSM. It is clear that NITA offers significant CPU savings, the average wall-clock time per time step is 1.733 *s* compared with 3.375 *s* for using the SIMPLE algorithm and 20 sub-iterations, this makes NITA about two times faster than the use of SIMPLE based iterative scheme. The simulation performed for 4 periods using NITA took about 23 hours on 16 cores *Intel Xeon E5-2680 v2 (Ivy Bridge) @ 2.8 GHz* whereas the same configuration needed over 45 hours to simulate the same number of periods. Taking into account the total time of simulation which includes I/O operations and files case and data

files writing an average increase of 4% was observed which still gives advantage to the NITA schemes, making the case for its use in future studies.

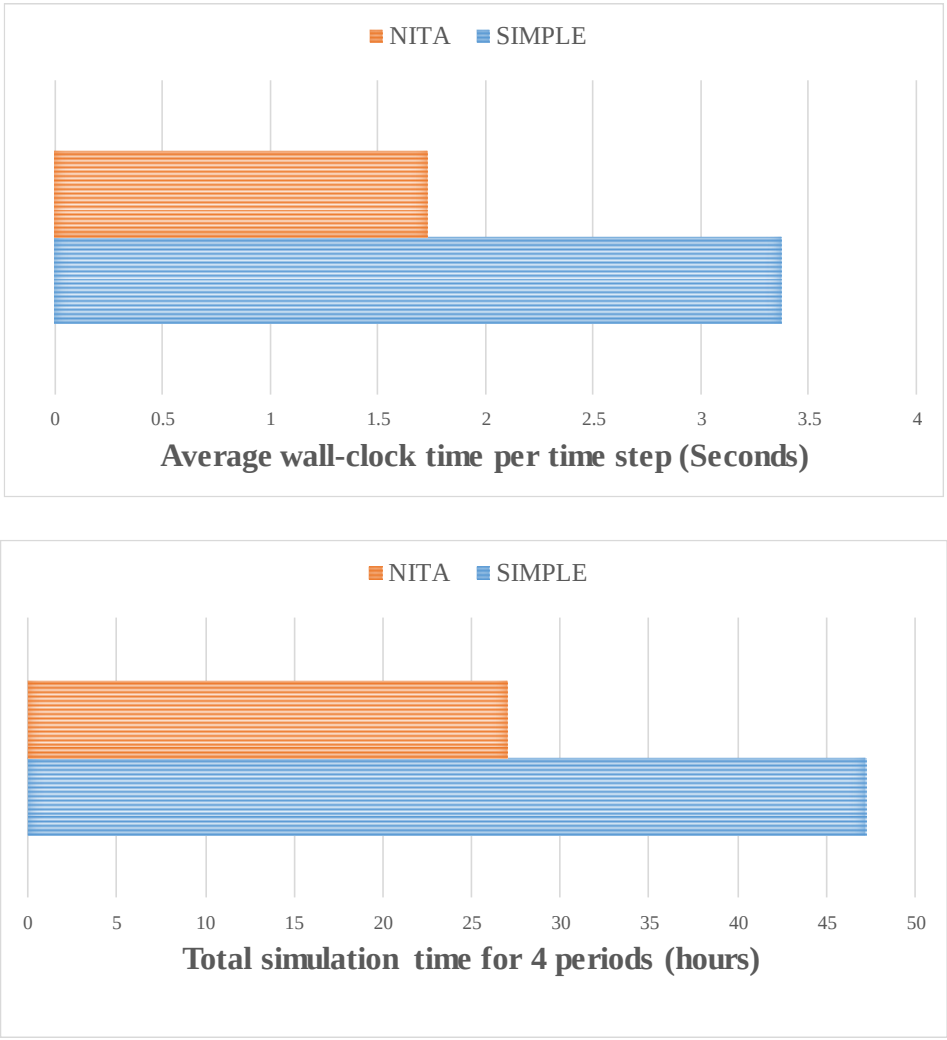

Figure 4.25: Performance comparison between NITA and SIMPLE.

4.4.2. Unsteady Morphing Initial Results

Following the validation of the unsteady CFD predictions using dynamic mesh, unsteady simulations are carried out, where the airfoil TE portion undergoes time-dependent morphing from its baseline position to a maximum deflection at TE, equal to 5% of the chord.

The purpose is to first demonstrate proof-of-concept of the methodology presented to analyse a dynamically morphed airfoil, reveal some trends and investigate some underlying flow physics. In particular, the dynamic evolution of the lift and drag coefficients are presented and the flow field is analysed.

The unsteady morphing analysis is carried out at higher AoA (14° and16°) around the stall with the aims of: 1) investigating some rich dynamic flow features that have not been explored in previous studies, and 2) looking into the possible effects that morphing could exercise on the flow to possibly delay the stall. To the authors' knowledge, this is the first time a continuous dynamic morphing trailing-edge airfoil is being simulated using dynamic meshing in ANSYS Fluent.

For the unsteady analysis, simulations start from a converged steady state solution. Three time steps ($\Delta t = 10^{-3}s$, $10^{-4}s$, $4\times10^{-5}s$) were investigated in order to ensure time step independence while 20 sub-iterations per time step were used to ensure numerical stability.

Instead of the SIMPLE algorithm used for the steady case, the coupled algorithm was used for the unsteady calculations given its more efficient and robust implementation, using a courant number of 1. An overall flow time of 12 seconds was simulated to illustrate flow responses with respect to airfoil geometry change. For AoA=14°, all three time steps gave similar results, confirming that the study is time step independent.

For a time step of $\Delta t = 10^{-4}\,s$, the time histories of lift and drag coefficients for two angles of attack are presented in Figure 4.26: at 14°, which is just at the start of stall, and at 16°, which is beyond the stall point (but not deep stall). The maximum deflection for the dynamically morphing flap is achieved after $t = 1\,s$. For both

cases, the dynamic lift rises with time as the flap is dynamically morphed, attaining maximum lift values shortly before the maximum flap deflection is reached. Beyond maximum flap deflection, however, the lift coefficient behaviour is markedly different for the two angles of attack.

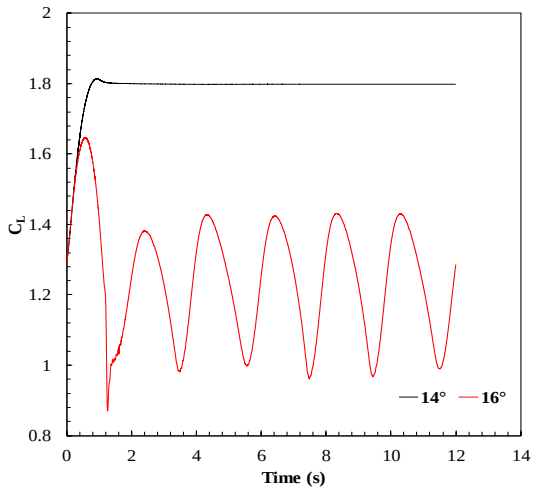

a) Lift coefficient

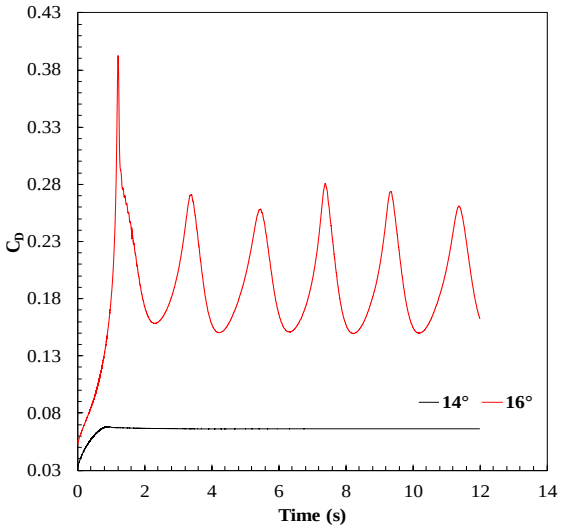

b) Drag coefficient

Figure 4.26: Time histories of unsteady a) lift coefficient and b) drag coefficient at 14° and 16° AoA, $\Delta t = 10^{-4}$ s.

At AoA = 14°, it is observed that a recirculation zone, or separation bubble resides on the upper surface of the airfoil near its trailing edge, and grows in size as the flap is dynamically morphed, reaching maximum size at maximum deflection but without any vortex shedding. The drag coefficient time history at AoA = 14° is similar to the lift coefficient's time history. On the other hand, at AoA = 16° the lift coefficient drops sharply beyond maximum deflection. Afterward, the lift coefficient settles down into a regular, oscillating time history with two vortex shedding patterns: the first with a period and Strouhal number of 2.4*s* and 0.018 respectively, the second with a period of 0.05*s* and a Strouhal number of 0.58 respectively, all while exhibiting small scale oscillations observed at the peaks of each cycle.

Figure 4.27 gives an in-depth visualisation of the flow evolution for the 16° AoA. During the dynamic morphing, the separation bubble present on the trailing edge slowly extends to cover most of the airfoil upper surface at $t = 1$ *s* then it undergoes small-scale oscillations without complete separation. However, a small separation bubble is also observed around the trailing-edge; this bubble grows steadily till it bursts, forming a vortex shedding pattern, which could explain the sudden drop in lift and surge in drag observed around $t = 1.5$ *s*.

Nevertheless, the bubble forming at the trailing edge afterwards is smaller than the initial one, giving weaker shedding which, again, may explain the lower amplitude of the lift and drag oscillations after the initial transient period. The drag exhibits similar behaviour but notably the drag peak always coincides with minimum lift; this is synonymous with vortex shedding. Compared to the baseline NACA 0012, the dynamic TEF seems to destabilize the steady bubble residing on the airfoil upper surface, causing more unsteadiness in the flow.

It is important to study the effects of morphing frequency on aerodynamic forces i.e. what would be the flow response to different frequencies at which the morphing flap is deflected, and what would be the dynamic response of the flow at various angles of attack. This will be discussed in the next chapter.

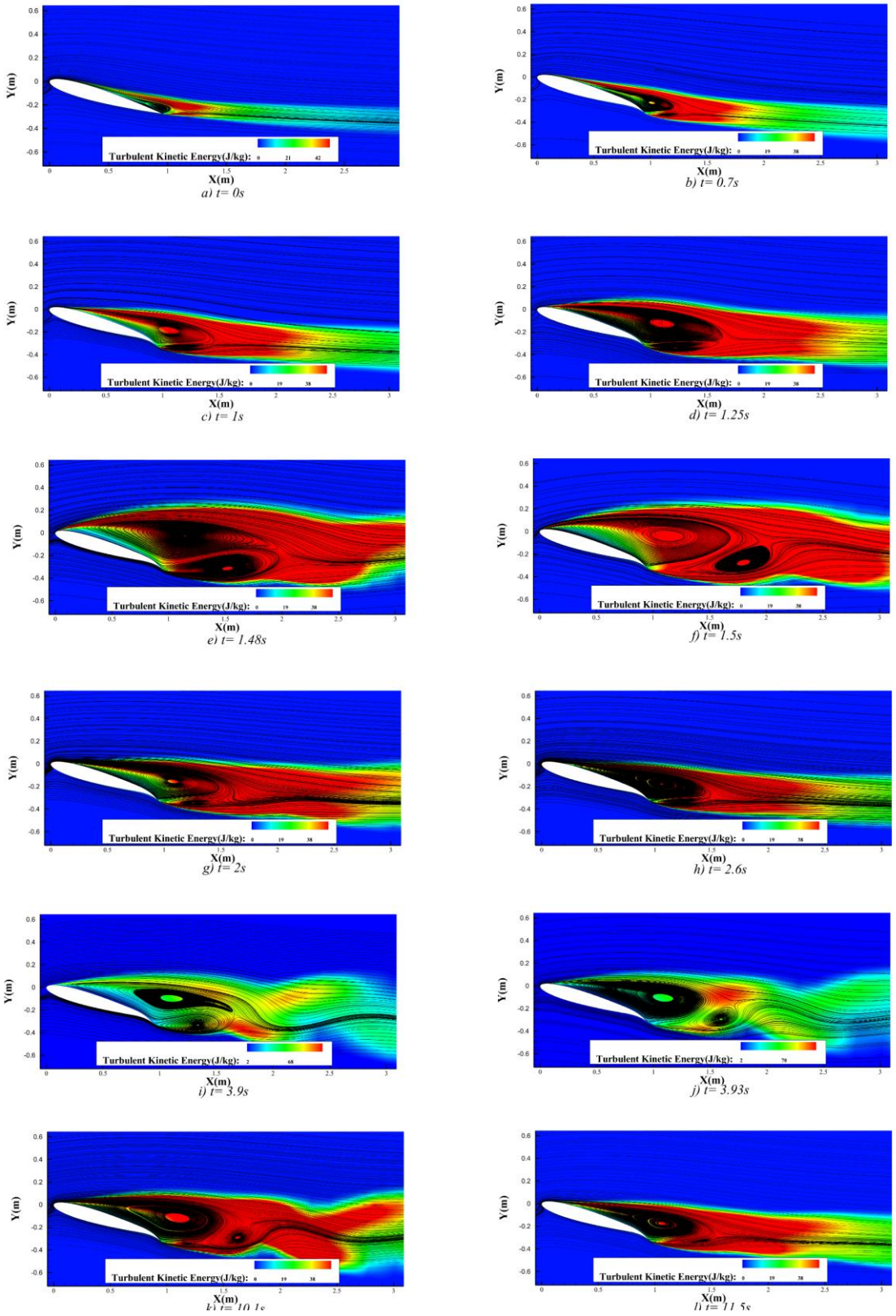

Figure 4.27: Time history of TKE and flow streamlines around the NACA 0012 airfoil with a dynamic morphing flap, at AoA= 16°.

4.5. Summary

Aerodynamic performance analysis of the NACA 0012 airfoil with a morphing trailing-edge flap was performed using commercial CFD solver Fluent, by means of a modified parametrisation method implemented in a User-Defined Function (UDF). The simulation of the morphing flap was facilitated with the use of a dynamic mesh. Steady CFD results for the deformed mesh were compared with a re-generated mesh to assess the accuracy of the dynamic mesh scheme, followed by a comparative study between a morphed and a flapped airfoil. Finally, unsteady predictions were validated against pitching airfoils experiment and a proof of concept case study of an unsteady morphing airfoil CFD investigation was carried out.

The following conclusions can be drawn:

i. Deformed mesh gave results similar to the re-generated mesh with small discrepancies of less than 1%, confirming the validity of the geometry and mesh deformation scheme.
ii. Steady state CFD results obtained from Fluent gave an average of 6% higher lift and drag coefficients compared with OpenFOAM. Both Fluent and OpenFOAM over-predicted the drag coefficient compared with XFOIL.
iii. For the same maximum deflection (5% of the chord), the morphing airfoil produced higher lift in comparison to a flapped airfoil, but at the expense of a drag penalty. An average increase in aerodynamic efficiency C_L/C_D of 6.5% is observed.
iv. The morphed airfoil reaches a peak aerodynamic efficiency at 8° angle of attack about 13% higher than the flapped one, after this angle the efficiency decreases until an angle of 13°. Beyond this angle, the flapped airfoil exhibits slightly better aerodynamic performance.
v. Unsteady CFD prediction using a dynamic mesh were used for pitching airfoil and satisfactory results were obtained when compared to experimental work.

vi. Unsteady analysis of a continuously morphing airfoil has been carried out successfully as proof of concept.

The next chapter will present the results of a study investigating the flow response to downward 2D dynamic morphing TEF deformed with various frequencies.

“The purpose of computing is insight, not numbers.”

Richard Hamming

5. 2D Downward Dynamic Morphing Flap

Chapter 5

Contents

5.1. Overview

In Section 4.3.2, it was concluded that the aerodynamic performance of an airfoil fitted with a morphing TEF offers an average of 6.5% increase in lift-to-drag ratio compared with a traditional hinged TEF. However, the study of a dynamic morphing airfoil would enhance the fundamental understanding of the flow. In this chapter, an exploratory parametric CFD study investigating forces (lift and drag) response to downward dynamic morphing TEF deflection with various frequencies is presented.

5.2. Problem Definition

Active flow control (AFC) through continuous actuation was explored in the literature (Cattafesta and Sheplak, 2011), where continuous actuations are performed in order to actively affect the flow, reduce drag and mitigate separation. However, the work performed in this chapter focuses on downward flap deflection (pulse-like actuator) rather than continuous AFC, therefore throughout the remainder of the thesis when AFC is mentioned it will exclusively designate

continuous flow control methods. Continuous AFC using harmonically morphing configurations will be explored in detail in Chapter 6.

When it comes to the differences between continuous and pulse-like actuations, Medina *et al.* (2018) argue that the transient response for pulse-like actuators could be utilized to produce a higher lift than the one achieved with periodic forcing, basing these conclusions on the work performed by Amitay and Glezer (2006). Founded on these assumptions, Medina *et al.* (2018) conducted a series of thorough experiments to investigate the flow response to a high rate deflection (rapid) of conventional flaps in order to increase the present understanding of such mechanisms.

To comprehend what is considered as rapid, or high rate, it is useful to look at the convective time $\frac{tU_\infty}{c}$ ($\frac{tU_\infty}{c} = 1$ represents the time needed for a parcel of fluid to convect from the LE to TE (Medina *et al.*, 2017)). For a typical flight, the flap motion time is approximately 10 convective times (Medina *et al.*, 2017). In this work, a range of flap motion time from 5 to 20 convective times was explored.

Medina *et al.* (2017) performed their experiment in a water tunnel, a 50% chord TEF of a NACA 0006 was deflected from 0º to 20º at various frequencies at attached and separated flow conditions to observe the lift coefficient response to flap actuations. Observations showed that a spike, which was proportional to the flap pitch rate, was captured in the lift coefficient time history in addition to no lag in the lift response to the actuation. The effect of the direction of the flap deflection was also investigated (Medina *et al.*, 2018; Medina *et al.*, 2017) and it was found that the forces are highly dependent on the actuation direction in the separated flow. Yet, these experiments were conducted at a low Reynolds number (~ 40,000) which is an order of magnitude lower if such a mechanism is to be used in applications such as the enabling of aggressive manoeuvres or gust load alleviation on aircraft.

However, morphing flaps would offer a better alternative to the hinged flaps used in Medina *et al.* (2018) experiment, as their implementation would result in a lower weight penalty (smart materials act as actuators and load bearing structures

simultaneously, reducing the need for extra actuation systems (Karagiannis *et al.*, 2014)). In addition, morphing flaps would smoothly cover a larger deflection range compared with traditional flaps (Barbarino *et al.*, 2011) which are limited by the actuators mechanisms that often constrain them to a discrete range of motions. Furthermore, exploring rapid flap deflection at a higher Reynolds number would allow a better understanding of the flow response in conditions that are more realistic.

To the author's best knowledge, studies exploring the response of flow when subjected to rapid morphing flap deflections, rather than hinged-flap, have not yet been addressed in the literature, by means of either experimental work or numerical simulations, at high or low Reynolds numbers.

5.3. Computational Setup

In order to study the effect that various morphing frequencies could have on the flow and on the dynamic evolution of lift and drag, a parametric study is proposed in this chapter. The Reynolds number investigated is still in the moderate range (Re = 0.62×10^6) but it is slightly different from the one used in chapter 4 (0.675×10^6). This change was performed in order to closely match published data available in the aeroacoustic experiment of Brooks *et al.* (1989) pertinent to the subsequent chapter, and therefore will be fixed throughout the rest of the thesis.

All test cases investigated started with a NACA 0012 airfoil with a chord $c = 0.2286$ *m*, a Reynold number of Re = 0.62×10^6 based on the chord and Mach number of

Table 5.1: Summary of the cases investigated for the rapid flap deflection.

w_{te} = 0.05%c, AoA =8º				
Frequencies (Hz)	2	4	6	8
w_{te} = 0.05%c, AoA =10º				
Frequencies (Hz)	2	4	6	8
w_{te} = 0.05%c, AoA =12º				
Frequencies (Hz)	2	4	6	8

0.115, in a freestream velocity of $U_\infty = 40\, m/s$ with standard sea-level conditions.

The parametrization method used for the TEF motion is the modified version introduced in section 4.2, for this study the start location of the morphing flap was maintained at x_s = 75% of the chord and the value of maximum deflection at the trailing edge w_{te} = 5% of the chord. Table 5.1 summarises the parameters used for the study.

A pressure-based solver included in the commercial software ANSYS Fluent (ANSYS, 2018) is used for all the subsequent unsteady calculations. The fractional Step Method (FSM) NITA scheme was used for time advancement as it results in significant CPU savings. A least square cell based spatial discretization was used for all the gradients. Moreover, the momentum equation discretization employs a Bounded Central Differencing (BCD) scheme with a second order scheme for all the remaining quantities.

Turbulence closure was provided by the SBES turbulence model (Menter, 2016). In the present work, the *k*-ω SST turbulence model with the intermittency transition model was used for the RANS region, and the Wall-Adapting Local Eddy-viscosity (WALE) for the LES region.

The use of a hybrid RANS-LES model in this 2D study is for the purpose of demonstrating trends, determining resolutions and giving guidance for future quasi-3D simulations. Which would give an estimate of computational resources needed for future applications.

For validation purposes, XFOIL (Drela, 1989b) was used to provide lift and drag predictions for the baseline NACA 0012 airfoil.

Dynamic mesh schemes implemented in ANSYS Fluent were utilized to deform the mesh. Diffusion-based smoothing was the primary smoothing method used given its suitability for structured meshes and higher quality preservation near deformed walls (ANSYS, 2018). However, as shown in section 4.2.2 a limited unstructured region was used around the TE in order to avoid high skewed cells at the TE by making use of the remeshing option in ANSYS Fluent and ensure high quality elements are preserved during the morphing as it is illustrated in Figure 5.1.

The flow domain consists of a NACA 0012 airfoil with a sharp TE, the pressure far-field is placed at 30-chord lengths (30*c*) from the TE. A structured O-grid type mesh was generated around the airfoil (Figure 5.2). The mesh had a total number of cells of 350,000 cells, with 1,400 points around the airfoil and 200 points in the streamwise direction clustered toward the TE. The inflation layer was refined to

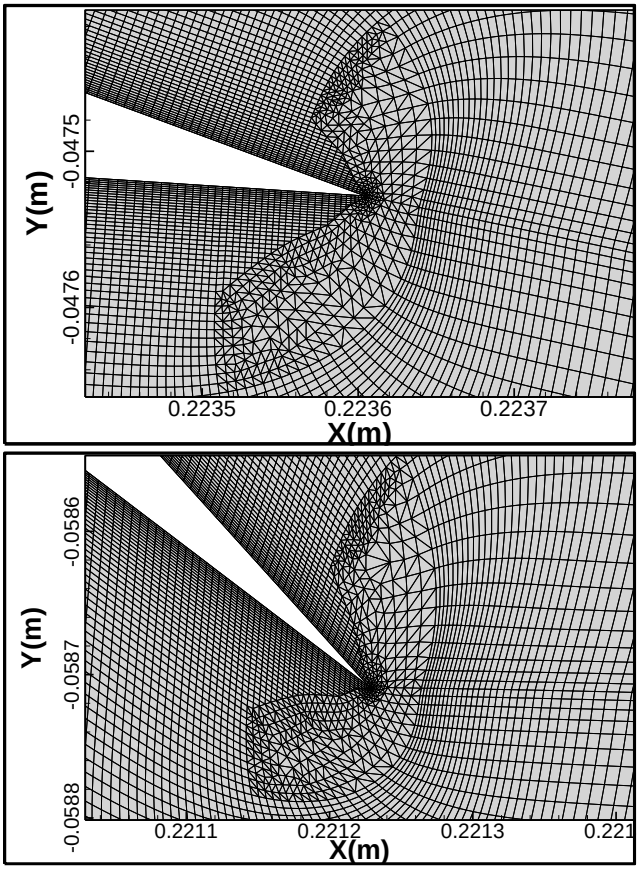

Figure 5.1: Unstructured patch around the TEF: (top) before and (down) after mesh deformation.

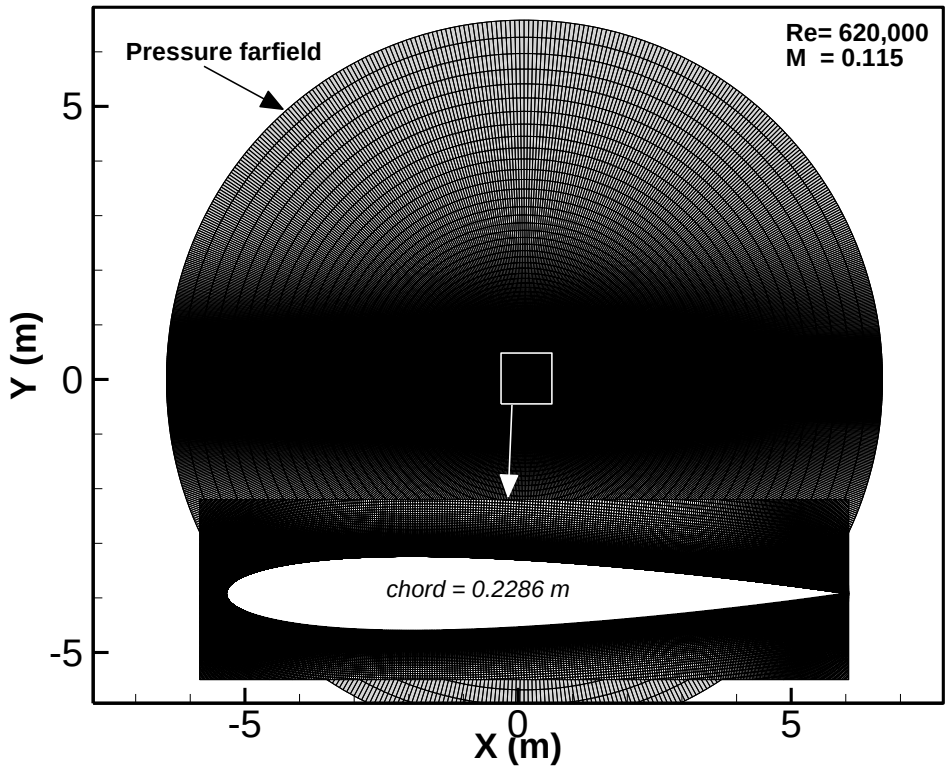

Figure 5.2: Details of the computational domain used.

achieve y^+ smaller than 0.5. These mesh characteristics were based on the fine mesh tested in in the previous chapter, which are also suitable for the aeroacoustic study in Chapter 5.

A second order transient formulation was used for all the transient simulations. A time step of $\Delta t=10^{-5}s$ was employed, all simulations were run for at least 0.8 *s* (~4.5× flow-through times).

5.4. Validation and Verification

Figure 5.3 shows the numerical results obtained using Fluent and XFOIL compared against the experimental results by Sheldahl *et al.* (1981) for both C_L and C_D for the range of AoA from 0° to 16°.

Overall, a good agreement is present between Fluent and XFOIL and Sheldahl *et al.* (1981) experimental data in the linear region, up to 10º where the average difference between the two predictions is 5%.

Fluent predictions are in better agreement with the test data in the linear region for both lift and drag, but the experimental data in Sheldahl *et al.* (1981) seems to show an early stall for the airfoil at about 11º while Fluent predictions show a higher stall AoA at 13º with an 8.6 % higher $C_{L,max}$. XFOIL does not capture the stall and overpredicts it as well.

A few possible reasons could explain the discrepancy observed between the numerical predictions and the test data. In the experimental work performed by Church *et al.* (2018) investigating a NACA 0021 airfoil at lower Reynolds numbers (less than 200,000), it was found that data from Sheldahl *et al.* also underpredicted the stall angle and $C_{L,max}$. It was concluded that experimental data from Sheldahl *et al.* is not representative of the NACA 0021 airfoil mainly because the data at pre and early stall were calculated using the `PROFILE` computer code. Furthermore, data obtained from Ladson *et al.* (1988) shows that for a Re = 2M , Sheldahl *et al.* data

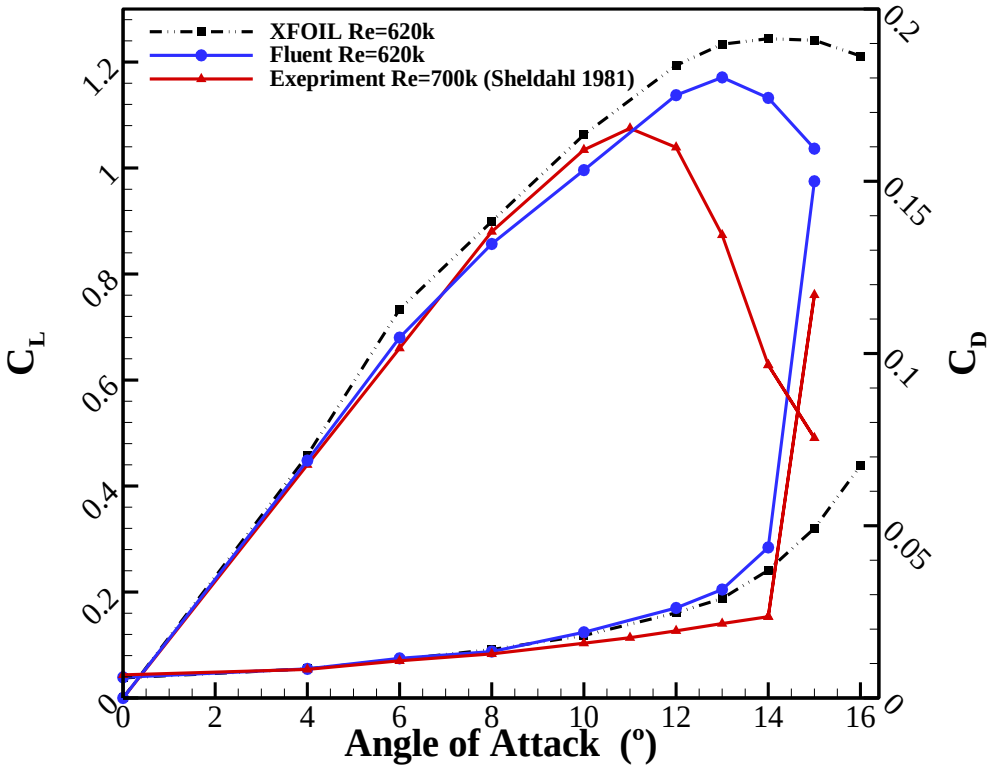

Figure 5.3:Results for C_L and C_D obtained from SBES simulation compared with XFOIL predictions and experimental results for the NACA 0012 airfoil from Sheldahl et al. (1981).

underpredicts the stall angle by at least 2º, which is similar to the findings of this study. The overprediction in $C_{L,max}$ value could be explained by the fact that using a purely 2D configuration results generally in overpredicting lift.

Similar trends are observed in the drag where good agreement is present between Fluent, XFOIL and test data up to the pre-stall region (AoA= 10º) where the discrepancies grow. At 14 º, both Fluent and the test data show a steep increase in drag indicating a deep stall.

5.5. Rapid Morphing TEF

Figure 5.4 shows the transient lift and drag response to the rapid morphing TEF deflection at various actuating frequencies. Morphing commences at t = 0.5 s after the flow transients had enough time to reach a steady state.

At 8º and 10º AoA, lift and drag coefficients exhibit similar transient behaviour. The lift starts increasing linearly from the static values up until the flap reaches its final position where the lift converges to a steady state which is similar for all cases. The slope at which the lift increases during the morphing motion is proportional to the frequency, the higher the frequency the steeper the slope.

The transient drag response shows a noticeable difference compared with lift evolution; an overshoot ensues in the drag values before the flap reaches its final position; the amplitude of the spike observed is also proportional to the frequency with higher frequencies causing larger overshoots.

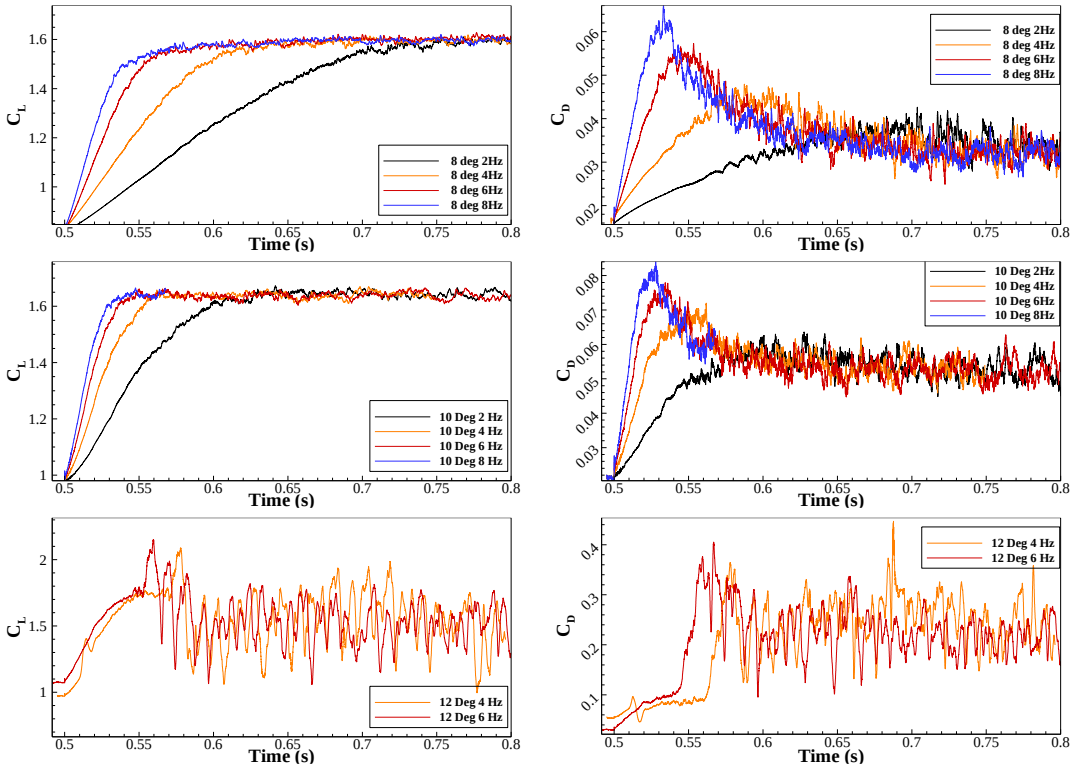

Figure 5.4:Lift and drag coefficient response to rapid morphing flap for all the cases studied.

For AoA=12º, the flow response is different from the lower angles studied, at this AoA the NACA 0012 is in a pre-static stall region, the increasing camber coupled with the rapid deflection motion causes the airfoil to stall.

Both the lift and drag coefficients display similar trends, before morphing starts a vortex street that forms in the wake of the baseline airfoil with a shedding frequency of 50 Hz corresponding to a Strouhal number (S_t) based on the airfoil thickness of 0.1. As the morphing flap deflects a linear increase in the lift and drag coefficient is observed with a slight overshoot in the C_D values at t = 0.52 s.

Nevertheless the airfoil does not recover to the steady state (as it does at 8º and 10º) causing the airfoil to experience large-scale oscillations (of S_t = 0.3) in the lift and drag coefficient around higher values of both C_L and C_D.

The aerodynamic efficiency illustrated in Figure 5.5 provides an additional understanding of the loads response, two representative cases are shown: AoA= 10º and 12º both at a morphing frequency of 8Hz.

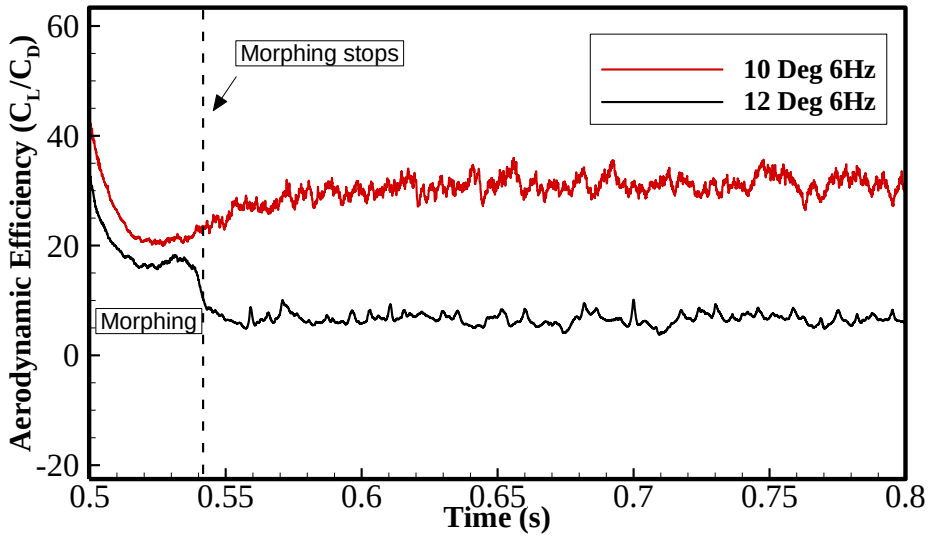

Figure 5.5: Aerodynamic efficiency during the morphing TEF deflection.

The efficiency starts from the baseline value for both AoA then it starts to linearly decrease until it reaches $t = 0.51$ *s* where the rate of decrease accelerates due to the overshoot in C_D. For the 10º case, the efficiency recovers to higher values where it settles at an average C_L/C_D of 26 after experiencing a 30% drop. In contrast, at AoA =12º, after the morphing motion stops, the efficiency does not recover but drops further when the dynamic stall process starts.

Further insight into the flow behaviour during the rapid morphing flap deflection could be gained by qualitative examination of the flow.

Figure 5.6 shows the vorticity contours for the airfoil during the morphing process at AoA = 10º and a morphing frequency of 8 *Hz*. At this AoA, the airfoil experiences TE flow separation, which causes shed vortices to convect downstream, forming a vortex shedding pattern in the wake.

When the deforming motion starts, the TEF causes a region of separated flow to develop with the detachment of vortices at the TE inducing an upstream roll-up of the vortex. This vortex interacts with the thickening shear layer at the start of the morphing flap. This interaction results in a shed vortex, which then convects downstream along the flap; this could be the cause of the spike observed in the

drag. When this initial larger vortex convects, the same cycle repeats but the resulting vortices are smaller compared with the initial vortex.

Medina *et al.* (2018) observed a spike in the lift, the flap motion time was of the order of one a convective time or less $\left(\sim \frac{tU_\infty}{c}\right)$ whereas in this study the morphing flap motion time is larger (between 5 to $20\frac{tU_\infty}{c}$) which could explain the absence of the overshoot in the lift in the current study. Additionally, Medina *et al.* (2018) only studied the lift response and did not study the drag response as it was performed in this work, therefore comparing the drag response between the two cases was not possible.

Another noticeable feature of the flow is the appearance of what seems to be a LBL (Laminar Boundary Layer) on the pressure surface near the morphing flap caused by the deflection; this can be better seen in Figure 5.7.

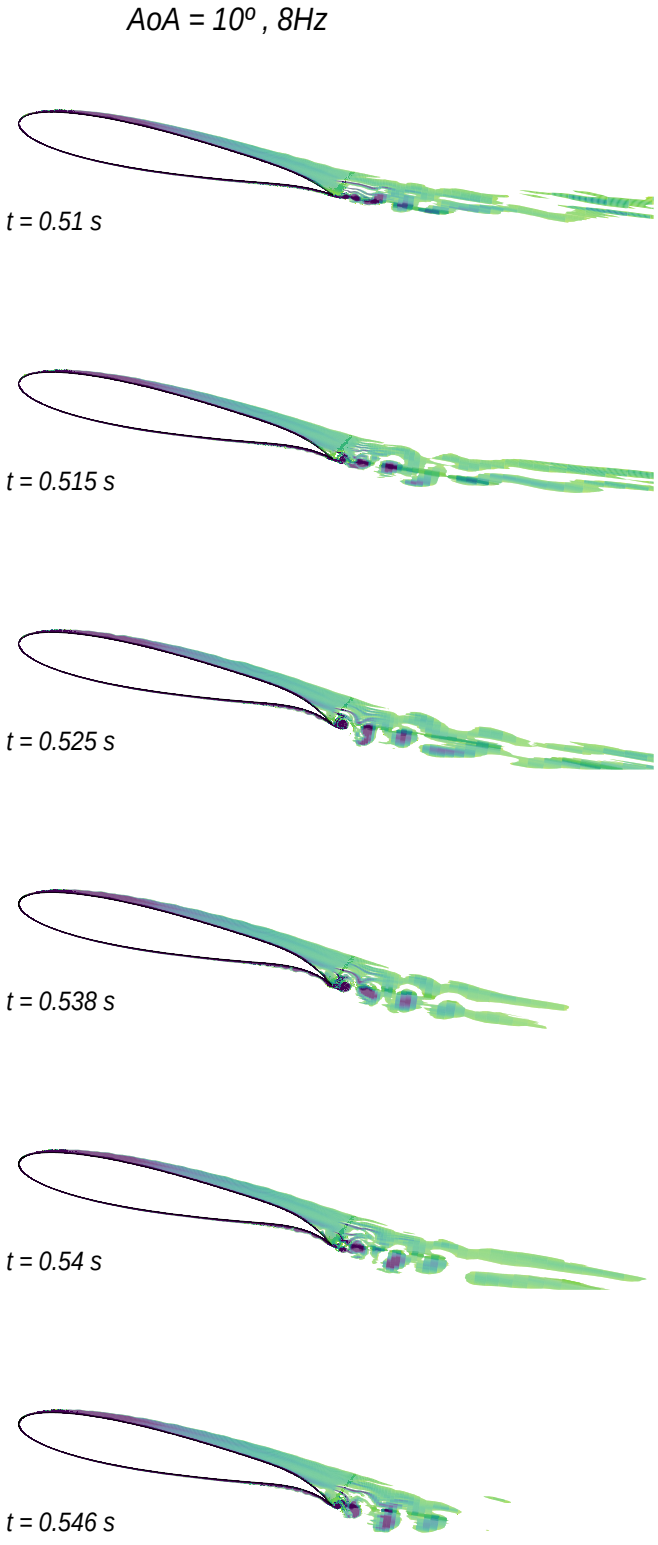

Figure 5.6: Instantaneous contours of the vorticity showing the evolution of the turbulent structures at AoA =10º and 8 Hz.

Figure 5.7: Close-up showing the flow features around the TE and the formation of LBL at the pressure surface.

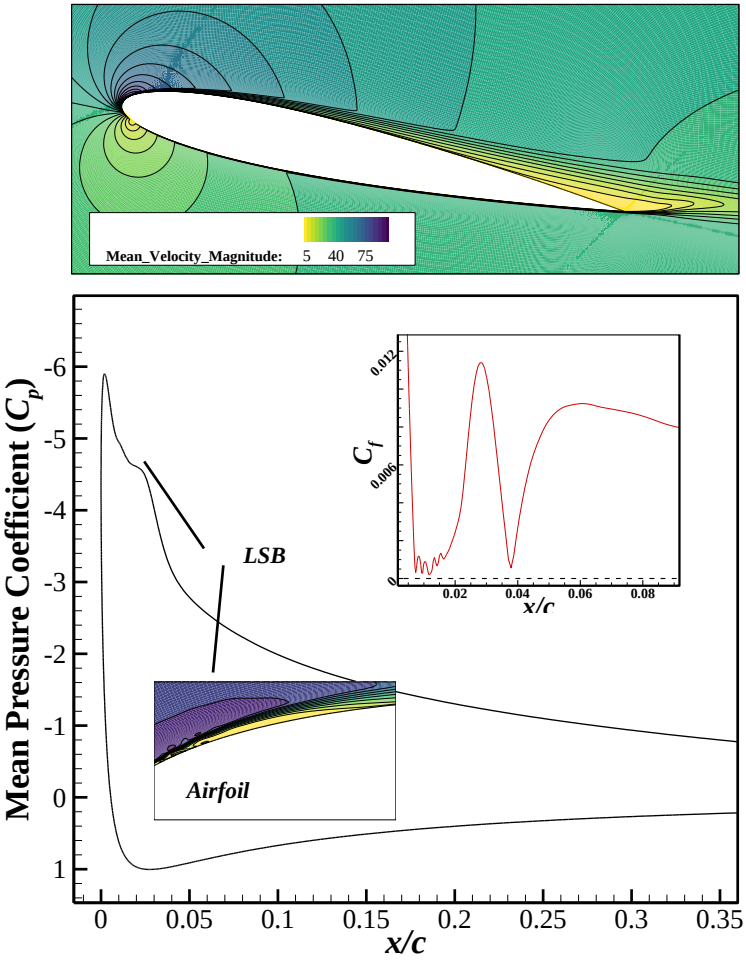

Figure 5.8: Mean velocity magnitude contours (top). Mean pressure coefficient (C_p), skin friction coefficient (C_f) (down) for NACA 0012 at AoA =12º.

The response at a higher AoA is strikingly different. At AoA = 12º the airfoil is in a pre-stall region with separation occurring at the TE, but the flow on most regions of the airfoil is still attached as is illustrated by the mean velocity contours in Figure 5.8. The boundary layer is characterised by the presence of a small Laminar Separation Bubble (LSB) near the leading edge. The signature of the LSB is shown in Figure 5.8 in both the pressure and skin-friction coefficient in addition to a close-up of the mean velocity magnitude. The LBL instabilities are also captured just upstream of the LSB.

The LSB triggers the transition from a laminar to a turbulent BL at x/c = 0.0123 where C_f ~ 0. This LSB causes a separation-induced transition resulting in a turbulent boundary layer developing downstream starting at x/c = 0.04. This behaviour near the transition was captured due to the use of the intermittency transition model. Similar behaviour of both C_p and C_f has been associated in the

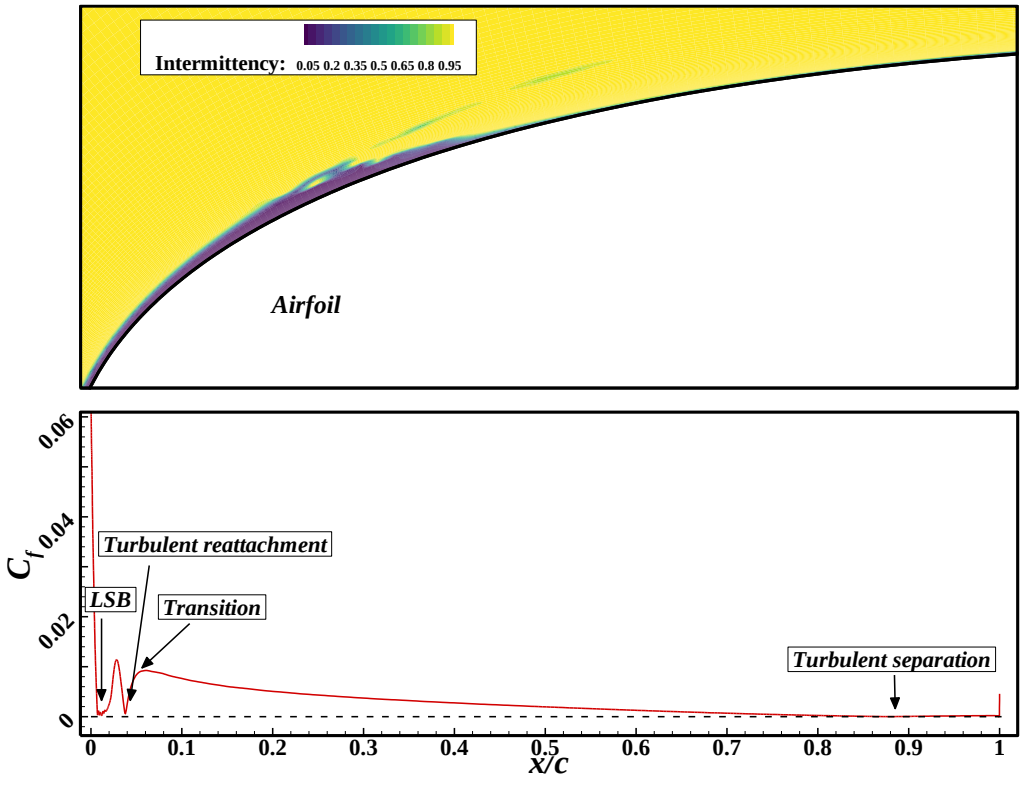

Figure 5.9: Intermittency contours (top) and mean skin friction coefficient (C_f) (down) on the suction side of a NACA 0012 at AoA =12º.

literature with LSB triggering the onset transition when captured by transitional models (Langtry and Menter, 2005).

The transition could also be captured in the intermittency contours (Figure 5.9) where a value of 0 indicates a laminar BL and a value of 1 indicates a turbulent BL. On the pressure side, the flow is completely laminar. At the TE, the turbulent boundary layer eventually separates due to the large adverse pressure gradient there, as illustrated in the C_f plot in Figure 5.9.

Figure 5.10 and Figure 5.11 show the vorticity contours at 12º AoA for two different frequencies 2 *Hz* and 8 *Hz*. Overall, both cases do not display striking differences, perhaps the only difference is the size and vorticity of the initial vortex forming just before the morphing motion stops. Nevertheless, qualitative inspection of the flow response to the rapid morphing deflection could provide further insight into the mechanism by which the dynamic stall occurs.

When the morphing motion starts, the turbulent separation at the TE appears to propagate upstream, and contrary to the 10º case, the propagation accelerates on the airfoil surface with the increasing camber. The dynamic stall appears to be triggered when the turbulent structures interact with the LSB present near the LE, causing the LSB to burst creating a large vortex which convects downstream, at the same time it creates a small Leading Edge Vortex (LEV). The turbulent boundary layer becomes separated and begins to form a second vortex which when it convects downstream it merges with a counter-clockwise TE vortex. This mechanism seems to sustain the dynamic stall.

A remarkable similarity in the flow response could be found between rapid downward morphing flap deflection and ramp-type pitch up motion at similar AoA. For instance, Benton *et al.* (2018) studied a NACA 0012 airfoil experiencing a rapid pitch up motion at a Re = 1M using high fidelity LES, and they have made similar observations when it comes to the mechanism initiating the dynamic stall.

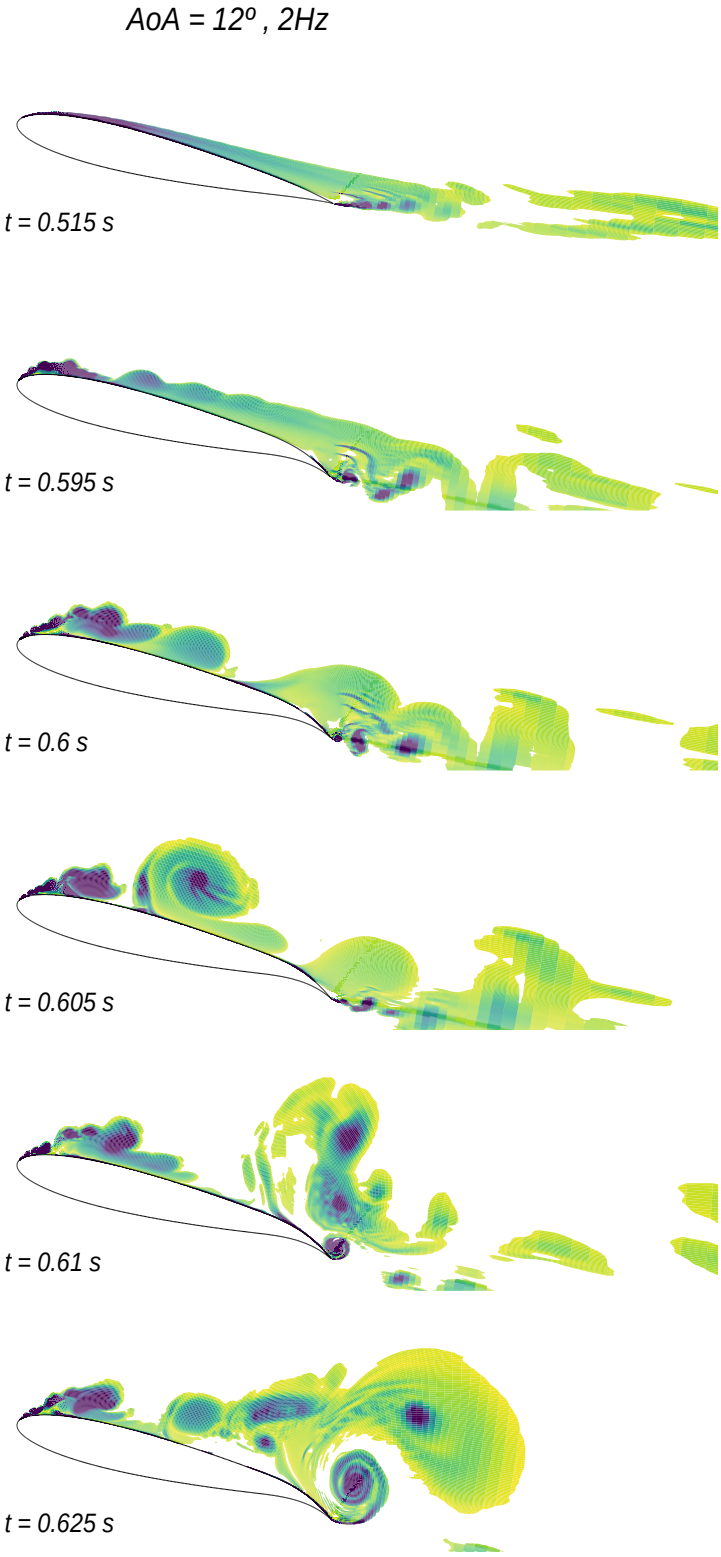

Figure 5.10: Instantaneous contours of the vorticity showing the evolution of the turbulent structures at AoA =12º and 2 Hz.

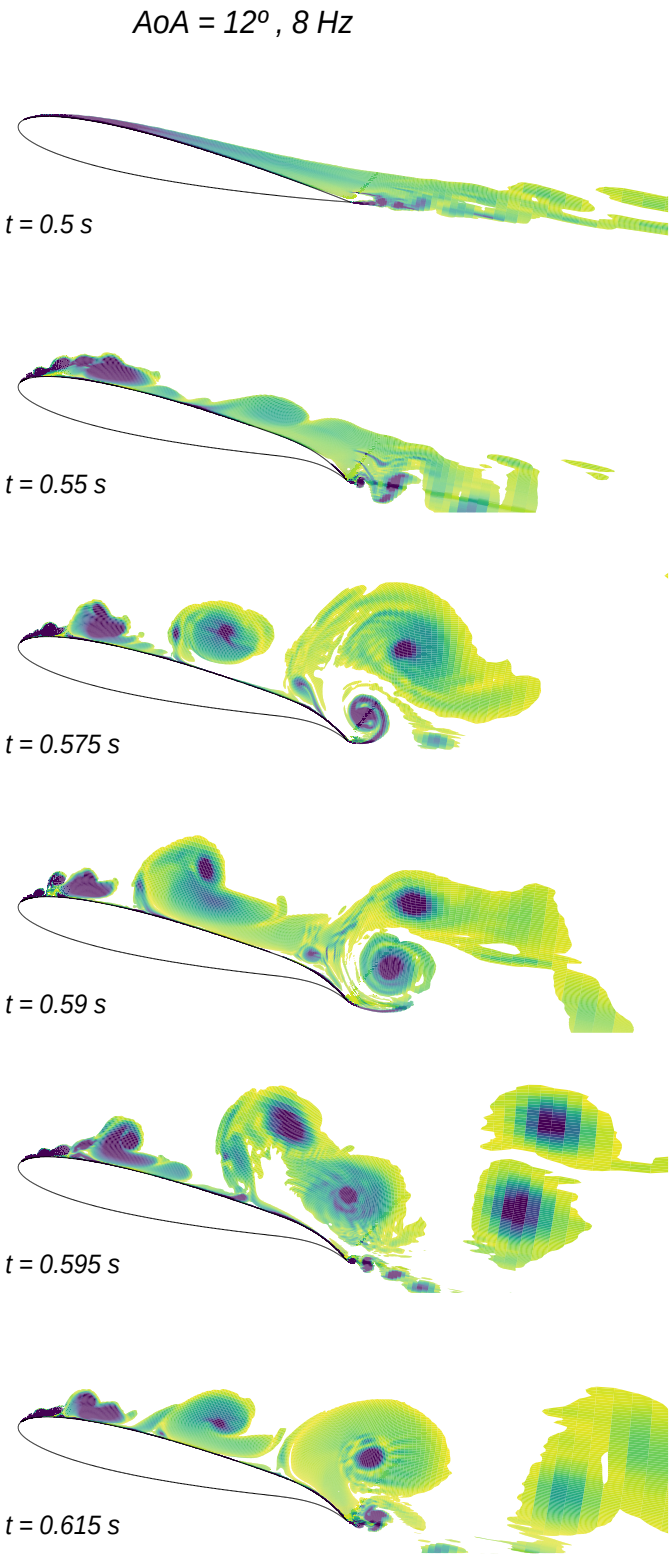

Figure 5.11: Instantaneous contours of the vorticity showing the evolution of the turbulent structures at AoA =12º and 8 Hz.

5.6. Summary

The flow response to a rapid deflection of a morphing TEF has been investigated using the SBES turbulence model at AoA in the pre-stall region. Various morphing frequencies have been explored and the lift and drag coefficient response analysed.

Both lift and drag responses showed a proportional relation between the morphing frequency and the slope at which these quantities evolve. Interestingly, an overshoot in the drag coefficient has been captured, but not in the lift coefficient. Its amplitude is also proportional to the actuation frequency used; higher frequencies were causing larger overshoots. The aerodynamic efficiency during the morphing process experienced up to 30% decrease due to the drag overshoot.

Qualitative results gave insight into the flow response to the rapid morphing deflection. At an AoA =12º, the morphing causes turbulent structures to propagate upstream, interact with a Laminar Separation Bubble (LSB) causing it to burst, which initiates a dynamic stall. This behaviour was observed in the literature for rapid pitch up airfoils.

This chapter focused mainly on 2D downward deflection with relatively low frequencies and high amplitude. In contrast, high frequency, low amplitude continuous harmonic morphing will be explored in the next chapter as a mean of aerodynamic and aeroacoustic active flow control.

“What man-made machine will ever achieve the complete perfection of even the goose's wing?”

Abbas Ibn Firnas, 852

6. Aerodynamic and Aeroacoustic study of 2D Harmonic Morphing Trailing-Edge Flap

Chapter 6

Contents

6.1. Overview

In this chapter, the numerical framework developed in the previous chapter is further extended to include the aerodynamic and aeroacoustic study of harmonically morphing TEFs. First, the unsteady parametric method introduced in Chapter 4 is further modified to model the harmonic morphing in Section 6.2. Then, a brief theoretical background for the Ffowcs-Williams and Hawkings (FW-H) acoustic analogy used for the far-field noise prediction is presented (Section 6.3). Finally, the framework was used to perform a parametric study of the effects of the morphing frequency and amplitude on the aerodynamic and aeroacoustic performance of the harmonically morphing TEF.

6.2. Mathematical Model of the Harmonic Morphing

The parametrization method used for the TEF motion is a modified version of the method introduced in Chapter 4. It consists of the baseline NACA 0012 thickness distribution as defined in Eq 3.40 added to the unsteady parametrization of the camber line as defined in Eq 4.1.

Eq 4.1 is adapted so that the entire range of motion (i.e. upward and downward flap deflection) can be achieved; this change is reflected in Eq 6.1. In Eq 6.1, the morphing start time (t_{start}) is included to control the start of the morphing at any set time:

$$y_c = \begin{cases} 0\ , & 0 \le \bar{x} < x_s \ and \ \ t < t_{start} \\ \frac{-w_{te}\sin(2\pi f(t-t_{start}))(\bar{x}-x_s)^3}{(1-x_s)^3}, & \bar{x} \ge x_s \ and \ \ t \ge t_{start} \end{cases} \tag{6.1}$$

where $f = 1/T$ is the morphing frequency and x_s is the start location for the morphing.

Using this parametrization method, the dynamic mesh update methods included in ANSYS Fluent are utilized in order to deform the mesh and the geometry whilst maintaining a high quality mesh in the process as explained in Chapter 4.

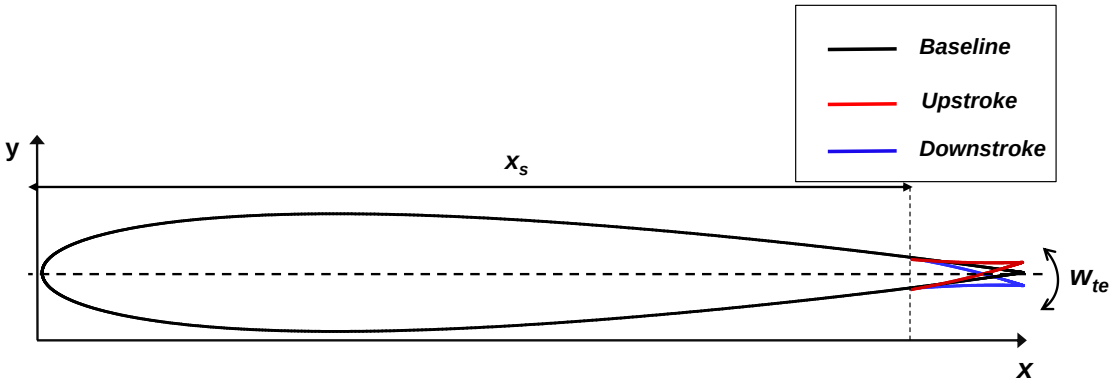

Figure 6.1: Harmonic morphing TEF modelled by the unsteady parametrization method.

6.3. Ffowcs-Williams and Hawkings Model

Computational Aeroacoustics (CAA) requires a time-accurate unsteady solution of the Navier-Stokes equations to obtain pressure distribution, velocity components, and density on source surfaces. It needs as well acoustic analogies in order to predict accurately the noise. The FW-H formulation (Williams and Hawkings, 1969) is the most general form of Lighthill's acoustic analogy (Lighthill, 1952). By manipulating the conservation equations (continuity, momentum), Williams and Hawkings (1969) were able to construct an inhomogeneous wave equation (Eq 6.2) which is the basis of the FW-H model:

$$\frac{1}{a_o^2}\frac{\partial^2 p'}{\partial t^2} - \nabla^2 p' = \frac{\partial^2}{\partial x_i \partial x_j}\{T_{ij}H(f)\} - \frac{\partial}{\partial x_i}\{[P_{ij}n_j + \rho u_i(u_n - v_n)]\delta(f)\} + \frac{\partial}{\partial t}\{[\rho_o v_n + \rho(u_n - v_n)]\delta(f)\} \quad (6.2)$$

where u_i = fluid velocity component in the x_i direction

u_n = fluid velocity component normal to the surface $f = 0$

v_i = surface velocity components in the x_i direction

v_n = surface velocity component normal to the surface

$\delta(f)$ = Dirac delta function

H(f) = Heaviside function

p' = the sound pressure at the far field

T_{ij} = the Lighthill's stress tensor

a_0 = far-field sound speed

($f = 0$) = corresponds to the source (emission) surface

P_{ij} = is the compressive stress tensor

n_j = is the unit normal vector pointing toward the exterior region

In ANSYS Fluent, Eq 6.2 is integrated analytically, assuming the absence of obstacles between the sources and receivers. The solution integrals consist of

surface and volume integrals. Surface integrals are the contribution from monopole and dipole acoustic sources whereas volume integrals embody the quadrupole sources. The quadrupoles are dropped in ANSYS Fluent as their contribution becomes negligible for low subsonic flows (ANSYS, 2018)

6.3.1. 2D vs 3D analysis

Since most significant noise generation mechanisms are three-dimensional (3D), the FW-H formulation used in this study is preferred for more practical cases. Unfortunately, the computational cost of generating high fidelity unsteady flow data for full 3D cases is restrictive, especially for complicated setups where coupling with other models is needed like rotating and deforming bodies (Garipova *et al.*, 2016). Furthermore, the flow features generating noise in the spanwise direction can be two-dimensional or pseudo-two-dimensional in nature (Lockard, 2000) like the Laminar Boundary Layer-Vortex shedding noise (LBL-VS)) (Brooks *et al.*, 1989) which is a prominent noise source for airfoils at moderate Reynolds numbers (Nash *et al.*, 1999; Brooks *et al.*, 1989). Various studies have confirmed the two-dimensional nature of the LBL-VS (e.g. De Gennaro *et al.*, 2017; Golubev *et al.*, 2014; Singer *et al.*, 2000).

Therefore, 2D simulations could be used for aeroacoustic predictions at moderate Reynolds numbers, not as a replacement for 3D simulations, but for the purpose of demonstrating trends, giving approximations of noise levels, and determining resolutions and guidance for the 3D simulations. Singer *et al.* (2000) demonstrated the ability of 2D aeroacoustics simulations of a TE slat to capture all of the important features observed in both experimental work and 3D simulations. The same study also noted that a scaling parameter must be selected to account for the spanwise effects, which is often done empirically.

Finally, Golubev *et al*. (2011) performed an extensive 2D analysis using an Implicit LES (ILES) code and compared their findings to experimental work and later on to the full 3D ILES results (Golubev *et al.*, 2012). The use of the 2D approach was justified by the fact that even though the investigated flow is fundamentally unsteady, the flow regime investigated is primarily laminar with possible local

separation zones. This enables the 2D analysis to adequately describe the tonal noise since the mechanism of its generation is inherently 2D as explained by Golubev *et al.* (2013). The overall comparison between the 2D and 3D simulations was found to be satisfactory, justifying therefore the use of the 2D assumption. The only significant difference between 2D and 3D was the discrepancy in broadband noise levels and the over prediction of SPL levels by the 2D approach. However, such differences can be corrected which is the approach taken in this chapter, which is discussed in the next section 6.5.2.

6.3.2. Source correlation length and acoustic corrections

To compute the sound using 2D flow results, a source correlation length is needed in order to evaluate the FH-W equations in the spanwise direction since the formulation is always 3D. Nevertheless, this comes with the assumption that the surface pressure along the entire correlation length chosen is fluctuating with a constant intensity along the entire span. However, as shown by Kato *et al.* (1993), this cannot be assumed for all the structures, particularly the small turbulent eddies. This assumption results in the overprediction of the Sound Pressure Level (SPL), as much as 14 *dB* in some cases (Kato *et al.*, 1993; Orselli *et al.*, 2009), thus showing a need for a further correction to account for such effects.

A number of correction methods have been proposed with varying levels of complexity. Kato *et al.* (1993) proposed a relatively simple correction to account for the differences between the simulated and the real (experimental) span generated noise, by introducing an equivalent coherence length which assumes that the pressure fluctuations are the same along the defined coherence length (same definition as the source correlation length used in ANSYS Fluent). Kato's corrections were successfully implemented in various studies such as Orselli *et al.* (2009), or adapted for long-span bodies as demonstrated by Seo *et al.* (2007). Another correction formula for both the span size and the position of the microphone was proposed in Hansen and Bies (1995), and was successfully used by De Gennaro *et al.* (2017). This latter correction is formulated in Eq 6.3 and used subsequently.

$$SPL_{corr} = Span_{corr} + Dist_{corr}$$

$$= 10\log_{10}\left[\frac{\tan^{-1}\left(\frac{S_0}{r_{e,0}}\right) + \frac{\sin\left[2.\tan^{-1}\left(\left({}^{S_0}/_{r_{e,0}}\right)\right]\right)}{2}}{\tan^{-1}\left(\frac{S_1}{r_{e,0}}\right) + \frac{\sin\left[2.\tan^{-1}\left(\left({}^{S_1}/_{r_{e,0}}\right)\right]\right)}{2}}\right] + 20\log_{10}\left(\frac{r_{e,1}}{r_{e,0}}\right) \quad (6.3)$$

where:

S_0 = Span length simulated

S_1 = Span length targeted (i.e. experimental setup)

$r_{e,0}$ = Microphone distance in the simulation

$r_{e,1}$ = Microphone targeted

6.4. Computational Methodology

In this chapter, a numerical framework for the aerodynamic and aeroacoustic study of harmonically morphing TEFs is introduced. First, the unsteady parametric method introduced in Chapter 4 is further modified to model the harmonic morphing. The latter was implemented in a UDF with appropriate smoothing techniques employed for mesh deformation. Then, a brief theoretical background for the Ffowcs-Williams and Hawkings (FW-H) acoustic analogy used for the far-field noise prediction is presented.

Finally, the framework is applied in a parametric study of the effects of the morphing frequency and amplitude on the aerodynamic and aeroacoustic performance of the harmonically morphing TEF, using both RANS and SBES turbulence models. To the author's best knowledge, this is the first instance where a framework integrating UDFs with Fluent dynamic mesh tools to investigate aerodynamic and aeroacoustic effects of morphing TEFs is used

Three cases are presented. First, a validation study on the unmorphed NACA 0012 airfoil at Re = 0.62×10^6 is performed and results are compared with published

Table 6.1: Summary of flow configurations analysed.

Configuration	Reynolds number	Angle of attack(°)	Mach number
Unmorphed case	0.62×10^6	4	0.115
Unmorphed case: 2D SBES vs 3D LES	0.408×10^6	5	0.115
Harmonically Morphing TEF	0.62×10^6	4	0.115

experimental and numerical data. Second, a 3D LES study performed by Wolf *et al.* (2012) is replicated using the 2D SBES simulation and differences between the 2D and 3D predictions are discussed. Finally, a case study of a periodically morphing TEF is investigated at two frequencies (100 *Hz* and 800 *Hz*) for a fixed morphing amplitude (0.01% of the chord), then at a fixed frequency (100 *Hz*) and two amplitudes (0.01% and 0.1% of the chord). The effects of the periodic morphing on the acoustic spectra, tonal noise specifically, and aerodynamic performance are then observed and discussed.

The accuracy of the computational framework developed is assessed in 2D by comparing the results obtained with the experimental data of Brooks *et al.* (1989). Their experiment investigated a NACA 0012 wing with a chord of 0.2286 *m*, a span of 0.4 *m* and a sharp TE in a low turbulence core of a free jet located in an anechoic chamber. The Reynolds number was 0.62×10^6, at a freestream velocity of 40 *m/s* (Mach number = 0.115). More details of the setup can be found in Brooks *et al.* (1989).

Additionally, to gain further understanding of the differences between 2D and 3D simulations, a study conducted by Wolf *et al.* (2012) is replicated using the current 2D approach. Wolf *et al.* (2012) investigated a similar setup by Brooks *et al.* (1989) using compressible LES though the conditions were slightly different; $c = 0.1524m$, a Re = 0.408×10^6, AoA= 5° and Mach number = 0.115. In addition, instead of a sharp TE, a rounded TE was used. Further details pertinent to this case study can

be found in Wolf *et al.* (2012). Once the validity of the computational approach is established, the proposed framework is applied to model a harmonically morphing TEF and to survey the effects that specific morphing frequencies and amplitudes have on the tonal noise levels, acoustic spectra, and aerodynamic performance. Table 6.1 summarizes the cases studied in this chapter.

6.5. Numerical Procedure

The flow domain consists of a NACA 0012 airfoil with a sharp TE, the pressure far-field was placed at least 30 chord lengths (30*c*) from the TE and a structured O-grid type mesh (Figure 6.2) was generated around the airfoil. Three sets of meshes were generated to determine mesh independency. The sizes of the grids were 60k, 100k and 400k cells for the coarse, medium and fine grid respectively. The number of points on the surface of the airfoil ranged from 600 to 1600 points for the finest mesh, the inflation layer was refined to achieve a y^+ between 0.5 and 1, with a growth rate of 1.1.

NITA scheme was used as it results in significant computational savings (Menter, 2012). A 2nd order upwind discretization scheme was used for pressure, density and diffusion quantities and the least-squares cell based spatial discretization for the gradients. For the momentum terms, a central differencing scheme was used to limit the numerical dissipation in order to capture smaller structures relevant for the acoustics analysis.

A second order transient formulation was used for all the simulations. A time step of $\Delta t=10^{-5}s$ was employed in the simulation, it was found that the majority of the cells in the important flow regions had a CFL number smaller than unity, which guarantees the stability of the NITA scheme and follows best practices when using Scale Resolved Simulations (SRS) (Menter, 2012). Diffusion-based smoothing was applied for all the simulation cases, with a boundary-distance parameter equal to 1.5 for a greater preservation of the near-wall mesh.

The FH-W acoustic analogy was used for the far-field noise prediction. The acoustics data was acquired in all simulations for at least 20,000 time steps after a

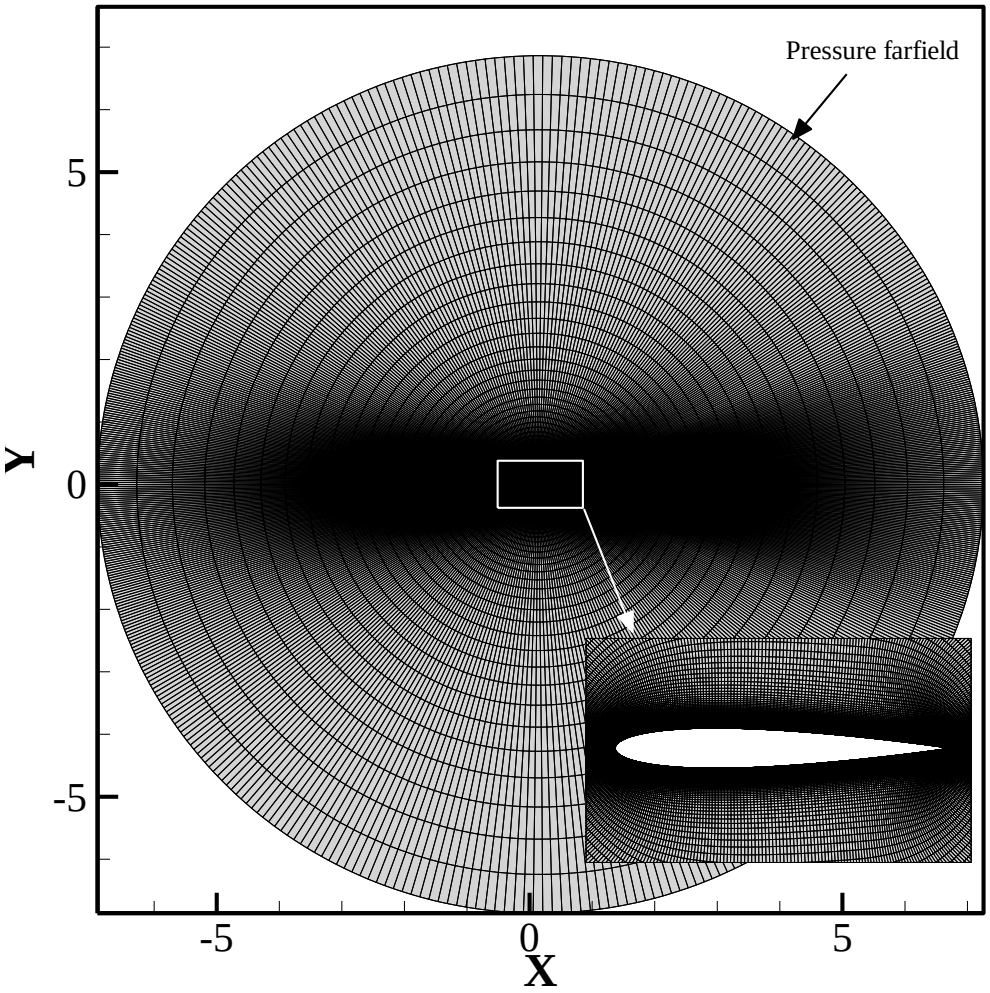

Figure 6.2: Details of the O-grid computational domain.

minimum of two flow-through times. In order to re-create the same setup as Brooks *et al.* (1989), the acoustic receiver was placed perpendicular to the airfoil TE at about 1.22 *m* away in all cases. Finally, the two-dimensional FW-H acoustic analogy implemented in Fluent needs a source correlation length as an input parameter to account for the spanwise direction of the airfoil in order to evaluate the integrals (ANSYS, 2018). This length is problem-dependent and usually can be obtained from empirical correlations or numerical experimentation *(*Kato *et al.*, 1993; Orselli *et al.*, 2009; Singer *et al.*, 2000). Numerical experimentations for the present case showed that a correlation length in the vicinity of 0.5*c* produced the best SPL levels for the main tones compared with Brooks' experiment (Brooks *et al.*, 1989).

6.6. Results and Discussion

6.6.1. Verification and Validation

Results from the previously mentioned cases are presented in the following. First, the 2D predictions of the unmorphed NACA 0012 are compared with Brooks' experiment and published 2D RANS results at Re = 0.62×10^6. This setup will be the one used later on for the harmonic morphing case study. The next section presents the results of a comparative study between the 2D results and 3D LES results obtained by Wolf *et al.* (2012) of the same setup as Brooks*'* experiment but at a slightly lower Re = 0.408×10^6.

Unmorphed case: M = 0.115, AoA = 4º, Re = 0.62×10^6

In order to establish mesh independency of the obtained results, three sets of meshes were investigated, and the difference in lift and drag coefficients was monitored. Results showed that the difference in lift coefficient between the fine and coarse mesh was less than 1%.

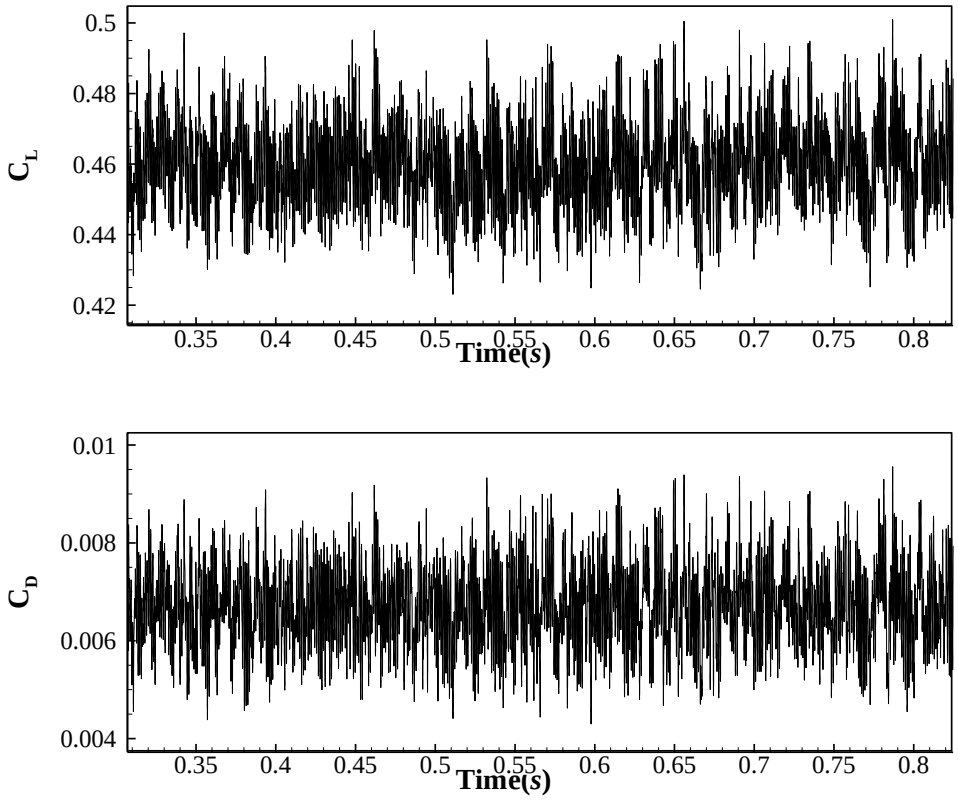

Figure 6.3: Time history of lift (top) and drag (bottom) coefficients for unmorphed NACA 0012 at AoA = 4º.

Figure 6.3 presents the instantaneous lift and drag coefficient data, the mean (time-averaged) values will be compared with published numerical results from an unsteady RANS study by De Gennaro *et al.* (2017) and with experimental results for a Reynolds number of 0.7×10^6 of Sheldahl and Klimas (1981). Table 6.2 summarizes the time-averaged aerodynamic coefficients compared with published data. The lift coefficients for all studies compare well. For the drag coefficient, the SBES and URANS results have a 5.33% difference. Compared with the experimental study, both SBES and URANS underpredict the drag by 9.63% and 12.34%, respectively. The presence of the LBL instabilities is confirmed by various fluctuations present on the suction side of the instantaneous pressure coefficient

plot (Figure 6.4). LBL instabilities move downstream to interact with the laminar separation bubble present near the TE on the pressure side.

This interaction gives rise to an acoustic source located in the near wake similar to what was proposed by Nash *et al.* (1999). Such interaction mechanism can be observed clearly in both vertical velocity and the Turbulent Kinetic Energy (TKE) contours (Figure 6.5).

Table 6.2: Comparison of time-averaged aerodynamic coefficients between current study and published data.

Coefficients	SBES	URANS	Experiment
C_L	0.45	0.46	0.44
C_D	0.0075	0.0071	0.0083

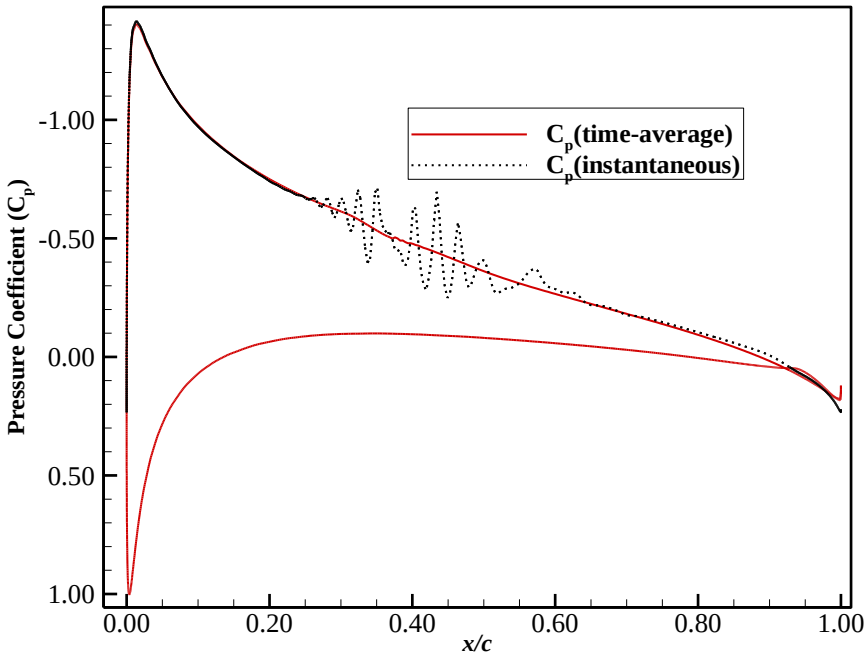

Figure 6.4: Instantaneous and time-averaged pressure coefficient for unmorphed NACA 0012 at AoA = 4°, showing LBL instabilities on the suction side.

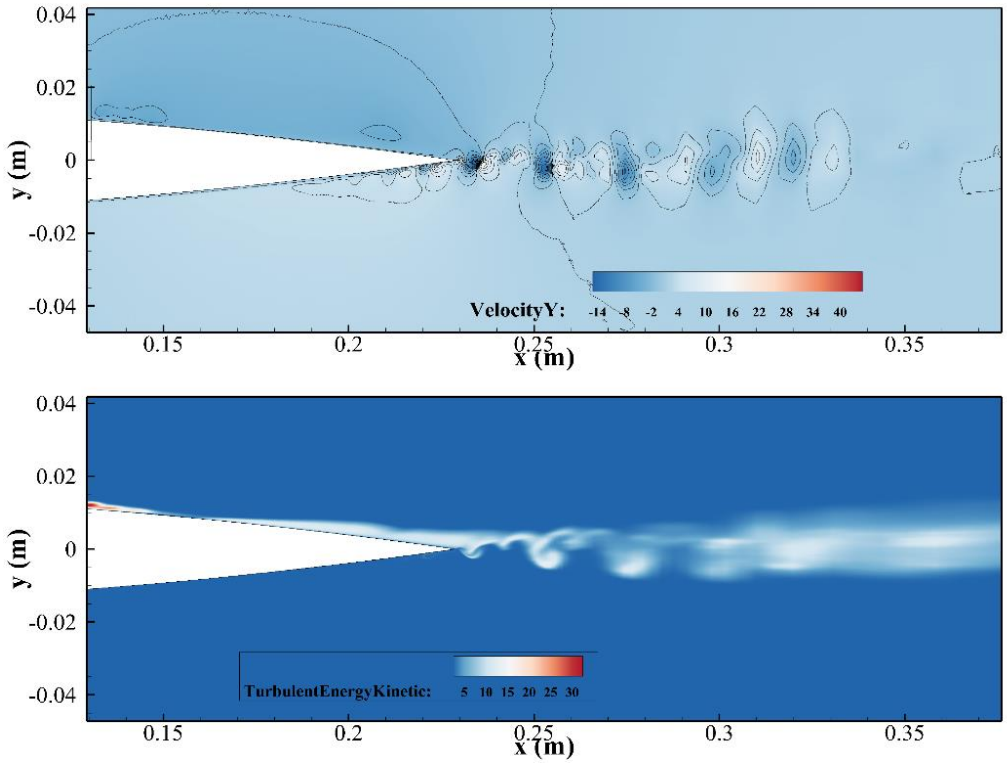

Figure 6.5: Vertical velocity contours (Up) and TKE contours (Down) showing instability regions on the

Figure 6.6 shows the Sound Pressure Levels (SPL) in one-third octave band ($SPL_{1/3}$) obtained using FW-H analogy for the three grids studied, compared with experimental results from *Brooks et al.* (1989) and URANS results of De Gennaro *et al.* (2017). The three sets of grids were able to show very similar behaviour when it comes to predicting the location and amplitude of the main tone and higher harmonic. The most prominent difference could be observed at higher frequencies, as the coarse mesh seems to overpredict the SPL compared with both the fine mesh and the experiment.

Overall, the 2D FW-H simulation was able to accurately replicate the main tone location (~1.6 *kHz*) and SPL (75 *dB* observed in the experiment), which is in accordance with the tonal structure expected from literature (Paterson *et al.*, 1973; Arbey and Bataille, 1983). Results obtained using SBES gave a slightly more

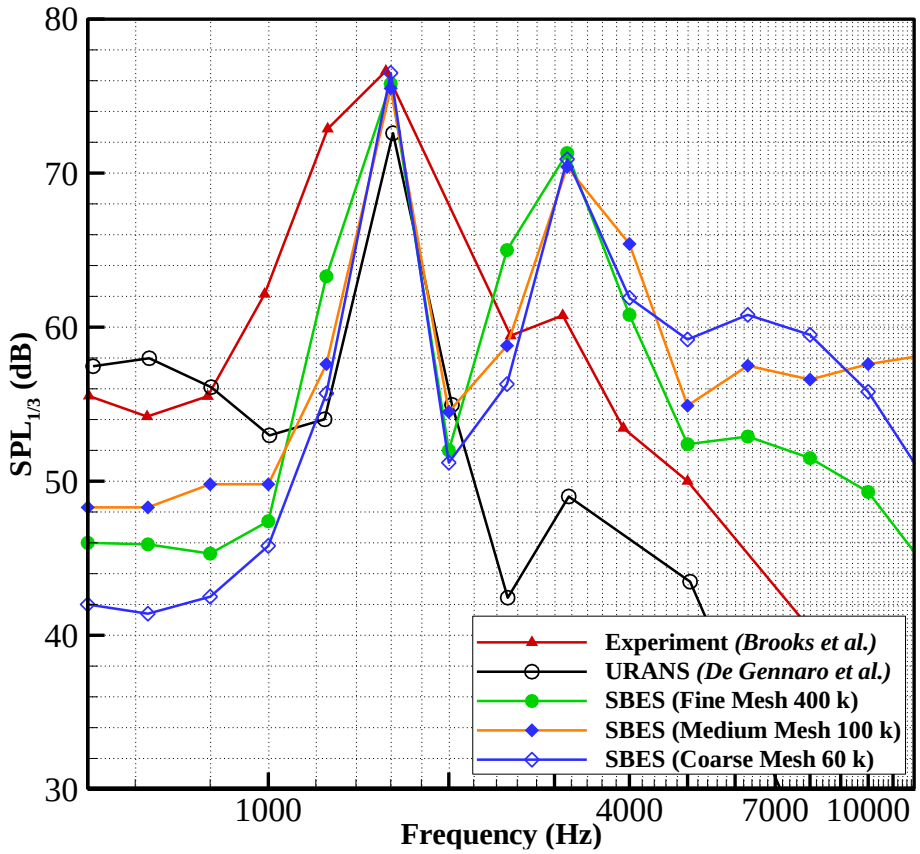

Figure 6.6: SPL in one-third octave band ($SPL_{1/3}$) for the coarse, medium and fine mesh using SBES compared with experimental data from Brooks et al. (1989) and URANS results from De Gennaro et al. (2017).

accurate sound level at the main tone compared with the URANS study. For the off-tone regions, both URANS and SBES cannot predict the broadband part of the spectrum, due to the turbulent boundary layer – TE (TBL-TE) noise generation mechanism being highly three-dimensional. This may explain the differences observed in the broadband spectra. A clear difference between the URANS and SBES can be seen at the higher harmonic location (~ 32 *kHz*), for which the URANS underpredicts the sound level whereas the SBES slightly overpredicts it.

The SBES overprediction might originate from the LES region of the flow, since the pressure fluctuations do not dissipate in the spanwise direction causing an overprediction especially in high frequency regions (corresponding to small turbulent eddies). A similar overprediction was observed in previous 2D studies (Kato *et al.*, 1993; Singer *et al.*, 2000; Trümner and Mundt, 2017). Finally, De

Gennaro *et al.* (2017) showed that the weight of the broadband component is negligible in the third octave band which might explain why the SPL of the main peak is not affected.

Unmorphed 2D vs 3D case: M = 0.115, AoA = 5º, Re = 0.408×10^6

This section presents the results of a comparative study performed for the purpose of gaining an additional understanding of possible differences between 2D and 3D predictions. Given the prohibitive computational cost of performing a 3D scale resolving simulation, the study conducted by Wolf *et al.* (2012) was replicated using 2D simulations. Wolf *et al.* (2012) performed a 3D simulation of Brooks's experiment using a compressible LES approach that required over 45 million mesh

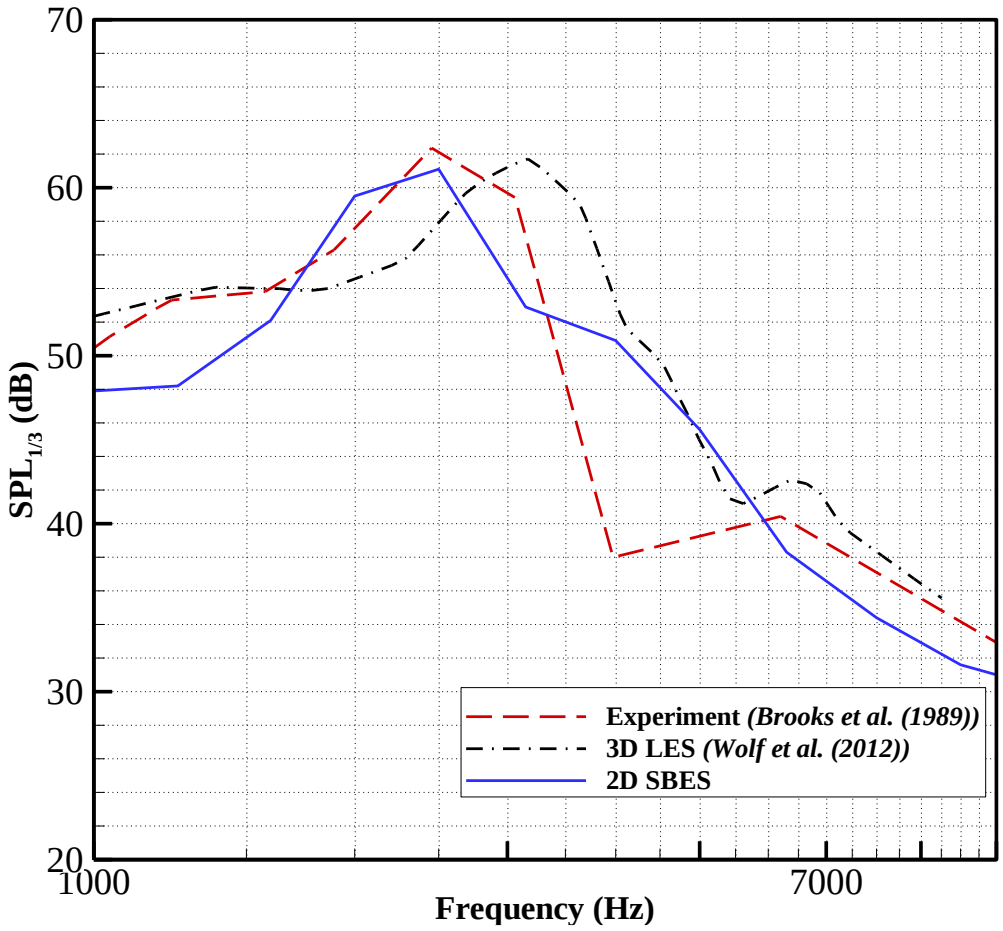

Figure 6.7: SPL in one-third octave band ($SPL_{1/3}$) for the 2D SBES predictions compared with experimental data from Brooks et al. (1989) and 3D LES results from Wolf et al. (2012).

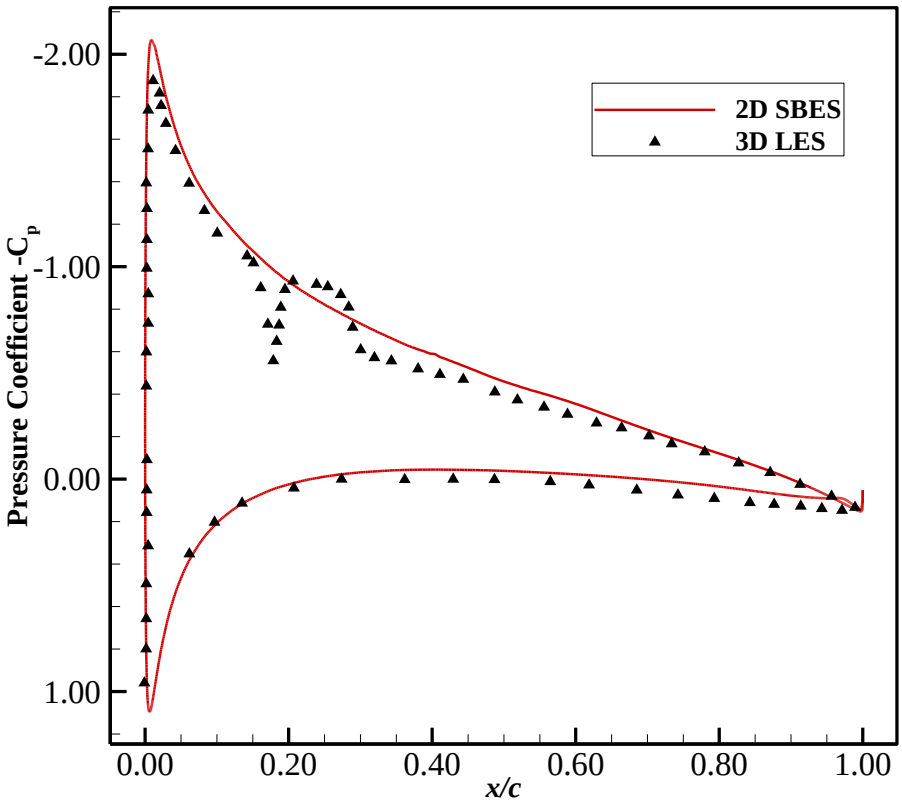

Figure 6.8: Time averaged pressure coefficient (-Cp) for the unmorphed NACA 0012 at AoA = 5º for 2D SBES predictions compared with 3D LES results from Wolf et al. (2012).

cells. For the 2D simulation, the same setup of the validation simulation was used, whilst ensuring to adjust the chord length in order to match the Reynolds number as in Wolf's work.

Figure 6.7 shows the Sound Pressure Levels (SPL) in one-third octave band ($SPL_{1/3}$) obtained using 2D SBES and the FW-H analogy compared with both experimental results (Brooks *et al.*, 1989) and the 3D LES results (Wolf *et al.*, 2012). The overall agreement between the 2D predictions and the experiment is satisfactory; the 2D simulation was able to predict correctly the location and SPL level of the main tonal peak at 2.5 *kHz* and a difference of 2 dB in SPL levels compared with the experiment. As expected, the broadband region shows a distinct discrepancy compared with the experiment. On the other hand, 3D LES results seem to predict well the broadband noise, yet a shift in the main tone peak location is observed in the 3D LES predictions (at ~ 3*kHz*). This difference between the 3D

LES and experiment could be explained by the tripping method employed in LES (suction and blowing near the LE) which was different from the experiment (trip wire).

Figure 6.8 shows a comparison between the time-average C_p obtained using the 3D LES simulations of Wolf *et al.* (2012) and the one obtained by the current 2D

SBES model. An overall reasonable agreement is observed between the two. However, the effect that the tripping has on the suction side is clear in the 3D LES results, this tripping mechanism affecting the boundary layer thickness could be the origin in the shift observed. Another variable in the 3D LES result is the use of a rounded TE instead of a sharp TE as in the experiment. The rounded TE maybe inducing recirculation areas around the TE region which would affect the TE tonal noise being generated, thereby contributing to the difference obtained by Wolf *et al.* (2012) in the tonal peak location. This is illustrated in Figure 6.9 where a side-by-side comparison of the time-averaged Mach number is presented showing the differences in TE geometry and flow behaviour between the two cases.

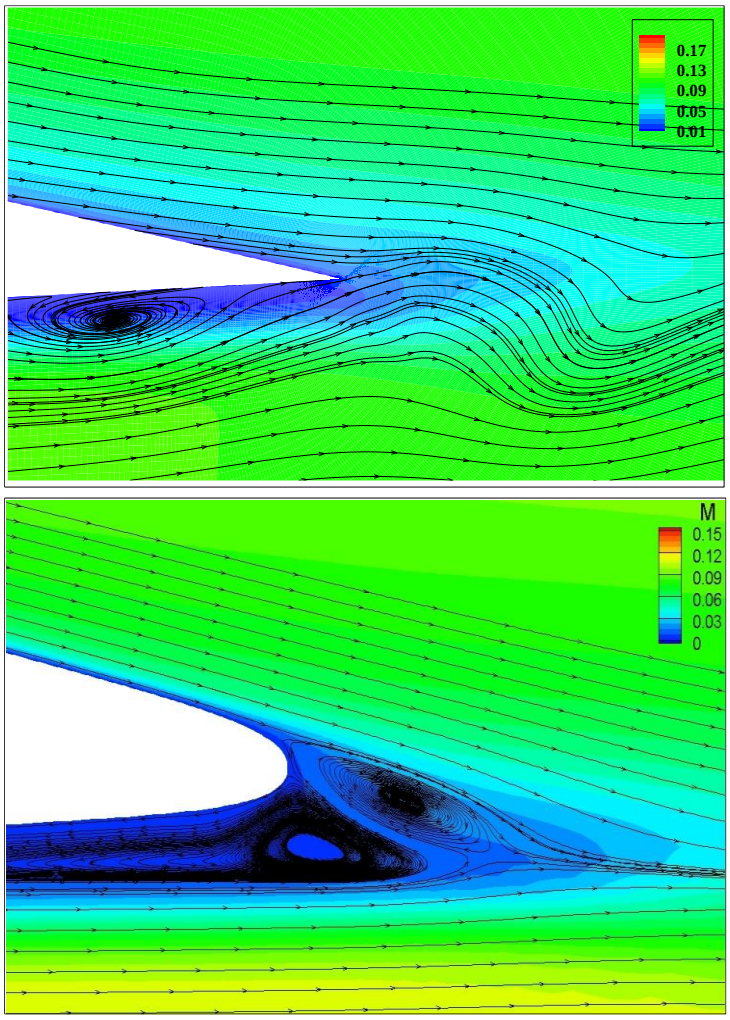

Figure 6.9: Time-averaged Mach number for the current 2D SBES prediction (up) and 3D LES results (down) from Wolf et al. (2012).

6.6.2. Harmonically Morphing Trailing-Edge Flap

Having established the validity of the current 2D approach in correctly predicting tonal noise, this section presents a preliminary aeroacoustic study of a NACA 0012 fitted with a harmonically morphing TEF in order to provide a practical example using the developed framework. The effects of harmonic morphing on the tonal noise are discussed afterwards.

Two case studies are considered: in the first case, the morphing frequency f was fixed at 100 *Hz* and two maximum deflection values were studied: $w_{te} = \pm 0.01\%c$ and $w_{te} = \pm 0.1\%c$. These deflection values were inspired by similar published tests

(Jodin *et al.*, 2017; Scheller *et al.*, 2015). In the second case, the frequency was modified to $f = 800\ Hz$ at $w_{te} = \pm 0.01\%c$ to compare it with the 100 *Hz* case and observe possible effects of changing the frequency for a fixed amplitude. All the numerical settings used are the same as the 0.62×10^6 unmorphed validation case; a statistically converged baseline NACA 0012 solution was obtained before engaging the dynamic meshing tool and starting the harmonic morphing after two flow-through time ($0.4\ s$).

Throughout the harmonic morphing cycles, the grid was preserved at high quality; the TEF deformation had no impact on the average values of the orthogonal quality and the cell equiangle skewness, the impact on the maximum values of these quantities was negligible (0.04% difference). A diffusion parameter of 1.5 was used which enabled the deformation to diffuse well in the farfield, keeping the mesh near the wall intact and thus guaranteeing a good resolution of the near-wall flow.

The time-averaged aerodynamic coefficients for the fixed 100 *Hz* case are practically unchanged at both amplitudes as only a 0.3% difference in C_L and C_D was obtained compared with the unmorphed baseline results. On the other hand, when the TEF is harmonically morphed at $f = 800\ Hz$, the average lift coefficient increased by about 0.7% while the drag coefficient decreased by 1.5 %, giving an effective increase in the aerodynamic efficiency (C_L/C_D) of about 3%. This confirms that in addition to effects on tonal noise, the harmonic morphing of the TEF could also result in some aerodynamic benefits for particular combinations of frequency and amplitude. Jodin *et al.* (2017) observed similar effects and demonstrated that a reduction in large-scale instabilities and the breakdown of the LCSs due to a morphing flap contributed to a 5% decrease in drag.

Figure 6.10 illustrates the acoustic pressure data collected at the receiver location for the cases studied. The pressure fluctuations appear to have similar amplitudes for all cases. A deeper comprehension can be gained from Figure 6.11 where the Power Spectral Density (PSD) plots obtained for the morphing configurations compared with the baseline NACA 0012 are presented. The main observation that can be drawn from the morphing cases and the baseline comparison is that the main

tone location associated with LBL-VS tonal noise is shifted to a higher frequency, from 1.6 *kHz* to about 2 *kHz*. In addition, sub-harmonics are captured clearly with higher PSD levels for the morphing cases at location 900 *Hz* which was not captured for the baseline study.

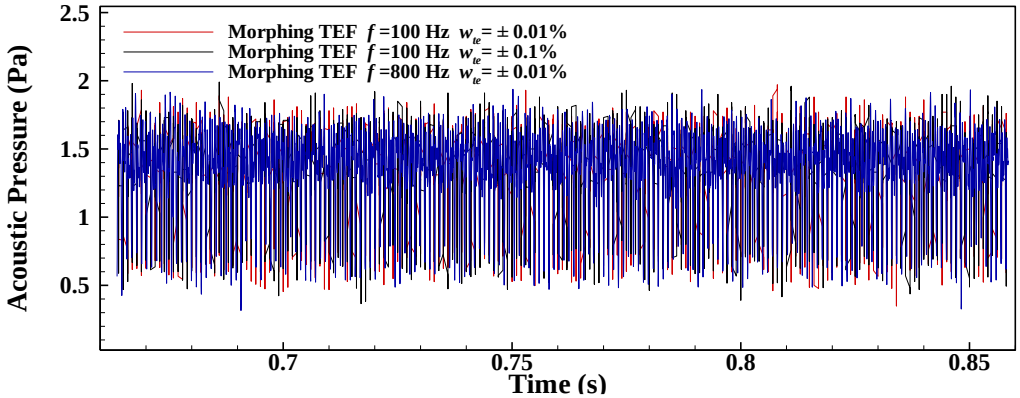

Figure 6.10: Acoustic pressure signal at the receiver for all the morphing cases.

When changing the morphing amplitudes from 0.01% to 0.1%, the peak associated with the morphing actuation frequency increases in power. The increase is proportional to the increase in morphing amplitude possibly due to larger amplitudes inducing more disturbances in the near-wake. This indicates that the morphing amplitudes could cause an increase in noise that is related to the physical oscillation.

Increasing the morphing frequency from 100 *Hz* to 800 *Hz* does not appear to have significant effect on the broadband region of the spectra. However, a sharp tonal peak is observed at the morphing frequency location, which indicates that the amplitude of 0.01% of the chord is possibly too small to cause any significant changes in the wake.

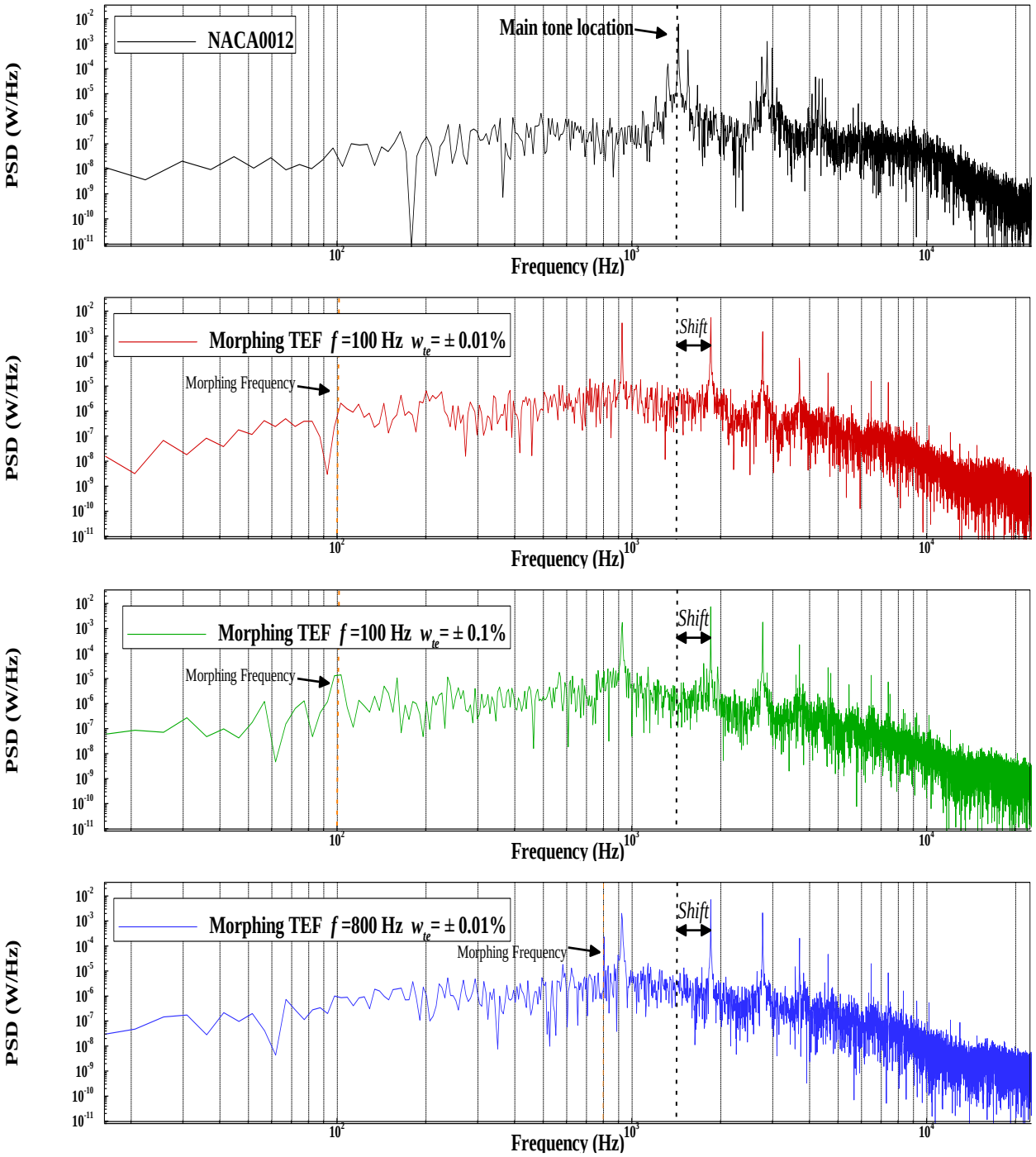

Figure 6.11: Power Spectral Density for the acoustic pressure signals obtained from FW-H simulation for all the morphing cases.

Figure 6.12 shows the SPL in one-third octave band comparing the baseline case and the morphing cases, confirming results presented in the spectral analysis of Figure 6.11. The effect of the 100 *Hz* morphing frequency on the spectra is similar between the two amplitudes, with the exception of a clear difference in the SPL levels near the 100 *Hz* location where the case with 0.1% amplitude seems to have a 9 *dB* higher SPL. The shift in the peak associated with the LBL-VS is clearly observed in the one third band plot, and a 1.5 *dB* noise reduction is associated with it. Possible explanations of these phenomena are discussed in the next section. Finally, the first superharmonic located at about 4000 *Hz* experienced a significant 10 *dB* reduction, compared with the first superharmonic captured in the baseline airfoil case.

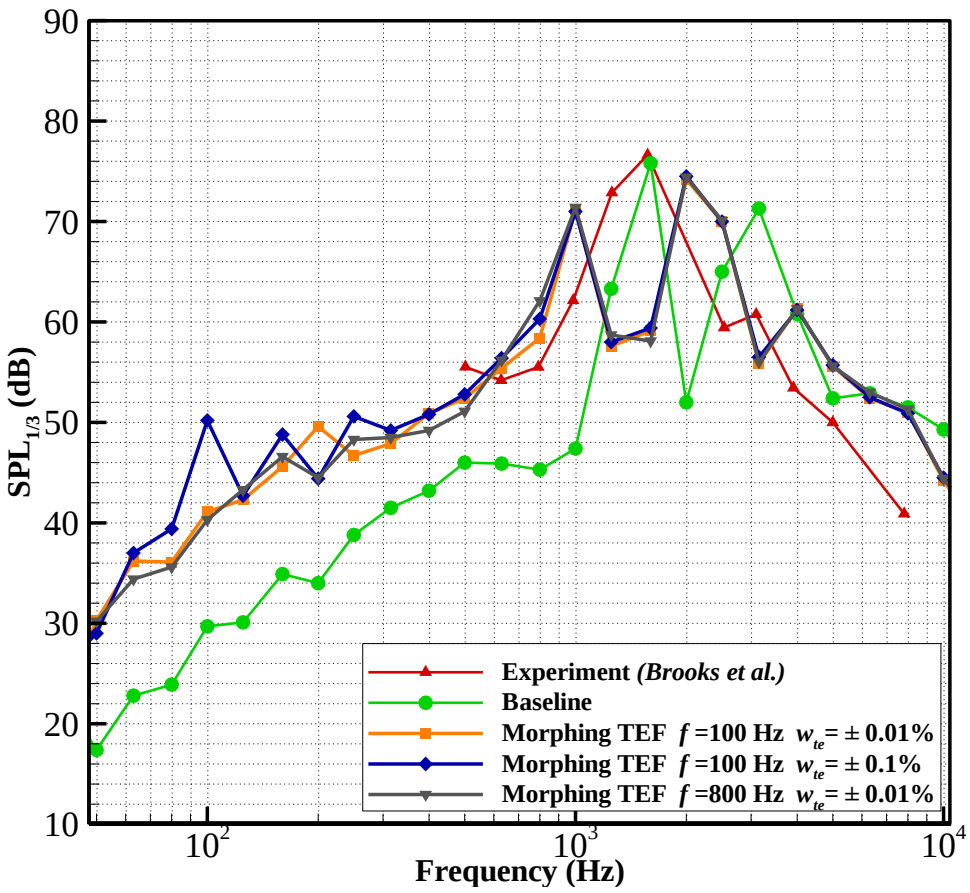

Figure 6.12: SPL in one-third octave band comparing the baseline NACA 0012 SBES results to the morphing TEF cases; wte =±0.01%, ±0.1%, for f = 100 Hz and 800 Hz. Experimental data from Brooks et al. (1989) is also plotted for reference.

Effect of Harmonic Morphing

The underlying mechanism causing the observed shift in the tonal peak, the SPL reduction and the increase in the aerodynamic efficiency is not yet clear from the current study. The decrease in drag indicates a change in the wake structure induced by the harmonic motion, which would possibly introduce a change towards higher frequency turbulent structures causing larger flow structures to break down at the TE. Similar effects on the drag were observed by Munday *et al.* (2013) when using active forcing to alter the wake structure. It was found that under certain conditions, the actuations reduce the drag and yield a more streamlined wake structure by elongating it. This occurred when the forcing frequency was chosen to be close to the natural shedding frequency, resulting in a lock-on effect. Nevertheless, the same study by Munday *et al.* (2013) observed instances where the actuation made the wake less streamlined and shortened, which increased the drag.

In the current study, the range of frequencies tested were all lower than the natural shedding frequency (1.6 *kHz*) which means that even if a lock-on took place, it was a lock-on with one of the subharmonics which would explain the observed behaviour. In order to acquire a fundamental understanding of this harmonic morphing mechanism and exploit it as an efficient active flow control method for both aerodynamic and aeroacoustic enhancement, it is necessary to study a range of forcing frequencies in both the lock-on and no lock-on regions. Of course, to do an in-depth analysis of the turbulent structures would require higher-fidelity 3D LES or even DNS, which is beyond the scope of the present study.

6.7. Summary

In this chapter, a framework to perform aerodynamic and aeroacoustic studies of harmonically morphing TEF was presented. It is based on a modified unsteady parametrization method defining the TEF motion, and dynamic mesh tools for mesh deformation. This framework can be applied to 2D and 3D problems; however, given the prohibitive computational cost of 3D simulations and the large number of possible parameters to consider, the study is restricted to 2D harmonic morphing and its effect on tonal noise.

A hybrid turbulence model, SBES, was used and its performance benchmarked for 2D cases. A 2D aeroacoustic study of an unmorphed NACA 0012 airfoil was also performed using the developed framework. Results compare well with published numerical and experimental data. It was found that the SBES model was able to accurately predict the location and amplitude of the main tone frequency related to the laminar boundary-layer instabilities. The structure of the main tone captured is also in good agreement with published literature. In addition, a comparative study between 2D SBES predictions and published 3D LES results was conducted. It was found that the 2D simulations capture well the tonal noise given its pseudo 2D generation mechanisms.

Results for three morphing configurations were presented. Two morphing amplitudes of 0.01% and 0.1% at a fixed frequency (f =100 *Hz*,), then the amplitude was fixed at 0.01% and two frequencies studied (100 *Hz* and 800 *Hz*). It was found that up to 3% increase in aerodynamic efficiency was possible using the 800 *Hz* frequency, whereas the 100 *Hz* frequency had negligible impact on the aerodynamic efficiency.

In terms of aeroacoustic effects, the morphing TEF appears to shift the main tone to a higher frequency (from 1.6 *kHz* to 2 *kHz*) with a noise reduction of 1.5 *dB* for the main tone and up to 10 *dB* for the first superharmonic. The underlying mechanism causing these effects is still unclear but a possible lock-on with a subharmonic could be the cause for the change in the wake structure producing the observed frequency shift and drag reduction.

The next chapter will supplement the framework developed in chapter 4, and applied in chapter 5 on 2D downward morphing flap, by expanding it to include the analysis of a realistic 3D morphing wing with seamless side-edge transition and downward morphing flap. This would enable a direct comparison between 2D and 3D predictions and identify possible differences between the two approaches.

“The error therefore lyeth neither in the abstract nor in geometry, nor in physicks, but in the calculator, that knoweth not how to adjust his accompts.”

Galileo Galilei, 1632

7. Morphing Wing with Seamless Side-edge Transition

Chapter 7

Contents

7.1. Overview

The aim of this chapter is to extend the work done in Chapter 4 from 2D to 3D. First, the problem defined in section 7.2. Then in section 7.3, a parametrization to model a morphing wing with seamless side-edge transition is introduced. Additionally, a comparative steady CFD analysis between a wing equipped with a morphing TEF and seamless transition (i.e. statically morphed), and a wing with a conventional hinged flap and unsealed side-edge gaps is performed. Finally, a study of a dynamically morphing TEF with a seamless transition is presented and comparison between 2D and 3D configurations is given.

7.2. Problem Definition

Most studies to date have simplified flap side-edge morphing problems to static morphing, thereby overlooking the dynamic effects that the deforming motion of both the flap and of the side-edge transition might have on the flow field, or its contribution to the airframe noise. In chapter 4, we introduced a framework to study dynamically morphing airfoils by modifying a parametrization method to include time, and integrating it within the commercial software ANSYS Fluent with the help of a UDF. Nevertheless, to capture the physics of a real-life morphing wing, the problem needs to be extended to 3D, taking care of modelling the wing's deformation in 3D particularly the seamless side-edge transition.

In this chapter, a comparative steady CFD analysis between a wing equipped with a morphing TEF and seamless transition already deflected (i.e. statically morphed), and a wing with a conventional hinged flap and unsealed side-edge gaps is presented. The seamless transition is based on the recent concept introduced by Woods *et al.* (2016) (Figure 2.32) which still lacks a comparative performance analysis.

Secondly, a modified transition function will be introduced to model the transition between the static and morphing part of the wing. Then, the aerodynamic performance of the dynamically morphing TEF is investigated for three morphing frequencies, and results are compared with the ones obtained in the 2D analysis in previous chapters.

All configurations were studied at flow conditions similar to previous chapters (Re = 0.62×10^6, Mach number of 0.115). A range of Angles of Attack (AoA) from 4º to 14º was considered for the steady analysis and the results at AoA = 6º and 8º are presented for the dynamically morphing TEF for three frequencies 4 *Hz*, 6 *Hz* and 8 *Hz*.

7.3. 3D Extension for the Unsteady Parameterization

In order to model the deformation of the wing, it is important to define time dependant the mathematical formula that analytically models such deformations. For the present problem, two parametrization methods are required. The TEF deformation is parametrized using the modified method used in chapter 4. The unsteady camber distribution (Eq 4.1) is added to the NACA 0012 thickness distribution (Eq 3.46) in order to obtain the desired deformation.

Moving from 2D to 3D raises the issue of implementing an unsteady parametrization to model the side-edge transition between the morphing and non-morphing parts. Woods *et al.* (2016) proposed a simple parametric formula (Eq. 7.1) which yields a smooth continuous profile suitable for our application but viable only for the static cases:

$$w_{te}(\bar{z}) = h.\cos\left(\frac{\pi\bar{z}}{l}\right) - h \tag{7.1}$$

where $w_{te}(\bar{z})$ is the vertical TEF displacement for the transition part, $\bar{z}$ is the non-dimensional transition distance along the span and h is the half-amplitude of the control surface deflection.

In the camber distribution, defined in Eq 4.1, w_{te} is a constant and does not change, but when a seamless distribution is required. The vertical displacement of the TEF becomes dependent on the spanwise coordinates $\bar{z}$. Therefore, the unsteady camber distribution for the seamless transition portion ($\bar{x} \geq x_s$) during morphing ($t_{start} \leq t \leq \frac{T}{4}$) is written as the following:

$$y_c = \begin{cases} \dfrac{-w_{te}(\bar{z}).\sin\left(\frac{2\pi(t-t_{start})}{T}\right)(\bar{x}-x_s)^3}{(1-x_s)^3}, & tr_{start} \leq \bar{z} \leq tr_{end} \\ 0, & \bar{z} \leq tr_{start} \; or \; \bar{z} \geq tr_{end} \end{cases} \tag{7.2}$$

where t is time and T is the complete period of the TEF motion, tr_{start} and tr_{end} are the transition start and end location respectively. At $t = t_{start}$ the morphing

commences and the baseline is deflected until it reaches the maximum deflection value of *h* thus simulating the deforming motion. The morphing flap used the same camber definition as in Eq 4.1.

Figure 7.1 illustrates the final geometry resulting from the implementation of the 3D parametrization method, from three point of views. The figure clearly illustrates the gradual morphing from the baseline wing (left) to the final morphed wing with a seamless side-edge transition (right).

7.4. Computational Setup

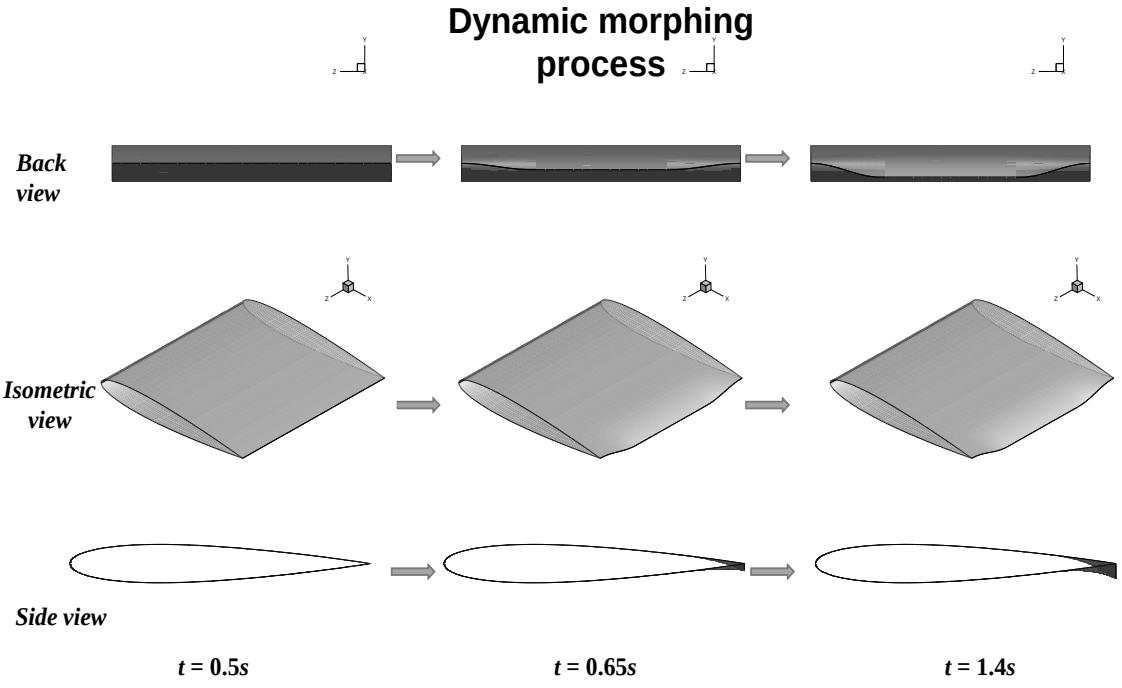

Figure 7.1: Illustration showing the dynamic morphing process driven by the modified unsteady parametrization method.

7.4.1. 3D Steady RANS of a statically morphed TEF vs a hinged flap

To check the superiority of the morphing flap design compared with the traditional one, an analysis is performed to study the differences in the aerodynamic behaviour between a seamless transition flap with sealed side-edge gaps and a conventional

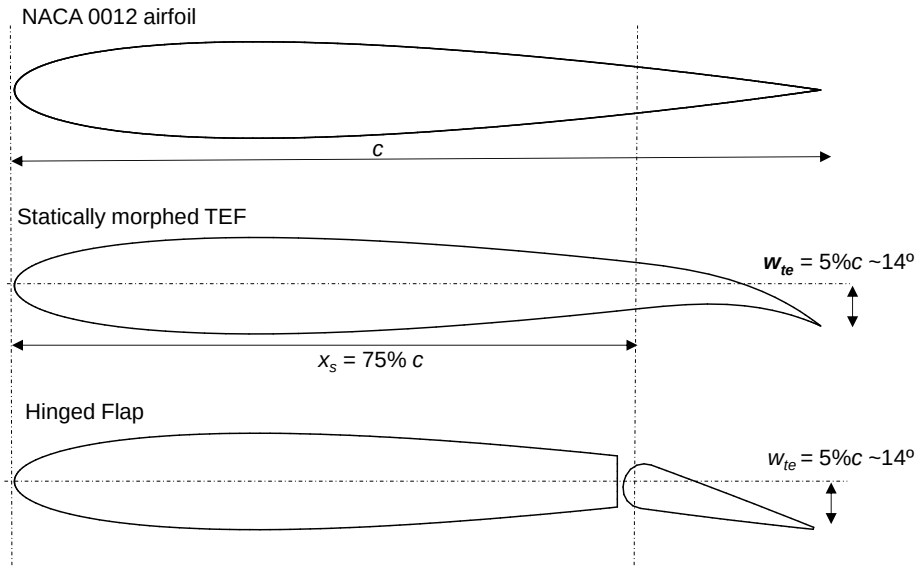

Figure 7.2: Mid-span slices showing the configurations studied and their dimensions.

hinged flap with a gap. A rectangular NACA 0012 wing demonstrator with a chord c = 0.2286 m and a span S = 0.2286 m was investigated. The statically morphed TEF with the transition portion was set to be 40% of span with 5% allocated to each side of the transition. The same proportion (40%) is used for the wing with the hinged flap, where all side-edge gaps have a width of 1% of the chord c. Both wings were deflected to the same position, a vertical distance of 5% of the chord (approximately equal to 14º flap deflection angle). To gain further insight on how the flaps affect the performance, steady state CFD was also performed for the baseline NACA 0012 wing. Figure 7.2 summarizes all configurations studied while Figure 7.4 illustrates the 3D view of the morphed and hinged flap concepts.

It is worth mentioning that a plain flap design for the hinged flap was chosen in order to provide similar size to the morphing TEF even though it is not the optimal aerodynamic design as opposed to built-in or split flaps for instance.

A steady state RANS study using the software package ANSYS Fluent was conducted for the cases mentioned with a series of grids generated around each configuration with the number of cells ranging between 1.5-2 M, and refinement

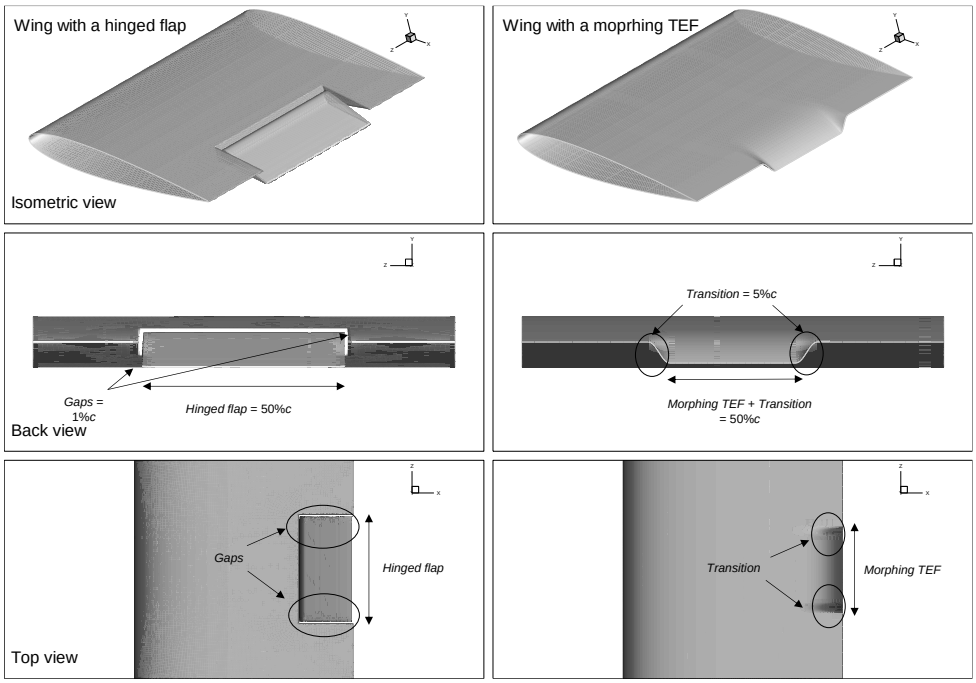

Figure 7.4: 3D models of the statically morphed wing and the hinged flap wing from various views.

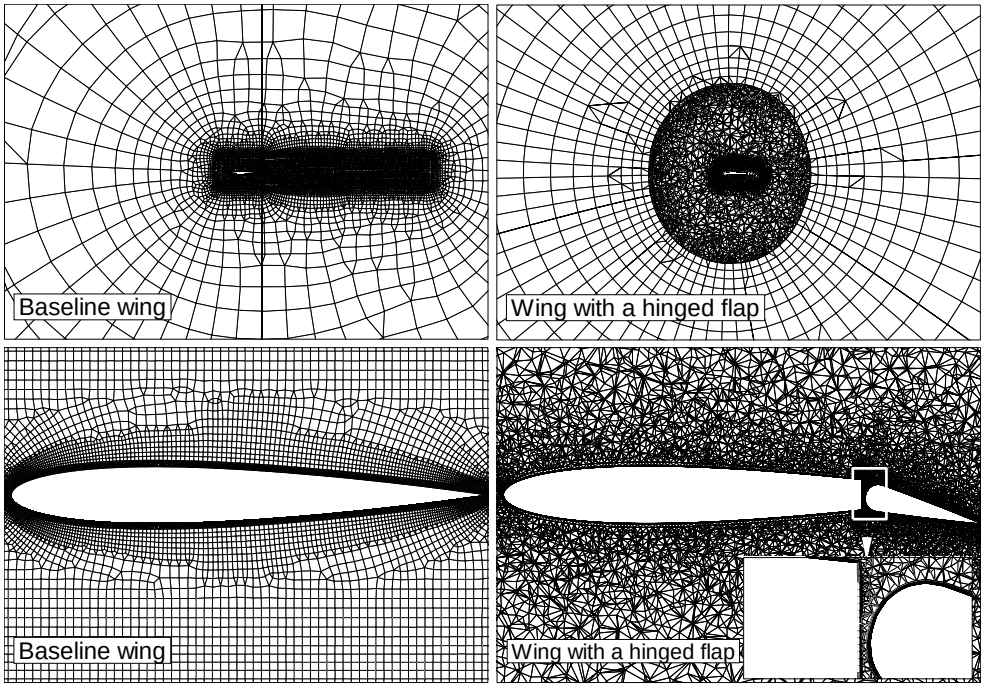

Figure 7.3: Computational domains used for the steady RANS and a close-up of the baseline NACA0012 wing, (a) hinged flap wing (b).

regions placed around the wing and wake region. The farfield was placed at least 15 chord lengths away from the wing's TE. A maximum near-wall first-layer grid resolution of $y^+ < 1$ was targeted. Hybrid grids (consisting of prism layer covering the boundary layer and tetrahedral elements outside) were favoured for cases where the geometries had gaps or if the geometry was deforming. Hybrid meshes are faster to generate while keeping good mesh quality metrics. Furthermore, having tetrahedral elements offers the possibility to use local re-meshing to remove skewed elements. Finally, a structured C-grid was used for the statically morphed wing giving the relative simplicity of the geometry. Figure 7.3 illustrates the computational domains used.

The pressure-velocity coupling is achieved using the coupled algorithm; the least squares cell based spatial discretization was used for all gradients. Moreover, the intermittency k-ω SST model was used for turbulence closure; a 2nd order upwind scheme was utilized for the momentum and turbulence equations discretization. In order to eliminate possible influence of wing tip vortices in this analysis, the wing was modelled as a semi-infinite wing where the width of the domain matches the span of the studied wing, and a symmetry boundary condition was imposed on the sidewalls of the domain. All simulations were run until the C_L, C_D statistically converged, and all the residuals dropped below 10^{-5}.

7.4.2. Unsteady RANS and dynamic meshing

The unsteady RANS was performed using the baseline mesh generated for the NACA 0012 wing at AoA=6º and 8º, it was initialized from converged steady state simulation results, and run until both C_L and C_D statically converged before engaging the dynamic meshing solver and starting the wing deformation.

In order to deform the mesh, diffusion-based smoothing was applied. Diffusion smoothing was chosen given its capability of better preserving mesh quality compared with other smoothing schemes (ANSYS, 2018) despite its higher computational cost compared with the spring-based smoothing for instance. In addition, re-meshing was used for cells having a skewness greater than 0.8. Figure 7.5 shows the mesh before and after the deformation of the TEF.

All the solver settings were similar to the steady analysis, additionally a 2nd order transient discretization was used with a time step $\Delta t = 10^{-4}s$ with a maximum of 20 iterations per time step and residual criteria of 10^{-5}.

7.5. Results and Discussion

7.5.1. Baseline comparative study

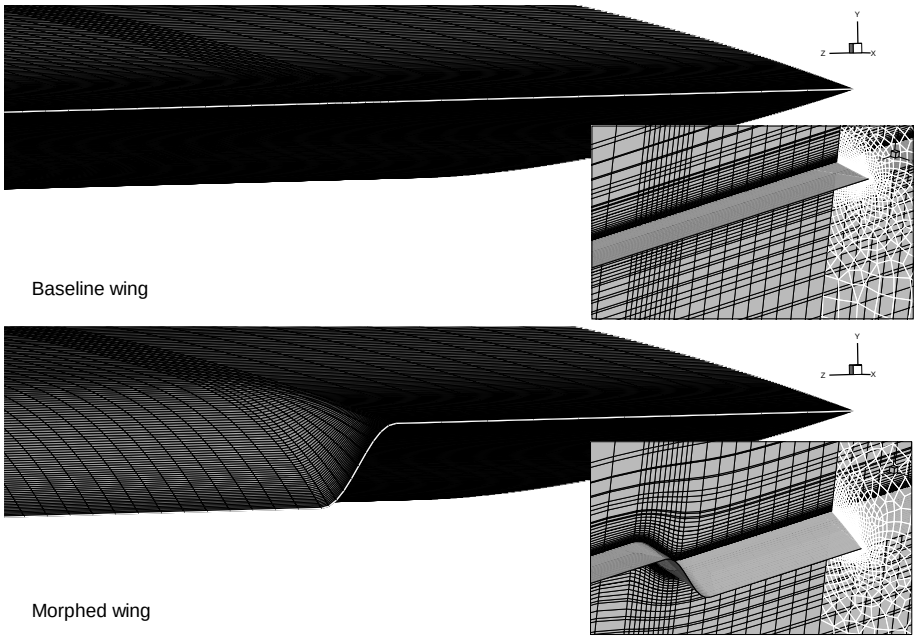

Figure 7.5: Direct comparison between the baseline mesh (upper) and the mesh after the TEF deformation (lower).

The lift and drag coefficients are plotted in Figure 7.6, for the baseline NACA 0012 wing compared with numerical results obtained for the NACA 0012 airfoil using Fluent (results from Chapter 4) and XFOIL. In addition, wind tunnel results of a 2D NACA 0012 wing with side plates at similar Re number (~0.7×10^6), are plotted for reference.

Both lift and drag results from the baseline NACA 0012 wing compare well to the 2D numerical predictions and wind tunnel tests, especially in the linear region of the flow. However discrepancies appear near the stall region as explained in

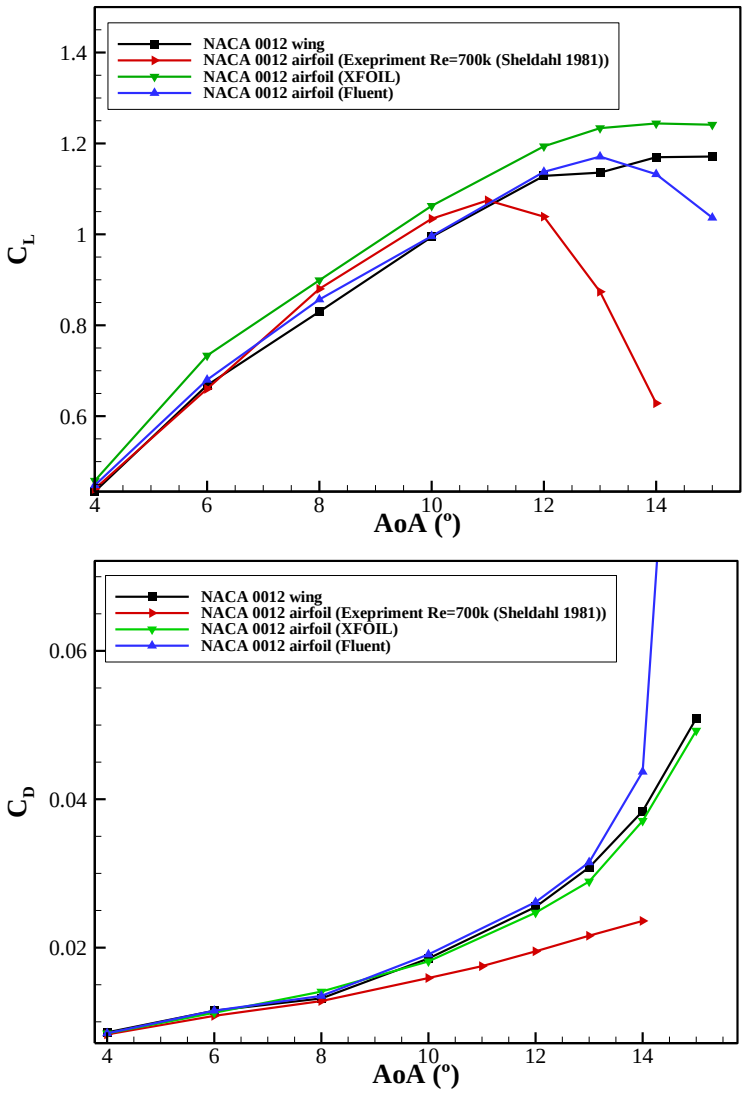

Figure 7.6: C_L and C_D results for the baseline NACA 0012 wing compared with numerical results obtained for the NACA 0012airfoil using Fluent and XFOIL in addition to experimental results for the NACA 0012 airfoil from Sheldah al. (1981).

Chapter 4 the experimental results produced by Sheldahl *et al.* (1981) predicts an early stall at AoA = 11º. In contrast, all numerical simulations predict a higher stall AoA: the 2D unsteady Fluent results predict stall at AoA = 13º whereas the steady NACA 0012 wing predictions and XFOIL do not predict the stall before the maximum AoA = 15º studied. This may be expected due to the numerical damping which characterises steady analysis as it tends to capture the mean flow rather than resolving smaller scale unsteadiness which is reflected in the later stall captured.

Drag coefficient predictions show also good agreements between 2D and 3D predictions in the linear regions up to AoA = 13º where discrepancies grow larger as the airfoil enters stall.

7.5.2. Statically morphed TEF vs hinged flap

Figure 7.7 shows comparative results for C_L and C_D and the aerodynamic efficiency (C_L/C_D) for the baseline NACA 0012 wing, the wing equipped with a morphed flap and the one with a hinged flap in addition to the 2D prediction of an airfoil with a morphed TEF.

Comparing the aerodynamic performance of the wing equipped with the TEF and a seamless transition with the traditional hinged TEF gives an insight into their behaviour. When it comes to lift generation, the morphed wing unfailingly produces an average of 22% higher lift compared with the hinged flap configuration for a constant drag reduction for the morphed wing of 25% throughout the AoA in the pre-stall compared with the hinged flap configuration.

Another key difference between the two configurations is that the wing with a hinged flap experiences an earlier stall characterised by the drop in the lift coefficient at AoA = 12º whereas the morphed flap enters the stall region at AoA

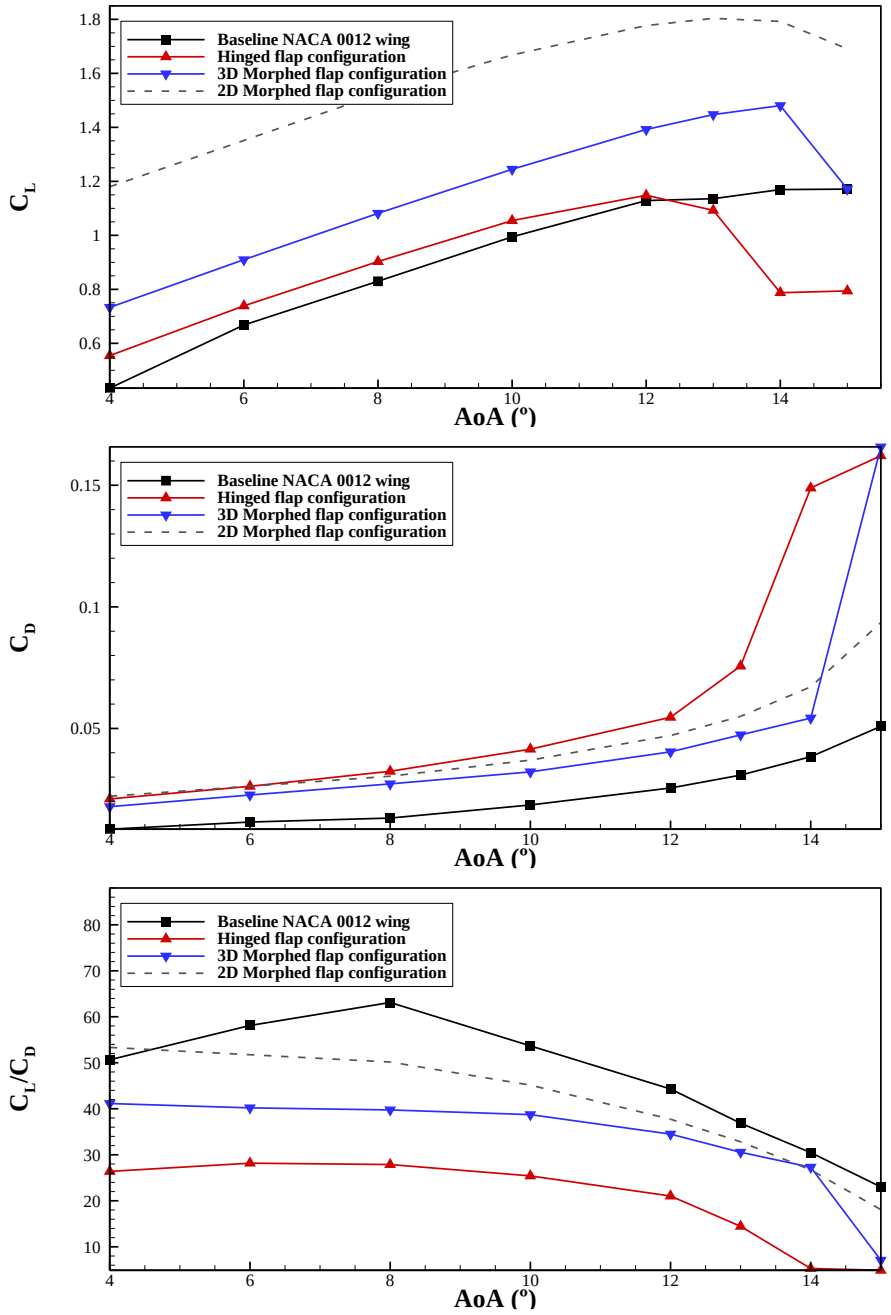

Figure 7.7: Comparative results for C_L and C_D and the aerodynamic efficiency (C_L/C_D) for the baseline NACA 0012 wing, the wing equipped with a morphed flap and the one with a hinged flap in addition to the 2D prediction of an airfoil with a morphed TEF.

= 14º where a drop in the lift coefficient is also observed with a sharp increase in the drag coefficient.

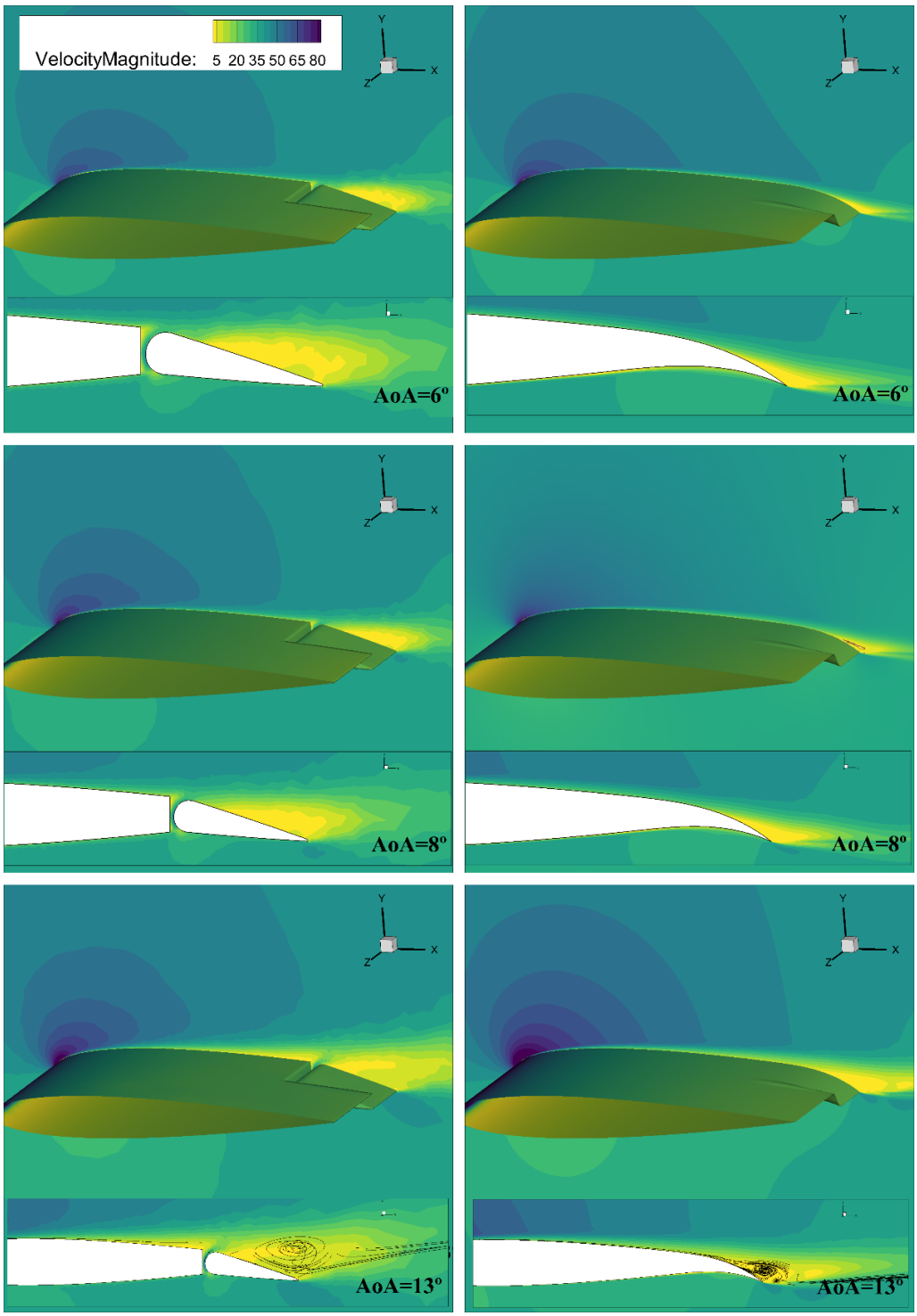

Figure 7.8: Velocity contours comparison at mid-span between the wing with the hinged and a morphed TEF at AoA = 6º, 8º and 13º. The close ups show the side view at mid-span for both configurations.

Compared to the baseline wing both wings, equipped with hinged or morphed TEF, produce higher lift and experience stall earlier than the NACA 0012 wing, which is expected as the flaps induce a higher camber pushing back the stall AoA while increasing the produced lift.

The large difference in the lift produced could be explained by the fact that the morphed wing has two side transition portions deflecting with the flap, creating additional deflection in the camber. This contributes to the extra lift to some extent, whereas the side edges of the hinged flap are static which does not contribute to lift as much as the seamless transition.

Likewise, the presence of the gaps in the hinged flap wing induces extra recirculation areas and cavity flows between the gaps while reducing the effective lifting surface. Such effects are particularly significant for the main gap present between the wing and the flap, which gets larger the more the flap is deflected; this may explain the lower aerodynamic efficiency observed for the hinged flap.

Figure 7.8 illustrates the differences observed between the wing with the seamless transition and the one with a hinged flap at three AoA. Recirculation regions are clearly shown in the velocity contours, and the higher the AoA the larger those regions are. Unlike the wing with the seamless transition, a separation region on the pressure side of the flap seems to be constantly present, growing larger at higher AoA. In contrast, the velocity field distribution is smoother around the morphed wing. The close ups within Figure 7.8 show the presence of flow leakage through the gaps in the hinged flap configuration with a jet flow emanating from the main gap and increasing in strength with higher AoA.

Figure 7.9 further illustrates the differences between both configurations. Velocity vectors clearly demonstrate the effect of the presence of the flap side-edge gaps, side tip vortices are forming at the tips of the flaps and due to the pressure leakage between the suction and pressure side of the wing, flow is rapidly drawn into the gaps creating local jet flows on the suction side. The bottom of Figure 7.9 shows that the wake of the configuration with the hinged flap is more energized and

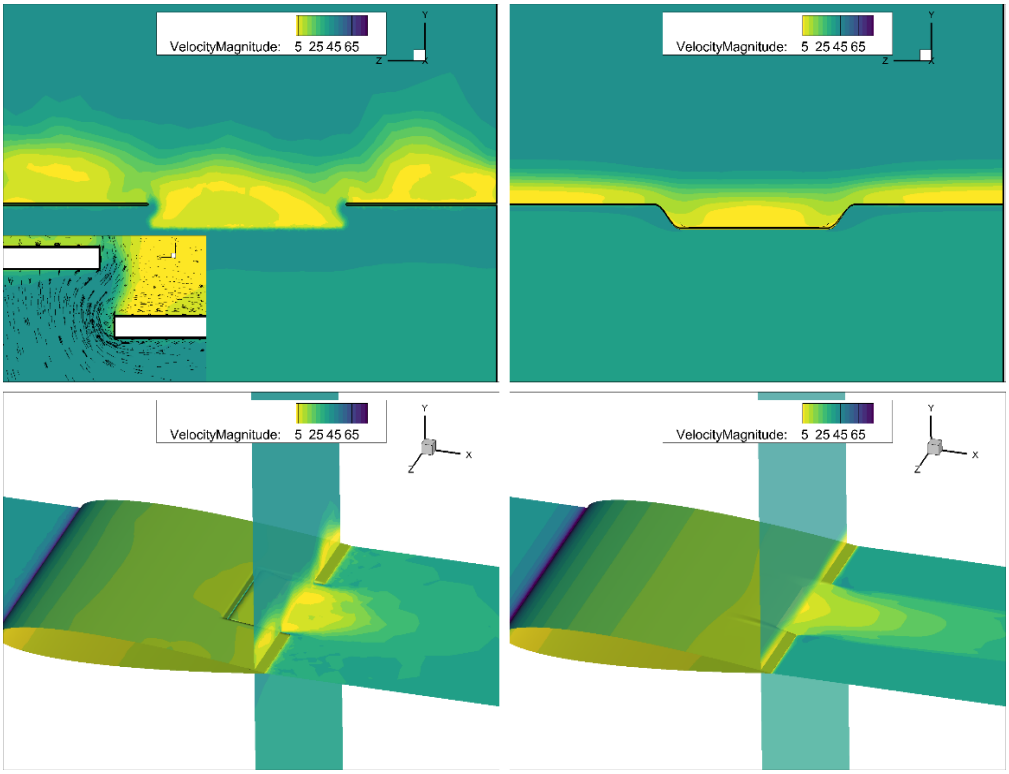

Figure 7.9: Top: Velocity contours and vectors of the wing with a morphed TEF flap (top right) compared with the one with a hinged flap (top left) on a plane placed at x=0.99c at AoA= 13º. Bottom: wake flow structure visualisation by means of velocity contours with a slice at y=0 and x=0.95c.

turbulent compared with the morphed wing. The side-edge vortices seem to roll to the static sides of the wings triggering more turbulent flow to develop whereas the seamless side-edge transition appears to allow a more orderly development of the flow which may contribute to drag reduction observed.

Figure 7.10 and Figure 7.11 give a deeper insight into the behaviour of the flow around the configurations studied by presenting the C_p and C_f distributions at the mid-span location, and at x = 0.80 c location (close after the gap at 0.75c).

At the mid-span location (z = 0.5 S) a direct comparison between the FishBAC morphed flap concept and a hinged flap can be made. The C_p is larger around the entire morphed section for all three AoA which explain the extra lift generated compared with the hinged flap case (Figure 7.6). Two peaks are noticeable in the pressure distribution of the hinged flap case near the location of the gaps, indicating the presence of the jet flow coming from the pressure side to the suction side

through the gaps. This behaviour could also be clearly detected from the C_f plots as well where the separation is characterized by peak near the gaps.

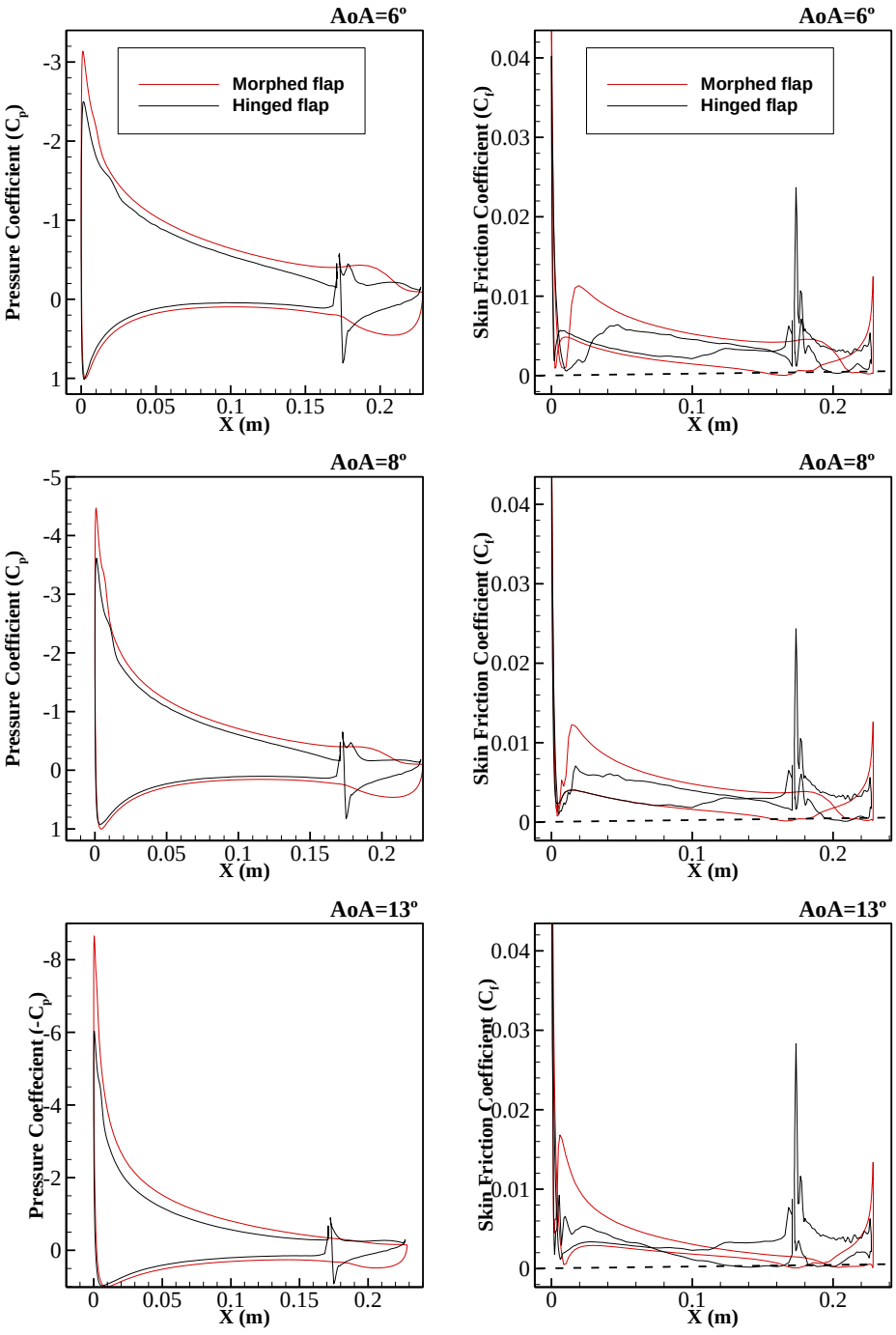

Figure 7.10: C_p and C_f comparison between the wing with a morphing TEF and seamless transition and the wing with a hinged flap, mid-span location at AoA =6°, 8° and 13° from top to bottom.

Differences in C_p distribution are not only present near the flap region, but also on the main wing where the distribution is larger for the wing with a morphed TEF

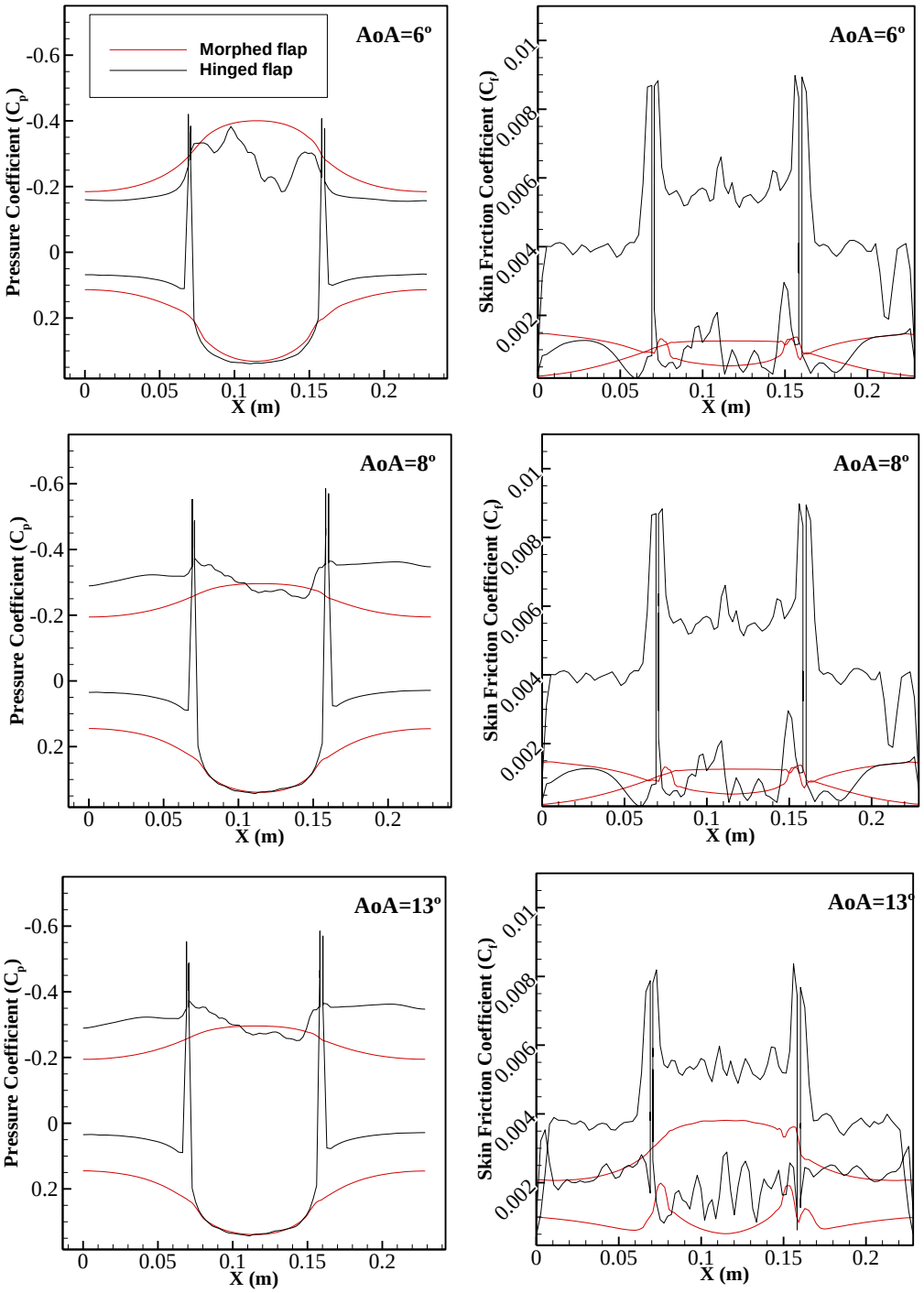

Figure 7.11: C_p and C_f comparison between the wing with a morphing TEF and seamless transition and the wing with a hinged flap, x = 0.8c location at AoA =6°, 8° and 13° from top to bottom.

indicating that the perceived camber for the morphed flap is greater from the hinged flap case.

From the C_f plots sharp peaks associated with the separation happening near the main gap characterizes the distribution of the hinged flap configuration whereas the transition from the main wing of the morphed flap occurs smoothly which is the main reason the wing with a seamless morphed TEF produced an average of 2% less drag.

Figure 7.12 shows C_p and C_f in the spanwise direction at $x = 0.8c$ which is located shortly after the flap starts at x = 0.75*c*. This graph gives a clear illustration of the differences a seamless transition and an unsealed side-edge flap could produce. The morphed flap C_p distribution is continuous and exhibits an overall similarity in size between the two configurations with the peaks produced because of the unsealed gaps. The increased contribution of the side-edge seamless transition to the lift is clearly shown for the static side-edge as well.

Finally, when it comes to C_f a large difference in size is observed, the hinged flap distribution is larger and overall more turbulent (as exhibited by the oscillation in the C_f distribution). This large difference could be because the configuration chosen for this study is a simple flap, not an enclosed flap or traditional high-lift device. This makes the main gap more influential, triggering the separation over the discrete flap (as clearly observed in the velocity contours of Figure 7.12) which contributes to the extra drag observed and overall loss in the aerodynamic efficiency.

2D and 3D static morphed flap comparison

As Chapter 4 and 5 dealt exclusively with 2D morphing configurations, it would be useful to compare 2D and 3D approaches to comprehend the differences that

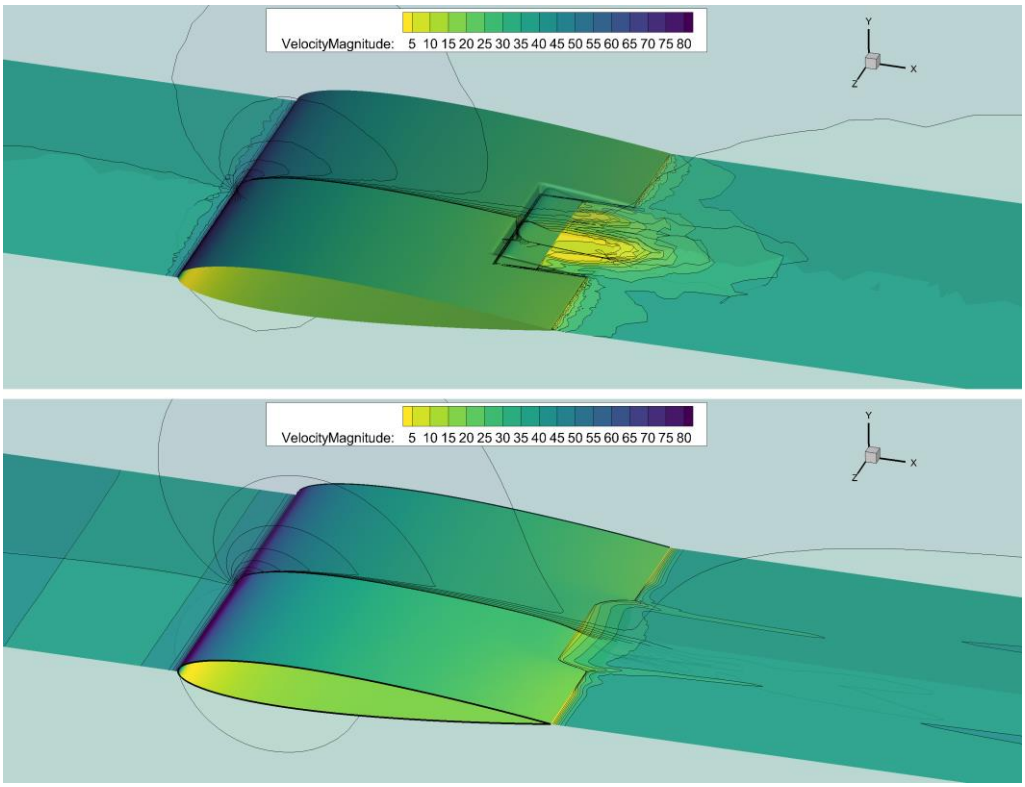

Figure 7.12: Visualisation of flow separation by means of velocity contours with a slice at y=0 and x=0.95c comparing the wing with a morphing TEF and seamless transition (bottom) and the wing with a hinged flap (top).

might arise from the simplification of a 2D studies as opposed to more realistic 3D depictions of morphing concepts.

Figure 7.6 shows the predictions of the 2D morphed flap compared with the 3D morphing wing with the seamless side-edge transition. It is not a surprise that the 2D predictions estimate a higher lift by over 40% compared with the 3D predictions. This is mainly because a 2D simulation assumes that in the spanwise direction the entire span is a flap whereas in the current 3D simulation only 40% of the span is a morphing flap in addition to the seamless transition.

Similar remarks could be made when it comes to the drag coefficient prediction; the 2D simulation overpredicts the drag by as much as 34% due to the same reasons explained for the lift. Nevertheless, it is worth mentioning that 3D effects are included in the 3D prediction of the seamless morphing wing, such as flap tip

vortices arising from the presence of the seamless side-edge transition as illustrated in Figure 7.13 for instance.

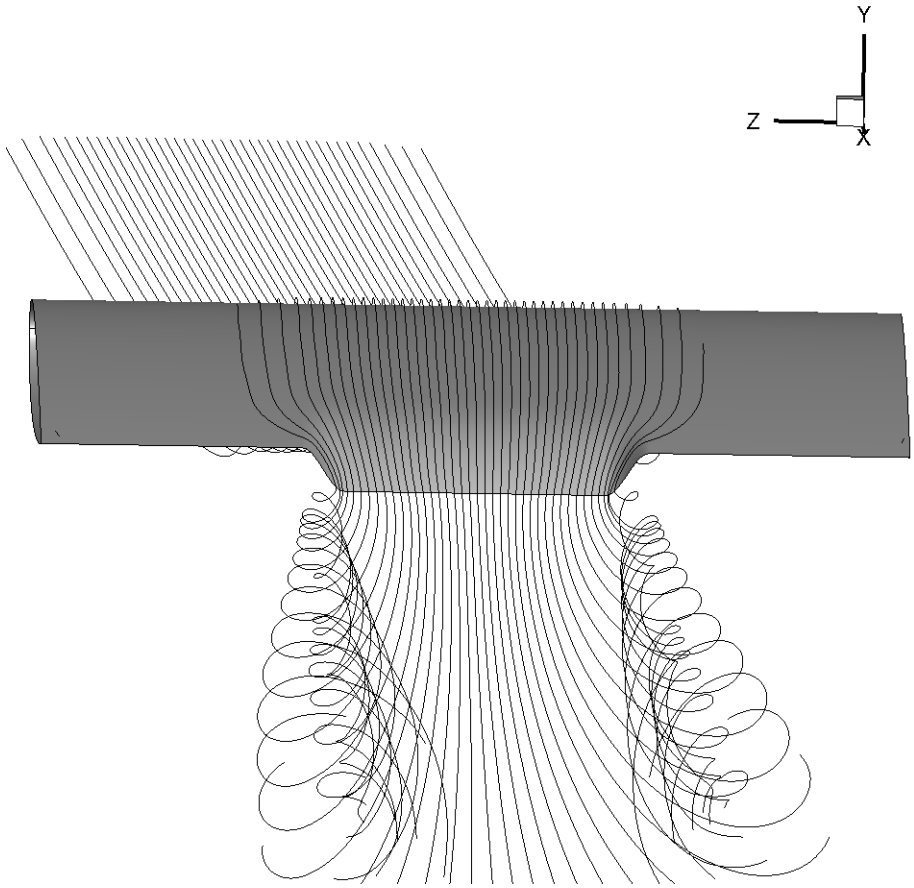

Figure 7.13: Tip vortices generated by the presence of seamless side-edge transition.

7.6. Unsteady RANS of a 3D dynamically morphing TEF

Figure 7.14 shows the instantaneous C_L and C_D obtained for the dynamically morphing TEF, for which the dynamic morphing begins at $t_{start} = 0.2s$ after the baseline has reached a statically converged state. When the morphing begins the lift and drag coefficients start increasing in a quasi-linear fashion as was observed for the 2D dynamic morphing (Chapter 5).

Throughout the morphing process, small oscillations about a mean are observed, giving an indication of the presence of a growing vortex shedding. Shortly before

the morphing stops, the overshoots in C_D observed in the 2D study are also observed in 3D. The amplitude of the peak is proportional to the morphing frequency, the highest morphing frequency explored (8 *Hz*) resulted in a higher peak with an overshoot of 30% compared with the mean value of the coefficient after morphing stops.

After the morphing ends, both lift and drag coefficients reach a converged state where constant oscillations are observed in the coefficient as can be clearly seen on the embedded figures in Figure 7.14.

These predictions are in fact more realistic compared to the statically morphed wing, as in real life scenarios, the flap will be deployed dynamically which gives rise to unsteady phenomena that could influence the performance such as the sudden peak in drag observed before the final TEF position.

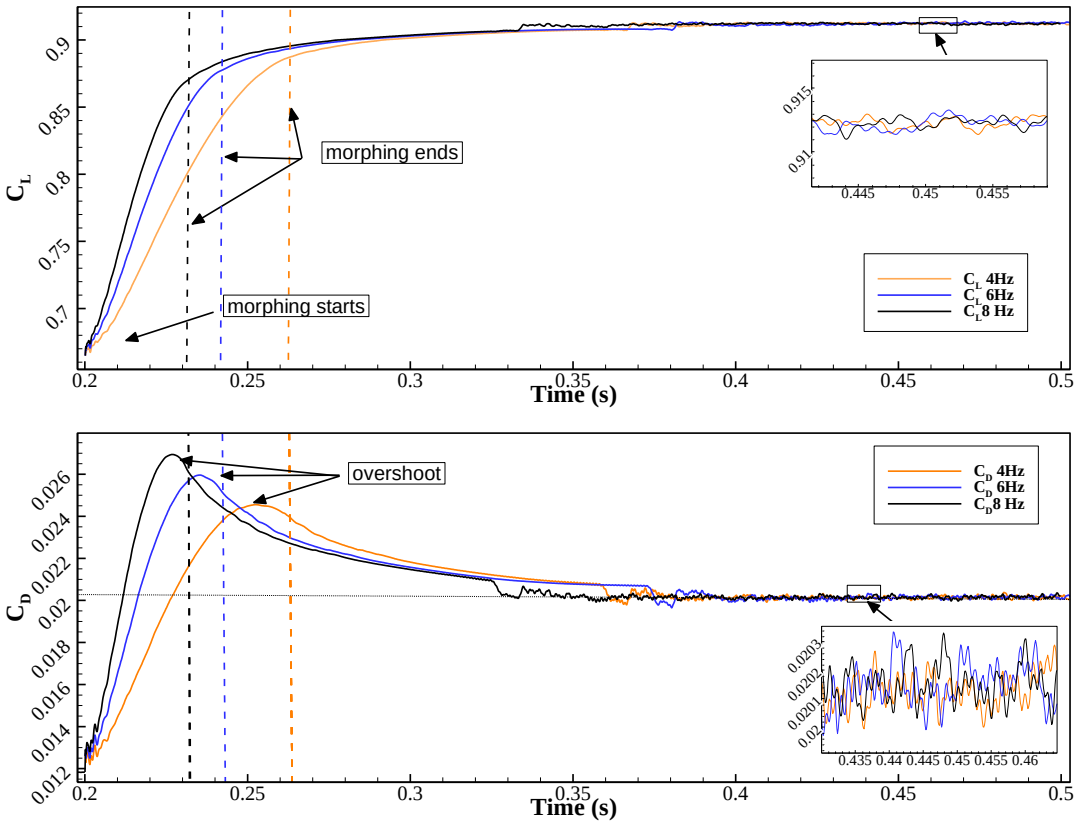

Figure 7.14: Time history of C_L and C_D for the dynamically morphing TEF at AoA=6° for three morphing frequencies.

For further insight into the unsteady morphing process, the instantaneous C_p and C_f distributions at the mid-span ($z=0.5S$) and at $x = 0.8c$ are presented in Figure 7.15 and Figure 7.16 respectively. The figures show various instances from the start of the morphing until after the morphing ends.

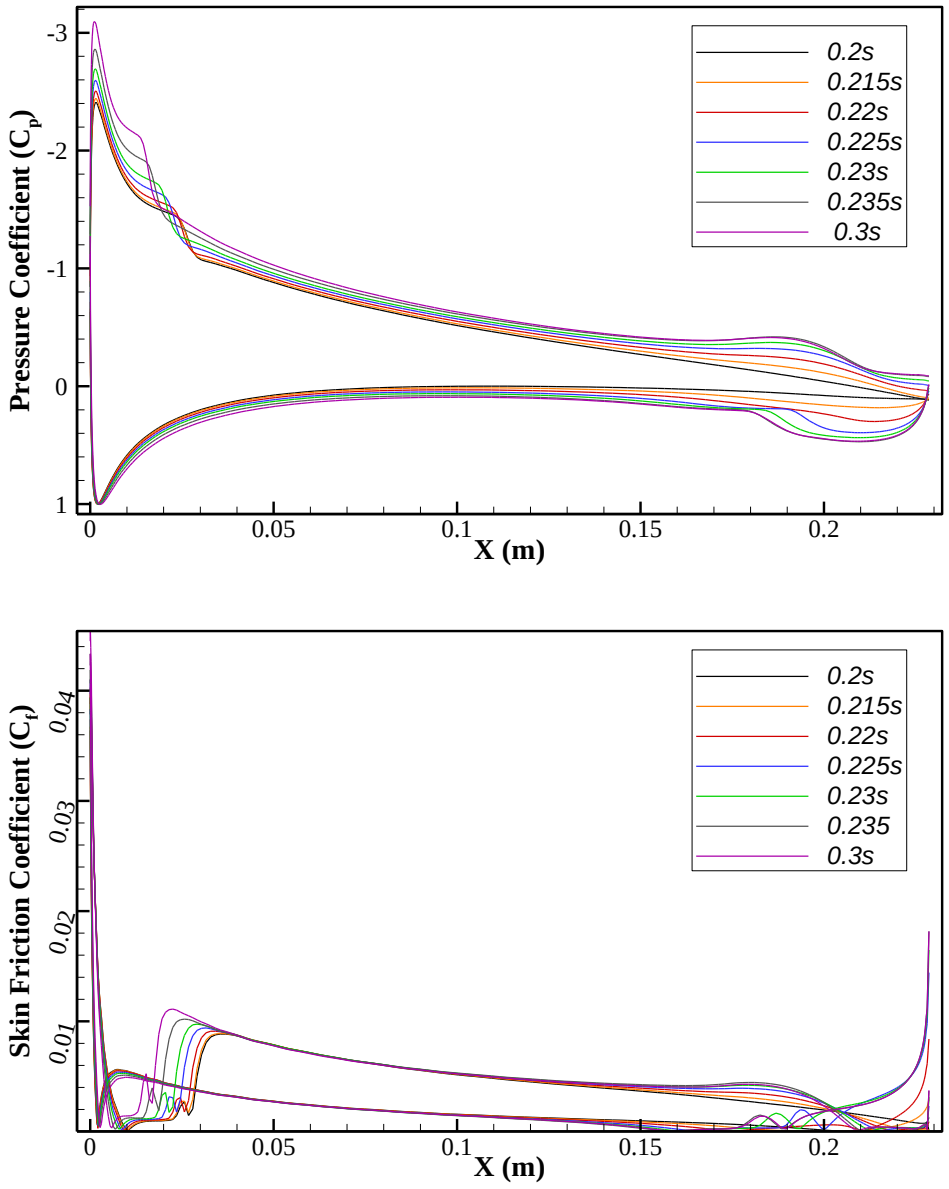

Figure 7.15: Instantaneous C_p (top) and C_f (bottom) distributions for the dynamically morphing TEF at AoA=6º on a mid-span slice (z=0.5S).

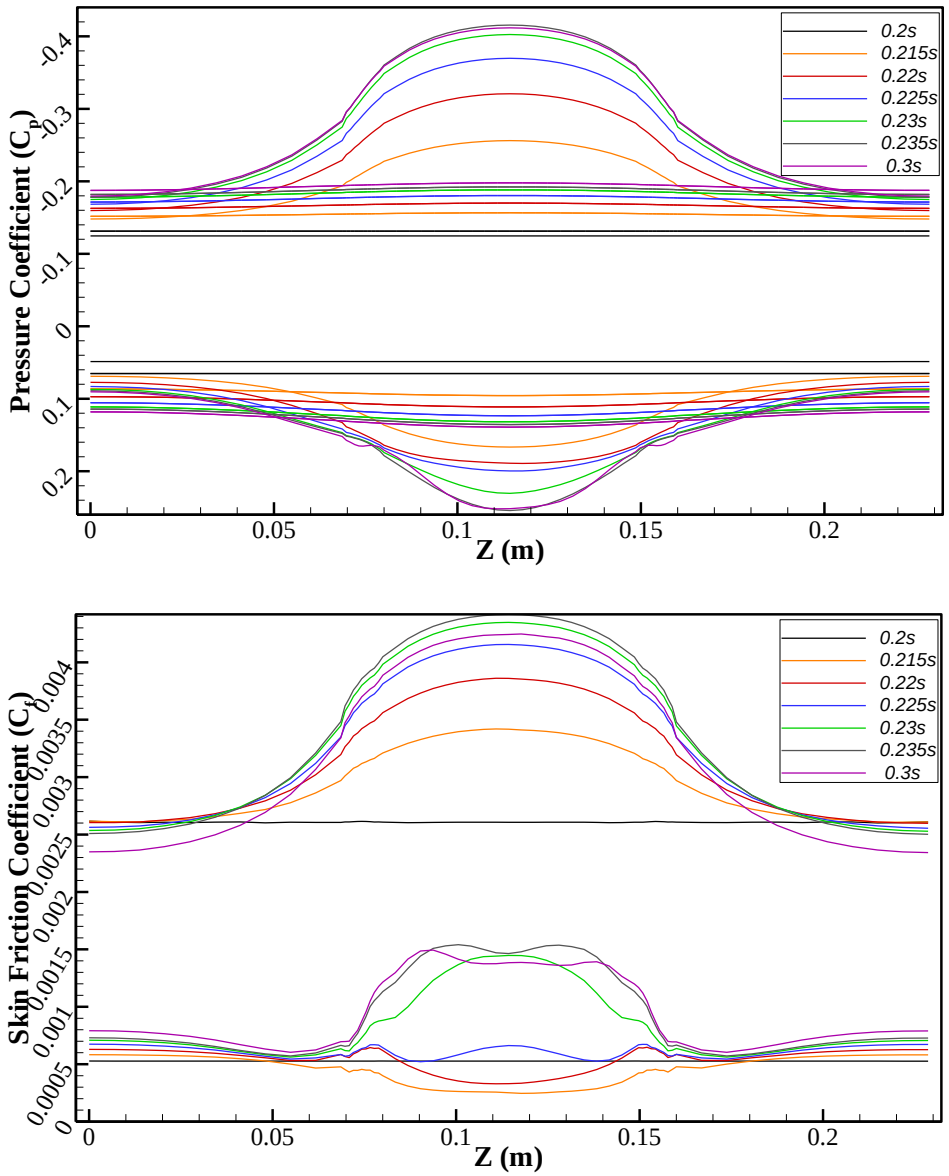

Figure 7.16: Instantaneous C_p (top) and C_f (bottom) for the dynamically morphing TEF at AoA=6° on a slice at x=0.8c.

C_p plots clearly illustrate the effect the increase in camber has on the pressure distribution. The C_p distribution gets larger as the TEF deflection increases which generates more lift. Additionally, instantaneous C_p distribution shows that an LSB (located initially at 10% of the chord location (x = 0.024 m)) moves upstream towards the leading edge during the morphing, and settling at the 5% of the chord

station (x = 0.013 m) when the flap reaches the maximum morphing deflection prescribed (5% of the chord).

The effects of varying the camber are also present in the C_f distribution. The flow appears to be laminar for the baseline at the beginning of morphing, however the more the flap is deflected the more turbulent the boundary layer becomes. The transition to turbulent BL is clearly seen in the peaks, and it appears that it gets closer to the LE the more the main flap is deflected indicating that the transition is triggered by the LSB. A similar conclusion was drawn in Chapter 4 when the SBES model was used along with the intermittency transition modelling. In addition, the transient behaviour of the turbulent separation at the flap is also clearly captured where it appears that with larger deflection, the separation point moved upstream.

At $x = 0.8c$, the C_p distribution shows the effects of the seamless side-edge transitions and how they allow a gradual increase in the pressure distribution, blending well the C_p values on the morphing flap with the static side edge part. It also shows the massive contribution in lift induced by the downward deflection of the flap.

The spanwise distribution of C_f ($x = 0.8c$) indicates the presence of a growing recirculation area at the TE, with the largest regions present at the mid-section of the morphing flap. It is worth noting that the distributions of C_p and C_f are mostly symmetrical around mid-span.

Further qualitative understanding of this process could be gained by the inspection of the instantaneous velocity and turbulent intensity contours during the morphing process, as illustrated in Figure 7.17 and Figure 7.18 respectively.

At $t = 0.2$ *s*, typical behaviour of symmetrical airfoils with a small separation pocket near the TE can be seen. This separation bubble grows larger as morphing gradually occurs, and the separation region expands with a more prominent effect on the wake regions. Flow around the flap region becomes more separated at $t = 0.215$ *s*, where tip vortices start to form around the seamless transition part, which

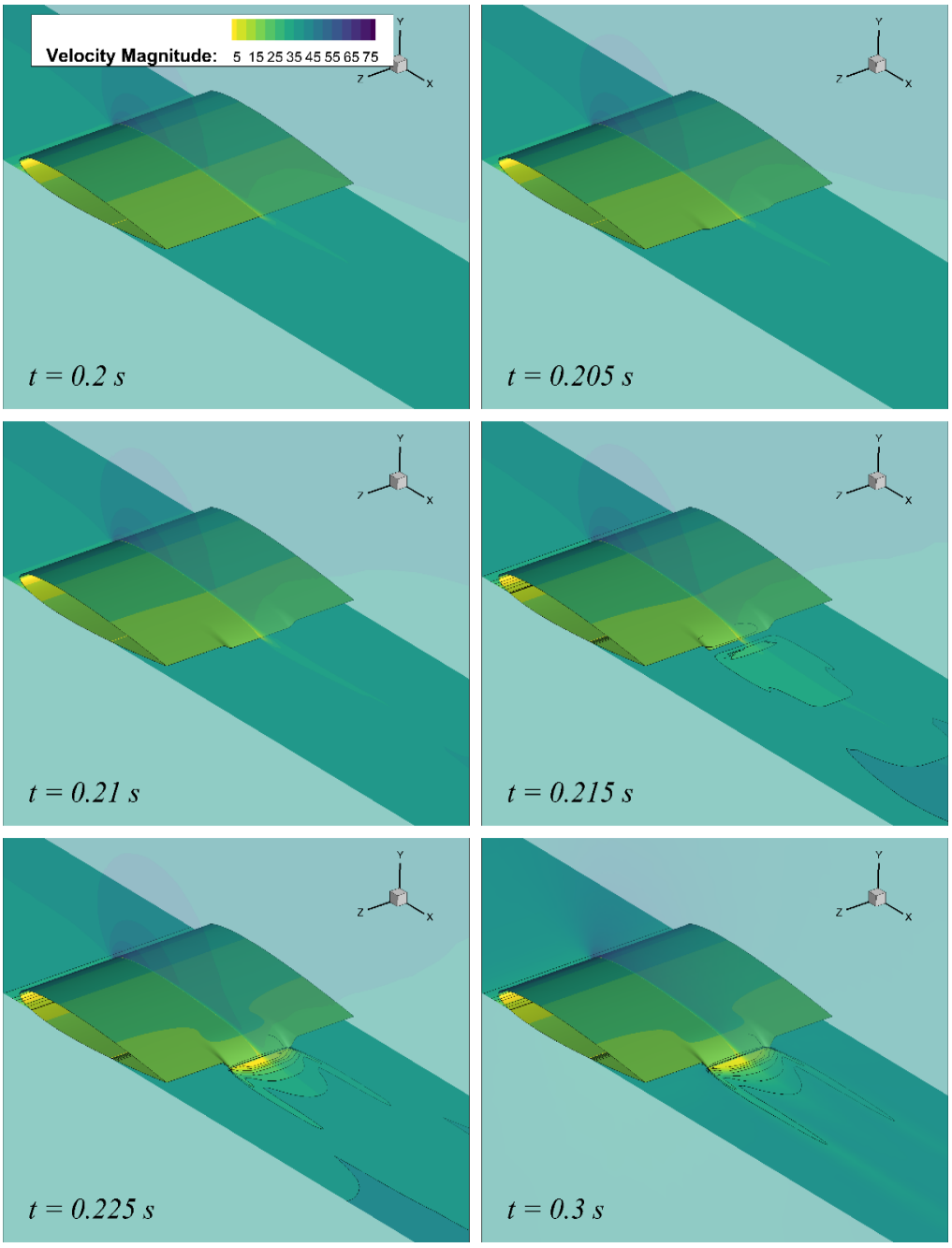

Figure 7.17: Instantaneous velocity contours placed at 3 stations at 6 time instances illustrating the dynamic morphing process of a 3D wing with seamless side-edge transitions at AoA=6º and a morphing frequency of 8 Hz .

becomes clearer when the TEF reaches its final position. After morphing, an elongated separation region is present in the wake. The effect of tip vortices on the wake are also clearly identifiable, especially in the turbulent intensity contours where three regions are identified; a central region related to the flow separation

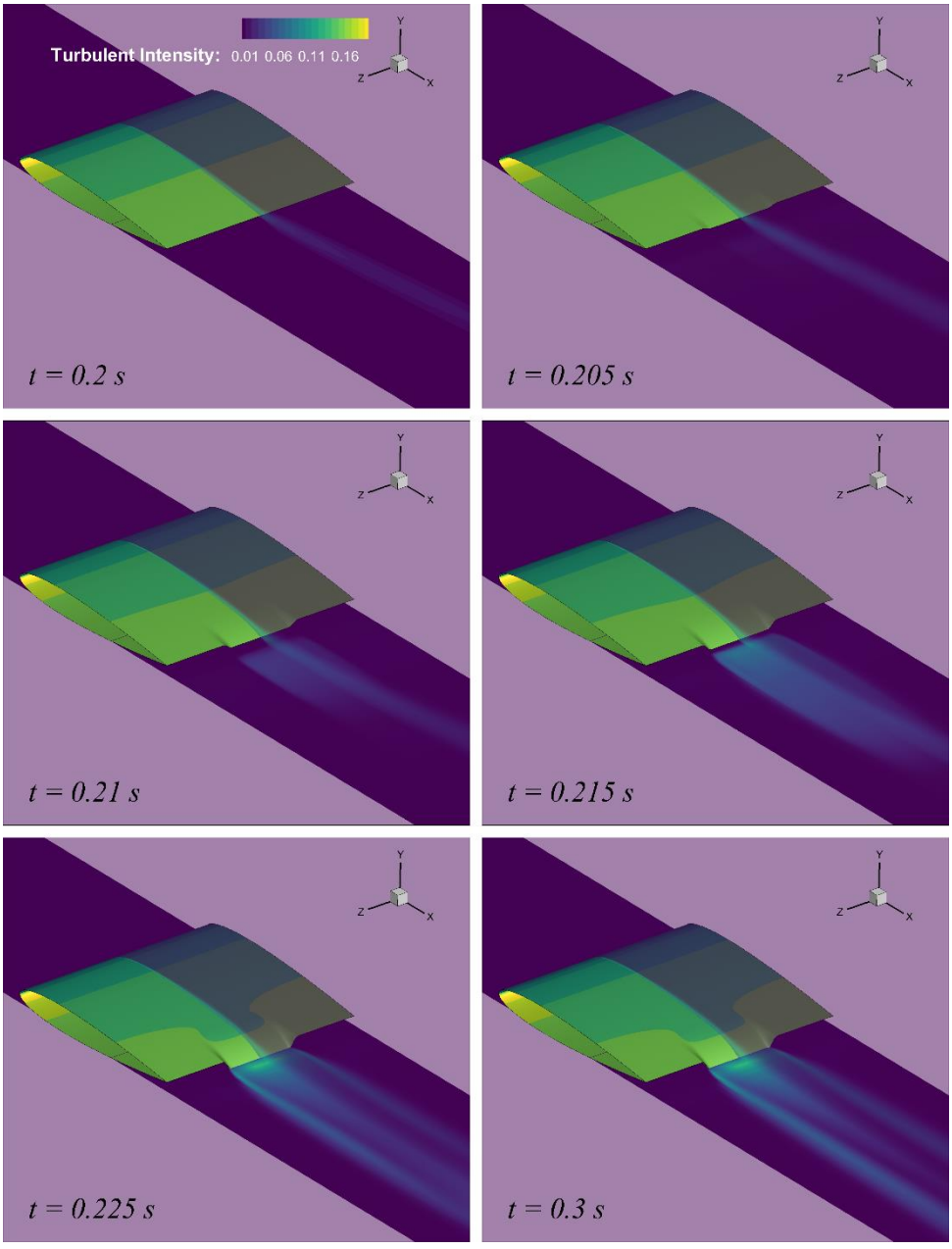

Figure 7.18: Instantaneous turbulent intensity contours placed at 3 stations and 6 time instances illustrating the dynamic morphing process of a 3D wing with seamless side-edge transitions at AoA=6º and a morphing frequency of 8 Hz .

attributed to the morphing flap and two side regions resulting from the wakes of the two seamless transitions.

2D and 3D dynamically morphed flap comparison

As in chapter 4, a 2D dynamically morphing flap was investigated. It is interesting to see if the dynamic response is captured in a similar way in both analysis. Figure 7.19 compares 2D predictions from Chapter 4 and 3D predictions from the current chapter. A similar trend to the one observed in the static morphing case is observed here with the 2D study overpredicting the values of the lift and drag coefficients by over 40%, which are due to the assumption made in 2D that the entire span is equipped with a morphed flap (2D approximations are similar to an infinite wing). However, the dynamic trends are the same, an overshoot in C_D is observed in both the 2D and 3D studies. Yet, in the 2D study the overshoot is about 10% larger than in the 3D study.

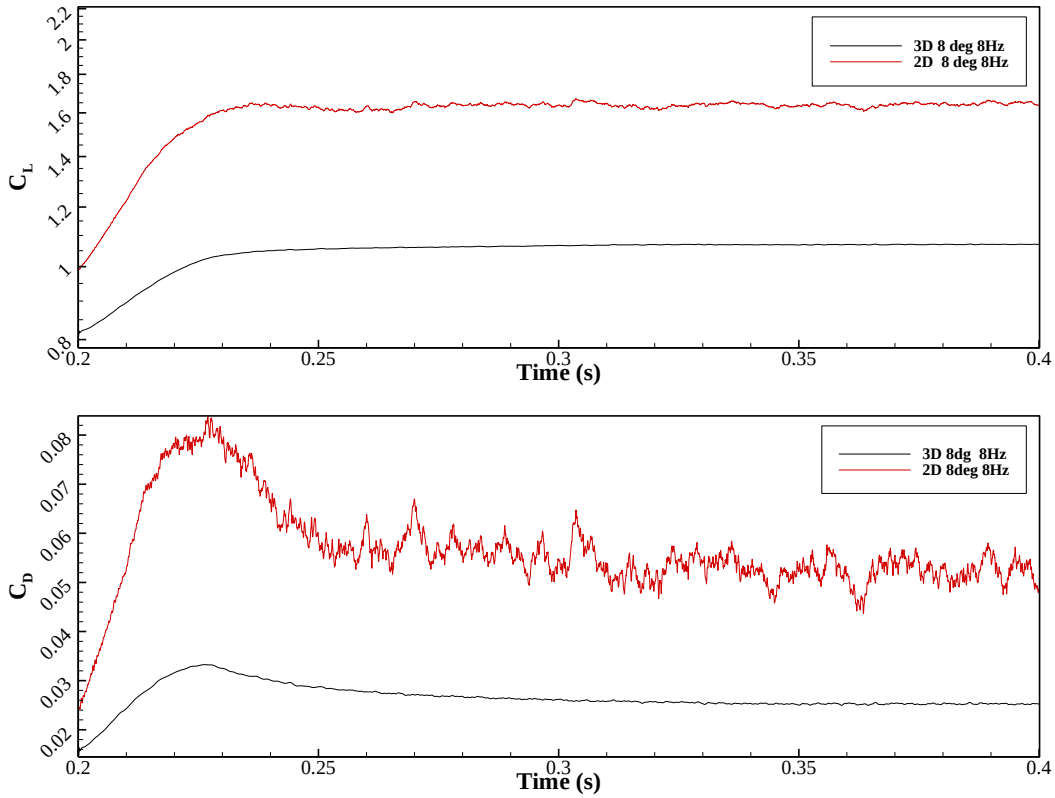

Figure 7.19: Instantaneous C_L and C_D for the dynamically morphing TEF at AoA=8° and a morphing frequency 8 Hz.

Another difference is the amplitude of the oscillations observed. The 2D predicts stronger turbulent structures, however this is mainly due to the difference in the turbulence models used for these particular cases, as the 2D study referenced here was obtained using the SBES turbulence model whereas the 3D used the *SST k-ω*.

7.7. Summary

In order to perform the unsteady analysis of dynamically morphing TEF with seamless transition, a parametrization method was modified and implemented in a UDF to drive the dynamic mesh in ANSYS Fluent. First, a 3D steady RANS analysis of a statically morphed TEF with seamless transition was performed and results compared with both the baseline wing and with a traditional hinged flap configuration at a Re = 0.62×10^6 for a range of angles of attack.

It was found that the baseline NACA 0012 wing produced results comparable with published experimental data and previous numerical work for the NACA 0012 airfoil.

Moreover, the morphed wing with the seamless side-edge transition was found to have an average of 22% higher lift compared with the hinged flap configuration for a constant drag reduction for the morphed wing of 25% throughout the AoA in the pre-stall resulting in up to 40% aerodynamic enhancements.

Finally, the parametrization method was successfully implemented and unsteady flow analysis at AoA = 6º was performed offering the possibility to include the deformation motion in the modelling of such morphing configurations.

Results for three morphing frequencies showed that due to unsteady effects an overshoot in the drag coefficient was observed for all the configurations studied, which is consistent with the results obtained in chapter 4. It was also found that the 2D analysis tends to overestimate the lift and drag compared with a 3D realistic concept which is due to the assumption that the entire wing span is morphing.

“But nearly all the grandest discoveries of science have been but the rewards of accurate measurement and patient long-continued labour in the minute sifting of numerical results.”

Lord Kelvin, 1871

8. Conclusions and Future Work

Chapter 8

This chapter concludes the thesis with a brief synopsis of the main conclusions and contributions of the present research work. Some directions for future research are also outlined.

8.1. Research Summary and Conclusions

The focus of this thesis has been twofold: firstly, to develop a framework to perform aerodynamic and aeroacoustic studies of dynamically morphing wings. Secondly, to gain a deeper understanding of the morphing process by applying the developed framework to a range of interconnected morphing applications.

The framework has been developed by integrating an unsteady parametrization method specifically modified to model the morphing motion in time. This method is then integrated in the commercial software ANSYS Fluent through the development of a User-Defined Function (UDF) targeted at controlling dynamic mesh schemes to deform the mesh to adapt to morphing geometry in which the flow physics and aeroacoustics were explored, both in the 2D and 3D cases.

A range of applications was explored, using either RANS (*k-ω SST*) or the high fidelity hybrid RANS-LES (SBES) turbulence models. The flow response to a rapid downward deflection of a morphing TEF has been investigated using the SBES turbulence model at AoA in the pre-stall region, for which various morphing frequencies have been explored and the lift and drag coefficient response analysed. Additionally, an aerodynamic and aeroacoustic study was performed to explore the use of active flow control employing harmonically morphing TEF. Finally, the framework was expanded to 3D by modifying further the unsteady parametrization method to model a dynamically morphing wing with a seamless side-edge

transition. The main conclusions and contributions made in each of the cases addressed in this doctoral thesis are summarised below.

8.1.1. 2D downward dynamic morphing TEF

i. A modified unsteady parametrisation method was developed and implemented. The deformed mesh gave results similar to the re-generated mesh with small discrepancies of less than 1%, confirming the validity of the geometry and mesh deformation scheme.

ii. Steady state CFD results obtained from Fluent agreed well with published numerical and experimental results.

iii. A pitching airfoil case was used as a benchmark to assess and validate unsteady predictions obtained using dynamic mesh; good agreement was obtained with both experimental and numerical results confirming the capability of the solver to accurately predict flow behaviour even when subjected to large mesh deformations.

iv. For the same maximum deflection (5%c), the morphing flap produced higher lift in comparison to a hinged flap, but at the expense of a drag penalty. An average increase in aerodynamic efficiency C_L/C_D of 6.5% is observed.

v. The 2D morphed flap reaches a peak aerodynamic efficiency at 8° AoA, about 13% higher than the hinged flap. After this angle, the efficiency decreases until an angle of 13°. Beyond this angle, the flapped airfoil exhibits slightly better aerodynamic performance, and this trend is qualitatively confirmed by published 3D wind tunnel tests.

vi. For the dynamically morphing TEF, both lift and drag responses showed a proportional relationship between the morphing frequency and the slope at which these quantities evolve. Interestingly, an overshoot in the drag coefficient has been captured, but not in the lift coefficient. Its amplitude is also proportional to the actuation frequency used; higher frequencies were causing larger overshoots. The aerodynamic efficiency during the morphing process experienced up to 30% decrease due to the drag overshoot.

vii. Qualitative results gave insight into the flow response to the rapid morphing deflection. At an AoA =12º, the morphing causes turbulent structures to propagate upstream which interact with a Laminar Separation Bubble (LSB) near the LE causing it to burst, which initiates a dynamic stall. This behaviour was observed in the literature for rapid pitch-up airfoils.

The framework developed and applied on 2D downward flap deflection not only allowed the confirmation of morphing mechanism's superiority compared to traditional hinged flap, but it also confirmed the presence of dynamic effects that need deeper investigations in order to fully understand the morphing process and harness such dynamic effects for future applications.

8.1.2. 2D Harmonic Morphing Trailing-Edge Flap

Given the potential of active flow control using harmonic morphing and the need for a practical numerical framework to perform aerodynamic and aeroacoustic investigation of such devices, the framework was expanded further to allow this class of analysis.

i. The SBES model was able to predict accurately the location and amplitude of the main tone frequency related to the laminar boundary-layer instabilities. The structure of the main tone captured is also in good agreement with published literature.
ii. This framework can be applied to 2D and 3D problems; however, given the prohibitive computational cost of 3D simulations and the large number of possible parameters to consider, the study is restricted to 2D harmonic deformations and their effects on tonal noise.
iii. A comparative study between 2D SBES predictions and published 3D LES results was conducted. It was found that the 2D simulations capture well the tonal noise given its pseudo 2D generation mechanisms.
iv. Results for three morphing scenarios were presented. Two morphing amplitudes of 0.01% and 0.1% of the chord at a fixed frequency (f = 100 *Hz*,), then the amplitude was fixed at 0.01% and two frequencies studied (100 *Hz* and 800 *Hz*). It was found that up to 3% increase in aerodynamic

efficiency was possible using the 800 *Hz* frequency (half the vortex shedding frequency), whereas the 100 *Hz* frequency had negligible impact on the aerodynamic efficiency.

v. In terms of aeroacoustic effects, the morphing TEF appears to shift the main tone to a higher frequency (from 1.6 *kHz* to 2 *kHz*) with a noise reduction of 1.5 *dB* for the main tone and up to 10 *dB* for the first superharmonic.

vi. The underlying mechanism causing these effects is still unclear but a possible lock-on with a subharmonic could be the cause for the change in the wake structure producing the observed frequency shift and drag reduction.

The study focusing on the aerodynamic and aeroacoustic effects of harmonically morphing TEF showed that the complex interaction between the morphing structure and flow could result in significant aerodynamic enhancements and possible aeroacoustic benefits as well, but with the condition that the right frequency/amplitude pair is chosen to optimize both the aerodynamic and aeroacoustic benefits. This task needs a thorough numerical investigation which is made possible by the framework presented in this work.

8.1.3. 3D dynamic morphing TEF with seamless side-edge transition

i. The framework was expanded to a realistic 3D morphing wing incorporating a seamless side-edge transition based on newly developed prototypes in the literature.

ii. Steady CFD results comparing a wing with a morphing TEF and a wing equipped with a hinged discrete flap showed that the morphing produces higher lift and lower drag, resulting in an enhanced aerodynamic efficiency (C_L/C_D) of up to 40%.

iii. The enhanced efficiency is attributed to the seamless transition's contribution to the lift. The extra drag produced by the hinged flap is due to the presence of the gaps around the discrete flap triggering an early separation at the start of the flap.

iv. 3D dynamic morphing results for three morphing frequencies showed the presence of an overshoot in the drag coefficient for all the configurations studied, which is consistent with the results obtained in Chapter 4.

The 3D extension of the framework allowed the investigation of a more realistic morphing concept, which permits a direct comparison between 2D and 3D analysis. This study concluded that 2D tends to generally overestimate both the lift and drag compared with the 3D realistic concept, which is due to the assumption in 2D that the entire wing span is morphing whereas in a realistic 3D case only the portion designated experiences the camber change.

As an overall conclusion, the framework presented in this thesis allows the extension of the current boundaries of morphing wings analysis by providing a tool to produce high fidelity investigation of morphing motion dynamic effects, which were dominantly neglected in the previous studies.

The framework also provides a significant enhancement to the current prediction capabilities available in literature, which helps in the efforts of the maturing and integration of morphing technology in aerospace structures and beyond.

8.2. Suggestions for Future Work

Based on the developed framework and the outcome of the research, the following suggestions for future work are proposed.

Higher fidelity parametric sweep

The use of wall resolved 3D simulation (e.g. LES) is needed in order to resolve smaller scale turbulent structures, which would enrich the understanding of how the flow responds to rapid dynamic morphing flap deflection. As done already in this thesis, investigating the effects of the flap size, the morphing angle and type of deflection will be important as well as the ability to resolve the unsteady flow physics observed for dynamic morphing cases. When it comes to harmonic morphing, it will be interesting to test a wider range of morphing frequency /

amplitude pairs in order to explore optimal configurations that could enhance the aerodynamic performance further while keeping the same noise level if not reducing it.

Higher angles of attack

AoA in massively separated flows should be investigated with a flap deflection time of the order of one convective time to gain further understanding, enable possible stall mitigation, and load alleviation capabilities using the downward flap deflection method. Likewise, exploring the use of the harmonic morphing at higher angles of attack is imperative given the higher impact expected and the practical applications possible (e.g. noise and drag reduction during take-off). Moreover, this framework will also allow the exploration of 3D harmonic forcing at high AoA in both the streamwise and spanwise directions.

Beyond symmetrical airfoils

In this thesis, the NACA 0012 was explored due to it being historically a reference airfoil for aerodynamic studies with a plethora of experimental and numerical data available. However, the framework presented allows us to easily investigate a range of symmetrical and non-symmetrical airfoils and beyond including e.g. supercritical and thin airfoils. This should be explored for future applications. Furthermore, it is important to study the morphing concept incorporated on realistic swept wings for a better evaluation of their respective performance.

Beyond morphing trailing-edge flaps

This work has focused mainly on camber change induced by a morphing TEF due to how efficient variable camber is in changing wings characteristics to fit various flight phases (cruise, take-off and landing). However, this framework could also be utilised to study the effect of a morphing leading edge, replicating a droop nose for instance, or even experimenting with local high frequency oscillations for LEV suppression. Finally, other aerospace bodies such as the engine nacelles could also be investigated.

Beyond aerospace

Finally, bio-inspiration is a trend affecting all fields of science and engineering, and even though morphing thrived in the aerospace industry, its applications extend way beyond this field. In the future, it would be stimulating to see this framework applied to study the dynamic effects of a morphing tidal turbine blade for instance, to improve its power output or on the blades of a vertical or horizontal wind turbine to improve their efficiencies and reduce their noise. These are some examples of possible applications of morphing outside the aerospace engineering field, but only imagination is the limit.

References

ACARE (2010) *Beyond Vision 2020*. Brussels: European Commission.

Ader, C. (1897) *Éole (avion)*. Available from: https://fr.wikipedia.org/wiki/Éole_(avion) [Accessed 26 September 2018].

Afonso, F., Vale, J., Lau, F. and Suleman, A. (2017) Performance based multidisciplinary design optimization of morphing aircraft. *Aerospace Science and Technology*. 67 pp. 1–12. doi:10.1016/j.ast.2017.03.029.

Ai, Q., Kamliya Jawahar, H. and Azarpeyvand, M. (2016) Experimental investigation of aerodynamic performance of airfoils fitted with morphing trailing edges. In: *54th AIAA Aerospace Sciences Meeting* AIAA SciTech Forum. 2 January 2016 San Diego, California, USA: American Institute of Aeronautics and Astronautics. pp. 1563. doi:10.2514/6.2016-1563.

Ai, Q., Weaver, P.M., Barlas, T.K., Olsen, A.S., Madsen, H.A. and Andersen, T.L. (2019) Field testing of morphing fl aps on a wind turbine blade using an outdoor rotating rig. *Renewable Energy*. 133 pp. 53–65. doi:10.1016/j.renene.2018.09.092.

Airoldi, A., Crespi, M., Quaranti, G. and Sala, G. (2012) Design of a Morphing Airfoil with Composite Chiral Structure. *Journal of Aircraft*. 49 (4), pp. 1008–1019. doi:10.2514/1.C031486.

Ajaj, R.M., Friswell, M.I., I Saavedra Flores, E., Keane, A., Isikveren, A.T., Allegri, G. and Adhikari, S. (2013) An integrated conceptual design study using span morphing technology. *Journal of Intelligent Material Systems and Structures*. 25 (8), pp. 989–1008. doi:10.1177/1045389X13502869.

Altshuler, D.L., Bahlman, J.W., Dakin, R., Gaede, A.H., Goller, B., Lentink, D., Segre, P.S. and Skandalis, D.A. (2015) The biophysics of bird flight: functional relationships integrate aerodynamics, morphology, kinematics, muscles, and sensors. *Canadian Journal of Zoology*. 93 (12), pp. 961–975. doi:10.1139/cjz-2015-0103.

Amitay, M. and Glezer, A. (2006) Flow transients induced on a 2D airfoil by pulse-modulated actuation. *Experiments in Fluids*. 40 (2), pp. 329–331. doi:10.1007/s00348-005-0069-6.

Anderson, J.D. and Wendt, J. (2009) *Computational Fluid Dynamics*. John F. Wendt (ed.). Berlin, Heidelberg: Springer Berlin Heidelberg.

ANSYS (2018) *Release 18.2, Help System*.

Arbey, H. and Bataille, J. (1983) Noise generated by airfoil profiles placed in a uniform laminar flow. *Journal of Fluid Mechanics*. 134 pp. 33–47.

doi:10.1017/S0022112083003201.

Baier, H. (2015) Morphing Enabling Technologies for Propulsion System Nacelles Project Final Report *DTIC Document*.

Barbarino, S., Bilgen, O., Ajaj, R.M., Friswell, M.I. and Inman, D.J. (2011) A Review of Morphing Aircraft. *Journal of Intelligent Material Systems and Structures*. 22 (9), pp. 823–877. doi:10.1177/1045389X11414084.

Batina, J.T. (1990) Unsteady Euler airfoil solutions using unstructured dynamic meshes. *AIAA Journal*. 28 (8), pp. 1381–1388. doi:10.2514/3.25229.

Beaverstock, C., Woods, B., Fincham, J., Friswell, M., Beaverstock, S.C., Woods, K.B., Fincham, H.J., Friswell, I.M., Beaverstock, C., Woods, B., Fincham, J. and Friswell, M. (2015) Performance Comparison between Optimised Camber and Span for a Morphing Wing. *Aerospace* . 2 (3), pp. 524–554. doi:10.3390/aerospace2030524.

Benton, S.I. and Visbal, M.R. (2018) The onset of dynamic stall at a high, transitional Reynolds number. *Journal of Fluid Mechanics*. 861 pp. 860–885. doi:10.1017/jfm.2018.939.

Bies, D.A. and Hansen, C.H. (1988) *Engineering Noise Control*. Abingdon, UK: Taylor & Francis.

Bilgen, O., Friswell, M.I., Kochersberger, K.B. and Inman, D.J. (2011) Surface Actuated Variable-Camber and Variable-Twist Morphing Wings Using Piezocomposites. *Structures, Structural Dynamics and Materials Conference*. 19 (April), pp. 1–13. doi:10.2514/6.2011-2072.

Bilgen, O., Kochersberger, K.B., Inman, D.J. and Ohanian, O.J. (2010) Novel, Bidirectional, Variable-Camber Airfoil via Macro-Fiber Composite Actuators. *Journal of Aircraft*. 47 (1), pp. 303–314. doi:10.2514/1.45452.

Boer, A.D., Zuijlen, A. Van and Bijl, H. (2007) Mesh movement based on radial basis function interpolation. *Fourth MIT Conference on Computational Fluid and Solid Mechanics*. 85 (11–14), pp. 784–795. doi:10.1016/j.compstruc.2007.01.013.

Bonnema, K. and Smith, S. (1988) *AFTI/ F-111 Mission Adaptive Wing*. U.S. Air Force Wright Aeronautical Labs., Rept. AFWAL-TR-88-3082, Wright–Patterson AFB, OH

Bottasso, C.L., Detomi, D. and Serra, R. (2005) The ball-vertex method: A new simple spring analogy method for unstructured dynamic meshes. *Computer Methods in Applied Mechanics and Engineering*. 194 (39–41), pp. 4244–4246. doi:10.1016/j.cma.2004.08.014.

Bourdin, P., Gatto, A. and Friswell, M. (2006) The Application of Variable Cant

Angle Winglets for Morphing Aircraft Control. In: *24th AIAA Applied Aerodynamics Conference*. 5 June 2006 Reston, Virigina: American Institute of Aeronautics and Astronautics. pp. 1–13. doi:10.2514/6.2006-3660.

Bowman, J., Sanders, B. and Weisshaar, T. (2002) Evaluating the Impact of Morphing Technologies on Aircraft Performance. In: *43rd AIAA/ASME/ASCE/AHS/ASC Structures, Structural Dynamics, and Materials Conference*. 22 April 2002 Reston, Virigina: American Institute of Aeronautics and Astronautics. pp. 1–11. doi:10.2514/6.2002-1631.

Brissenden R. F., Heath A. R., Conner D. W., S.M.L. (1980) *Assessment of Variable Camber for Application to Transport Aircraft*. Contractor Report. Seattle,: Boeing Commercial Airplane Company, Preliminary Design Department.

Brooks, T.F., Pope, D.S. and Marcolini, M. (1989) Airfoil self-noise and prediction *National Aeronautics and Space Administration Reference Publication Number 1218*.

Burdette, D.A., Kenway, G.K., Lyu, Z. and Martins, J. (2015) Aerostructural Design Optimization of an Adaptive Morphing Trailing Edge Wing. *56th AIAA/ASCE/AHS/ASC Structures, Structural Dynamics, and Materials Conference*. (January), pp. 1–13. doi:10.2514/6.2015-1129.

Campbell, R.L. (1992) An Approach to Constrained Aerodynamic Design with Application to Airfoils. *NASATechnical Paper 3260*. (November), .

Carruthers, a. C., Walker, S.M., Thomas, a. L.R. and Taylor, G.K. (2010) Aerodynamics of aerofoil sections measured on a free-flying bird. *Proceedings of the Institution of Mechanical Engineers, Part G: Journal of Aerospace Engineering*. 224 pp. 855–864. doi:10.1243/09544100JAERO737.

Cattafesta, L.N. and Sheplak, M. (2011) Actuators for Active Flow Control. *Annual Review of Fluid Mechanics*. 43 (1), pp. 247–272. doi:10.1146/annurev-fluid-122109-160634.

Chen, G., Zhang, Z., Tian, Z., Li, L., Dong, X. and Ju, H. (2017) Design of a CFD scheme using multiple RANS models for PWR. *Annals of Nuclear Energy*. 102 pp. 349–358. doi:10.1016/j.anucene.2016.12.030.

Chew, C.S., Yeo, K.S. and Shu, C. (2006) A generalized finite-difference (GFD) ALE scheme for incompressible flows around moving solid bodies on hybrid meshfree-Cartesian grids. *Journal of Computational Physics*. 218 (2), pp. 510–548. doi:10.1016/j.jcp.2006.02.025.

Church, B., Paschereit, C.O., Holst, D., Saverin, J., Pechlivanoglou, G., Tüzüner, E. and Nayeri, C.N. (2018) Experimental Analysis of a NACA 0021 Airfoil Section Through 180-Deg Angle of Attack at Low Reynolds Numbers for Use in Wind Turbine Analysis. *Journal of Engineering for Gas Turbines and*

Power. 141 (4), pp. 041012. doi:10.1115/1.4041651.

Concilio, A. and Lecce, L. (2018) Chapter 1 - Historical Background and Current Scenario. In: Antonio Concilio, Ignazio Dimino, Leonardo Lecce, and Rosario B T - Morphing Wing Technologies Pecora (eds.). *Morphing Wing Technologies*. (no place) Butterworth-Heinemann. pp. 3–84. doi:10.1016/B978-0-08-100964-2.00001-0.

Cooper, J.E., Chekkal, I., Cheung, R.C.M., Wales, C., Allen, N.J., Lawson, S., Peace, A.J., Cook, R., Standen, P., Hancock, S.D. and Carossa, G.M. (2015) Design of a Morphing Wingtip. *Journal of Aircraft*. 52 (5), pp. 1394–1403. doi:10.2514/1.C032861.

David Oxley and David Goodger (2016) *Air Passenger Forecasts Global Report UPDATED*. pp. 1–4. A joint venture between IATA and Tourism Economics.

Daynes, S. and Weaver, P.M. (2012) A morphing trailing edge device for a wind turbine. *Journal of Intelligent Material Systems and Structures*. 23 (6), pp. 691–701. doi:10.1177/1045389X12438622.

Di, G., Wu, Z. and Huang, D. (2017) The research on active flow control method with vibration diaphragm on a NACA0012 airfoil at different stalled angles of attack. *Aerospace Science and Technology*. 69 pp. 76–86. doi:10.1016/j.ast.2017.06.020.

Ding, H., Shu, C., Yeo, K.S. and Xu, D. (2004) Simulation of incompressible viscous flows past a circular cylinder by hybrid FD scheme and meshless least square-based finite difference method. *Computer Methods in Applied Mechanics and Engineering*. 193 (9–11), pp. 727–744. doi:10.1016/j.cma.2003.11.002.

Ding, Z., Zhu, H. and Friedman, M.H. (2002) Coronary artery dynamics in vivo. *Annals of Biomedical Engineering*. 30 (4), pp. 419–429. doi:10.1114/1.1467925.

Drela, M. (2003) Implicit Implementation of the Full e^n Transition Criterion. In: *21st AIAA Applied Aerodynamics Conference* Fluid Dynamics and Co-located Conferences. (no place) American Institute of Aeronautics and Astronautics. doi:10.2514/6.2003-4066.

Drela, M. (1989a) Integral boundary layer formulation for blunt trailing edges. In: *7th Applied Aerodynamics Conference*. 31 July 1989 Reston, Virigina: American Institute of Aeronautics and Astronautics. pp. 2166. doi:10.2514/6.1989-2166.

Drela, M. (1989b) XFOIL: An analysis and design system for low Reynolds number airfoils *Conference on Low Reynolds Number Airfoil Aerodynamics* Volume 54 p.pp. pp 1-12. doi:10.1007/978-3-642-84010-4_1.

Du, G. and Sun, M. (2010) Effects of wing deformation on aerodynamic forces in hovering hoverflies. *Journal of Experimental Biology*. 213 (13), pp. 2273–2283. doi:10.1242/jeb.040295.

Ebrahimi, A. and Hajipour, M. (2018) Flow separation control over an airfoil using dual excitation of DBD plasma actuators. *Aerospace Science and Technology*. 79 pp. 658–668. doi:10.1016/j.ast.2018.06.019.

Ennos, a. R. (1995) Mechanical Behaviour in Torsion of Insect Wings, Blades of Grass and other Cambered Structures. *Proceedings of the Royal Society B: Biological Sciences*. 259 (1354), pp. 15–18. doi:10.1098/rspb.1995.0003.

European Commission, Dareki, M., Edelstenne, C., Enders, T., Fernandez, E., Hartman, P., Herteman, J.-P., Kerkloh, M., King, I., Ky, P., Mathieu, M., Orsi, G., Schotman, G., Smith, C., et al. (2011) Flightpath 2050: europe's vision for aviation. *Isbn: 978-92-79-19724-6*. pp. 28. doi:10.2777/50266.

Farhat, C., Degand, C., Koobus, B. and Lesoinne, M. (1998) Torsional springs for two-dimensional dynamic unstructured fluid meshes. *Computer Methods in Applied Mechanics and Engineering*. 163 (1–4), pp. 231–245. doi:10.1016/S0045-7825(98)00016-4.

Farin, G. (1993) P. Bézier: How a Simple System Was Born. In: *Curves and Surfaces for Computer-Aided Geometric Design*. (no place) Elsevier. pp. 1–12. doi:10.1016/B978-0-12-249052-1.50006-4.

Fincham, J.H., Ajaj, R.M. and Friswell, M.I. (2014) Aerodynamic Performance of Corrugated Skins for Spanwise Wing Morphing. In: *14th AIAA Aviation Technology, Integration, and Operations Conference*. 16 June 2014 Reston, Virginia: American Institute of Aeronautics and Astronautics. pp. 1–14. doi:10.2514/6.2014-2724.

Fincham, J.H.S. and Friswell, M.I. (2015) Aerodynamic optimisation of a camber morphing aerofoil. *Aerospace Science and Technology*. 43 pp. 245–255. doi:10.1016/j.ast.2015.02.023.

FlexSys (2016) *FlexSys*. Available from: http://www.flxsys.com/ [Accessed 27 January 2017].

Gabor, O.S., Koreanschi, A. and Botez, R.M. (2012) Low-speed aerodynamic characteristics improvement of ATR 42 airfoil using a morphing wing approach. *IECON Proceedings (Industrial Electronics Conference)*. pp. 5451–5456. doi:10.1109/IECON.2012.6388954.

Gad-el-Hak, M. (1998) *Introduction to Flow Control BT - Flow Control: Fundamentals and Practices*. In: Mohamed Gad-el-Hak and Andrew Pollard (eds.). Berlin, Heidelberg: Springer Berlin Heidelberg. pp. 1–107. doi:10.1007/3-540-69672-5_1.

Garipova, L.I., Batrakov, A.S., Kusyumov, A.N., Mikhaylov, S.A. and Barakos, G. (2016) Aerodynamic and acoustic analysis of helicopter main rotor blade tips in hover. *International Journal of Numerical Methods for Heat & Fluid Flow*. 26 (7), pp. 2101–2118. doi:10.1108/HFF-08-2015-0348.

De Gaspari, A. and Ricci, S. (2015) Knowledge-Based Shape Optimization of Morphing Wing for More Efficient Aircraft. *International Journal of Aerospace Engineering*. 2015 . doi:10.1155/2015/325724.

Geng, F., Kalkman, I., Suiker, A.S.J. and Blocken, B. (2018) Sensitivity analysis of airfoil aerodynamics during pitching motion at a Reynolds number of 1.35×105. *Journal of Wind Engineering and Industrial Aerodynamics*. 183 (November), pp. 315–332. doi:10.1016/j.jweia.2018.11.009.

De Gennaro, M., Kühnelt, H. and Zanon, A. (2017) Numerical Prediction of the Tonal Airborne Noise for a NACA 0012 Aerofoil at Moderate Reynolds Number Using a Transitional URANS Approach. *Archives of Acoustics*. 42 (4), pp. 653–675. doi:10.1515/aoa-2017-0069.

Gern, F., Inman, D.J. and Kapania, R.K. (2005) Computation of Actuation Power Requirements for Smart Wings with Morphing Airfoils. *AIAA Journal*. 43 (12), pp. 2481–2486. doi:10.2514/1.20367.

Gharali, K. and Johnson, D.A. (2013) Dynamic stall simulation of a pitching airfoil under unsteady freestream velocity. *Journal of Fluids and Structures*. 42 pp. 228–244. doi:10.1016/j.jfluidstructs.2013.05.005.

Ghommem, M., Hajj, M.R., Mook, D.T., Stanford, B.K., Beran, P.S., Snyder, R.D. and Watson, L.T. (2012) Global optimization of actively morphing flapping wings. *Journal of Fluids and Structures*. 33 pp. 210–228. doi:10.1016/j.jfluidstructs.2012.04.013.

Golubev, V., Nguyen, L., Roger, M. and Visbal, M. (2012) High-Accuracy Simulations of Flow-Acoustic Resonant Interactions in Airfoil Transitional Boundary Layers. In: *18th AIAA/CEAS Aeroacoustics Conference (33rd AIAA Aeroacoustics Conference)*. 4 June 2012 Reston, Virigina: American Institute of Aeronautics and Astronautics. pp. 4–6. doi:10.2514/6.2012-2136.

Golubev, V., Nguyen, L., Roger, M. and Visbal, M. (2011) On Interaction of Airfoil Leading and Trailing Edge Noise Sources in Turbulent Flow. In: *17th AIAA/CEAS Aeroacoustics Conference (32nd AIAA Aeroacoustics Conference)*. 5 June 2011 Reston, Virigina: American Institute of Aeronautics and Astronautics. pp. 2859. doi:10.2514/6.2011-2859.

Golubev, V. V., Nguyen, L., Mankbadi, R.R., Roger, M. and Visbal, M.R. (2014) On Flow-Acoustic Resonant Interactions in Transitional Airfoils. *International Journal of Aeroacoustics*. 13 (1–2), pp. 1–38. doi:10.1260/1475-472X.13.1-2.1.

Golubev, V. V, Nguyen, L., Mankbadi, R.R., Dudley, J.G. and Visbal, M.R. (2013) On Self-Sustained Flow-Acoustic Resonant Interactions in Airfoil Transitional Boundary Layers. In: *43rd Fluid Dynamics Conference*. 24 June 2013 Reston, Virginia: American Institute of Aeronautics and Astronautics. pp. 1–16. doi:10.2514/6.2013-2619.

Greenblatt, D. and Wygnanski, I.J. (2000) Control of flow separation by periodic excitation. *Progress in Aerospace Sciences*. 36 (7), pp. 487–545. doi:10.1016/S0376-0421(00)00008-7.

Harris, C.D. (1990) NASA supercritical airfoils. *NASA Technical Paper*. (2969), pp. 1–76.

Helenbrook, B.T. (2003) Mesh deformation using the biharmonic operator. *International Journal for Numerical Methods in Engineering*. 56 (7), pp. 1007–1021. doi:10.1002/nme.595.

Hicks, R.M. and Henne, P.A. (1978) Wing design by numerical optimization. *Journal of Aircraft*. 15 (7), pp. 407–412.

Huang, L., Huang, P.G., LeBeau, R.P. and Hauser, T. (2004) Numerical Study of Blowing and Suction Control Mechanism on NACA0012 Airfoil. *Journal of Aircraft*. 41 (5), pp. 1005–1013. doi:10.2514/1.2255.

Hubel, T.Y., Riskin, D.K., Swartz, S.M. and Breuer, K.S. (2010) Wake structure and wing kinematics: the flight of the lesser dog-faced fruit bat, Cynopterus brachyotis. *The Journal of experimental biology*. 213 (Pt 20), pp. 3427–3440. doi:10.1242/jeb.043257.

Hue, D., François, C., Dandois, J. and Gebhardt, A. (2017) Simulations of an aircraft with constant and pulsed blowing flow control at the engine / wing junction. *Aerospace Science and Technology*. 69 pp. 659–673. doi:10.1016/j.ast.2017.07.031.

ICAO (2017) *Presentation of 2017 Air Transport Statistical Results*. Available from: https://www.icao.int/annual-report-2017/Pages/the-world-of-air-transport-in-2017-statistical-results.aspx.

Ismail, N.I., Zulkifli, A.H., Abdullah, M.Z., Hisyam Basri, M. and Shah Abdullah, N. (2013) Computational aerodynamic analysis on perimeter reinforced (PR)-compliant wing. *Chinese Journal of Aeronautics*. 26 (5), pp. 1093–1105. doi:10.1016/j.cja.2013.09.001.

Jacobs, E., Ward, K. and Pinkerton, R. (1933) The characteristics of 78 related airfoil sections from tests in the variable-density wind tunnel. *National Advisory Committee for Aeronautics*. pp. 299–354. doi:10.1017/CBO9781107415324.004.

Jameson, A., Martinelli, L. and Pierce, N.A. (1998) Optimum Aerodynamic Design

Using the Navier-Stokes Equations. *Theoretical and Computational Fluid Dynamics*. 10 (1–4), pp. 213–237. doi:10.1007/s001620050060.

Jasak, H., Jemcov, A. and Tukovic, Z. (2007) OpenFOAM : A C ++ Library for Complex Physics Simulations. In: *International Workshop on Coupled Methods in Numerical Dynamics*. 2007 Dubrovnik, Croatia: IUC. pp. 1–20.

Javed, A., Djijdeli, K. and Xing, J.T. (2016) A coupled meshfree-mesh-based solution scheme on hybrid grid for flow-induced vibrations. *Acta Mechanica*. 227 (8), pp. 2245–2274. doi:10.1007/s00707-016-1614-5.

Jenett, B., Calisch, S., Cellucci, D., Cramer, N., Gershenfeld, N., Swei, S. and Cheung, K.C. (2016) Digital Morphing Wing: Active Wing Shaping Concept Using Composite Lattice-Based Cellular Structures. *Soft Robotics*. 00 (00), pp. soro.2016.0032. doi:10.1089/soro.2016.0032.

Jodin, G., Motta, V., Scheller, J., Duhayon, E., Döll, C., Rouchon, J.F. and Braza, M. (2017) Dynamics of a hybrid morphing wing with active open loop vibrating trailing edge by time-resolved PIV and force measures. *Journal of Fluids and Structures*. 74 pp. 263–290. doi:10.1016/j.jfluidstructs.2017.06.015.

Johnston, C., Neal, D., Wiggins, L., Robertshaw, H., Mason, W. and Inman, D. (2003) A Model to Compare the Flight Control Energy Requirements of Morphing and Conventionally Actuated Wings. In: *44th AIAA/ASME/ASCE/AHS/ASC Structures, Structural Dynamics, and Materials Conference*. 7 April 2003 Reston, Virigina: American Institute of Aeronautics and Astronautics. doi:10.2514/6.2003-1716.

Jones, G., Santer, M., Debiasi, M. and Papadakis, G. (2018) Control of flow separation around an airfoil at low Reynolds numbers using periodic surface morphing. *Journal of Fluids and Structures*. 76 pp. 536–557. doi:10.1016/j.jfluidstructs.2017.11.008.

Jones, G., Santer, M. and Papadakis, G. (2018) Control of low Reynolds number flow around an airfoil using periodic surface morphing: A numerical study. *Journal of Fluids and Structures*. 76 pp. 95–115. doi:10.1016/j.jfluidstructs.2017.09.009.

Jukes, T.N. and Choi, K.-S. (2009) Flow control around a circular cylinder using pulsed dielectric barrier discharge surface plasma. *Physics of Fluids*. 21 (8), pp. 084103. doi:10.1063/1.3194307.

Jung, Y.-Y. and Kim, J.-H. (2011) Unsteady Subsonic Aerodynamic Characteristics of Wing in Fold Motion. *International Journal of Aeronautical and Space Sciences*. 12 (1), pp. 63–68. doi:10.5139/IJASS.2011.12.1.63.

Jung, Y.Y. and Kim, J.H. (2013) Aeroelastic Behavior of Morphing Wing in Flutter Regions. *Applied Mechanics and Materials*. 284–287 pp. 442–445.

doi:10.4028/www.scientific.net/AMM.284-287.442.

Kamliya Jawahar, H., Ai, Q. and Azarpeyvand, M. (2018) Aerodynamic and Aeroacoustic Performance of Airfoils Fitted with Morphing Trailing-edges. *2018 AIAA/CEAS Aeroacoustics Conference*. doi:10.2514/6.2018-2815.

Kamliya Jawahar, H., Ai, Q. and Azarpeyvand, M. (2017) Experimental and Numerical Investigation of Aerodynamic Performance of Airfoils Fitted with Morphing Trailing-edges. In: *23rd AIAA/CEAS Aeroacoustics Conference*. 5 June 2017 Reston, Virginia: American Institute of Aeronautics and Astronautics. doi:10.2514/6.2017-3371.

Kansa, E.J. (1990) Multiquadrics-A scattered data approximation scheme with applications to computational fluid-dynamics-II solutions to parabolic, hyperbolic and elliptic partial differential equations. *Computers and Mathematics with Applications*. 19 (8–9), pp. 147–161. doi:10.1016/0898-1221(90)90271-K.

Karagiannis, D., Stamatelos, D., Spathopoulos, T., Solomou, A., Machairas, T., Chrysohoidis, N., Saravanos, D. and Kappatos, V. (2014) Airfoil morphing based on SMA actuation technology. *Aircraft Engineering and Aerospace Technology*. 86 (4), pp. 295–306. doi:10.1108/AEAT-10-2012-0194.

Kato, C., Iida, A., Takano, Y., Fujita, H. and Ikegawa, M. (1993) Numerical prediction of aerodynamic noise radiated from low Mach number turbulent wake. In: *31st Aerospace Sciences Meeting*. 11 January 1993 Reston, Virigina: American Institute of Aeronautics and Astronautics. doi:10.2514/6.1993-145.

Katz, A.J. (2009) *Meshless Methods for Computational Fluid Dynamics*. PhD, Stanford University.

Kaul, U.K. and Nguyen, N.T. (2015) A 3-D Drag Optimization Study of Variable Camber Continuous Trailing Edge Flap (VCCTEF) Using OVERFLOW. *33rd AIAA Applied Aerodynamics Conference*. (June), pp. 1–20. doi:10.2514/6.2015-2422.

Kaul, U.K. and Nguyen, N.T. (2016) Lift Optimization Study of a Multi-Element Three-Segment Variable Camber Airfoil. *34th AIAA Applied Aerodynamics Conference*. (June), pp. 1–22. doi:10.2514/6.2016-3569.

Kegerise, M.A., Cabell, R.H. and Cattafesta, L.N. (2007) Real-time feedback control of flow-induced cavity tones-Part 1: Fixed-gain control. *Journal of Sound and Vibration*. 307 (3–5), pp. 906–923. doi:10.1016/j.jsv.2007.07.063.

Keil, T.A. (1997) Functional morphology of insect mechanoreceptors. *Microscopy Research and Technique*. 39 (6), pp. 506–531. doi:110.1002/(SICI)1097-0029(19971215)39:6<506::AID-JEMT5>3.0.CO;2-B.

Khorrami, M.R., Humphreys, W.M., Lockard, D.P. and Ravetta, P.A. (2014a) Aeroacoustic Evaluation of Flap and Landing Gear Noise Reduction Concepts. In: *20th AIAA/CEAS Aeroacoustics Conference*. 16 June 2014 Atlanta, USA: American Institute of Aeronautics and Astronautics. pp. 1–28. doi:10.2514/6.2014-2478.

Khorrami, M.R., Lockard, D.P., Moore, J.B., Su, J., Turner, T.L., Lin, J.C., Taminger, K.M., Kahng, S.K. and Verden, S.A. (2014b) *Elastically deformable side-edge link for trailing-edge flap aeroacoustic noise reduction*. National Aeronautics and Space Administration (NASA), U.S. Patent 8,695,925.

Kim, H. and Liou, M. (2019) Flow simulation and drag decomposition study of N3-X hybrid wing-body configuration. *Aerospace Science and Technology*. 85 pp. 24–39. doi:10.1016/j.ast.2018.11.047.

Knupp, P.M. (2003) Algebraic Mesh Quality Metrics. *SIAM Journal on Scientific Computing*. 23 (1), pp. 193–218. doi:10.1137/s1064827500371499.

Knupp, P.M. (2007) Remarks on Mesh Quality. In: *45th AIAA Aerospace Sciences Meeting and Exhibit*. 2007 Reno, NV: . pp. 7–10.

Koomullil, R.P. and Soni, B.K. (2012) Flow simulation using generalized static and dynamic grids. *AIAA Journal*. 37 (12), pp. 1551–5557. doi:10.2514/3.14356.

Koreanschi, A., Oliviu, S.G. and Botez, R.M. (2014) New Numerical Study of Boundary Layer Behavior on A Morphing Wing-with-Aileron System. *32nd AIAA Applied Aerodynamics Conference*. (June), pp. 1–18. doi:10.2514/6.2014-3170.

Koreanschi, A., Sugar Gabor, O., Acotto, J., Brianchon, G., Portier, G., Botez, R.M., Mamou, M. and Mebarki, Y. (2017) Optimization and design of an aircraft's morphing wing-tip demonstrator for drag reduction at low speed, Part I – Aerodynamic optimization using genetic, bee colony and gradient descent algorithms. *Chinese Journal of Aeronautics*. 30 (1), pp. 149–163. doi:10.1016/j.cja.2016.12.013.

Kota, S., Hetrick, J. and Osborn, R. (2003) Design and application of compliant mechanisms for morphing. *24 Smart Structures and Materials 2003:* 5054 (734), pp. 24–33. doi:10.1117/12.483869.

Kota, S., Osborn, R., Ervin, G., Maric, D., Flick, P. and Paul, D. (2006) Mission Adaptive Compliant Wing – Design , Fabrication and Flight Test Mission Adaptive Compliant Wing. *Rtompavt*. pp. 1–19.

Krzysiak, A. and Narkiewicz, J. (2006) Aerodynamic Loads on Airfoil with Trailing-Edge Flap Pitching with Different Frequencies. *Journal of Aircraft*. 43 (2), pp. 407–418. doi:10.2514/1.15597.

Kudva, J.N. (2004) Overview of the DARPA smart wing project. *Journal of Intelligent Material Systems and Structures*. 15 (4), pp. 261–267. doi:10.1177/1045389X04042796.

Kulfan, B. and Bussoletti, J. (2006) 'Fundamental' Parameteric Geometry Representations for Aircraft Component Shapes. In: *11th AIAA/ISSMO Multidisciplinary Analysis and Optimization Conference*. 2006 pp. 547–591. doi:10.2514/6.2006-6948.

La, S., Joe, W.Y., Akbar, M. and Alsaidi, B. (2018) *Surveys on Skin Design for Morphing Wing Aircraft: Status and Challenges*. (January), pp. 1–22. doi:10.2514/6.2018-0315.

Lachenal, X., Daynes, S. and Weaver, P.M. (2013) Review of morphing concepts and materials for wind turbine blade applications. *Wind Energy*. 16 (2), pp. 283–307. doi:10.1002/we.531.

Ladson, C.L. (1988) Effects of independent variation of Mach and Reynolds numbers on the low-speed aerodynamic characteristics of the NACA 0012 airfoil section. *Nasa Tm 4074*. (4074), pp. 97. doi:10.1007/s13398-014-0173-7.2.

Lamar, J.E. and Herbert, H.E. (1982) *Production version of the extended NASA-Langley Vortex Lattice FORTRAN computer program. Volume 1: User's guide*.

Lampton, A., Niksch, A. and Valasek, J. (2010) Reinforcement learning of a morphing airfoil-policy and discrete learning analysis. *Journal of Aerospace Computing, Information, and Communication*. 7 (8), pp. 241–260.

Lane, K. and Marshall, D. (2010) Inverse Airfoil Design Utilizing CST Parameterization. In: *48th AIAA Aerospace Sciences Meeting Including the New Horizons Forum and Aerospace Exposition*. 4 January 2010 Reston, Virigina: American Institute of Aeronautics and Astronautics. pp. 2010. doi:10.2514/6.2010-1228.

Lane, K. and Marshall, D. (2009) A Surface Parameterization Method for Airfoil Optimization and High Lift 2D Geometries Utilizing the CST Methodology. *47th AIAA Aerospace Sciences Meeting including The New Horizons Forum and Aerospace Exposition*. (January), . doi:10.2514/6.2009-1461.

Langtry, R. and Menter, F. (2005) Transition Modeling for General CFD Applications in Aeronautics. In: *43rd AIAA Aerospace Sciences Meeting and Exhibit*. 10 January 2005 Reston, Virigina: American Institute of Aeronautics and Astronautics. pp. 522. doi:10.2514/6.2005-522.

Lee, T. and Gerontakos, P. (2004) Investigation of flow over an oscillating airfoil. *Journal of Fluid Mechanics*. 512 pp. 313–341. doi:10.1017/S0022112004009851.

Lee, T. and Gerontakos, P. (2009) Unsteady Airfoil with Dynamic Leading- and Trailing-Edge Flaps. *Journal of Aircraft*. 46 (3), pp. 1076–1081. doi:10.2514/1.42431.

Li, D., Zhao, S., Da Ronch, A., Xiang, J., Drofelnik, J., Li, Y., Zhang, L., Wu, Y., Kintscher, M., Monner, H.P., Rudenko, A., Guo, S., Yin, W., Kirn, J., et al. (2018) A review of modelling and analysis of morphing wings. *Progress in Aerospace Sciences*. 100 (June), pp. 46–62. doi:10.1016/j.paerosci.2018.06.002.

Liggett, N. and Smith, M.J. (2013) The physics of modeling unsteady flaps with gaps. *Journal of Fluids and Structures*. 38 pp. 255–272. doi:10.1016/j.jfluidstructs.2012.12.010.

Lighthill, M.J. (1952) On sound generated aerodynamically I. General theory. In: *Proc. R. Soc. Lond. A*. 1952 (no place) The Royal Society. pp. 564–587.

Liu, G.R. (2012) *Meshfree Methods: Moving Beyond the Finite Element Method, Second Edition*. CRC press.

Liu, G.R. and Liu, M.B. (2003) *Smoothed Particle Hydrodynamics - A Meshfree Particle Method*. World Scientific Publishing Co. Pte. Ltd.

Liu, X., Qin, N. and Xia, H. (2006) Fast dynamic grid deformation based on Delaunay graph mapping. *Journal of Computational Physics*. 211 (2), pp. 405–423. doi:10.1016/j.jcp.2005.05.025.

Lockard, D.P. (2000) Efficient, two-dimensional implementation of the Ffowcs Williams and Hawkings equation. *Journal of Sound and Vibration*. 229 (4), pp. 897–911. doi:10.1006/jsvi.1999.2522.

Luke, E., Collins, E. and Blades, E. (2012) A fast mesh deformation method using explicit interpolation. *Journal of Computational Physics*. 231 (2), pp. 586–601. doi:10.1016/j.jcp.2011.09.021.

Lynch, D.R. and O'Neill, K. (1980) Elastic grid deformation for moving boundary problems in two space dimensions. *Finite elements in water resources*. 2 .

Lyu, Z. and Martins, J.R.R.A. (2015) Aerodynamic Shape Optimization of an Adaptive Morphing Trailing-Edge Wing. *Journal of Aircraft*. 52 (6), pp. 1951–1970. doi:10.2514/1.C033116.

Macaraeg, M. (1998) Fundamental investigations of airframe noise. In: *4th AIAA/CEAS Aeroacoustics Conference*. 2 June 1998 Toulouse, France: American Institute of Aeronautics and Astronautics. pp. 123–132. doi:10.2514/6.1998-2224.

Macphee, D.W. and Beyene, A. (2019) Performance analysis of a small wind turbine equipped with fl exible blades. *Renewable Energy*. 132 pp. 497–508.

doi:10.1016/j.renene.2018.08.014.

Marques, M., Gamboa, P. and Andrade, E. (2009) Design of a Variable Camber Flap for Minimum Drag and Improved Energy Efficiency. *50th AIAA/ASME/ASCE/AHS/ASC Structures, Structural Dynamics, and Materials Conference*. (May), pp. 1–19. doi:doi:10.2514/6.2009-2196.

Martinz, A., Catalano, F., Martinz, A. and Catalano, F. (1997) Aerodynamic optimization study of a mission adaptive wing for transport aircraft. In: *15th Applied Aerodynamics Conference* Fluid Dynamics and Co-located Conferences. 23 June 1997 (no place) American Institute of Aeronautics and Astronautics. doi:10.2514/6.1997-2272.

Di Matteo, N., Guo, S., Ahmed, S. and Li, D. (2010) Design and Analysis of a Morphing Flap Structure for High Lift Wing. In: *51st AIAA/ASME/ASCE/AHS/ASC Structures, Structural Dynamics, and Materials Conference*. 12 April 2010 Reston, Virigina: American Institute of Aeronautics and Astronautics. pp. 1–12. doi:10.2514/6.2010-3096.

McGowan, A.-M.R., Washburn, A.E., Horta, L.G. and Bryant, R.G. (2002) Recent Results from NASA's Morphing Project. *SPIE's 9th Annual International Symposium on Smart Structures and Materials*. 4698 pp. 115. doi:10.1117/12.475056.

Medina, A. and Hemati, M. (2018) Separated Flow Response to Rapid Flap Deflection. In: *2018 AIAA Aerospace Sciences Meeting*. 8 January 2018 Reston, Virginia: American Institute of Aeronautics and Astronautics. pp. 1–15. doi:10.2514/6.2018-0574.

Medina, A., Ol, M. V., Mancini, P. and Jones, A. (2017) Revisiting Conventional Flaps at High Deflection Rate. *AIAA Journal*. 55 (8), pp. 2676–2685. doi:10.2514/1.J055754.

Melin, T. (2000) *A vortex lattice MATLAB implementation for linear aerodynamic wing applications*. Master thesis, Royal Institute of Technology, Sweden.

Menter, F. (2016) Stress-blended eddy simulation (SBES)—A new paradigm in hybrid RANS-LES modeling. In: *Notes on Numerical Fluid Mechanics and Multidisciplinary Design*. (no place) Springer. pp. 27–37. doi:10.1007/978-3-319-70031-1_3.

Menter, F.R. (2012) Best Practice: Scale-Resolving Simulations in ANSYS CFD. *ANSYS Inc.* (April), pp. 1–70. doi:10.1155/2013/859465.

Menter, F.R. (1994) Two-equation eddy-viscosity turbulence models for engineering applications. *AIAA Journal*. 32 (8), pp. 1598–1605. doi:10.2514/3.12149.

Moeng, C.-H. (1984) A Large-Eddy-Simulation Model for the Study of Planetary

Boundary-Layer Turbulence. *Journal of the Atmospheric Sciences*. 41 (13), pp. 2052–2062. doi:10.1175/1520-0469(1984)041<2052:ALESMF>2.0.CO;2.

Monner, H.P., Breitbach, E., Bein, T. and Hanselka, H. (2000) Design aspects of the adaptive wing - the elastic trailing edge and the local spoiler bump. *Aeronautical Journal*. 104 (1032), pp. 89–95. doi: 10.1017/S0001924000017814.

Moosavian, A., Chae, E.J., Pankonien, A.M., Lee, A.J. and Inman, D.J. (2017) *A parametric study on a bio-inspired continuously morphing trailing edge*. 10162 pp. 1016204. doi:10.1117/12.2257582.

Muijres, F.T., Johansson, L.C. and Hedenstrom, A. (2012) Leading edge vortex in a slow-flying passerine. *Biology Letters*. 8 (4), pp. 554–557. doi:10.1098/rsbl.2012.0130.

NASA (2009) *21st Century Aerospace Vehicle*. Available from: www.nasa.gov/centers/dryden/multimedia/imagegallery/Morph/ED01-0348-1.html [Accessed 8 August 2018].

NASA (2015) *F-111 Advanced Fighter Technology Integration*. Available from: www.nasa.gov/centers/dryden/multimedia/imagegallery/F-111AFTI/EC85-33205-07.html [Accessed 8 August 2018].

NASA (2017) *Hear This: 30 Percent Less Noise*. Available from: https://www.nasa.gov/centers/armstrong/feature/ACTE_30_percent_less_noise.html.

NASA (2006) *NASA Dryden Fact Sheet - X-5*. Available from: https://www.nasa.gov/centers/armstrong/news/FactSheets/FS-081-DFRC.html.

Nash, E.C., Lowson, M. V. and Mcalpine, A. (1999) Boundary-layer instability noise on aerofoils. *Journal of Fluid Mechanics*. 382 (1999), pp. S002211209800367X. doi:10.1017/S002211209800367X.

Nguyen, N. (2010) Project Elastically Shaped Future Air Vehicle Concept. *NASA Innovation Fund Award*.

Ni, Y., Hou, C., Wan, X. and Zhao, M. (2015) Transient Aeroelastic Responses of Folding Wing in Morphing Motion. In: *Proceedings of the 2015 International Conference on Advances in Mechanical Engineering and Industrial Informatics*. 2015 Paris, France: Atlantis Press. doi:10.2991/ameii-15.2015.253.

Nicassio, F., Scarselli, G., Pinto, F., Ciampa, F., Iervolino, O. and Meo, M. (2018) Low energy actuation technique of bistable composites for aircraft morphing. *Aerospace Science and Technology*. 75 pp. 35–46.

doi:10.1016/j.ast.2017.12.040.

Obradovic, B. and Subbarao, K. (2012) Modeling and Simulation of Morphing Wing Aircraft. *Morphing Aerospace Vehicles and Structures*. 48 (2), pp. 87–125. doi:10.1002/9781119964032.ch5.

Obradovic, B. and Subbarao, K. (2011) Modeling of Flight Dynamics of Morphing Wing Aircraft. *Journal of Aircraft*. 48 (2), pp. 391–402. doi:10.2514/1.C000269.

Orselli, R., Meneghini, J. and Saltara, F. (2009) Two and Three-Dimensional Simulation of Sound Generated by Flow Around a Circular Cylinder. In: *15th AIAA/CEAS Aeroacoustics Conference (30th AIAA Aeroacoustics Conference)*. 11 May 2009 Miami,Florida, USA: American Institute of Aeronautics and Astronautics. pp. 3270. doi:10.2514/6.2009-3270.

Parker, H.F. (1920) The Parker variable camber wing *National Advisory Committee for Aeronautics (NACA)* (Report No. 77). doi:10.1038/scientificamerican11011920-264supp.

Paterson, R.W., Vogt, P.G., Fink, M.R. and Munch, C.L. (1973) Vortex noise of isolated airfoils. *Journal of Aircraft*. 10 (5), pp. 296–302. doi:10.2514/3.60229.

Peter, F. and Stumpf, E. (2018) *Chapter 3 - The Development of Morphing Aircraft Benefit Assessment*. In: Antonio Concilio, Ignazio Dimino, Leonardo Lecce, and Rosario B T - Morphing Wing Technologies Pecora (eds.). (no place) Butterworth-Heinemann. pp. 103–121. doi:https://doi.org/10.1016/B978-0-08-100964-2.00003-4.

Piegl, L. and Tiller, W. (1996) The NURBS Book *Computer-Aided Design* 28 (8) p.pp. 665–666. doi:10.1016/0010-4485(96)86819-9.

Popov, A. V., Grigorie, L.T., Botez, R.M., Mamou, M. and Mébarki, Y. (2010) Closed-Loop Control Validation of a Morphing Wing Using Wind Tunnel Tests. *Journal of Aircraft*. 47 (4), pp. 1309–1317. doi:10.2514/1.47281.

Popov, A.V., Botez, R.M., West, N.D., Mamou, M., Mébarki, Y., Jahrhaus, B., Khalid, M. and Grigorie, L.T. (2009) Drag Reduction by Improving Laminar Flows Past Morphing Configurations. In: *AVT-168 NATO Symposium on Morphing Vehicles*. Evora, Portugal: . pp. 1–12.

Potsdam, M.A. and Guruswamy, G.P. (2001) A parallel multiblock mesh movement scheme for complex aeroelastic applications. *AIAA Paper*. (January), pp. 1–14. doi:10.2514/6.2001-716.

Rašuo, B. and Jazarević, V. (2017) Numerical Prediction of Aerodynamic Noise Generated from an Aircraft in Low Mach Number Flight Zhongyi Huang, Martin Stynes, and Zhimin Zhang (eds.). *PAMM*. 17 (1), pp. 685–686.

doi:10.1002/pamm.201710311.

Rauleder, J., Ondra, V. and Komp, D. (2018) Aerodynamic Performance of Morphing Blades and Rotor Systems. *AHS International 74th Annual Forum & Technology Display*. (July).

Reuther, J. and Jameson, A. (1995) A Comparison of Design Variables for Control Theory Based Airfoil Optimization *Technical Report, NASA Research Institute for Advanced Computer Science*.

Reynolds, O. (1895) On the Dynamical Theory of Incompressible Viscous Fluids and the Determination of the Criterion. *Philosophical Transactions of the Royal Society A: Mathematical, Physical and Engineering Sciences*. 186 (0), pp. 123–164. doi:10.1098/rsta.1895.0004.

Rivero, A.E., Fournier, S., Weaver, P.M., Cooper, J.E. and Woods, B.K.S. (2018) Manufacturing and characterisation of a composite FishBAC morphing wind tunnel model. In: *ICAST 2018: 29th International Conference on Adaptive Structures and Technologies*. 2018 Seoul, South korea: . pp. 1–14.

Rocha dos Santos, A.G., Caselato de Sousa, G.L., Sanches, A.C., Santos, O., Rade, D.A. and de Paula, A.A. (2018) Chordwise Actuation Effects on NACA 0012 Morphing Airfoils. In: *2018 Applied Aerodynamics Conference* AIAA AVIATION Forum. (no place) American Institute of Aeronautics and Astronautics. doi:10.2514/6.2018-3957.

SABRE (2018) *SABRE Research Project*. Available from: https://sabreproject.eu/#header [Accessed 15 April 2019].

Sagaut, P. (2006) *Large eddy simulation for incompressible flows: an introduction*. Springer Science & Business Media.

Samareh, J. (1999) A survey of shape parameterization techniques. *NASA Conference Publication*. (June), pp. 333–343. doi:10.2514/3.50489.

Samareh, J. (2000) Multidisciplinary aerodynamic-structural shape optimization using deformation (MASSOUD). In: *8th Symposium on Multidisciplinary Analysis and Optimization*. 2000 pp. 4911. doi:10.2514/6.2000-4911.

Samareh, J.A. (2001) Survey of shape parameterization techniques for high-fidelity multidisciplinary shape optimization. *AIAA Journal*. 39 (5), pp. 877–884. doi:10.2514/3.14814.

Sanders, B., Eastep, F.E. and Forster, E. (2003) Aerodynamic and Aeroelastic Characteristics of Wings with Conformal Control Surfaces for Morphing Aircraft. *Journal of Aircraft*. 40 (1), pp. 94–99. doi:10.2514/2.3062.

Scheller, J., Chinaud, M., Rouchon, J.F., Duhayon, E., Cazin, S., Marchal, M. and Braza, M. (2015) Trailing-edge dynamics of a morphing NACA0012 aileron

at high Reynolds number by high-speed PIV. *Journal of Fluids and Structures*. 55 (5213), pp. 42–51. doi:10.1016/j.jfluidstructs.2014.12.012.

Secanell, M., Gamboa, P. and Suleman, A. (2006) Design of a Morphing Airfoil Using Aerodynamic Shape Optimization. *AIAA Journal*. 44 (7), pp. 1550–1562. doi:10.2514/1.18109.

Sederberg, T.W. and Parry, S.R. (1986) Free-form deformation of solid geometric models. *ACM SIGGRAPH Computer Graphics*. 20 (4), pp. 151–160. doi:10.1145/15886.15903.

Seifert, A., Eliahu, S., Greenblatt, D. and Wygnanski, I. (1998) Use of Piezoelectric Actuators for Airfoil Separation Control. *AIAA Journal*. 36 (8), pp. 1535–1537. doi:10.2514/2.549.

Seigler, T.M. (2005) *Dynamics and control of morphing aircraft*.

Seigler, T.M., Neal, D.A., Bae, J.-S. and Inman, D.J. (2007) Modeling and Flight Control of Large-Scale Morphing Aircraft. *Journal of Aircraft*. 44 (4), pp. 1077–1087. doi:10.2514/1.21439.

Selim, M. and Koomullil, R. (2016) Mesh Deformation Approaches – A Survey *Journal of Physical Mathematics* 7 (2). doi:10.4172/2090-0902.1000181.

Seo, J.H. and Moon, Y.J. (2007) Aerodynamic noise prediction for long-span bodies. *Journal of Sound and Vibration*. 306 (3–5), pp. 564–579. doi:10.1016/j.jsv.2007.05.042.

Sheldahl, R.E. and Klimas, P.C. (1981) Aerodynamic characteristics of seven symmetrical airfoil sections through 180-degree angle of attack for use in aerodynamic analysis of vertical axis wind turbines. *Chemistry &* SAND80-211 pp. 118. doi:10.2172/6548367.

Silva, W.A. and Bartels, R.E. (2004) Development of reduced-order models for aeroelastic analysis and flutter prediction using the CFL3Dv6. 0 code. *Journal of Fluids and Structures*. 19 (6), pp. 729–745.doi: 10.1016/j.jfluidstructs.2004.03.004.

Singer, B.A., Lockard, D.P. and Brentner, K.S. (2000) Computational Aeroacoustic Analysis of Slat Trailing-Edge Flow. *AIAA Journal*. 38 (9), pp. 1558–1564. doi:10.2514/2.1177.

Smagorinsky, J. (1963) General Circulation Experiments With the Primitive Equations. *Monthly Weather Review*. 91 (3), pp. 99–164. doi:10.1175/1520-0493(1963)091<0099:gcewtp>2.3.co;2.

Smith, K., Butt, J., von Spakovsky, M. and Moorhouse, D. (2007) A Study of the Benefits of Using Morphing Wing Technology in Fighter Aircraft Systems. In: *39th AIAA Thermophysics Conference* Fluid Dynamics and Co-located

Conferences. 25 June 2007 Reston, Virigina: American Institute of Aeronautics and Astronautics. pp. 1–12. doi:10.2514/6.2007-4616.

Smith, S.B. and Nelson, D.W. (1990) Determination of the Aerodynamic Characteristics of the Mission Adaptive Wing. *Journal of Aircraft*. 27 (11), pp. 950–958. doi:10.2514/3.45965.

Smithsonian (1899) *Wing-Warping Concept*. Available from: airandspace.si.edu/multimedia-gallery/5791hjpg?id=5791 [Accessed 8 August 2018].

Sobester, A. (2015) *Aircraft Geometry Codes - Parametric Models for Optimization, scripte in Python, Rhino and Matlab*. Available from: https://aircraftgeometrycodes.wordpress.com/author/sobester/ [Accessed 27 January 2017].

Sóbester, A. and Forrester, A.I.J. (2014) Aircraft Aerodynamic Design: Geometry and Optimization. *Aircraft Aerodynamic Design: Geometry and Optimization*. pp. 1–246. doi:10.1002/9781118534748.

Sobieczky, H. (1999) Parametric Airfoils and Wings. *Recent Development of Aerodynamic Design Methodologies. Inverse Design and Optimization: Notes on Numerical Fluid Mechanics, Vol. 68*. 68 pp. 71–87. doi:10.1007/978-3-322-89952-1_4.

Spadoni, A. and Ruzzene, M. (2007) Static aeroelastic response of chiral-core airfoils. *Journal of Intelligent Material Systems and Structures*. 18 (10), pp. 1067–1075. doi:10.1177/1045389X06072361.

Spalart, P.R. (2009) Detached-Eddy Simulation. *Annual Review of Fluid Mechanics*. 41 (1), pp. 181–202. doi:10.1146/annurev.fluid.010908.165130.

Spalart, P.R., Jou, W.-H., Stretlets, M. and Allmaras, S.R. (1997) Comments on the Feasibility of LES for Wings and on the Hybrid RANS/LES Approach, Advances in DNS/LES. In: *Proceedings of the First AFOSR International Conference on DNS/LES*. 1997 LA, USA: Greyden Press. pp. 4–8.

Spalart, Pr. and Allmaras, S. (1992) A one-equation turbulence model for aerodynamic flows. In: *30th aerospace sciences meeting and exhibit*. 1992 pp. 439. doi:10.2514/6.1992-439.

Stanewsky, E. (2001) Adaptive wing and flow control technology. *Progress in Aerospace Sciences*. 37 (7), pp. 583–667. doi:10.1016/S0376-0421(01)00017-3.

Şugar Gabor, O., Koreanschi, A. and Botez, R.M. (2016) A new non-linear vortex lattice method: Applications to wing aerodynamic optimizations. *Chinese Journal of Aeronautics*. 29 (5), pp. 1178–1195. doi:10.1016/j.cja.2016.08.001.

Şugar Gabor, O., Koreanschi, A., Botez, R.M., Mamou, M. and Mebarki, Y. (2016) Numerical simulation and wind tunnel tests investigation and validation of a morphing wing-tip demonstrator aerodynamic performance. *Aerospace Science and Technology*. 53 pp. 136–153. doi:10.1016/j.ast.2016.03.014.

Szodruch, J. and Hilbig, R. (1988) Variable wing camber for transport aircraft *Progress in Aerospace Sciences* 25 (3) p.pp. 297–328. doi:10.1016/0376-0421(88)90003-6.

Takahashi, H., Yokozeki, T. and Hirano, Y. (2016) Development of variable camber wing with morphing leading and trailing sections using corrugated structures. *Journal of Intelligent Material Systems and Structures*. 27 (20). doi:10.1177/1045389X16642298.

Takizawa, K., Henicke, B., Puntel, A., Spielman, T. and Tezduyar, T.E. (2012) Space-Time Computational Techniques for the Aerodynamics of Flapping Wings. *Journal of Applied Mechanics*. 79 (1), pp. 010903. doi:10.1115/1.4005073.

Le Tallec, P. and Mouro, J. (2001) Fluid structure interaction with large structural displacements. *Computer Methods in Applied Mechanics and Engineering*. 190 (24–25), pp. 3039–3067. doi:10.1016/S0045-7825(00)00381-9.

Taylor, G.K., Carruthers, A.C., Hubel, T.Y. and Walker, S.M. (2012) Wing Morphing in Insects, Birds and Bats: Mechanism and Function. In: *Morphing Aerospace Vehicles and Structures*. (no place) John Wiley & Sons, Ltd. pp. 11–40. doi:10.1002/9781119964032.ch2.

Thill, C., Downsborough, J.D., Lai, S.J., Bond, I.P. and Jones, D.P. (2010) Aerodynamic study of corrugated skins for morphing wing applications. *Aeronautical Journal*. 114 (1154), pp. 237–244. doi:10.1017/S0001924000003687.

Troldborg, N., Sørensen, J.N., Mikkelsen, R. and Sørensen, N.N. (2014) A simple atmospheric boundary layer model applied to large eddy simulations of wind turbine wakes. *Wind Energy*. 17 (4), pp. 657–669. doi:10.1002/we.1608.

Trümner, J. and Mundt, C. (2017) Comparison of Two Different CAA Methods for the Prediction of Far-Field Noise from Heated and Unheated Jets. In: *7th European Conference for Aeronautics and Aerospace Sciences*. 2017 Milan, Italy. pp. 1–14.

Tucker, V. a (1992) Pitching equilibrium, wing span and tail span in a gliding Harris' hawk, Parabuteo unicinctus. *J. Exp. Biol.* 165 pp. 21–41. 1477-9145.

Tucker, V.A. and Heine, C. (1990) Aerodynamics of Gliding Flight in a Harris' Hawk, Parabuteo Unicinctus. *Journal of Experimental Biology*. 149 pp. 469–489.

Urnes, J. and Nguyen, N. (2013) A Mission Adaptive Variable Camber Flap Control System to Optimize High Lift and Cruise Lift to Drag Ratios of Future N+3 Transport Aircraft. In: *AIAA-2013-214, Aerospace Sciences Meetings*. 2013 pp. 1–24. doi:10.2514/6.2013-214.

Valasek, J. (2012) *Morphing Aerospace Vehicles and Structures*. John Wiley & Sons.

Valasek, J., Doebbler, J., Tandale, M.D. and Meade, A.J. (2008) Improved Adaptive–Reinforcement Learning Control for Morphing Unmanned Air Vehicles. *IEEE Transactions on Systems, Man, and Cybernetics, Part B (Cybernetics)*. 38 (4), pp. 1014–1020. doi:10.1109/TSMCB.2008.922018.

Verstraete, M.L., Preidikman, S., Roccia, B.A. and Mook, D.T. (2015) A Numerical Model to Study the Nonlinear and Unsteady Aerodynamics of Bioinspired Morphing-Wing Concepts. *International Journal of Micro Air Vehicles*. 7 (3), pp. 327–345. doi:10.1260/1756-8293.7.3.327.

Walker, S.M., Thomas, A.L.R. and Taylor, G.K. (2010) Deformable wing kinematics in free-flying hoverflies. *Journal of the Royal Society, Interface / the Royal Society*. 7 (42), pp. 131–142. doi:10.1098/rsif.2009.0120.

Walker, S.M., Thomas, A.L.R. and Taylor, G.K. (2009) Deformable wing kinematics in the desert locust: how and why do camber, twist and topography vary through the stroke? *Journal of the Royal Society, Interface / the Royal Society*. 6 (38), pp. 735–747. doi:10.1098/rsif.2008.0435.

Wang, Z. and Przekwas, A. (1994) Unsteady flow computation using moving grid with mesh enrichment. In: *32nd Aerospace Sciences Meeting and Exhibit*. 10 January 1994 Reston, Virigina: American Institute of Aeronautics and Astronautics. doi:10.2514/6.1994-285.

Weisshaar, T. (2006) Morphing aircraft technology-new shapes for aircraft design. *Multifunctional Structures / Integration of Sensors and Antennas*. pp. O1-1 – O1-20. doi:10.14339/RTO-MP-AVT-141.

Williams, J.E.F. and Hawkings, D.L. (1969) Sound Generation by Turbulence and Surfaces in Arbitrary Motion. *Philosophical Transactions of the Royal Society A: Mathematical, Physical and Engineering Sciences*. 264 (1151), pp. 321–342. doi:10.1098/rsta.1969.0031.

Winant, C.D. and Browand, F.K. (1974) Vortex pairing : the mechanism of turbulent mixing-layer growth at moderate Reynolds number. *Journal of Fluid Mechanics*. 63 (02), pp. 237. doi:10.1017/S0022112074001121.

Wittmann, J., Steiner, H. and Sizmann, A. (2009) Framework for Quantitative Morphing Assessment on Aircraft System Level. In: *50th AIAA/ASME/ASCE/AHS/ASC Structures, Structural Dynamics, and Materials Conference*. 4 May 2009 Reston, Virigina: American Institute of Aeronautics

and Astronautics. pp. 1–18. doi:10.2514/6.2009-2129.

Wlezien, R., Horner, G., McGowan, A., Padula, S., Scott, M., Silcox, R. and Simpson, J. (1998) The Aircraft Morphing Program. *39th AIAA/ASME/ASCE/AHS/ASC Structures, Structural Dynamics, and Materials Conference and Exhibit*. 30 (5), pp. 176–187. doi:10.2514/6.1998-1927.

Wolf, W.R. and Lele, S.K. (2012) Trailing-Edge Noise Predictions Using Compressible Large-Eddy Simulation and Acoustic Analogy. *AIAA Journal*. 50 (11), pp. 2423–2434. doi:10.2514/1.J051638.

Wolff, T., Ernst, B. and Seume, J.R. (2014) Aerodynamic behavior of an airfoil with morphing trailing edge for wind turbine applications. *Journal of Physics: Conference Series*. 524 (1), pp. 012018. doi:10.1088/1742-6596/524/1/012018.

Woods, B.K.S., Fincham, J.H.S. and Friswell, M.I. (2014) Aerodynamic Modelling of the Fish Bone Active Camber Morphing Concept Aerodynamic Modelling of the Fish Bone Active Camber Morphing Concept. *RAeS Applied Aerodynamics Conference*. Vol. 25(7) (July), . doi:0.1177/1045389X14521700.

Woods, B.K.S., Bilgen, O. and Friswell, M.I. (2014) Aerodynamic Modelling of the Fish Bone Active Camber Morphing Concept. In: *Royal Aeronautical Society Conference on Advanced Aero Concepts, Designs and Operations*. 2014 Bristol, UK: . pp. 772–785.

Woods, B.K.S., Ajaj, R.M., Saavedra Flores, E.I., Friswell, M.I. and Allegri, G. (2013) Wind tunnel testing of the fish bone active camber morphing concept. *Journal of Intelligent Material Systems and Structures*. 22 (7), pp. 364–375. doi:10.1177/1045389X11411121.

Woods, B.K.S. and Friswell, M.I. (2012) Preliminary investigation of a fishbone active camber concept. In: *Proceedings of the ASME 2012 conference on smart materials, adaptive structures and intelligent systems*. 2012 Stone Mountain, Georgia, USA: . pp. 555–563.

Woods, B.K.S., Parsons, L., Coles, A.B., Fincham, J.H.S. and Friswell, M.I. (2016) Morphing elastically lofted transition for active camber control surfaces. *Aerospace Science and Technology*. 55 pp. 439–448. doi:10.1016/j.ast.2016.06.017.

Wootton, R.J. (2006) Geometry and mechanics of insect hindwing fans: a modelling approach. *Proceedings of the Royal Society of London. Series B: Biological Sciences*. 262 (1364), pp. 181–187. doi:10.1098/rspb.1995.0194.

Wootton, R.J., Evans, K.E., Herbert, R. and Smith, C.W. (2000) The hind wing of the desert locust (Schistocerca gregaria Forskål). I. Functional morphology and mode of operation. *Journal of Experimental Biology*. 203 pp. 2921–2931.

Zhang, G.Q. and M. Yu, S.C. (2012) Unsteady Aerodynamics of a Morphing Tandem-Wing Unmanned Aerial Vehicle. *Journal of Aircraft*. 49 (5), pp. 1315–1323. doi:10.2514/1.C031652.

Zhang, T. tian, Wang, Z. guo, Huang, W. and Yan, L. (2018) A review of parametric approaches specific to aerodynamic design process. *Acta Astronautica*. 145 (December 2017), pp. 319–331. doi:10.1016/j.actaastro.2018.02.011.

Zhu, F. and Qin, N. (2013) Intuitive Class/Shape Function Parameterization for Airfoils. *AIAA Journal*. 52 (1), pp. 17–25. doi:10.2514/1.j052610.

Appendix A. MATLAB code implementing the CST

A.1 Modified CST method for a morphing airfoil

As it was mentioned earlier, the CST has several characteristics that made it suitable for our application of the unsteady parametrisation of a morphing airfoil.

In order to introduce the variable terms, we need to know the class of morphing we are targeting:

i. Morphing for control

This type of morphing involves a morphing of a part of the wing responsible for the control of the aircraft, such us the morphing of the trailing edge with small continuous deformations in order to perform the mission attributed to flaps in classic configurations (Bourdin *et al.,* 2006).

This morphing strategy does not involve the change of the basic shape of the airfoil, but only the deflection of the trailing edge, and the same goes with the leading edge.

i. Morphing for mission adaptation or optimization

As opposed to the first strategy, this one involves the shape deformation of the airfoil in order for it to be suitable for a different type of mission (Bourdin *et al*., 2006).

An example of this is changing regime from long range to higher performances or higher manoeuvrability, to cope with the switch from a subsonic to supersonic regime where different classes of airfoils are more suitable or just in different phases of the flight such as taking off and landing.

A.1.1 Trailing edge deflection

We can introduce a function with a time variable to both surfaces in order to model the trailing edge deflection in the classic formulation of the CST upper and lower surfaces (2.12).

One of the properties of the CST method is that the higher the order of the term the closer to the x/c = 1 point, therefore for a trailing edge deflection the control term should of a higher order than the Bernstein's polynomials order with time dependent coefficient, which depends on how we want the morphing speed, frequency or amplitude.

An example of the term can be written as follow:

$$\zeta_{control}(\psi, t) = y(t)\psi^{kp} \tag{A.1}$$

where *y(t)* is a time dependant function to control the deflection rate and direction and k is a coefficient that insures a higher order of the function is achieved.

For instance, using $y(t) = -0.01t$, and using a 5th order Bernstein polynomial for both upper and lower surface and k = 3, a trailing edge thickness of 0.001ψ we get the following equations:

$$\begin{aligned}\zeta_u(\psi) = \sqrt{\psi} * (1-\psi)[&p_{u0} * (1-\psi)^5 + p_{u1}.5\psi * (1-\psi)^4 \\ &+ p_{u2}10\psi^2(1-\psi)^3 + p_{u3} * 10\psi^3 * (1-\psi)^2 \\ &+ p_{u4} * 5\psi^4.(1-\psi) + p_{u5} * \psi^5] \\ &+ p_{uLE}\psi.\sqrt{(1-\psi)}.(1-\psi)^4 - 0.01t.\psi^{15} \\ &+ 0.01.\psi\end{aligned} \tag{A.2}$$

$$\begin{aligned}&\zeta_l(\psi) = \sqrt{\psi} * (1-\psi)[p_{l0} * (1-\psi)^5 + p_{l1}.5\psi * (1-\psi)^4 + \\ &p_{l2}10\psi^2\,(1-\psi)^3 + p_{l3} * 10\psi^3 * (1-\psi)^2 + p_{l4} * 5\psi^4.(1- \\ &\psi) + p_{l5} * \psi^5] + p_{lLE}\psi.\sqrt{(1-\psi)}.(1-\psi)^4 - 0.01t.\psi^{15} + \\ &0.01.\psi\end{aligned}$$

The Bernstein coefficients can be obtained by a square fit method; Figure A.2 shows the unsteady trailing edge deflection of a unit airfoil.

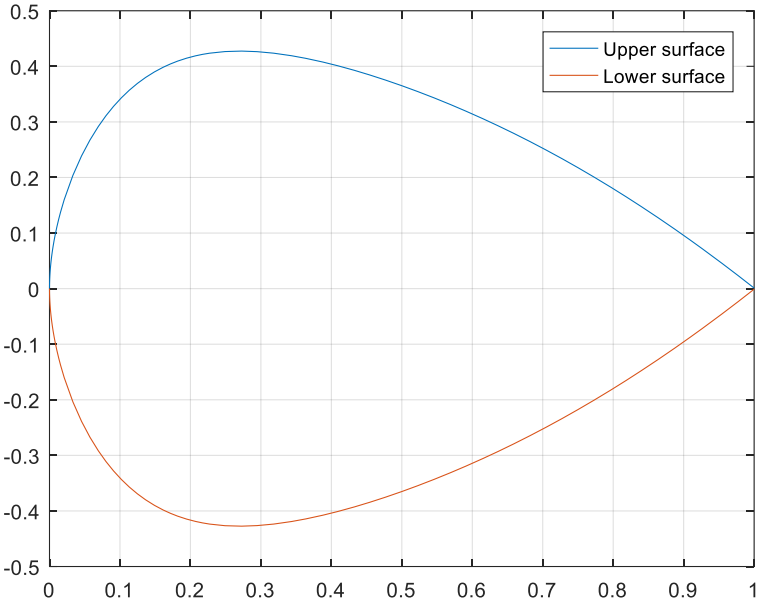

Figure A.1: Trailing edge of a unit airfoil at t = 0s.

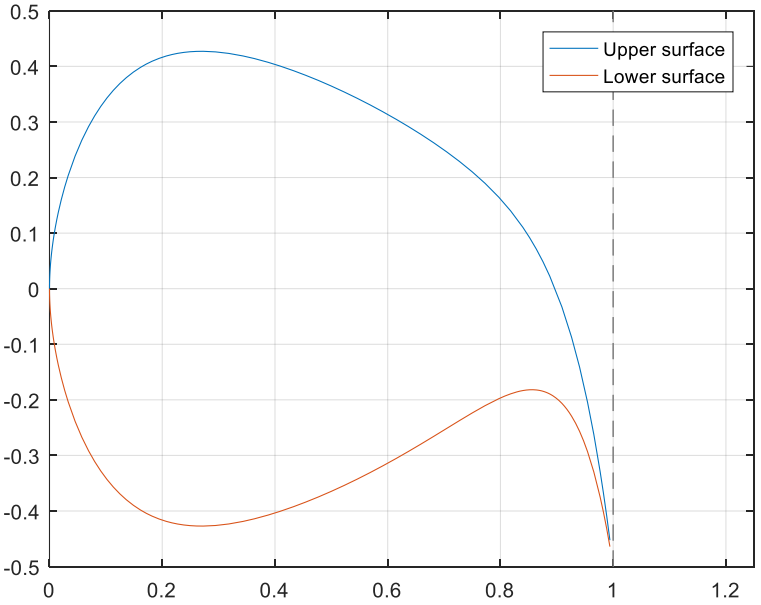

Figure A.2: Trailing edge a unit airfoil at t =50s.

To alter completely the shape of the airfoil, the coefficients must be changed to optimize the airfoil for the surrounding conditions or by targeting a specific airfoil.

For instance, if we have the starting coefficients of one airfoil and the ones we need to morph to, we can make every coefficient of the first airfoil change gradually to reach the coefficients of the second one therefore morph the first airfoil to the second one.

A.1.2 Thickness change with fixed camber

Another way to describe the airfoil is by separating the thickness and camber parts.

In order to obtain the upper surface, we addition the half camber function and the half thickness distribution and for the lower surface we subtract them.

The half thickness equation is using the CST coefficient as follow:

$$\zeta_t(\psi) = \psi^{0.5}.(1-\psi).0.5.\left[\sum_{i=0}^{p} \overline{(P_u(\iota) - P_l(\iota))}\binom{p}{i}\psi^i(1-\psi)^{p-i}\right] + 0.5.\psi.(\Delta\zeta_u - \Delta\zeta_l) + 0.5.x\sqrt{(1-x)}(P_{LE,u} - P_{LE,l})(1-x)^p \quad \text{(A.3)}$$

in addition, the half camber equation is as follow:

$$\zeta_c(\psi) = \psi^{0.5}.(1-\psi).0.5.\left[\sum_{i=0}^{p} \overline{(P_u(\iota) + P_l(\iota))}\binom{p}{i}\psi^i(1-\psi)^{p-i}\right] + 0.5.\psi.(\Delta\zeta_u + \Delta\zeta_l) + 0.5.x\sqrt{(1-x)}(P_{LE,u} + P_{LE,l})(1-x)^p \quad \text{(A.4)}$$

The upper and lower surface coordinates equation can be written as follow:

$$\zeta_u(\psi) = \zeta_t(\psi) + \zeta_c(\psi)$$
$$\zeta_u(\psi) = \zeta_t(\psi) + \zeta_c(\psi) \quad \text{(A.5)}$$

Using this formulation, we can separately act on different components of the airfoil while fixing the other component. Figure A.3 shows an unchanged NACA 23012 airfoil and Figure A.4 shows the change of the thickness with fixed camber, and Figure A.5 shows the change of the camber with fixed thickness.

A MATLAB code was written where the above method was implemented (Appendix A), and coupled with an open source Aircraft Geometry toolbox developed by (Sóbester and Forrester, 2014; Sobester, 2015) .

The CST coefficients of any desired airfoil are obtained from the toolbox, which is coupled with the CST equations to obtain the unsteady representations of the deformation desired. Figure A.4 and A.5 illustrate the trailing edge deformation of a NACA 23012 ,trailing-edge deflected and the lower part of the deformed leading edge of a NACA 2412.

A.1.3 Harmonic deformations

It is possible as well to include different periodic motions of the trailing edge for instance by using cosine or sine function in the control function.

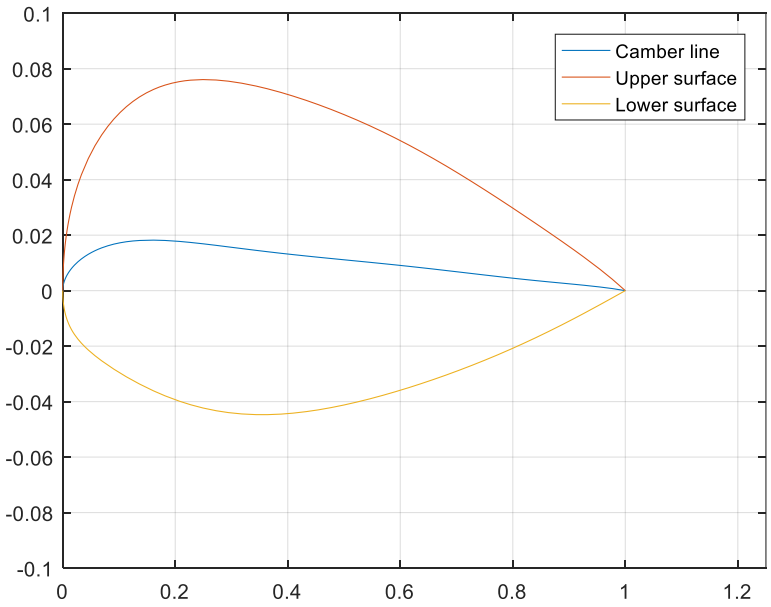

Figure A.3: None deformed NACA 23012.

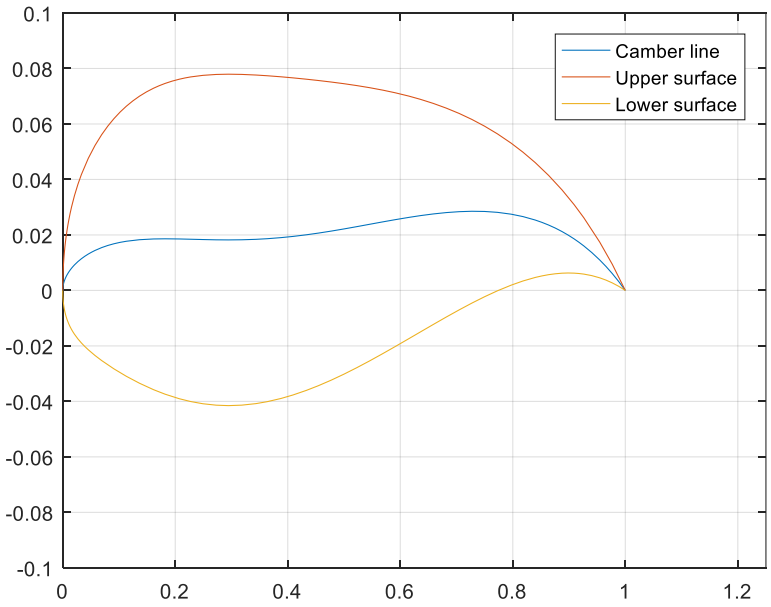

Figure A.1.4: NACA 23012 with deformed camber.

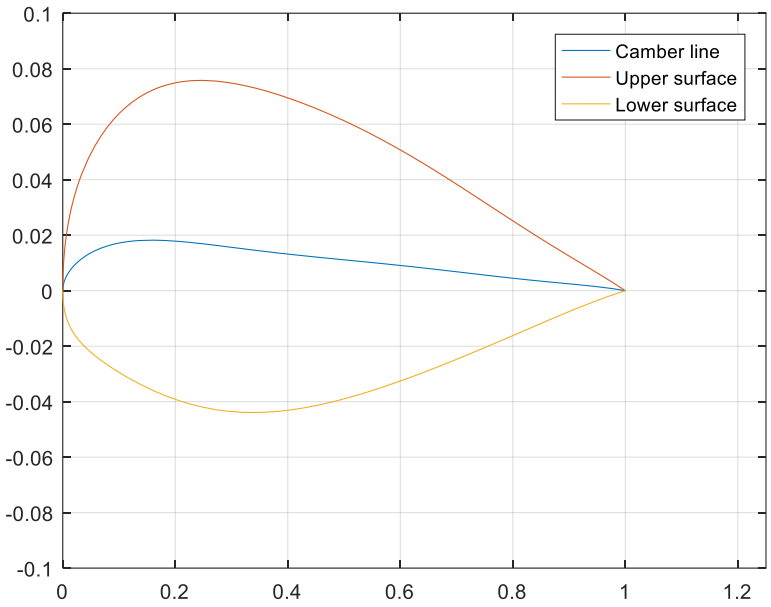

Figure A.5: NACA 23012 with deformed thickness.

A.2 u-CST MATLAB code

```
%%%%%%%%%%%%%%%%%%%%%%%%%%%%%%%%%%%%%%%%%%%%%%%%%%%%%%%%%%%%%%%%%%%%%%%%%%%%
                                    %%%%%

     % Unsteady CST (u-CST) parametrization method for variable camber.



                     %   Chawki Abdessemed, UWE Bristol

%%%%%%%%%%%%%%%%%%%%%%%%%%%%%%%%%%%%%%%%%%%%%%%%%%%%%%%%%%%%%%%%%%%%%%%%%%%%
                                    %%%%%



%define the target airfoil then calculates the coefficients using the Aircra
ftGeometryToolbox



  Airfoil =   naca5(0.3, 0.15, 12, 'High', 100, 0); nBPUpper = 5; nBPLower =
 5;

 [CSTCoeffUpper,CSTCoeffLower] = findcstcoeff(Airfoil,nBPUpper,nBPLower,1);


% Coefficient of the upper surface



   pu0= CSTCoeffUpper(1);

   pu1=CSTCoeffUpper(2);

   pu2=CSTCoeffUpper(3);

   pu3=CSTCoeffUpper(4);

   pu4=CSTCoeffUpper(5);

   pu5=CSTCoeffUpper(6);

   puZ=CSTCoeffUpper(7);

   puLE=CSTCoeffUpper(8);



   PU=[pu0 pu1 pu2 pu3 pu4 pu5 puZ puLE];
```

```
 %Coefficient of the lower surface

   pl0=CSTCoeffLower(1);

   pl1=CSTCoeffLower(2);

   pl2=CSTCoeffLower(3);

   pl3=CSTCoeffLower(4);

   pl4=CSTCoeffLower(5);

   pl5=CSTCoeffLower(6);

   plZ=CSTCoeffLower(7);

   plLE=CSTCoeffLower(8);


 PL=[pl0 pl1 pl2 pl3 pl4 pl5 plZ plLE];


 %%%%%%%%%%%%%%%%%%%%%%%%%%define  equations %%%%%%%%%%%%%%%%%%%%%%%%%%

for t=0:1:10;


%%%%%%%%%%%%%%%%%%%% %Upper surface polynomial %%%%%%%%%%%%%%%%%%%%%%%%%%


 Zu= @(x)sqrt(x)*(1-x)*(pu0*(1-x)^5+pu1*5*x*(1-x)^4+pu2*10*x^2*(1-x)^3 ...

 +pu3*10*x^3*(1-x)^2+pu4*5*x^4*(1-x)+pu5*(x^5))+puLE*x*sqrt(1-x)*(1-
x)^5 ...

 -0.005*(t)*(x)^15+0*x;


%%%%%%%%%%%%%%%%%%%%%%%%%%%%%%%%%%%%%%%%%%%%%%%%%%%%%%%%%%%%%%%%%%%%%%%%%%%%%%%


%%%%%%%%%%%%%%%%%%%%%%%%%%Lower surface polynomial %%%%%%%%%%%%%%%%%%%%%%%%%%


Zl= @(x)sqrt(x)*(1-x)*(pl0*(1-x)^5+pl1*5*x*(1-x)^4+pl2*10*x^2*(1-x)^3 ...

+pl3*10*x^3*(1-x)^2+pl4*5*x^4*(1-x)+pl5*x^5)+plLE*x*sqrt(1-x)*(1-x)^5-
0.005* ...

(t)*(x)^15+(0*x);
```

```
%%%%%%%%%%%%%%%%%%%%%%%%%%%%%%%%%%%%%%%%%%%%%%%%%%%%%%%%%%%%%%%%%%%%%%%%%%%%%%%%

 %%%%%%%%%%%%%%%%%%%%%%%%%%%%%%% Camber line%%%%%%%%%%%%%%%%%%%%%%%%%%%%%%%

 Zc=@(x)sqrt(x)*(1-x)*0.5*[(pu0+pl0)*(1-x)^5+(pu1+pl1)*5*x*(1-
x)^4+(pu2+pl2) ...

     *10*x^2*(1-x)^3+(pu3+pl3) * ...

 10*x^3*(1-x)^2 + ...

 (pu4+pl4)*5*x^4*(1-x)+(pu5+pl5)*x^5-.05*t*x^3]+0.5*(puLE+plLE)*x*sqrt(1-
x) ...

 *(1-x)^5+(puZ+plZ)*x*0.5;


%%%%%%%%%%%%%%%%%%%%%%%%%%%%%%%%%%%%%%%%%%%%%%%%%%%%%%%%%%%%%%%%%%%%%%%%%%%%%%%%

%%%%%%%%%%%%%%%%%%%%%%%%%%Thickness upper%%%%%%%%%%%%%%%%%%%%%%%%%%%%%%%%%%%%


  Zt=@(x)sqrt(x)*(1-x)*0.5*[(pu0-pl0)*(1-x)^5+(pu1-pl1)*5*x*(1-
x)^4+(pu2+ ...

      -pl2)*10*x^2*(1-x)^3+(pu3+-pl3) * ...

   10*x^3*(1-x)^2 + ...

  (pu4-pl4)*5*x^4*(1-x)+(pu5-pl5)*x^2.5]+0.5*(puLE-plLE)*x*sqrt(1-x)*(1-
x)^5 ...

  +-0*(puZ-plZ)*x*0.5;


%%%%%%%%%%%%%%%%%%%%%%%%%%%%%%%%%%%%%%%%%%%%%%%%%%%%%%%%%%%%%%%%%%%%%%%%%%%%%%%%

%%%%%%%%%%%%%%%%%%%%Thickness lower%%%%%%%%%%%%%%%%%%%%%%%%%%%%%%%%%%%%%%%%%%%%
%


Ztl= @(x)-sqrt(x)*(1-x)*0.5*[(pu0-pl0)*(1-x)^5+(pu1-pl1)*5*x*(1-x)^4+(pu2+-
pl2) ...

    *10*x^2*(1-x)^3+(pu3+-pl3) * ...
```

```
  10*x^3*(1-x)^2 + ...

   (pu4-pl4)*5*x^4*(1-x)+(pu5-pl5)*t*x^2.5]+-0.5*(puLE-plLE)* ...

   x*sqrt(1-x)*(1-x)^5+-0*(puZ-plZ)*x*0.5;



%%%%%%%%%%%%%%%%%%%%%%%%%%%%%%%%%%%%%%%%%%%%%%%%%%%%%%%%%%%%%%%%%%%%%%%%%%%%
  %%%%%%%%%%%%%%%%%%%%%%%%%Thickness plus camber upper%%%%%%%%%%%%%%%$%%%%%

 ZCplusTu =@(x)sqrt(x)*(1-x)*0.5*[(pu0+pl0)*(1-x)^5+(pu1+pl1)*5*x*(1-
x)^4+ ...

     (pu2+pl2)*10*x^2*(1-x)^3+(pu3+pl3) * ...

   10*x^3*(1-x)^2 + ...

  (pu4+pl4)*5*x^4*(1-x)+(pu5+pl5)*x^5]+0.5*(puLE+plLE)*x*sqrt(1-x)*(1-
x)^5 ...

  +(puZ+plZ)*x*0.5 + ...

  [sqrt(x)*(1-x)*0.5*[(pu0-pl0)*(1-x)^5+(pu1-pl1)*5*x*(1-x)^4+(pu2+-
pl2) ...

  *10*x^2*(1-x)^3+(pu3+-pl3) * ...

 10*x^3*(1-x)^2 + ...

 (pu4-pl4)*5*x^4*(1-x)+(pu5-pl5)*x^5-.05*t*x^3]+0.5*(puLE-plLE)*x*sqrt(1-
x) ...

 *(1-x)^5+(0.02)*x*0.5];



%%%%%%%%%%%%%%%%%%%%%%%%%Thickness plus camber lower%%%%%%%%%%%%%%%%%%%%%%




  ZCplusTl =@(x)sqrt(x)*(1-x)*0.5*[+(pu0+pl0)*(1-x)^5+(pu1+pl1)*5*x*(1-
x)^4 ...

      +(pu2+pl2)*10*x^2*(1-x)^3+(pu3+pl3) * ...

  10*x^3*(1-x)^2 + ...

  (pu4+pl4)*5*x^4*(1-x)+(pu5+pl5)*x^5]+0.5*(puLE+plLE)*x*sqrt(1-x)*(1-
x)^5 ...

  +(puZ+plZ)*x*0.5 - ...
```

```
   [sqrt(x)*(1-x)*0.5*[(pu0-pl0)*(1-x)^5+(pu1-pl1)*5*x*(1-x)^4+(pu2+-
pl2) ...

   *10*x^2*(1-x)^3+(pu3+-pl3) * ...

  10*x^3*(1-x)^2 + ...

  (pu4-pl4)*5*x^4*(1-x)+(pu5-pl5)*x^5+.05*t*x^3]+0.5*(puLE-plLE)* ...

  x*sqrt(1-x)*(1-x)^5+(0.02)*x*0.5];

 %%%%%%%%%%%%%%%%%%%%%%%%%%%%%%%%%%%%%%%%%%%%%%%%%%%%%%%%%%%%%%%%%%%%%%%

%%%%%%%%%%%%%%%%%%%% Plotting %%%%%%%%%%%%%%%

%Plot upper surface CST

%fplot(Zu,[0,1]);


   %hold on;

%Plot lower surface CST


   % fplot(Zl,[0,1]);


    %Plot camber


    %hold off;

    fplot(Zc,[0,1]);

     hold on;

    %Plot upper thickness

    %fplot(Zt,[0,1]);


   %Plot lower thickness


    %fplot(Ztl,[0,1]);
```

```
    %Plot   thickness + camber

    fplot(ZCplusTu,[0,1]);

    %Plot   thickness - camber

    fplot(ZCplusTl,[0,1]);

      grid on
      legend('Camber line','Upper surface','Lower surface')

    axis([0 1.25 -0.1 0.1])
    %axis auto
     hold off;
          pause(.1);
    % f=getframe;
  %  M(2*t)=f;
%%%%%%%%%%%%%%%%%%%%%%%%%%%%%%%%%%%%%%%%%%%%%%%%%%%%%%%%%%%%

end;
```

Appendix B. UDF for 2D Downward Dynamic Morphing Flap

```
/*********************************************************************/
                /* UDF for 2D Downward Dynamic Morphing Flap.

                        Chawki Abdessemed, UWE Bristol

                     Up/Down  = name shown in Fluent GUI

                                                                     */
/*********************************************************************/
#include "udf.h"

#define Thick       0.12        /*Airfoil thickness 12/100 in NACA 0012 */
#define FTT         0.20001     /*Time in s when the morphing starts*/
#define chord       0.2286      /*Airfoil chord*/


DEFINE_GRID_MOTION(Up, domain, dt, time, dtime)
{
  Thread *tf = DT_THREAD (dt);
  face_t f;
  Node *node_p;
  real  x, y,z,thickness,camber,theta,yupper,dy_c,x_s,xupper,W_te,T_max,Tmor
ph,freq;
  int n;
    freq    =   6;                  /*Morphing frequency*/
    Tmorph= 1/(4*freq);             /*Time in s needed for the morphing*/

    T_max = FTT+Tmorph;             /*Flow time in s when the morphing stops
*/
    W_te= 0.05*chord;               /*Maximum flap deflection */
    x_s = 0.75*chord;               /*location where the morphing starts */


/* Set/activate the deforming flag on adjacent cell zone, which      */
/* means that the cells adjacent to the deforming wall will also be  */
/* deformed, in order to avoid skewness.   */

  SET_DEFORMING_THREAD_FLAG (THREAD_T0 (tf));

/* Loop over the deforming boundary zone's faces;                    */
/* inner loop loops over all nodes of a given face;                  */
/* Thus, since one node can belong to several faces, one must guard  */
/* against operating on a given node more than once:                 */

  begin_f_loop (f, tf)
    {
      f_node_loop (f, tf, n)
        {
          node_p = F_NODE (f, tf, n);

          /* Update the current node only if it has not been         */
          /* previously visited:                                     */


          if (NODE_POS_NEED_UPDATE (node_p))
            {
```

```
              /* Set flag to indicate that the current node's        */
              /* position has been updated, so that it will not be   */
              /* updated during a future pass through the loop:      */
              NODE_POS_UPDATED (node_p);

            x     = NODE_X (node_p);
            z     = NODE_Z (node_p);


            /*Airfoil thickness distribution */

        thickness= (chord*Thick / 0.2) * (0.2969*sqrt(x/chord)-
0.1260*x/chord-0.3516*pow((x/chord),2) + 0.2843*pow((x/chord),3)-
0.1036*pow((x/chord),4));

            /*Loop over the morphing portion*/
        if ( x > x_s) {

            /*define  motion before T_MAX*/

            if ( CURRENT_TIME >= FTT && CURRENT_TIME <= T_max) {


            /*morphing flap*/


                                camber =-(W_te*sin(2*M_PI*(CURRENT_TIME-
FTT)*freq)*pow((x-x_s),3))/(pow((chord-x_s),3));

                                dy_c= (-3*W_te*sin(2*M_PI*(CURRENT_TIME-
FTT)*freq))*pow((x-x_s),2)/(pow((chord-x_s),3));


                                theta = atan(((-3*W_te*sin(2*M_PI*(CURRENT_TIME-
FTT)*freq))*pow((x-x_s),2)/(pow((chord-x_s),3))));

                                xupper = x - thickness*sin(theta);

                                yupper =camber + thickness*cos(theta);

                                NODE_Y (node_p) = yupper ;


            }
            /*morphing stops*/
             if ( CURRENT_TIME > T_max) {


                                camber =-(W_te*sin(2*M_PI*Tmorph*freq)*pow((x-
x_s),3))/(pow((chord-x_s),3));

                                dy_c= (-3*W_te*sin(2*M_PI*Tmorph*freq))*pow((x-
x_s),2)/(pow((chord-x_s),3));

                                theta = atan(((-
3*W_te*sin(2*M_PI*Tmorph*freq))*pow((x-x_s),2)/(pow((chord-x_s),3))));

                                xupper = x - thickness*sin(theta);

                                yupper =camber + thickness*cos(theta);

                                NODE_Y (node_p) = yupper ;
```

```
                }
                }

            }
          end_f_loop (f, tf);
          }

        }
        }

DEFINE_GRID_MOTION(Down, domain, dt, time, dtime)
{
  Thread *tf = DT_THREAD (dt);
  face_t f;
  Node *node_p;
  real  x, y,z,thickness,camber,theta,yupper,dy_c,x_s,xupper,W_te,T_max,Tmor
ph,freq;
  int n;
    freq    =   6;                  /*Morphing frequency*/
    Tmorph= 1/(4*freq);             /*Time in s needed for the morphing*/

    T_max = FTT+Tmorph;             /*Flow time in s when the morphing stops
*/
    W_te= 0.05*chord;               /*Maximum flap deflection */
    x_s = 0.75*chord;               /*location where the morphing starts */


/* Set/activate the deforming flag on adjacent cell zone, which      */
/* means that the cells adjacent to the deforming wall will also be  */
/* deformed, in order to avoid skewness.                             */
  SET_DEFORMING_THREAD_FLAG (THREAD_T0 (tf));


/* Loop over the deforming boundary zone's faces;                    */
/* inner loop loops over all nodes of a given face;                  */
/* Thus, since one node can belong to several faces, one must guard  */
/* against operating on a given node more than once:                 */

  begin_f_loop (f, tf)
    {
      f_node_loop (f, tf, n)
        {
          node_p = F_NODE (f, tf, n);

          /* Update the current node only if it has not been         */
          /* previously visited:
          */

          if (NODE_POS_NEED_UPDATE (node_p))
            {
              /* Set flag to indicate that the current node's        */
              /* position has been updated, so that it will not be   */
              /* updated during a future pass through the loop:      */
              NODE_POS_UPDATED (node_p);

              x     = NODE_X (node_p);
              z     = NODE_Z (node_p);


            /*Airfoil thickness distribution */
```

```
        thickness= (chord*Thick / 0.2) * (0.2969*sqrt(x/chord)-
0.1260*x/chord-0.3516*pow((x/chord),2) + 0.2843*pow((x/chord),3)-
0.1036*pow((x/chord),4));

        if ( x > x_s) {
            if ( CURRENT_TIME>=FTT && CURRENT_TIME <= T_max) {


                                camber =-(W_te*sin(2*M_PI*(CURRENT_TIME-
FTT)*freq)*pow((x-x_s),3))/(pow((chord-x_s),3));

                                dy_c= (-3*W_te*sin(2*M_PI*(CURRENT_TIME-
FTT)*freq))*pow((x-x_s),2)/(pow((chord-x_s),3));


                                theta = atan(((-3*W_te*sin(2*M_PI*(CURRENT_TIME-
FTT)*freq))*pow((x-x_s),2)/(pow((chord-x_s),3))));

                                slope = sin(theta);

                                xlower = x + thickness*slope;

                                lower= camber - thickness*cos(theta);

                                NODE_Y (node_p) = lower ;


            }
             if ( CURRENT_TIME >= T_max) {


                           camber =-(W_te*sin(2*M_PI*Tmorph*freq)*pow((x-
x_s),3))/(pow((chord-x_s),3));

                                dy_c= (-3*W_te*sin(2*M_PI*Tmorph*freq))*pow((x-
x_s),2)/(pow((chord-x_s),3));

                                theta = atan(((-
3*W_te*sin(2*M_PI*Tmorph*freq))*pow((x-x_s),2)/(pow((chord-x_s),3))));

                                slope = sin(theta);

                                xlower = x + thickness*slope;

                                lower= camber - thickness*cos(theta);

                                NODE_Y (node_p) = lower ;

                  }
                  }

            }
          end_f_loop (f, tf);
          }

        }
        }

/************************************************************************/
/*                                                                      */
/*                      End of the UDF.                                 */
/*                                                                      */
/************************************************************************/
```

Appendix C. UDF for 2D Harmonic Morphing Trailing-Edge Flap

```
/************************************************************************/
            /* UDF for 2D Harmonic Morphing Trailing-Edge Flap.

                  Chawki Abdessemed, UWE Bristol

       morphing_upper/lower  = name shown in Fluent GUI
                            dt  = thread
                          time  = current time
                         dtime  = time step
                                                                        */
/************************************************************************/
#include "udf.h"

#define T_max   1           /*Flow time in s when the morphing stops*/
/*#define   x_morph     0.75        /*location where the morphing starts */

#define W_te    0.001*0.2286
#define x_s     0.75*0.2286
#define Thick   0.12
/*#define period    0.0034*/
#define freq    1600
#define FTT     0.8005
#define chord   0.2286


DEFINE_GRID_MOTION(morphing_upper, domain, dt, time, dtime)
{
  Thread *tf = DT_THREAD (dt);
  face_t f;
  Node *node_p;
  real  x, y, thickness,camber,theta,yupper,dy_c,slope,xupper;
  int n;

/* Set/activate the deforming flag on adjacent cell zone, which      */
/* means that the cells adjacent to the deforming wall will also be  */
/* deformed, in order to avoid skewness.                             */
  SET_DEFORMING_THREAD_FLAG (THREAD_T0 (tf));

/* Compute the angles:                                               */


/* Loop over the deforming boundary zone's faces;                    */
/* inner loop loops over all nodes of a given face;                  */
/* Thus, since one node can belong to several faces, one must guard  */
/* against operating on a given node more than once:                 */

  begin_f_loop (f, tf)
    {
      f_node_loop (f, tf, n)
        {
          node_p = F_NODE (f, tf, n);

          /* Update the current node only if it has not been         */
          /* previously visited:                                     */
          if (NODE_POS_NEED_UPDATE (node_p))
            {
```

```
              /* Set flag to indicate that the current node's        */
              /* position has been updated, so that it will not be   */
              /* updated during a future pass through the loop:      */
              NODE_POS_UPDATED (node_p);

              x     = NODE_X (node_p);

            /**[0.298222773*sqrt(x) - 0.127125232*x - 0.357907906*x2 + 0.291
984971*x3 - 0.105174606*x4]*/

            thickness= (chord*Thick / 0.2) * (0.2969*sqrt(x/chord)-
0.1260*x/chord-0.3516*pow((x/chord),2) + 0.2843*pow((x/chord),3)-
0.1036*pow((x/chord),4));


        if ( CURRENT_TIME>FTT) {
            if( x>=x_s) {


                camber =-(W_te*sin(2*M_PI*(CURRENT_TIME-FTT)*freq)*pow((x-
x_s),3))/(pow((chord-x_s),3));

                dy_c= (-3*W_te*sin(2*M_PI*(CURRENT_TIME-FTT)*freq)*pow((x-
x_s),2))/(pow((chord-x_s),3));


                theta = atan(((-3*W_te*sin(2*M_PI*(CURRENT_TIME-
FTT)*freq))*pow((x-x_s),2)/(pow((chord-x_s),3))));



                xupper = x - thickness*sin(theta);


                yupper =camber + thickness*cos(theta);



                    NODE_Y (node_p) = yupper ;
            }
            }
        }

          }

  end_f_loop (f, tf);
  }

}

DEFINE_GRID_MOTION(morphing_lower, domain, dt, time, dtime)
{
  Thread *tf = DT_THREAD (dt);
  face_t f;
  Node *node_p;
  real  x, y, thickness,camber,theta,lower,dy_c,xlower,slope;
  int n;

/* Set/activate the deforming flag on adjacent cell zone, which      */
/* means that the cells adjacent to the deforming wall will also be  */
/* deformed, in order to avoid skewness.                             */
  SET_DEFORMING_THREAD_FLAG (THREAD_T0 (tf));
```

```
/* Compute the angles:                                                */


/* Loop over the deforming boundary zone's faces;                     */
/* inner loop loops over all nodes of a given face;                   */
/* Thus, since one node can belong to several faces, one must guard   */
/* against operating on a given node more than once:                  */

  begin_f_loop (f, tf)
    {
      f_node_loop (f, tf, n)
        {
          node_p = F_NODE (f, tf, n);

          /* Update the current node only if it has not been          */
          /* previously visited:                                      */
          if (NODE_POS_NEED_UPDATE (node_p))
            {
              /* Set flag to indicate that the current node's         */
              /* position has been updated, so that it will not be    */
              /* updated during a future pass through the loop:       */
              NODE_POS_UPDATED (node_p);

              x     = NODE_X (node_p);

            thickness= (chord*Thick / 0.2) * (0.2969*sqrt(x/chord)-
0.1260*x/chord-0.3516*pow((x/chord),2) + 0.2843*pow((x/chord),3)-
0.1036*pow((x/chord),4));

if ( CURRENT_TIME>FTT) {

            if(x >=x_s){


                camber =-(W_te*sin(2*M_PI*((CURRENT_TIME-FTT)*freq))*pow((x-
x_s),3))/(pow((chord-x_s),3));

                dy_c= (-3*W_te*sin(2*M_PI*(CURRENT_TIME-FTT)*freq))*pow((x-
x_s),2)/(pow((chord-x_s),3));


                theta = atan((-3*W_te*sin(2*M_PI*(CURRENT_TIME-
FTT)*freq))*pow((x-x_s),2)/(pow((chord-x_s),3)));

                slope = sin(theta);

                xlower = x + thickness*slope;


                lower= camber -thickness*cos(theta);



                    NODE_Y (node_p) = lower ;
            }
          }
        }
          }
          }

  end_f_loop (f, tf);

}
```

```
/************************************************************************/
/*                                                                      */
/*  End of the UDF.                                                     */
/*                                                                      */
/************************************************************************/
```

Appendix D. UDF for 3D Morphing Wing with Seamless Side-edge Transition

```
/************************************************************************/
       /*UDF for 3D Morphing Wing with Seamless Side-edge Transition.

                  Chawki Abdessemed, UWE Bristol

                        Up/lower  = name shown in Fluent GUI
                             dt   = thread
                           time   = current time
                          dtime   = time step

                                                                      ***/
/************************************************************************/
#include "udf.h"


#define Thick       0.12        /*Airfoil thickness 12/100 in NACA 0012 */
#define FTT         0.20001     /*Time in s when the morphing starts*/
#define chord       0.2286      /*Airfoil chord*/


DEFINE_GRID_MOTION(Up, domain, dt, time, dtime)
{
  Thread *tf = DT_THREAD (dt);
  face_t f;
  Node *node_p;
  real  x, y,z,thickness,camber,theta,yupper,dy_c,xupper,W_t,T_max,Tmorph,fr
eq,W_te,x_s,h,l,ltrans_start,ltrans_end,rtrans_start,rtrans_end;
  int n;
    freq    =   6;                  /*Morphing frequency*/
    Tmorph= 1/(4*freq);             /*Time in s needed for the morphing*/

    T_max = FTT+Tmorph;             /*Flow time in s when the morphing stops
*/
    W_te= 0.05*chord;               /*Maximum flap deflection */
    x_s = 0.75*chord;               /*location where the morphing starts */

    h   =   -0.025*chord;           /*h the half-
amplitude of the TEF deflection*/
    l   = 0.05*chord;               /*l the seamless transition size*/
    ltrans_start    = 0.3*chord;    /*left transition start*/
    ltrans_end  = 0.35*chord;       /*left transition end*/
    rtrans_start    = 0.65*chord;   /*Right transition start*/
    rtrans_end  = 0.7*chord;        /*Right transition end*/

/* Set/activate the deforming flag on adjacent cell zone, which      */
/* means that the cells adjacent to the deforming wall will also be  */
/* deformed, in order to avoid skewness.   */

  SET_DEFORMING_THREAD_FLAG (THREAD_T0 (tf));

/* Loop over the deforming boundary zone's faces;                    */
/* inner loop loops over all nodes of a given face;                  */
/* Thus, since one node can belong to several faces, one must guard  */
/* against operating on a given node more than once:                 */

  begin_f_loop (f, tf)
```

```
    {
      f_node_loop (f, tf, n)
        {
          node_p = F_NODE (f, tf, n);

          /* Update the current node only if it has not been         */
          /* previously visited:                                     */


          if (NODE_POS_NEED_UPDATE (node_p))
            {
              /* Set flag to indicate that the current node's        */
              /* position has been updated, so that it will not be   */
              /* updated during a future pass through the loop:      */
              NODE_POS_UPDATED (node_p);

            x     = NODE_X (node_p);
            z     = NODE_Z (node_p);

            /*definition of transition function*/

            W_t = (h*cos(M_PI*z/l)-h) ;

            /*Airfoil thickness distribution */

        thickness= (chord*Thick / 0.2) * (0.2969*sqrt(x/chord)-
0.1260*x/chord-0.3516*pow((x/chord),2) + 0.2843*pow((x/chord),3)-
0.1036*pow((x/chord),4));
            /*Loop over the morphing portion*/

        if ( x > x_s) {
        if (z>ltrans_start || z< rtrans_end){
            /*define  motion before T_MAX*/

            if ( CURRENT_TIME >= FTT && CURRENT_TIME <= T_max) {
            /*transition modeling*/
                    if ( z > ltrans_start && z < ltrans_end) {

                                camber =-(W_t*sin(2*M_PI*(CURRENT_TIME-
FTT)*freq)*pow((x-x_s),3))/(pow((chord-x_s),3));

                                dy_c= (-3*W_t*sin(2*M_PI*(CURRENT_TIME-
FTT)*freq))*pow((x-x_s),2)/(pow((chord-x_s),3));

                                theta = atan(((-3*W_t*sin(2*M_PI*(CURRENT_TIME-
FTT)*freq))*pow((x-x_s),2)/(pow((chord-x_s),3))));

                                xupper = x - thickness*sin(theta);

                                yupper =camber + thickness*cos(theta);

                                NODE_Y (node_p) = yupper ;
                    }

                    if ((z > rtrans_start) && z < rtrans_end){
                                camber =-(W_t*sin(2*M_PI*(CURRENT_TIME-
FTT)*freq)*pow((x-x_s),3))/(pow((chord-x_s),3));

                                dy_c= (-3*W_t*sin(2*M_PI*(CURRENT_TIME-
FTT)*freq))*pow((x-x_s),2)/(pow((chord-x_s),3));

                                theta = atan(((-3*W_t*sin(2*M_PI*(CURRENT_TIME-
FTT)*freq))*pow((x-x_s),2)/(pow((chord-x_s),3))));
```

```
                                xupper = x - thickness*sin(theta);

                                yupper =camber + thickness*cos(theta);

                                NODE_Y (node_p) = yupper ;
                        }
                /*morphing flap*/
                        if (z >= ltrans_end && z <= rtrans_start) {

                                camber =-(W_te*sin(2*M_PI*(CURRENT_TIME-
FTT)*freq)*pow((x-x_s),3))/(pow((chord-x_s),3));

                                dy_c= (-3*W_te*sin(2*M_PI*(CURRENT_TIME-
FTT)*freq))*pow((x-x_s),2)/(pow((chord-x_s),3));


                                theta = atan(((-3*W_te*sin(2*M_PI*(CURRENT_TIME-
FTT)*freq))*pow((x-x_s),2)/(pow((chord-x_s),3))));

                                xupper = x - thickness*sin(theta);

                                yupper =camber + thickness*cos(theta);

                                NODE_Y (node_p) = yupper ;

                           }

                }
                /* when morphing stops*/
                 if ( CURRENT_TIME > T_max) {
                        if (z > ltrans_start  && z < ltrans_end) {

                                camber =-(W_t*sin(2*M_PI*Tmorph*freq)*pow((x-
x_s),3))/(pow((chord-x_s),3));

                                dy_c= (-3*W_t*sin(2*M_PI*Tmorph*freq))*pow((x-
x_s),2)/(pow((chord-x_s),3));

                                theta = atan(((-
3*W_t*sin(2*M_PI*Tmorph*freq))*pow((x-x_s),2)/(pow((chord-x_s),3))));

                                xupper = x - thickness*sin(theta);

                                yupper =camber + thickness*cos(theta);

                                NODE_Y (node_p) = yupper ;
                           }
                        if (z > rtrans_start && z < rtrans_end){
                                camber =-(W_t*sin(2*M_PI*Tmorph*freq)*pow((x-
x_s),3))/(pow((chord-x_s),3));

                                dy_c= (-3*W_t*sin(2*M_PI*Tmorph*freq))*pow((x-
x_s),2)/(pow((chord-x_s),3));

                                theta = atan(((-
3*W_t*sin(2*M_PI*Tmorph*freq))*pow((x-x_s),2)/(pow((chord-x_s),3))));

                                xupper = x - thickness*sin(theta);

                                yupper =camber + thickness*cos(theta);

                                NODE_Y (node_p) = yupper ;
```

```
                    }
                    if (z >= ltrans_end && z <= rtrans_start) {

                            camber =-(W_te*sin(2*M_PI*Tmorph*freq)*pow((x-
x_s),3))/(pow((chord-x_s),3));

                            dy_c= (-3*W_te*sin(2*M_PI*Tmorph*freq))*pow((x-
x_s),2)/(pow((chord-x_s),3));

                            theta = atan(((-
3*W_te*sin(2*M_PI*Tmorph*freq))*pow((x-x_s),2)/(pow((chord-x_s),3))));

                            xupper = x - thickness*sin(theta);

                            yupper =camber + thickness*cos(theta);

                            NODE_Y (node_p) = yupper ;


                        }

                }
                }
        }
            }
          end_f_loop (f, tf);
          }

        }
        }

DEFINE_GRID_MOTION(Down, domain, dt, time, dtime)
{
  Thread *tf = DT_THREAD (dt);
  face_t f;
  Node *node_p;
  real  x, y,z,thickness,camber,theta,yupper,dy_c,xupper,W_t,T_max,Tmorph,fr
eq,W_te,x_s,h,l,ltrans_start,ltrans_end,rtrans_start,rtrans_end;
  int n;

    freq    =   6;                  /*Morphing frequency*/
    Tmorph= 1/(4*freq);             /*Time in s needed for the morphing*/

    T_max = FTT+Tmorph;             /*Flow time in s when the morphing stops
*/
    W_te= 0.05*chord;               /*Maximum flap deflection */
    x_s = 0.75*chord;               /*location where the morphing starts */

    h   =   -0.025*chord;           /*h the half-
amplitude of the TEF deflection*/
    l   = 0.05*chord;               /*l the seamless transition size*/
    ltrans_start    = 0.3*chord;    /*left transition start*/
    ltrans_end  = 0.35*chord;       /*left transition end*/
    rtrans_start    = 0.65*chord;   /*Right transition start*/
    rtrans_end  = 0.7*chord;        /*Right transition end*/


/* Set/activate the deforming flag on adjacent cell zone, which      */
/* means that the cells adjacent to the deforming wall will also be  */
/* deformed, in order to avoid skewness.                             */
  SET_DEFORMING_THREAD_FLAG (THREAD_T0 (tf));
```

```
/* Loop over the deforming boundary zone's faces;                    */
/* inner loop loops over all nodes of a given face;                  */
/* Thus, since one node can belong to several faces, one must guard  */
/* against operating on a given node more than once:                 */

  begin_f_loop (f, tf)
    {
      f_node_loop (f, tf, n)
        {
          node_p = F_NODE (f, tf, n);

          /* Update the current node only if it has not been         */
          /* previously visited:
          */

          if (NODE_POS_NEED_UPDATE (node_p))
            {
              /* Set flag to indicate that the current node's        */
              /* position has been updated, so that it will not be   */
              /* updated during a future pass through the loop:      */
              NODE_POS_UPDATED (node_p);

              x     = NODE_X (node_p);
              z     = NODE_Z (node_p);
            /*definition of transition function*/

            W_t = (h*cos(M_PI*z/l)-h) ;

            /*Airfoil thickness distribution */
        thickness= (chord*Thick / 0.2) * (0.2969*sqrt(x/chord)-
0.1260*x/chord-0.3516*pow((x/chord),2) + 0.2843*pow((x/chord),3)-
0.1036*pow((x/chord),4));

        if ( x > x_s) {
        if (z>ltrans_start || z< rtrans_end){
            if ( CURRENT_TIME>=FTT && CURRENT_TIME <= T_max) {

                    if ( z > ltrans_start && z < ltrans_end) {


                              camber =-(W_t*sin(2*M_PI*(CURRENT_TIME-
FTT)*freq)*pow((x-x_s),3))/(pow((chord-x_s),3));

                              dy_c= (-3*W_t*sin(2*M_PI*(CURRENT_TIME-
FTT)*freq))*pow((x-x_s),2)/(pow((chord-x_s),3));

                              theta = atan(((-3*W_t*sin(2*M_PI*(CURRENT_TIME-
FTT)*freq))*pow((x-x_s),2)/(pow((chord-x_s),3))));

                              xlower = x + thickness*sin(theta);

                              lower= camber - thickness*cos(theta);

                              NODE_Y (node_p) = lower ;
                          }


                    if (z > rtrans_start && z < rtrans_end){

                              camber =-(W_t*sin(2*M_PI*(CURRENT_TIME-
FTT)*freq)*pow((x-x_s),3))/(pow((chord-x_s),3));
```

```
                                dy_c= (-3*W_t*sin(2*M_PI*(CURRENT_TIME-
FTT)*freq))*pow((x-x_s),2)/(pow((chord-x_s),3));

                                theta = atan(((-3*W_t*sin(2*M_PI*(CURRENT_TIME-
FTT)*freq))*pow((x-x_s),2)/(pow((chord-x_s),3))));

                                xlower = x + thickness*sin(theta);

                                lower= camber - thickness*cos(theta);

                                NODE_Y (node_p) = lower ;

                        }
                        if (z >= ltrans_end && z <= rtrans_start) {

                                camber =-(W_te*sin(2*M_PI*(CURRENT_TIME-
FTT)*freq)*pow((x-x_s),3))/(pow((chord-x_s),3));

                                dy_c= (-3*W_te*sin(2*M_PI*(CURRENT_TIME-
FTT)*freq))*pow((x-x_s),2)/(pow((chord-x_s),3));


                                theta = atan(((-3*W_te*sin(2*M_PI*(CURRENT_TIME-
FTT)*freq))*pow((x-x_s),2)/(pow((chord-x_s),3))));


                                xlower = x + thickness*sin(theta);

                                lower= camber - thickness*cos(theta);

                                NODE_Y (node_p) = lower ;
                        }


                    /*stops*/

                }
                 if ( CURRENT_TIME >= T_max) {

                    if (z > ltrans_start && z < ltrans_end) {

                                camber =-(W_t*sin(2*M_PI*Tmorph*freq)*pow((x-
x_s),3))/(pow((chord-x_s),3));

                                dy_c= (-3*W_t*sin(2*M_PI*Tmorph*freq))*pow((x-
x_s),2)/(pow((chord-x_s),3));

                                theta = atan(((-
3*W_t*sin(2*M_PI*Tmorph*freq))*pow((x-x_s),2)/(pow((chord-x_s),3))));

                                xlower = x + thickness*sin(theta);

                                lower= camber - thickness*cos(theta);

                                NODE_Y (node_p) = lower ;
                            }

                    if (z > rtrans_start && z < rtrans_end){

                                camber =-(W_t*sin(2*M_PI*Tmorph*freq)*pow((x-
x_s),3))/(pow((chord-x_s),3));
```

```
                                dy_c= (-3*W_t*sin(2*M_PI*Tmorph*freq))*pow((x-
x_s),2)/(pow((chord-x_s),3));

                                theta = atan(((-
3*W_t*sin(2*M_PI*Tmorph*freq))*pow((x-x_s),2)/(pow((chord-x_s),3))));

                                xlower = x + thickness*sin(theta);

                                lower= camber - thickness*cos(theta);

                                NODE_Y (node_p) = lower ;
                        }

                            if (z >= ltrans_end && z <= rtrans_start) {

                                camber =-(W_te*sin(2*M_PI*Tmorph*freq)*pow((x-
x_s),3))/(pow((chord-x_s),3));

                                dy_c= (-3*W_te*sin(2*M_PI*Tmorph*freq))*pow((x-
x_s),2)/(pow((chord-x_s),3));

                                theta = atan(((-
3*W_te*sin(2*M_PI*Tmorph*freq))*pow((x-x_s),2)/(pow((chord-x_s),3))));

                                xlower = x + thickness*sin(theta);

                                lower= camber - thickness*cos(theta);

                                NODE_Y (node_p) = lower ;
                            }

                        }
                        }
                }
                    }
                  end_f_loop (f, tf);
                  }

                }
                }

/************************************************************************/
/*                                                                      */
/*                        End of the UDF.                               */
/*                                                                      */
/************************************************************************/
```